Title
Decay of stratified turbulent wakes behind a bluff body

Author
Chongsiripinyo, Karu

Publication Date
2019

UNIVERSITY OF CALIFORNIA SAN DIEGO

Decay of stratified turbulent wakes behind a bluff body

A dissertation submitted in partial satisfaction of the
requirements for the degree
Doctor of Philosophy

in

Engineering Sciences (Mechanical Engineering)

by

Karu Chongsiripinyo

Committee in charge:

Professor Sutanu Sarkar, Chair
Professor Juan C. del Alamo
Professor Ken Melville
Professor Eugene R. Pawlak
Professor Antonio L. Sánchez

2019

The dissertation of Karu Chongsiripinyo is approved, and it is acceptable in quality and form for publication on microfilm and electronically:

Chair

University of California San Diego

2019

DEDICATION

To my parents, Wichai and Suwanna, who have sacrified so much to give me the opportunity to become that which I am capable of becoming.

EPIGRAPH

Turbulence teaches me a fascinating nature of my self,
deterministically chaotic on one end and non-existent on the other.

TABLE OF CONTENTS

LIST OF FIGURES

LIST OF TABLES

ACKNOWLEDGEMENTS

I would like to express my utmost appreciation to my thesis advisor, Professor Sutanu Sarkar, who gave me the opportunity to be part of this scientific community. His remarkable patience, continuous encouragement, and positive attitude allowed me to persevere during difficult moments, learn from mistakes, and grow up. Professor Sutanu has prepared me to be not only an independent researcher and efficient programmer, but also a good teacher. I am grateful to have conducted my research under his guidance over the past six years.

I would like to thank the other members of my thesis committee for their comments and discussions: Professor Ken Melville, Professor Eugene R. Pawlak, Professor Juan C. del Alamo, and Professor Antonio L. Sánchez. Besides my thesis committee, I would like to acknowledge a few other members of the MAE and SIO faculties for their classes: Professor James W. Rottman, Professor Stefan Llewellyn Smith, Professor Forman A. Williams, Professor Thomas R. Bewley, Professor Kraig Winters, and Professor Alison Marsden. I would also like to thank Professor Elias Balaras and Dr. Antonio Posa for sharing their unstratified-flow *Eddy* code which was then extensively modified to simulate stratified wakes.

I want to take this opportunity to express my sincere thank to my undergraduate research advisor Professor Asi Bunyajitradulya at Chulalongkorn University, Thailand, whose research philosophy has left a profound impact on the way I think; my masters thesis advisor Professor Donghyun You currently at Pohang University of Science and Technology (POSTECH), South Korea, who introduced me to high-performance scientific computing; and my former masters thesis advisor Professor C. Fred Higgs at Carnegie Mellon University, who introduced me to computational fluid dynamics. I would also like to acknowledge Professor Kanat Tangwongsan currently at Mahidol University, Thailand, who was my roommate during my stay in Pittsburgh and laid my foundational understanding

of Computer Science.

It has been an immense pleasure working in the Computational Fluid Dynamics Laboratory (CFD Lab). I will miss my past and present lab mates as much as I missed my family when I left Thailand nine years ago. I thank them for their friendship, support, and assistance over the past several years. I look up to Hieu and think of him as my big brother. Matt taught me how to be more organized. Eric has always shared with me his personal experiences. Narsimha's late night shift occasionally overlapped with my early morning hours. I enjoyed regular tennis matches with Vamsi. I liked Anikesh's enthusiasm in regularly giving me random challenges. Masoud's joyfulness and positive attitude are contagious. Iman's healthy life style motivated me to take better care of myself. Conversing with Alex about business ideas, scuba diving and Elon Musk was really enjoyable. Vicky has taught me to be more humble and a better listener. I have failed to emulate Jose's work-life balance but succeeded to imitate his humor. I admire Pranav for his consistency and his will to strive for excellence. I am glad Sungwon joined our lab and shared his experience with us. Lastly, I enjoyed welcoming Sheel to join our Computational Wake Dynamics Laboratory (CWD Lab), a subset of the CFD Lab.

I have thoroughly enjoyed my time in La Jolla with the pleasant weather all year round, Tuesday discount fish tacos at Rubio's, expensive blue fin tuna sashimi at the Nijiya market, runs along Mission Bay, bike rides at Fiesta Island, marathons at Coronado Island, early mornings at RIMAC gym, meditative walks along La Jolla Shores beach, and long solitary hours coding and debugging. Most importantly, my experiences in La Jolla have transformed my world view. Conducting research has encouraged me to question and reflect on myself. It has enabled me to, as objectively as possible, construct a model that better represents how the world works.

Financial support was provided by the Office of Naval Research (ONR) Grant Numbers N00014-15-1-2718 administered by program managers Dr. Ron Joslin, Dr. Tom

Fu, and Dr. Joe Gorski. This work was supported by a grant of computer time from the Department of Defense (DOD) High Performance Computing Modernization Program (HPCMP). Simulations contained in this thesis were performed on Cray XC30/40/50 (Onyx, Conrad, Gordon, Armstrong, Shepard), SGI ICE X (Topaz), Cray XE6m (Copper), and Cray XE6 (Garnet).

The content of Chapter 3, in full, is a reprint of the material as it appears in Chongsiripinyo K., Pal A., and Sarkar S., "On the vortex dynamics of flow past a sphere at Re=3700 in a uniformly stratified fluid", *Phys. Fluids.*, 29(2), 020704, 2017. The dissertation author was the primary researcher and author of this paper.

The content of Chapter 4, in full, is a reprint of the material as it appears in Chongsiripinyo K. and Sarkar S., "Effect of stratification on the turbulent wake behind a sphere at Re=10,000", *10th International Symposium on Turbulence and Shear Flow Phenomena (TSFP10)*, Chicago, USA, 2017. The dissertation author was the primary researcher and author of this paper.

The content of Chapter 5, in full, is a reprint of the material as it appears in Chongsiripinyo K., Pal A., and Sarkar S., "Scaling laws in the axisymmetric wake of a sphere", *Direct and Large-Eddy Simulation XI* (ERCOFTAC Series), pp. 439-444, 2019, Springer. The dissertation author was the primary researcher and author of this paper.

The content of Chapter 6, Chongsiripinyo K. and Sarkar S., "Decay of turbulent wakes behind a disk in homogeneous and stratified fluids", has been submitted for publication in *J. Fluid Mech.* The dissertation author was the primary researcher and author of this paper.

The contents of Appendices are parts of unpublished technical reports written by the dissertation author.

VITA

2019	Ph.D., Engineering Sciences (Mechanical Engineering), University of California San Diego, La Jolla, CA. *"Decay of stratified turbulent wakes behind a bluff body"*
2012	M.S., Mechanical Engineering, Carnegie Mellon University, Pittsburgh, PA. *"Effects of the interface position of water-air flow on turbulent wall structures"*
2008	B.S., Mechanical Engineering, Chulalongkorn University, Bangkok, Thailand. *"Experimental investigation of mixing structure in the near field of a jet in crossflow"*

PROFESSIONAL EXPERIENCE

Fall 2012 - Fall 2014, Spring 2015 - Winter 2019
Graduate research assistant, University of California San Diego
Department of Mechanical and Aerospace Engineering

Fall 2017, Winter 2017, Spring 2018, Winter 2019
Teaching assistant, University of California San Diego
Department of Mechanical and Aerospace Engineering

Winter 2009, Spring 2009
Teaching assistant, Chulalongkorn university
International School of Engineering

Fall 2008, Winter 2009
Teaching assistant, Chulalongkorn university
Department of Mechanical Engineering

Summer 2005 - Summer 2008
Mechanical design engineer, Plasma-Z Engineering Innovator

Summer 2006
Research intern, Chevron Thailand Exploration and Production, Ltd

PUBLICATIONS AND CONFERENCES

Chongsiripinyo K. and Sarkar S., “Decay of turbulent wakes behind a disk in homogeneous and stratified fluids”, *J. Fluid Mech. (submitted)*, 2019.

Chongsiripinyo K, Pal A., and Sarkar S., “On the vortex dynamics of flow past a sphere at Re=3700 in a uniformly stratified fluid”, *Phys. Fluids.*, 29(2), 020704, 2017.

Chongsiripinyo K., Pal A., and Sarkar S., “Scaling laws in the axisymmetric wake of a sphere”, *Direct and Large-Eddy Simulation XI* (ERCOFTAC Series), pp. 439-444, 2019, Springer.

Chongsiripinyo K. and Sarkar S., “Effect of stratification on the turbulent wake behind a sphere at Re=10,000”, *10th International Symposium on Turbulence and Shear Flow Phenomena (TSFP10)*, Chicago, USA, 2017.

Chongsiripinyo K. and Sarkar S., “Into the far wake of the moderately stratified turbulent wake using hybrid spatially-evolving/temporal-model simulation”, *(manuscript completed)*.

Chongsiripinyo K. and You D., “Effects of the interface position of water-air flow on turbulent wall structures”. *J. Mech. Sci. Technol.*, 32(2), 689-695, 2018.

VanDine A., Chongsiripinyo K., and Sarkar S., “Hybrid spatially-evolving DNS model of flow past a sphere”, *Comput. Fluids*, 171, 41-52, 2018.

Ortiz-Tarin JL, Chongsiripinyo K. and Sarkar S., “Stratified flow past a prolate spheroid”, *in preparation for submission to Phys Rev Fluids.*.

Puthan P, Jalalibidgoli M, Ortiz-Tarin JL, Chongsiripinyo K. and Sarkar S., “Numerical investigation of wake past three-dimensional oceanic ridge generated by steady current: boundary effect on vortex shedding”, *in preparation for submission to Ocean Model.*.

Lee S, S.M. Iman Gohari, Chongsiripinyo K. and Sarkar S., “Direct Numerical Simulation of Stratified Ekman layer over a rough surface”, *in preparation for submission to Phys Rev Fluids.*.

Nidhan S., Ortiz Tarin JL., Chongsiripinyo K., and Sarkar S., “Dynamics mode decomposition of stratified wake behind a sphere”, *49th American Institute of Aerodynamics and Astrodynamics Fluid Dynamics Conference and Exhibit*, Dallas, USA, 2019.

Chongsiripinyo K. and Sarkar S., “Decay of stratified turbulent wakes behind a disk at a moderately high Reynolds number”, *71th APS DFD*, Atlanta, USA, 2018.

Puthan P, Jalalibidgoli M, Ortiz Tarin JL., Chongsiripinyo K., and Sarkar S., “Influence of bottom boundary conditions on flow past a three-dimensional hill”, *71th APS DFD*, Atlanta, USA, 2018.

Chongsiripinyo K. and Sarkar S., "A numerical study of moderately stratified wake using hybrid simulations", *12th Southern California Flow Physics Symposium*, Los Angeles, USA, 2018.

Ortiz Tarin JL., Chongsiripinyo K., and Sarkar S., "Stratified flow over a prolate spheroid", *71th APS DFD*, Atlanta, USA, 2018.

Chongsiripinyo K. and Sarkar S., "Body-inclusive simulations of stratified turbulent wakes", *ASME Leadership Summit*, La Jolla, San Diego, 2018.

Ortiz Tarin JL., Chongsiripinyo K., and Sarkar S., "Stratified turbulent wake of a prolate spheroid", *70th APS DFD*, Colorado, USA, 2017.

Chongsiripinyo K. and Sarkar S., "On the decay of stratified wake: A numerical study", *70th APS DFD*, Colorado, USA, 2017.

Jalali M, Ortiz Tarin JL., Chongsiripinyo K, Sarkar S and Pawlak G.R., "Vortex dynamics and wake turbulence in stratified flow past three-dimensional obstacles", *Ocean Science Meeting*, Oregon, USA, 2018.

Chongsiripinyo K. and Sarkar S., "Stratified flow past a sphere at Re = 10,000", *11th Southern California Flow Physics Symposium*, San Diego, USA, 2017.

Pal A., Chongsiripinyo K. and Sarkar S., "Dynamics of flow over a sphere at Re= 3700 in moderate to highly stratified environments", *International Symposium on Stratified Flows*, San Diego, USA, 2016.

Chongsiripinyo K., Pal A., and Sarkar S., "Coherent structures and enstrophy dynamics in highly stratified flow past a sphere at Re= 3700", *69th APS DFD*, Oregon, USA, 2016.

Chongsiripinyo K. and Sarkar S., "Direct simulations of unstratified and stratified turbulent flows past a sphere using a body-conforming grid", *67th APS DFD*, San Francisco, USA, 2014.

Chongsiripinyo K. and You D., "Direct numerical simulations of two-phase channel flows", *Bennett Conference*, Pittsburgh, Pensylvania, USA, 2012.

Limdumrongtum P., Chongsiripinyo K., Nontiwatwanich P., Pimpin A., and Bunyajitradulya A., "Investigation of Mixing Structure in The Near Field of Swirling Jets in Crossflow". *ME-NETT23*, Chiang Mai, Thailand, 2009.

Chongsiripinyo K., Limdumrongtum P., Pimpin A., and Bunyajitradulya A., "Investigation of Mixing Structure in The Near Field of A Jet in Crossflow", *ME-NETT22*, Bangkok, Thailand, 2008.

ABSTRACT OF THE DISSERTATION

Decay of stratified turbulent wakes behind a bluff body

by

Karu Chongsiripinyo

Doctor of Philosophy in Engineering Sciences (Mechanical Engineering)

University of California San Diego, 2019

Professor Sutanu Sarkar, Chair

The dissertation investigates buoyancy effects in turbulent bluff-body wakes that evolve in stratified fluids. The investigation utilizes high-resolution numerical simulations and employs a body-inclusive approach to describe the flow from the body into the far wake unlike the usual temporal-model approximation of most prior stratified-wake simulations. The dissertation is composed of three main parts. The first part focuses on the dynamics of vorticity that accounts for the unexpected regeneration and increase of turbulence in the near-to-intermediate wake when stratification increases in the regime of low body Froude numbers. The second part characterizes buoyancy effects on the evolution of turbulent kinetic energy in a sphere wake at moderate Froude number and an intermediate Reynolds

number. The third part concerns the decay of a disk wake at relatively high Reynolds number and a wide range of Froude numbers, constitutes the major contribution of this thesis, and is summarized below.

Large-eddy simulations (LES) of flow past a disk are performed at $Re = U_b L_b / \nu = 50,000$ and at $Fr = U_b / N L_b = \infty, 50, 10, 2$; U_b is the free-stream velocity, L_b is the disk diameter, ν is the fluid kinematic viscosity, and N is the buoyancy frequency.

In the axisymmetric wake in a homogeneous fluid, it is found that the mean streamwise velocity deficit (U_0) decays in two stages; $U_0 \propto x^{-0.9}$ during $10 < x/L_b < 65$ followed by $U_0 \underset{\sim}{\propto} x^{-2/3}$. Consequently, none of the simulated stratified wakes is able to exhibit the classical 2/3 decay exponent of U_0 in the interval before buoyancy effects set in. The turbulent characteristic velocity, taken as $K^{1/2}$ with K the turbulent kinetic energy (TKE), satisfies $K^{1/2} \underset{\sim}{\propto} x^{-2/3}$ after $x/L_b \approx 10$.

Turbulent wakes are affected by stratification within approximately one buoyancy time scale ($N t_b \approx 1$) after which, provided that $Re_h Fr_h^2 \geq 1$, we find 3 regimes: weakly stratified turbulence (WST), intermediately stratified turbulence (IST), and strongly stratified turbulence (SST). The regime boundaries are delineated by the turbulent horizontal Froude number $Fr_h = u'_h / N L_{Hk}$; here, u'_h and L_{Hk} are r.m.s horizontal velocity and TKE-based horizontal wake width. WST begins when Fr_h decreases to $O(1)$, spans $1 \lesssim N t_b \lesssim 5$ and, while the mean flow is strongly affected by buoyancy in WST, turbulence is not. Thus, while the mean flow transitions into the so-called non-equilibrium (NEQ) regime, turbulence remains approximately isotropic in WST. The next stage of IST, identified by progressively increasing turbulence anisotropy, commences at $N t_b \approx 5$ once Fr_h decreases to $O(0.1)$. During IST, the mean flow has arrived into the NEQ regime with a constant decay exponent, $U_0 \propto x^{-0.18}$, but turbulence is still in transition. The exponent of 0.18 for the disk wake is smaller than the approximately 0.25 exponent found for the stratified sphere wake. When Fr_h decreases by another order of magnitude to $Fr_h \sim O(0.01)$, the wake transitions into the third regime of SST that is identified based on the asymptote of turbulent vertical Froude number ($Fr_v = u'_h/Nl_v$) to a $O(1)$ constant. During SST that commences at $Nt_b \approx 20$, turbulence is strongly anisotropic ($u'_z \ll u'_h$), and, both u'_h and U_0 satisfy $x^{-0.18}$ decay signifying the arrival of the NEQ regime for both turbulence and mean flow. Turbulence is patchy and temporal spectra are broadband in the SST wake.

Energy budgets reveal that stratification has a direct and positive influence on the prolongation of wake life. During the WST/early-IST stage, energy budgets show that the mean buoyancy flux acts to augment the MKE before the additional augmentation by reduced turbulent production. On the other hand, during WST/early-IST, the decay of TKE is faster than the unstratified case because of negative buoyancy flux (a sink that serves to increase turbulent potential energy) and increased dissipation and, additionally, also by the reduced production. In the late-IST/early-SST stages, production is enhanced and, additionally, there is injection from turbulent potential energy so that the TKE decay slows down. Only in the SST stage, when NEQ is realized for both the mean and turbulence, the turbulent buoyancy flux becomes negative again, acting as a sink of TKE.

Chapter 1

Introduction

1.1 Turbulent flows

Turbulence in a fluid remains the most difficult unsolved problem in classical mechanics. It is ubiquitous in nature, widespread in industrial applications, and often considered as the natural state of fluid flow. Multi-scale, random, diffusive, and dissipative are descriptive of the state of motion referred to as turbulent flow. While there is no rigorous definition for the phenomenon of turbulence, one can easily differentiate a turbulent flow from other states of motion by its characteristic descriptions. For instance, is the flow in figure 1.1 turbulent?

- **Multi-scale phenomenon**. If we were to sketch a photo to resemble the drawing of fluid motion by Leonardo Da Vinci from the 16^{th} century, we would draw a number of somewhat circular shapes of different sizes where smaller circles were placed inside the boundary of a bigger one. We would then continued to fill in yet more even smaller circles inside the small circles and so on. We would carefully outline our “eddies” so that they could fit into the bigger eddies. This exercise illustrates the multiscale

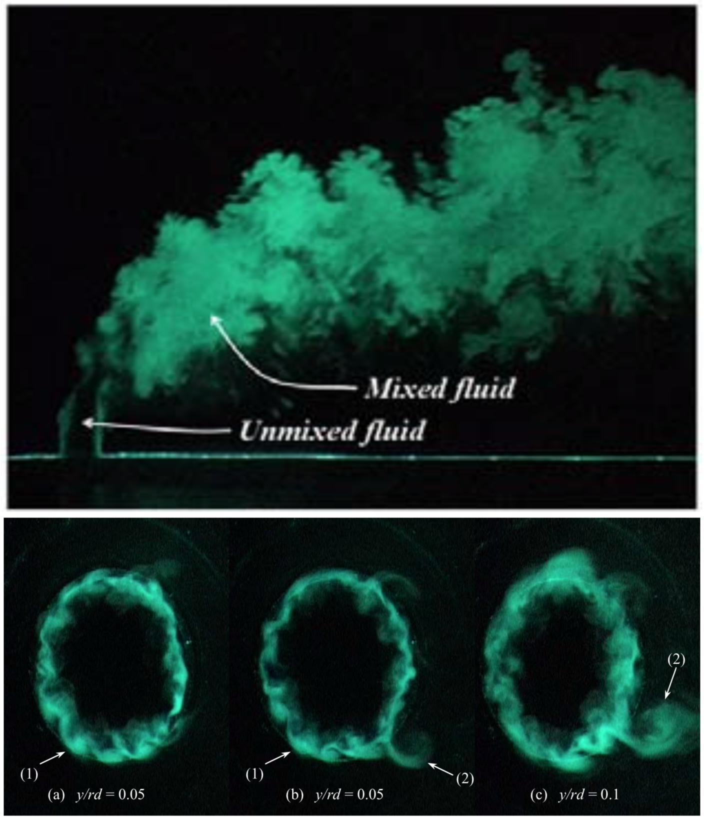

Figure 1.1: Visualization of a jet in crossflow, side-view (top) and top-view (bottom). The figure is taken from Chongsiripinyo *et al.* (2008).

nature of turbulence. Apart from the multi-scale property, the concepts of energy cascade and similarity play a crucial role in the theory of turbulence formulated by Andrey Nikolaevich Kolmogorov in 1941. As beautifully depicted by Lewis Fry Richardson, ‘Big whirls have little whirls, That feed on their velocity; And little whirls have lesser whirls, And so on to viscosity.’

- **Randomness**. The picture we drew representing a snapshot of a time-varying motions appears unpredictable and chaotic. Especially for those tiny structures embedded in a larger circle, we could call their motions loosely as random fluctuations. Perhaps, a hummingbird might describe them differently! Nevertheless, Newton’s laws of motion, being the underlying physical mechanism, are deterministic. One

Figure 1.2: Leonardo da Vinci's illustration of the turbulent flows.

often, therefore, refers to the phenomenon as 'deterministic chaos'.

- **Diffusion**. Turbulent flow is considered to possess "super diffusivity" which, in fact, is the enhanced transport by turbulent advection. G.I. Taylor originated the idea of turbulent advection and published a paper titled 'Diffusion by continuous movements' in 1922, Taylor (1922). Taylor's paper led to the idea of velocity correlation, considered to be one of the three most important workhorses in the statistical theory of turbulence (besides second-order structure function and energy spectrum). The paper was motivated by his earlier publication titled 'Eddy motion in the atmosphere', GI Taylor (1915), where Taylor observed that turbulent motion could diffuse heat and other diffusive scalars. In his 1922 paper, he started with the problem of random migration in one dimension and found that the amount of "diffusion" is proportional to the square-root of time provided that the process has gone for a sufficiently long time. The significance is that the dimensions of the coefficient multiplying time in Taylor's result is the same as that of the kinematic viscosity, thus qualifying as a diffusion coefficient. Diffusion by continuous movements is synonymous to transport by small-scale velocity fluctuations. This is why we often model Reynolds stresses as diffusion with a so-called "turbulent viscosity", that is a property of fluid motion and is not a material property.

- **Dissipation**. Turbulent flows exhibit small scales of motion where the effect of viscous dissipation in enhanced. The small scale motions have large vorticity that is the direct result of vortex stretching that increases the velocity gradient from that of the large-scale flow instabilities until vortex stretching is ultimately arrested on the scale where viscosity dominates (around $Re \sim O(1)$). According to a theorem of hydrodynamics, the total rate of dissipation is proportional to the volume integrated vorticity,

  $$-\frac{d}{dt}\int \frac{1}{2}\rho v^2 dV = \mu \int |\nabla \times \vec{v}|^2 dV, \tag{1.1}$$

  where $\vec{v}$ denotes velocity, ν is molecular viscosity, and V stands for volume. Thus, sustaining turbulence in a fluid requires a sufficient rate of energy injection to overcome small-scale irreversible conversion from kinetic energy to thermal energy.

The state of fluid motion can be characterized by competition between diffusion and advection acting upon linear momentum $\rho u_i'$. Pressure is a Lagrangian multiplier that imposes the solenoidal constraint on velocity, is related to the velocity through a Poisson equation, and does not change the essence of the following argument. Consider a control volume that bounds a region of fluid. The linear momentum of the control volume will keep increasing if $\rho u_i'$ is advected into the control volume, by u_j', with a rate faster than diffusion can react. If so, it leads to a more non-uniform distribution of linear momentum in the flow field or an increase in velocity gradient. Essentially, it is the competition between a mechanism that relaxes curvature in three-dimensional space versus another mechanism that promotes non-uniformity. In other words, if the diffusion timescale is larger than the advection timescale, the velocity field becomes locally non-uniform corresponding to an increase in vorticity (a building block of turbulent flows). The ratio between diffusion and advection time scales is given by the Reynolds number introduced by Osborne Reynolds in 1883,

$$Re = \frac{\tau_\nu}{\tau_i} = \frac{l^2/\nu}{l/u} = \frac{ul}{\nu}. \tag{1.2}$$

Turbulent flow is a collection of eddies of various Reynolds numbers, from $Re_\eta \sim O(1)$ to a sufficiently large Re_c. Since, dissipation peaks at $Re_\eta \sim O(1)$, turbulent flow can be characterized using a single number, $Re_c = UL/\nu$ where U and L are the characteristic velocity and characteristic length scale of the energy-containing range. On the other side, $Re_\eta \sim O(1)$ characterizes the smallest scale in turbulent flow, the Kolmogorov microscale. In between, but sufficiently far from the dissipative range, turbulent eddies in the inertial subrange manifest self-similarity as there is no external scale imposed from either side leading to the famous -5/3 exponent of the energy spectrum.

1.2 Density-stratified flows

Density-stratified flows behave differently than their unstratified counterparts due to the additional vertical gravitational body force that acts on fluid parcels whose density is different from the background stable configuration. A fluid parcel being in non-equilibrium seeks to return to its stable configuration with gravitational assist, i.e buoyancy. The magnitude of the vertical force of buoyancy is a function of gravity and deviation of density from the background. Density stratification can significantly affect a state of flow if the buoyancy force it introduces is comparable to inertial and viscous forces. For stratified flows, the so-called ‘buoyancy Reynolds number’ is analogous to the Reynolds number in which it serves as a good indicator for determining a state of a flow. The buoyancy Reynolds number,

$$Re_b = \frac{\varepsilon}{\nu N^2}, \tag{1.3}$$

can be considered a “modified Reynolds number” which accounts for the additional forces in stratified flow. Here, ε is the rate of dissipation of turbulent kinetic energy and N is the buoyancy frequency. Section 2.2 gives more details on the buoyancy Reynolds number via the scaling analysis of stratified turbulence. The results of chapter 6 support the notion that the flow state becomes or remains turbulent providing that the buoyancy Reynolds number is sufficiently large even when stratification is strong.

The other crucial dimensionless number that quantifies the strength of density stratification is Froude number,

$$Fr = \frac{\tau_b}{\tau_i} = \frac{N^{-1}}{l/u} = \frac{u}{Nl}. \tag{1.4}$$

Froude number, being the ratio between buoyancy time scale and inertial timescale, is the normalized temporal response of buoyancy effect. Small Froude number corresponds to strong stratification and vice-versa. While eddies in a stratified turbulent flow have a direct correlation between their sizes and their Reynolds number, there is an inverse correlation between their sizes and their Froude numbers. Therefore, it is possible for the existence of a region lying in wavenumber space that is far enough from the Ozmidov length scale, $l_o = (\varepsilon/N^3)^{1/2}$ (the largest scale at which an eddy can overturn), and from the Kolmogorov dissipative scale in which similarity can prevail for Kolmogorov-like turbulence. Results in chapter 6 show that a stratified turbulent wake may exhibit unstratified high-Reynolds-number isotropic decay of velocity fluctuations although the largest scales of the flow are affected by buoyancy.

Besides altering the characteristics of eddies at different scales, a stratified environment is known to suppress energy influx to turbulent motions. This is due to the tendency of a fluid element to return to a stable configuration. The suppression of vertical motion leads to a reduction of Reynolds stresses associated with vertical velocity fluctuation. This, in turn, reduces production of turbulent kinetic energy. This is generally true in the early response of a turbulent flow to stratification in which its local Reynolds number is large. The reduction in production of turbulent kinetic energy signifies that a stratified flow better retains mean kinetic energy in comparison to its unstratified counterpart while its turbulent portion is expected to be less energetic. Additionally, stratification enables a potential energy reservoir that is capable of receiving and injecting energy to the kinetic motions, both the mean and turbulent, through the so-called 'buoyancy flux'. The ability to store and transfer between two types of energy enables a stratified medium to periodically exchange energy. Stratified flow can, therefore, propagate energy in the form of a wave or specifically an 'internal gravity wave'.

1.3 Numerical simulations

Numerical simulations are a useful tool in the scientific endeavor to understand natural phenomena, describe reality, and also design engineering devices/products. Among the approaches of physical experiments, theories, and simulations, physical experiments are the only approach which have a direct connection with nature. Numerical simulations and the theoretical approach have helped us make tremendous progress in scientific efforts. Numerical simulations seek an approximate discrete solution to a governing equation (or a system of governing equations), derived from a physical law that is too complex to be solved analytically. Equations derived by mathematicians/theoreticians which are to be explored numerically need not relate to the real world as we perceive it. Indeed, numerical simulations can be used to explore exotic theories which describe phenomena that are not yet observable. However, from our engineering point of view, we utilize the Navier-Stokes equations currently known to be the best representation of the dynamics of a fluid. The Navier-Stokes equations, theorized by the French engineer/physicist Claude-Louis Navier and the Irish mathematician/physicist George Gabriel Stokes, have been tested against numerous experiments and remain the top candidate for describing flow motions.

Numerical simulation arrives at an approximate solution by solving a discrete version of a governing equations. The discretization is done typically for all independent variables, space and time, within the framework of the time-varying Navier-Stokes equations. We then seek out a proper numerical method or a combination of numerical methods for solving the discrete system as efficiently as possible. Normally, an accuracy of a numerical solution is inversely proportional to how fast we obtain it computationally. Depending on practicality, 70% accuracy could be sufficient for an engineer to make decisions with a high level of confidence.

With this information, the need for improved computational power and speed follows. Computing performance is quantified by operations per second or floating-point operations per second ('FLOPS') for real-number arithmetic. Questions such as 'How many FLOPS is enough?' depend upon what problem we are tackling. To elaborate, we provide an example adapted from Pacheco (1997). Suppose we would like to predict the weather over the entire state of California for the next day. Also, suppose that we want to model the atmosphere from sea level to an altitude of 10 kilometers, and we need to make a prediction of the weather at each hour for the next day. A standard approach is to put a computational box over the region of interest with a grid and then predict the weather at each vertex of the grid. Suppose we use a cubical grid, with each cube measuring 10 meters on each side. Since the area of the state of California is about 150,000 square miles or roughly 400,000 square kilometers, we'll need at least

$$400000\ \text{km}^2 \times 10\ \text{km} \times (\frac{1}{0.01})^3 \text{ cubes per km}^3 = 4 \times 10^{12} \text{ grid points.} \tag{1.5}$$

If it takes 100 calculations to determine the weather at a grid point, then it takes about 4^{14} calculations to predict the weather one hour from now. For 24 hours, we will need to make about $24 \times 4 \times 10^{14} \approx 10^{16}$ calculations. If we dare to use a single processing unit that is able to execute 1 billion (10^9) calculations per second, it will take about

$$10^{16} \text{ calculations}/10^9 \text{ calculations per second} = 10^7 \text{ seconds} \approx 115 \text{ days.} \tag{1.6}$$

This means that by the time the simulation is done, the weather would be 114 days ahead of us! Two additional points to be considered are that, first, using a time step so as to segment 1 hour using 100 calculations can be problematic and, second, using a cube of size 10 meters on each side may cause a numerical issue. Unless a chosen combination of governing equations and algorithms is numerically stable, we will not be able to perform the simulation in the first place.

There is a number of ways in which we can accelerate our weather prediction. First, we can use multiple processing units to tackle the problem rather than using a single core. A simulation that takes 115 days can be done in about 2 days if we use 64 CPUs providing that our choice of algorithm allows an efficient parallel scalability. The ideal scaling is to get the same work done N times faster on N CPUs as opposed to 1 CPU.

Second, we realize that fluid turbulence is multi-scale. Depending on our objective, we can choose not to resolve all scales down to the Kolmogorov microscale. Since capturing an eddy of size L requires resolution of approximately L/2 (similar to the idea of the Nyquist frequency), solving a high Reynolds number turbulent flow can be extremely time consuming. The process of deriving a governing equation that only contains a selected range of scales is called ‘filtering’. Generally, a low-pass filter is applied in which the resulting filtered Navier-Stokes equations govern the dynamics of large-scale eddies leaving the small-scale influence to be modeled. In weather prediction, for example, a system of filtered equations is almost always employed. On the other hand, solving the governing Navier-Stokes equations directly is what is referred to as performing a ‘Direct Numerical Simulation’ or DNS. ‘Large-Eddy Simulation’ or LES solves the filtered Navier-Stokes equations in which small-scale eddies beyond a certain size are modeled rather than directly solved. As LES models treat small-scale eddies as locally homogenous isotropic, the filter size has to lie in the inertial subrange in which such behavior is realized. Lastly, in the ‘Reynolds-Averaged Navier-Stokes’ or RANS, we model all turbulent activity and only solve for mean quantities. Obviously, DNS is the most computationally demanding and RANS is the least. In this work, we use DNS for simulations presented in chapter 3 and 5, while LES is used for simulations presented in 4, 5, and 6.

Chapter 2

Background

Wakes, in general, are distinctive disturbances from a background state caused by flow past an obstruction. The wake in a fluid has long been considered to be one of the canonical problems in fluid dynamics. Its ubiquity comes from the fact that wake formation requires only a non-zero relative velocity between an object and the fluid that the object is immersed in. Often we are unaware of its presence. Wakes can be found virtually everywhere from a very large to a very small scale, e.g. flow around topographic features such as islands and mountains, behind a moving vehicle, behind us while we are walking, behind an object in an air-circulated room, behind a droplet or a red blood cell, etc. While understanding application-scale wakes can, for example, help reduce fuel consumption, alter mixing efficiency and improving engine performance, large-scale wakes in the environment can have significant impact on local weather, air pollution, ocean stratification, etc.

Wakes in the ocean are almost always subject to stabilizing buoyancy forces at some point in their lifetime since the ocean interior has stable density stratification. Atmospheric wakes are subject to stabilizing buoyancy forces in the stable atmospheric boundary layer (ABL) but are destabilized by buoyancy in the convective ABL. An initial estimate of the influence of buoyancy can be obtained by comparing the buoyancy timescale to the integral time scale of the wake. The timescale of a wake can be calculated by assuming that the initial velocity deficit, U_c, is comparable to the relative velocity between the wake generator and the ambient flow, U_∞. The initial wake dimension, L_c, is comparable to the lengthscale of the wake-generating body, L. This gives $N^{-1}/LU_\infty^{-1} = Fr$ as a measure of the initial strength of stratification. A local downstream strength of stratification is inversely measured by the "deficit" Froude number, $Fr(x) = N^{-1}/L_c(x)U_c^{-1}(x)$, where x is the downstream distance from the body and $L_c(x)$ is the wake width. The value of $Fr(x)$ strictly decreases with increasing x, implying that even with initially weak stratification, a stratified wake will eventually be affected by stratification.

2.1 Evolution of stratified wakes

A stratified wake evolves through three distinct dynamical regimes referred to as the three-dimensional (3D), non-equilibrium (NEQ), and quasi-two-dimensional (Q2D) regimes as described by Spedding (1997). Even without an imposed mean velocity, de Bruyn Kops & Riley (2019) recently found that the patches of initially isotropic homogenous turbulence pass through different regimes analogous to those seen in the stratified wake behind a sphere as in the work by Spedding (1997). Consider a stratified wake resulting from a uniform flow past an axisymmetric body. The following sections explain each regime of decay.

2.1.1 The three-dimensional (3D) regime

In early development, given a sufficiently large initial $Fr = U_\infty/NL$, an initially axisymmetric stratified wake evolves as if in an unstratified fluid during the so-called 3D regime. Though the wake remains axisymmetric and appears largely unchanged, the buoyancy force progressively increases with respect to the inertial force. Considering a sufficiently high $Re = U_\infty L/\nu$ at which we expect the high-Re self-similarity solution where the decay rate of mean streamwise velocity deficit, $U_0 \propto x^{-2/3}$, and the spread of lateral wake dimension, $L \propto x^{1/3}$, (Townsend, 1976; Tennekes & Lumley, 1972; George, 1989), the inertial force and the buoyancy force (per unit mass) are proportional to

$$U_0^2 L^{-1} \propto x^{-5/3} \quad \text{and} \quad N^2 L \propto N^2 x^{1/3} \tag{2.1}$$

, respectively, in a stably stratified fluid where $N^2 = -g\rho_0^{-1}\partial_z \rho$ with ρ_0 and z being the reference density and the vertical direction. In other words, the local Froude number decays like

$$Fr^2 = \frac{U_0^2 L^{-1}}{N^2 L} \propto (Nx)^{-2} \rightarrow Fr \propto (Nx)^{-1} \tag{2.2}$$

or $Fr \sim (Nt)^{-1}$ where $t = x/U_\infty$. If we assume that turbulent quantities such as a component of velocity fluctuation or a lateral wake dimension scales with their mean flow counterparts, the local turbulent $Fr_t = u'/Nl \propto (Nx)^{-1}$ or $Fr_t \sim (Nt)^{-1}$. The decay of local Froude number for the homogeneous, isotropic high-Re turbulence of Saffman (1967) which assumes $E(k) \sim L_s k^2$ as $k \rightarrow 0$ (L_s is the Saffman integral) subjected to stable stratification will initially be $Fr \sim t^{-3/5}/Nt^{2/5} \sim (Nt)^{-1}$.

Riley *et al.* (1981); Riley & Lelong (2000) studied the decay of homogeneous turbulence in density-stratified fluids and found that the early evolution is expected to last for about one buoyancy time scale $Nt \approx 1$ after flow initiation. Similarly, Liu (1995) also found that the grid turbulence responses to stratification after one buoyancy period, specifically an abrupt reduction the decay rate of the turbulent kinetic energy occurs at $Nt/2\pi \approx 1$. In the experiment of decaying turbulent wakes in a stably stratified fluid, Spedding (1997) identified $Nt = 1.7 \pm 0.3$ as the location where the 3D regime ends.

2.1.2 The non-equilibrium (NEQ) regime

As the buoyancy force becomes comparable to the inertial force, quantified by the $Fr \approx 1$, the effect of stratification manifests and the stratified wake transitions towards the intermediate stage or the NEQ regime where the vertically-disturbed fluid seeks its equilibrium causing the wake's vertical span to decrease. While the effect of stratification directly acts upon large-scale components, small-scale structures whose timescale is not yet comparable to N^{-1} can be indirectly affected due to reduction of turbulence production (Pal *et al.*, 2017; Chongsiripinyo & Sarkar, 2017) and the modification of nonlinear dynamics via suppression of vortex stretching (Chongsiripinyo *et al.*, 2017). Even though 'wake-collapse' is used to qualify this regime, it is understood in the sense that the wake's vertical span decreases but the very definition of the wake involving deficit of mean streamwise momentum remains intact.

The NEQ period is the least understood because the wake adjusts to stratification by complex coupling in anisotropic (both in velocity components and in length scales) motions among buoyancy, inertial and viscous forces. However, its general attributes have been characterized. After the "collapse", it has been found that the decay rates of centerline mean deficit velocity, total kinetic energy, and turbulence are inhibited; turbulent-generated internal gravity waves propagate; and a complicated exchange between kinetic and potential energies takes place. In the universal evolution of a stratified wake proposed by Spedding (1997), the evolution of U_0 is experimentally found to be close to $U_0 \propto x^{-0.25}$. A similar substantial reduction of the wake decay from the unstratified rate of decay theoretically derived as $U_0 \propto x^{-2/3}$ has also been repeatedly observed in numerical simulations, Dommermuth *et al.* (2002); Brucker & Sarkar (2010); Diamessis *et al.* (2011); de Stadler *et al.* (2010); Redford *et al.* (2015); Pal *et al.* (2017); Chongsiripinyo & Sarkar (2017), and was theoretically described by Meunier *et al.* (2006). Associated with U_0

are the horizontal wake width (L_h) and the vertical wake height (L_v). While the rate of decay $U_0 \propto x^{-m}$ is fairly well established, the rates of growth for $L_{h,v}$ remain somewhat inconclusive. Meunier *et al.* (2006), using the conservation of momentum deficit, arrived at the relation $U_0 L_h L_v = \text{const} = U_\infty L (c_d/2)^{1/2}/8$ where c_d is the drag coefficient of a wake generator. The relation suggesting the constraint $L_h L_v = U_0^{-1}\text{const}$ is based, however, on the presumption that a downstream lateral profile of U_0 is Gaussian. Temporal-model towed-wake simulations of Brucker & Sarkar (2010) and Diamessis *et al.* (2011) show $L_h \propto x^{1/3}$ over a large portion of the wake development. During the NEQ phase, the vertical wake span L_v initially decreases (because of the "collapse") and has been found to slightly decrease later on (Brucker & Sarkar, 2010). We will look closely at the evolution of L_v in the disk-wake study of this thesis.

The stratified wake preserves kinetic energy as evidenced from a reduction in its rate of decay. According to Spedding (1997); Dommermuth *et al.* (2002); Diamessis *et al.* (2011), this is attributed to the 'restratification' effect where available potential energy is being transfered back to kinetic energy during the collapse via the buoyancy flux. Brucker & Sarkar (2010) argued that the implicit effect of stratification on production and dissipation of turbulent kinetic energy is another possibility and can be as important as buoyancy flux in the preservation of wake life. Recently, Redford *et al.* (2015) showed that the implicit effect of buoyancy, in which stratification modifies turbulent structures (associated with Reynolds stresses), leads to a substantial increase in turbulent production in the late wake rather than a decrease. Interestingly, the result of Redford *et al.* (2015) revealed that the direct effect of buoyancy plays a secondary role. Our simulations of flow over a disk in 6 compare the direct and indirect effects of buoyancy and offer an explanation of why stratified wakes 'live longer'.

The NEQ was experimentally found to last from $Nt \approx 2$ to $Nt \approx 50$ by Spedding (1997). However, the simulations of Brucker & Sarkar (2010); Diamessis *et al.* (2011)

later found that the duration of the NEQ regime is prolonged at higher Reynolds number. Diamessis *et al.* (2011) attributed the regime prolongation to instabilities, possible at high Re, in inclined shear layers. The theoretical model of Meunier *et al.* (2006) also indicated that the beginning of the quasi-two-dimensional regime that follows the NEQ regime is approximated at $x/D_m \approx Fr^{2/3}Re$, a function of both Fr and Re numbers.

2.1.3 The quasi-two-dimensional (Q2D) regime

The influence of stratification becomes progressively more prominent as the local Froude number keeps decreasing. This is because of the progressive increase in the flow inertial timescale that becomes significantly larger than that of the buoyancy. The stratified wake patch becomes increasingly two-dimensional due to the strong suppression of vertical motions. While the Q2D regime is often associated with the existence of 'pancake' vortices, the regime can be strictly characterized by the reduction of U_0. According to Spedding (1997), the regime happens much earlier at $Nt \approx 50$ while the two-dimensional pancake-like structures are found to emerge at $Nt \approx 250$ in the simulations of Brucker & Sarkar (2010). $Nt \approx 250$ can be translated into a downstream distance that depends on the initial Froude number. For example, pancake structures were found at $x/D \approx 6$ at the very low $Fr = 0.025$ by Chongsiripinyo *et al.* (2017), or $Nt \approx 250$ where D is the sphere diameter. Although pancake structures are widely observed in the far field of the stratified wake, they are in fact a generic feature of strongly stratified flows as their 'vertically-thin' manifestation is commonly caused by suppression of vertical motions. Investigations of the emergence and evolution of pancake-like coherent structures can be found, among others, in Flór *et al.* (1995); Riley & Lelong (2000); Beckers *et al.* (2001); Godoy-Diana & Chomaz (2003); Godoy-Diana *et al.* (2004); Praud (2005); Spedding *et al.* (1996b). Of interest is the work of Godoy-Diana *et al.* (2004) who suggested the viscous scaling $L_v \equiv L_h Re^{-1/2}$ based upon the conditions $Fr_h \ll 1$ and $ReFr_h^2 \ll 1$.

2.2 Scaling analysis of stratified turbulence

The introduction to high-Re stratified wakes explored in this dissertation would not be complete without a scaling analysis of the Navier-Stokes equations subject to density stratification. The analysis is performed with the focus on a highly-stratified environment. The Froude number is small, i.e. the horizontal velocity, U, the horizontal length scale, l_h, and the buoyancy frequency, N, are such that $Fr_h = U/Nl_h < O(1)$. Examination of the dominant balances in the nondimensional equations leads not only to the vertical length scale, l_v, but also the factor $\mathcal{R}$ related to the shear Richardson number suggesting that even for $Fr_h \ll 1$, turbulence can be obtained for sufficiently high Re. The governing equations are

$$\nabla_h^* \cdot u_h^* + \frac{\partial w^*}{\partial z^*} = 0, \tag{2.3}$$

$$\frac{\partial u_h^*}{\partial t^*} + (u_h^* \cdot \nabla_h^*) u_h^* + w^* \frac{\partial u_h^*}{\partial z^*} = -\frac{1}{\rho_0} \frac{\partial p^*}{\partial x_h^*} + \nu \frac{\partial^2 u_h^*}{\partial x_j^* \partial x_j^*}\,, \tag{2.4}$$

$$\frac{\partial w^*}{\partial t^*} + (u_h^* \cdot \nabla_h^*) w^* + w^* \frac{\partial w^*}{\partial z^*} = -\frac{1}{\rho_0} \frac{\partial p^*}{\partial z^*} + \nu \frac{\partial^2 w^*}{\partial x_j^* \partial x_j^*} - \frac{\widetilde{\rho}^* g}{\rho_0}\,, \tag{2.5}$$

$$\frac{\partial \widetilde{\rho}^*}{\partial t^*} + u_h^* \frac{\partial \widetilde{\rho}^*}{\partial x_h^*} + w^* \frac{\partial \widetilde{\rho}^*}{\partial z^*} + w^* \frac{\partial \overline{\rho}}{\partial z^*} = \kappa \frac{\partial^2 \widetilde{\rho}^*}{\partial x_j^* \partial x_j^*}\,. \tag{2.6}$$

Here, a superscript * denotes dimensional quantity and a subscript h denotes horizontal direction. $\widetilde{\rho}^*$ is deviation of density from the background density $\overline{\rho}$. The governing equations are non-dimensionalized by characteristic variables where U denotes the horizontal velocity scale while l_h and l_v denote the horizontal and vertical length scales, respectively. The quantity $\alpha = l_v/l_h$ is the vertical-to-horizontal aspect ratio. Since we are interested in pancake-vortex dynamics, the advection time scale l_h/U is used as the characteristic time scale rather than the buoyancy time scale, N^{-1}. Thus internal gravity waves on a faster time scale are excluded from the dynamics. The characteristic pressure fluctuation is $\rho_o U^2$. As noted earlier, Fr_h is the horizontal Fr number defined by $Fr_h = U/l_h N$ where buoyancy frequency is $N = [gC^*/\rho_0]^{1/2}$ and $C^* = -\partial\bar{\rho}(z)/\partial z^* \mid_{bg}$ is the background density gradient.

Characteristic vertical velocity, and characteristic density variation are yet to be determined. Let $\widetilde{\rho}_c$ and w_c be characteristic density variation and characteristic vertical velocity, respectively. Equation (2.6) can be non-dimensionalized as follows

$$\left[\frac{\widetilde{\rho}_c U}{l_h}\right]\frac{\partial\widetilde{\rho}}{\partial t} + \left[\frac{\widetilde{\rho}_c U}{l_h}\right] u_h^* \frac{\partial\widetilde{\rho}}{\partial x_h} + \left[\frac{w_c\widetilde{\rho}_c}{l_v}\right] w \frac{\partial\widetilde{\rho}}{\partial z} + \left[\frac{\partial\overline{\rho}}{\partial z^*} w_c\right] w = \frac{\kappa\widetilde{\rho}_c}{l_v^2}\left[\alpha^2\frac{\partial^2\widetilde{\rho}}{\partial x_h^2} + \frac{\partial^2\widetilde{\rho}}{\partial z^2}\right]. \qquad (2.7)$$

The first obvious choice in choosing $\widetilde{\rho}_c$ comes from equating the first (or second) term with the third term. This gives,

$$w_c|_1 = \frac{Ul_v}{l_h} \qquad (2.8)$$

which also is in agreement with the continuity equation. Another scaling, however, comes from equating the first term with the fourth term giving,

$$w_c|_2 = \frac{\widetilde{\rho}_c U}{[l_h(\partial\overline{\rho}/\partial z^*)]} = \frac{\widetilde{\rho}_c Fr_h g}{\rho_o N}. \qquad (2.9)$$

Both, the background density gradient and the horizontal motion are relevant to the problem. Therefore, equations (2.8) and (2.9) must constrain the vertical velocity to the same order of magnitude, i.e. $w_c|_1 = w_c|_2$. The vertical momentum equation (2.5) is non-dimensionalized based on $w_c|_2$ leading to

$$Fr_h^2\left[\frac{\partial w}{\partial t}+u_h\frac{\partial w}{\partial x_h}+\frac{\widetilde{\rho}_c g Fr_h}{\rho_o N U\alpha}w\frac{\partial w}{\partial z}\right]=-\frac{U^2\rho}{l_v\widetilde{\rho}_c g}\frac{\partial p}{\partial z}-\rho+\frac{Fr_h^2}{Re}\left[\frac{1}{\alpha^2}\frac{\partial^2 w}{\partial z^2}+\frac{\partial^2 w}{\partial x_h^2}\right]. \tag{2.10}$$

In the limit of strongly stratified flow with small viscous influence ($Fr_h \to 0$ and $Re \gg 1$), the temporal derivative of vertical velocity, advection terms, and viscous diffusion are smaller, by a factor of Fr_h^2, in comparison to the vertical pressure gradient and the baroclinic terms. Thus, the flow satisfies a hydrostatic balance to leading order. The vertical pressure gradient has to be balanced by density perturbation giving $U^2\rho/(l_v\widetilde{\rho}_c g) \sim O(1)$. This means that density variation varies as

$$\widetilde{\rho}_c=\frac{U^2\rho_o}{g l_v}\,. \tag{2.11}$$

The vertical length scale, l_v, can now be estimated as follows. Since the two vertical velocity scales are equal ($w_c|_2 = w_c|_1$), we can equate the right hand side of the equations (2.8) and (2.9) to obtain

$$l_v=\frac{\rho_c}{\rho_0}\frac{g}{N^2}\,, \tag{2.12}$$

which, upon using the expression for ρ_c given by equation (2.11) yields

$$l_v=\frac{U}{N}. \tag{2.13}$$

Notice that, the vertical length scale l_v was not suggested in advance as U/N but this scaling comes naturally based on the dominant balances in the limit of $Fr_h < O(1)$. The governing equations namely conservation of momentum, conservation of volume, and the density transport equation can now be written in the high-stratification regime as follows

$$\frac{\partial u_h}{\partial t}+u_h\frac{\partial u_h}{\partial x_h}+\frac{Fr_h^2}{\alpha^2}w\frac{\partial u_h}{\partial z}=-\frac{\partial p}{\partial x_h}+\frac{1}{Re\alpha^2}\frac{\partial^2 u_h}{\partial z^2}, \tag{2.14}$$

$$-\frac{\partial p}{\partial z}-\rho=0, \tag{2.15}$$

$$\frac{\partial u_h}{\partial x_h}+\frac{Fr_h^2}{\alpha^2}\frac{\partial w}{\partial z}=0, \tag{2.16}$$

$$\frac{\partial \widetilde{\rho}}{\partial t}+u_h\frac{\partial \widetilde{\rho}}{\partial x_h}+\frac{Fr_h^2}{\alpha^2}w\frac{\partial \widetilde{\rho}}{\partial z}=w+\frac{1}{RePr\alpha^2}\frac{\partial^2 \widetilde{\rho}}{\partial z^2}. \tag{2.17}$$

The relative magnitude of the vertical advection term $O(Fr_h^2/\alpha^2)$ and the viscous term $O(1/Re\alpha^2)$ distinguishes two dynamically different regimes by introducing the ratio of these two terms: $\mathcal{R}=ReFr_h^2$. For motions with large length scale $\mathcal{R}\gg 1$, the viscous and diffusion terms can be neglected. The governing equations can be rewritten in dimensional form as follows

$$\frac{\partial u_h^*}{\partial t}+u_h^*\frac{\partial u_h^*}{\partial x_h^*}+w^*\frac{\partial u_h^*}{\partial z^*}=-\frac{1}{\rho_o}\frac{\partial p^*}{\partial x_h^*}, \tag{2.18}$$

$$-\frac{1}{\rho_o}\frac{\partial p^*}{\partial z^*}-\frac{\widetilde{\rho}^* g}{\rho_o}=0, \tag{2.19}$$

$$\frac{\partial u_h^*}{\partial x_h^*}+\frac{\partial w^*}{\partial z^*}=0, \tag{2.20}$$

$$\frac{\partial \widetilde{\rho}^*}{\partial t^*} + u_h^* \frac{\partial \widetilde{\rho}^*}{\partial x_h^*} + w^* \frac{\partial \widetilde{\rho}^*}{\partial z^*} - N^2 \frac{\rho_o}{g} w^* = 0. \tag{2.21}$$

Following Billant & Chomaz (2001), an interesting part of these dimensional equations after scaling analysis is that equation (2.18) to (2.21) remain unchanged under a certain type of transformation. The governing equations are invariant under the following introduced variables,

$$N = \hat{N}/\beta, \quad z^* = \beta \hat{z}^*, \quad w^* = \beta \hat{w}^*, \quad \rho^* = (1/\beta)\hat{\rho}^*, \quad t^* = \hat{t}^*\,, \tag{2.22}$$

where β is a constant and the other variables remain unchanged. This implies that the time evolution of a solution of (2.18)–(2.21) can be deduced from the solution for any other frequency $\hat{N}$, $u_h^* = \hat{u}_h^*(x, y, zN, t)$. After non-dimensionalization of independent variables, a solution u_h^* is $u_h^* = \hat{u}_h^*(x/L_h, y/L_h, zN/U, tU/l_h)$. This suggests vertical length scale of $l_v = U/N$ which is identical to equation (2.13) confirming that when N increases, the vertical lengthscale decreases with an inverse proportionality.

If we follow the forward-cascade hypothesis where the dissipation is the ratio of fluctuating kinetic energy u^2 to the horizontal turn-over time scale l_h/u, the horizontal length scale can be written as $l_h = u^3/\epsilon$. This makes the parameter $\mathcal{R}$ to be

$$\mathcal{R} = ReFr_h^2 = \frac{ul_h}{\nu}\frac{u^2}{l_h^2 N^2} = \frac{u^3}{\nu N^2 (u^3/\epsilon)} = \frac{\epsilon}{\nu N^2} \tag{2.23}$$

which is identical to the buoyancy Reynolds number, $Re_b = \epsilon/\nu N^2$. Pal *et al.* (2016) found that Re_b is $O(1)$ in the region between $x/D = 1$ and 3, where turbulence regenerates behind the sphere for their $Fr = 0.125$ simulation. According to Brethouwer *et al.* (2007), if $\mathcal{R} \gg 1$, an energy cascade from large to small scale is possible allowing the existence of an inertial range in horizontal energy spectra. The inverse of factor $\mathcal{R}$ is also identical to the local Richardson number Ri defined in Riley & deBruynKops (2003) to be

$$Ri = \frac{-g}{\rho_o}\frac{\partial \rho_T}{\partial z} \Bigg/ \left[\left(\frac{\partial u}{\partial z}\right)^2 + \left(\frac{\partial v}{\partial z}\right)^2\right] = N^2/S_v^2. \tag{2.24}$$

Here, $\rho_T(\vec{x}, t) = \bar{\rho}(z) + \rho(\vec{x}, t)$ is the sum of the ambient and fluctuating density fields. Provided that dissipation from horizontal strain rate is small in comparison to dissipation from vertical strain rate, dissipation can be estimated as

$$\epsilon \sim \nu \left[\left(\frac{\partial u}{\partial z}\right)^2 + \left(\frac{\partial v}{\partial z}\right)^2\right]. \tag{2.25}$$

For a strongly stratified horizontal layer, with no energy accumulation on any scale, energy of large horizontal eddies u_h^2 is forwardly transferred with the time scale of l_h/u_h to smaller eddies and is dissipated at the same rate. Therefore,

$$\left[\left(\frac{\partial u}{\partial z}\right)^2 + \left(\frac{\partial v}{\partial z}\right)^2\right] \sim \frac{1}{\nu}\frac{u_h^3}{l_h}. \tag{2.26}$$

The Richardson number thus scales as

$$Ri = \frac{N^2}{\left(\frac{1}{\nu}\frac{u_h^3}{l_h}\right)} = \frac{N^2 l_h^2}{u_h^2}\frac{\nu}{u_h l_h} = \frac{1}{F_{l_h}^2}\frac{1}{Re_{l_h}} = \frac{1}{\mathcal{R}}. \tag{2.27}$$

Therefore, according to Riley & deBruynKops (2003), the flow will become or remain turbulent if approximately $Ri < 1$ or $\mathcal{R} > 1$. To further investigate that turbulence can be activated at low-Fr but $\mathcal{R} \geq 1$, investigation of higher-Re flow past a bluff body is desirable and motivates the presented simulations.

2.3 Dissertation questions

Previous investigations have provided a broad characterization of the turbulent wake under the influence of density stratification. However, it is apparent that several questions remain unanswered. The advancement in computer hardware which alleviates the limitation of low *Re* and the temporal models make possible the use of numerical approaches to answer these questions.

Recently, Pal *et al.* (2016) conducted a direct numerical simulation (DNS) of flow past a sphere in a stratified fluid at $Re = 3700$, the largest *Re* for a body-inclusive model at that time. Their results revealed that the cross-wake integrated TKE *increased* with increased stratification (decreased Froude number) beyond $Fr = U_\infty/ND < 0.5$. One remaining question regarding the TKE increase is whether the non-linear dynamics associated with the creation of subsequent small-scale eddies took place and turbulence was in fact 're-generated' at the very low Fr. This question is tackled in chapter 3 where we investigated the dynamics of near-field vorticity with emphasis on the prevalence of non-linear vortex stretching at low Fr.

The first body-inclusive simulation of flow past a heated sphere at $Re \sim O(10^4)$ was performed by de Stadler *et al.* (2014). While de Stadler *et al.* (2014) emphasized the passive-scalar mixing of the weakly-heated body, their results revealed a rate of decay of $U_0 \propto x^{-1}$ despite wake turbulence appeared to be fully-developed. A question which arose following comparison between the results of de Stadler *et al.* (2014) and Pal *et al.* (2017) is whether a sphere wake at $Re = 10^4$ but under stable density stratification would behave differently. This is explored and answered in chapter 4 where we look into the rate of U_0 decay as well as budgets of turbulent kinetic energy of stratified flow past a sphere at $Re = 10^4$. Additionally, a previous observation regarding the low-Re rate of U_0 decay at the immediate Reynolds number motivated us to look further into the classical proposed scaling laws of the axisymmetric wake. This work is presented in chapter 5.

Lastly, the scaling analysis of stratified turbulence poses questions that can only be answered with a sufficiently high-Re stratified wake that accesses stratified turbulence with low local Fr. The analysis introduced the so-called buoyancy Reynolds number (Re_b) and essentially suggested that if Re_b is sufficiently large, turbulence can be generated or sustained even at small values of local Fr. While the stratified turbulent regime has been under investigation, e.g. Riley & deBruynKops (2003); Lindborg (2006); Brethouwer *et al.* (2007); Riley & Lindborg (2008); Lindborg & Brethouwer (2008) among others, stratified turbulence has been computationally observed only in temporal-model simulations of wakes Brucker & Sarkar (2010); Diamessis *et al.* (2011) but not in a realistic body-generated stratified wake. Chapter 6 presents the first body-inclusive simulation of the stratified turbulent wake behind a disk at $Fr = 2$ where the stratified turbulence regime at low Fr and high Re_b is observed.

Chapter 3

On the vortex dynamics of flow past a sphere at Re = 3700 in a uniformly stratified fluid

3.1 Abstract

Vortex dynamics in the flow past a sphere in a linearly stratified environment is investigated numerically. Simulations are carried out for a flow with Reynolds number of $Re = 3700$ and for several Froude numbers ranging from the unstratified case with $Fr = \infty$ to a highly stratified wake with $Fr = 0.025$. Isosurface of Q criterion is used to elucidate stratification effects on vortical structures near the sphere and in the wake. Vortical structures in the unstratified case are tube-like and show no preference in their orientation. Moderate stratification alters the orientation of vortical structures but does not change their tube-like form. In strongly stratified cases with $Fr \leq 0.5$ there is strong suppression in vertical motion so that isotropically oriented vortex tubes of approximately circular cross-section are replaced by flattened vortex tubes that are horizontally oriented. At Fr

$= 0.025$, pancake eddies and surfboard-like inclined structures emerge in the near wake and have a regular streamwise spacing that is associated with the frequency of vortex shedding from the sphere. Enstrophy variance budget is used to analyze the vortical structure dynamics. Increasing stratification generally decreases enstrophy variance for $Fr \geq O(1)$ cases. The flow enters a new regime in strongly-stratified cases with $Fr \leq 0.25$: increasing the stratification increases enstrophy variance, especially near the body. Stratification distorts the cross-sectional distribution of enstrophy variance from a circular isotropic shape in the unstratified wake into different shapes, depending on Fr and distance from the sphere, that include: 1) elliptical distribution, 2) twin peaks suggestive of two-dimensional vortex shedding, and 3) triple-layer distribution where a relatively low enstrophy layer is sandwiched between upper and the lower layers with high enstrophy. In the near wake, vortex stretching by fluctuating and mean strain are both responsible for enhancing vorticity. Increasing stratification (decreasing Fr) to $O(1)$ values tends to suppress vortex stretching. Upon further reduction of Fr below 0.25, the vortex stretching takes large values near the sphere and, consequently, enstrophy variance in the near wake increases. The increase in vortex stretching is associated with unsteady, intermittent shedding of the boundary layer from the sides of the sphere in highly-stratified wakes with $Fr < 0.25$.

3.2 Introduction

Turbulence presents a spatially complex distribution of vorticity. Turbulent flow contains a wide range of vortical structures with various length scales and turn-over time scales. The influence of these vortical structures on turbulence dynamics from nonlinear cascade to scalar mixing to kinetic energy dissipation has been the subject of much study but less so in stratified flows. Stratification is ubiquitous in the environment and buoyancy affects the turbulent flows past marine swimmers, underwater submersibles, flying vehicles, underwater topography, islands and mountains.

Turbulent wakes in stratified fluid have been the subject of experimental study for over 30 years as summarized below but numerical turbulence-resolving simulations of the wake that include the body are relatively recent. Lin & Pao (1979) reviewed experimental studies that showed stratification suppresses vertical motion, promotes downstream horizontal coherent eddies, and enables propagation of internal gravity waves into the far field. Hanazaki (1988) numerically simulated stratified flow over a sphere at Reynolds number (Re) of 200 and Froude number $Fr_R \in [0.25{,}200]$ ($Fr_R = U/NR$, where U, N, and R are free stream velocity, buoyancy frequency, and radius of the sphere). DNS of Hanazaki (1988) provided visualization of downward motion of vertical velocity and isopycnal lines showing a lee wave behind the sphere at low Fr. Chomaz *et al.* (1992) experimentally showed that the downward motion induced by stratification delays separation. The downward motion also alters the separation region from circular to a bow-tie shape. Chomaz *et al.* (1993) identified four different regimes based on Fr where $Fr = U/ND$. For $Fr < 0.4$, the wake corresponds to triple-layer flow with two lee waves surrounding a layer of two-dimensional motion. Between Fr of 0.4 and 0.75, the saturated lee wave suppresses the separation region or splits it into two. Between Fr of 0.75 and 2, the wake progressively recovers its behavior in a homogeneous fluid. For Fr larger than 2.25, the near wake is similar to the homogeneous case.

A stratified wake at high Fr exhibits three distinct regions. The first region is the near wake (NW) where the wake spreads uniformly in all dimensions and turbulence behaves as it does in a homogeneous fluid. It is followed by a second non equilibrium (NEQ) regime identified by Spedding (1997) where there is an onset of stratification effect including conversion of stored potential energy to kinetic energy and anisotropy between horizontal and vertical motions. The third region (Q2D) is characterized by the existence of vertically suppressed two-dimensional eddies, the so-called “pancake vortices”. The formation mechanism of the pancake vortices has been debated. Pao & Kao (1977) states that it is due to the helical vortex shed by the sphere that persists into the far wake while Spedding (2001) attributes the mechanism to a combination of KH instability and spiral mode instabilities. Bonnier *et al.* (1998); Gourlay *et al.* (2001) argue that the existence of pancake vortices does not require coherent structures in the near wake. Later DNS by Dommermuth *et al.* (2002); Brucker & Sarkar (2010); Diamessis *et al.* (2011) also find pancake vortices in their temporal flow model with initial conditions that do not explicitly include coherent structures. Note that the temporal flow model refers to an approximation where the streamwise direction in the computational domain is assumed to be periodic, the Reynolds-averaged statistics evolve in time, and these statistics are obtained by streamwise averaging. The temporal approximation is applicable to a frame moving with the body velocity U, and is adequate if the wake deficit is small relative to U and if realistic initial conditions for the flow field can be prescribed. The numerical approach of this paper is a spatially evolving model where streamwise periodicity is not assumed and the Reynolds-averaged statistics, computed by temporal averaging, evolve as a function of streamwise distance. Pasquetti (2011) avoids ad-hoc prescription of the initial conditions in a temporal model by first performing body-inclusive spatially evolving simulation and then symmetrically embedding a subdomain from that simulation into a larger domain for the temporal model. Similar to experiments, Pasquetti (2011) found that an intermediate NEQ regime was followed by large scale quasi-2D structures in the late wake.

Investigation of coherent structures and vorticity statistics has provided useful information regarding the turbulent wake structure. Yun *et al.* (2006) numerically traced vortical structures behind a sphere at $Re = 3700$ and 10^4. Constantinescu & Squires (2004) visualized vortical structures using the method of Jeong & Hussain (1995) in the subcritical and supercritical regimes, where the boundary layer on the sphere surface is laminar and turbulent, respectively. These studies, however, did not include background density gradient. Spedding (1997) visualized vertical vorticity of stratified wake up to $Nt = 1600$ revealing large scale pancake vortices. Spedding (2002) examined vortical structure in wakes with $Fr \geq 2$ and stated that most of the late-time properties of long-lived vortex structure are independent of initial Froude number.

Recently Pal *et al.* (2016) performed DNS of stratified flow past a sphere at $Re = 3700$ over a wide range of Fr in the range $[0.025, \infty]$. They found that the near wake at $Fr = 0.5$ has very low fluctuation energy but further reduction of Fr to 0.25 and beyond regenerates turbulent fluctuations in the near wake. The turbulent kinetic energy (TKE) in the near wake ($x/D < 20$) of these low-Fr wakes became substantially larger than that in the unstratified case. The simulation data is analyzed in the present paper and new results on the behavior of the small scales are presented by analyzing the behavior of all components of enstrophy and its budget. We also examine the changes in vortex dynamics and coherent structures, identified using the Q-criterion, that are brought about by increased stratification. All prior numerical studies of the vorticity structure in a stratified wake have employed a temporal flow model for the simulations while the present study has the advantage of using a spatial flow model that includes the body. We address the following questions. How does stratification change vortical structures near the body and in the wake? Is there any qualitative difference in terms of enstrophy magnitude and distribution between the moderately and strongly stratified regimes? What are the mechanisms that are responsible for changes in enstrophy (a metric of small-scale fluctuations) induced by stratification?

3.3 Formulation

3.3.1 Governing equations

Continuity:

$$\frac{\partial u_i^*}{\partial x_i^*} = 0, \tag{3.1}$$

Momentum:

$$\frac{\partial u_i^*}{\partial t^*} + u_j^* \frac{\partial u_i^*}{\partial x_j^*} = -\frac{1}{\rho_0}\frac{\partial p^*}{\partial x_i^*} + \nu \frac{\partial^2 u_i^*}{\partial x_j^* \partial x_j^*} - \frac{\tilde{\rho}^*}{\rho_0} g \delta_{i3}, \tag{3.2}$$

Density:

$$\frac{\partial \rho^*}{\partial t^*} + u_j^* \frac{\partial \rho^*}{\partial x_j^*} = \kappa \frac{\partial^2 \rho^*}{\partial x_j^* \partial x_j^*}. \tag{3.3}$$

The * superscript denotes dimensional quantities. ν is the kinematic viscosity and κ is the density diffusivity. The density is decomposed into a background density, ρ_0, a linear variation in x_3 direction, $\bar{\rho}^*(x_3)$ and a fluctuation, $\tilde{\rho}^*(x_i, t)$:

$$\rho^* = \rho_0 + \bar{\rho}^*(x_3) + \tilde{\rho}^*(x_i, t), \tag{3.4}$$

where $\rho^* - \rho_0 \ll \rho_0$. Density variation enters the momentum equation only through the buoyancy term. These equations are non-dimensionalized using U (the free stream velocity), D (the diameter of the sphere), ρ_0, and $C^* = -\partial\bar{\rho}^*(x_3)/\partial x_3^* \mid_{(t=0)}$ that denotes the constant vertical gradient of background density. The new non-dimensional variables obtained are:

$$t = \frac{t^* U}{D}, \quad x_i = \frac{x_i^*}{D}, \quad u_i = \frac{u_i^*}{U}, \quad \rho = \frac{\rho^*}{\rho_0}, \quad \tilde{\rho} = \frac{\tilde{\rho}^*}{DC^*}, \quad p = \frac{\tilde{p}^*}{\rho_0 U^2}. \tag{3.5}$$

Substituting equation (3.5) into (3.1)-(3.3), we obtain the non-dimensionalized form as:

Continuity:

$$\frac{\partial u_i}{\partial x_i} = 0, \tag{3.6}$$

Momentum:

$$\frac{\partial u_i}{\partial t} + u_j \frac{\partial u_i}{\partial x_j} = -\frac{\partial p}{\partial x_i} + \frac{1}{Re}\frac{\partial^2 u_i}{\partial x_j \partial x_j} - \frac{1}{Fr^2}\tilde{\rho}\delta_{i3}, \tag{3.7}$$

Density:

$$\frac{\partial \rho}{\partial t} + u_j \frac{\partial \rho}{\partial x_j} = \frac{1}{RePr}\frac{\partial^2 \rho}{\partial x_j \partial x_j}. \tag{3.8}$$

Here, the relevant non-dimensional parameters are as follows: the Reynolds number, $Re = UD/\nu$, the Prandtl number, $Pr = \nu/\kappa$, and the Froude number, $Fr = U/(ND)$, where N is the buoyancy frequency defined by $N = [gC^*/\rho_0]^{1/2}$. In the following discussion, all variables referenced are non-dimensional unless otherwise noted.

3.3.2 Numerical scheme

The governing equations (A.38)–(A.40) are solved numerically using direct numerical simulation (DNS) in a cylindrical coordinate system on staggered grids. The sphere is represented by the immersed boundary method of Yang & Balaras (2006); Balaras (2004).

The governing equations are marched using a combination of explicit and implicit schemes. Implicit marching by the second order Crank-Nicolson (CN) scheme is performed for the viscous terms to alleviate the stiffness of the discretized system. The remaining terms are marched explicitly using a third-order Runge-Kutta (RK3) scheme. The periodic boundary condition in the azimuthal direction reduces the discretized Poisson equation into inversion of a pentadiagonal matrix. The pentadiagonal matrix system is solved using a direct solver, Yang & Balaras (2006). Inflow and convective outflow boundary conditions are applied at the inlet and outlet of the domain. In order to control spurious reflections from internal waves and other disturbances propagating out of the domain, sponge regions are employed near the free stream and inlet boundaries where the following relaxation terms are added to the governing equations:

$$-\phi(x_i)[u_i(x_i,t) - U_i], \qquad -\phi(x_i)[\rho(x_i,t) - \rho_\infty(x_3)]\,. \tag{3.9}$$

The sponge layer takes the form of a Rayleigh damping function which is designed in such a way that it gradually relaxes the velocities and density to their respective values at the boundaries. Here U_i is the freestream velocity and $\rho_\infty(x_3)$ is the density of the stratified background. This is accomplished by adding the explicit damping terms of equation (4.4) to the right hand side of equation (A.39) and (A.40), respectively. The variable $\phi(x_i)$ is constructed such that it increases quadratically from $\phi = 0$ to $\phi = 1$ over a sponge region of thickness 10 grid points at the inflow and at the freestream boundaries.

3.3.3 Parameters

Table 3.1 shows parameters for the eight simulations that range from an unstratified case to the highly-stratified case with $Fr = 0.025$. All simulations are performed with $Re = 3700$ and the number of points in the azimuthal direction is chosen to be $N_\theta = 128$.

Table 3.1: Simulation parameters. The sphere center is at $x = 0$, and the streamwise domain length is split into downstream (L_x^+) and upstream (L_x^-) portions; $L_x = L_x^+ + L_x^-$.

Case	L_x^+/D	L_x^-/D	L_r/D	N_x	N_r
Fr = ∞	80.1	13.8	16.2	4608	632
Fr = 3	80.1	13.8	59.7	4608	692
Fr = 1	80.1	25.7	59.7	4608	692
Fr = 0.5	79.3	39.2	59.7	4608	692
Fr = 0.25	79.3	39.2	59.7	4608	692
Fr = 0.125	79.3	39.2	59.7	4608	692
Fr = 0.05	23.3	39.2	59.7	3072	692
Fr = 0.025	23.3	39.2	59.7	3072	692

The choice of $Re = 3700$ allows validation against DNS of unstratified flow past a sphere by Rodriguez *et al.* (2011). The choice of $Pr = 1$ is justified by de Stadler *et al.* (2010). L_x/D and L_r/D are domain sizes in the streamwise and radial directions, respectively. Domain size in the radial direction and in the upstream direction for all stratified case are enlarged to allow free propagation of internal gravity waves. The total number of grid points is approximately 400 million. Grid stretching is used in radial and streamwise directions to concentrate points near the sphere surface in order to resolve the laminar boundary layer. The domain is decomposed only in the streamwise direction which reduces communication time between processors as compared to three-dimensional decomposition. Each simulation requires approximately 500 hours run time on 512 processors. Temporal averaging of data to compute statistics is performed over 80-100 time units or approximately a single flow-through time unit after statistical steady-state.

3.4 Methods of data analysis

The flow is statistically inhomogeneous in all directions. Thus, Reynolds-averaged statistics are obtained by averaging solely over time. Vorticity is computed in cylindrical coordinates prior to transformation into Cartesian coordinate. The total enstrophy can be decomposed into mean and fluctuating components. In the present paper, we examine the fluctuating enstrophy which hereafter is simply called enstrophy (the second term of the rhs in equation 3.11). Reynolds average is denoted with overline. Three dimensional visualization of vortices is done using the Q-criterion of Hunt *et al.* (1988) which defines a vortex by the region where the rate of rotation tensor, Ω_{ij}, exceeds strain rate tensor, S_{ij}. Large positive Q implies strong swirling motion.

$$u_i = \overline{u}_i + u'_i, \qquad \rho_i = \overline{\rho}_i + \rho'_i, \qquad \tilde{\rho}_i = \overline{\tilde{\rho}}_i + \tilde{\rho}'_i, \qquad p_i = \overline{p}_i + p'_i \tag{3.10}$$

$$\frac{1}{2}\left(\overline{\omega_i \omega_i}\right) = \frac{1}{2}\left(\overline{\omega}_i\, \overline{\omega}_i\right) + \frac{1}{2}\left(\overline{\omega'_i \omega'_i}\right);\ \omega_i = \epsilon_{ijk}\frac{\partial u_k}{\partial x_j} \tag{3.11}$$

$$Q = \frac{1}{2}(|\mathbf{\Omega}|^2 - |\mathbf{S}|^2);\ \Omega_{ij} = \frac{1}{2}\left(\frac{\partial u_i}{\partial x_j} - \frac{\partial u_j}{\partial x_i}\right),\ S_{ij} = \frac{1}{2}\left(\frac{\partial u_i}{\partial x_j} + \frac{\partial u_j}{\partial x_i}\right) \tag{3.12}$$

3.5 Results

The numerical method and grid resolution of the present DNS was validated using experimental measurements and numerical results available in the literature by Pal *et al.* (2016). Comparison of nondimensional vortex shedding frequency, $St = fD/U$, separation angle, φ_s, drag coefficient, C_d, and rearward stagnation pressure coefficient, C_{pb}, agree well with the previous investigations Schlichting & Gersten (1968); Kim & Durbin (1988); Sakamoto & Haniu (1990); Seidl *et al.* (1997); Tomboulides & Orszag (2000); Constantinescu & Squires (2004); Yun *et al.* (2006); Rodriguez *et al.* (2011) as discussed by Pal *et al.*

(2016).

3.5.1 Wake vortices

3.5.1.1 Vortex configuration

Figure 3.1 visualizes instantaneous vortical structures in the wake using the Q-criterion at Q = 1 for the unstratified case. Since Q, defined by equation (3.12), represents a region where the rate of rotation tensor Ω_{ij} exceeds the strain rate tensor S_{ij}, a high value of Q signifies intense rotation of fluid elements. Close to the body, vortex rings are shed from the sphere in the unstratified wake (figure 3.1). These rings remain circular before breaking down at around $x/D = 2.4$, Rodriguez *et al.* (2011). Immediately downstream of the transition, a bundle of entangled vortical structures emerges. These vortices are tube-like structures with high length-to-diameter aspect ratio, the so-called vortex tube. For both Fr, even though the vortex tubes in general do not have directional preference, the subset of streamwise-oriented tubular structures have high-magnitude streamwise vorticity and no preference for other vorticity components. In figure 3.1, the density of vortex tubes per unit volume based on $Q = 1$ decreases significantly after $x/D \approx 7$.

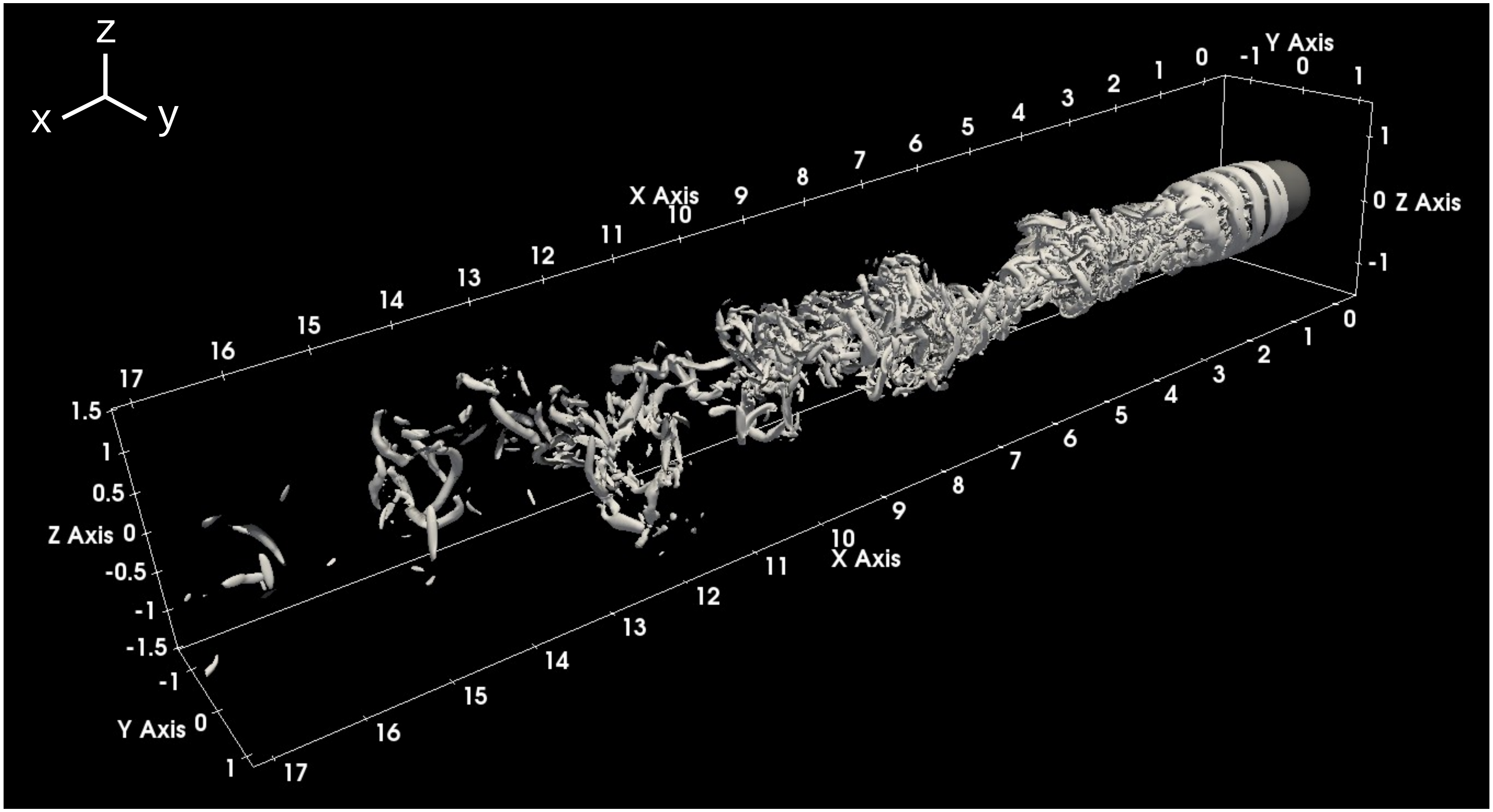

Figure 3.1: Iso-surface of Q criterion at Q = 1 for $Fr = \infty$. Note that the sphere center is at $x = 0$, $y = 0$ and $z = 0$.

Figure 3.2 shows vortices at higher magnitude of Q = 50. At this level of Q, vortical structures in the unstratified $Fr = \infty$ wake are present in the region $1.5 < x/D < 5$ while they are absent elsewhere. The fact that the strength (Q) of the vortex tubes spanning $1.5 < x/D < 5$ is higher than that of vortices shed from the body indicates that vortex shedding is not the only source of vorticity. The mechanisms generating vorticity will be explained later in section 3.5.3. Streaky structures closer to the sphere seem to have prefered orientation in the streamwise direction while this preference is lost away from the body. Stratification at $Fr = 1$, figure 3.2 (right), elongates the vortex tubes and thus increases their aspect ratio. The vortical structures have a vertical undulation owing to a steady lee wave pattern behind the body. The number density of vortical structures is significantly smaller than that in the unstratified wake showing suppression of enstrophy (will be quantified later) at this level of stratification. Stratification at $Fr = 0.5$ confines vortex tubes to streamwise-oriented regions as shown in figure 3.3. Two pairs of streaks are observed having their size longer than the sphere's diameter. That fluctuating enstrophy is suppressed by stratification is evident since vortical structures at $Fr = 0.5$ are barely observed even with Q = 5.

While vortical structures depicted by isosurface of Q for weak stratification ($Fr \geq 0.5$) bear some similarities to the unstratified case in terms of size, aspect ratio and orientation, structures at stronger stratification ($Fr = 0.125$) shown in figure 3.3 (right) are significantly different. From figure 3.3 (right), immediately after the sphere there is a stack of long thin flattened tubes that alternate on either side of the vertical center-plane. This is due to quasi two-dimensional vortex shedding from the sides of the sphere.

The azimuthal vorticity, ω_y, is organized into a triple layer as shown by the side view of the $Fr = 0.25$ case in Figure 3.4. The lee wave is apparent in the stratified case and the variability of vorticity is diminished. The vertical wake height is narrower in comparison to the unstratified case and the wake is bounded by the top and bottom shear layers which

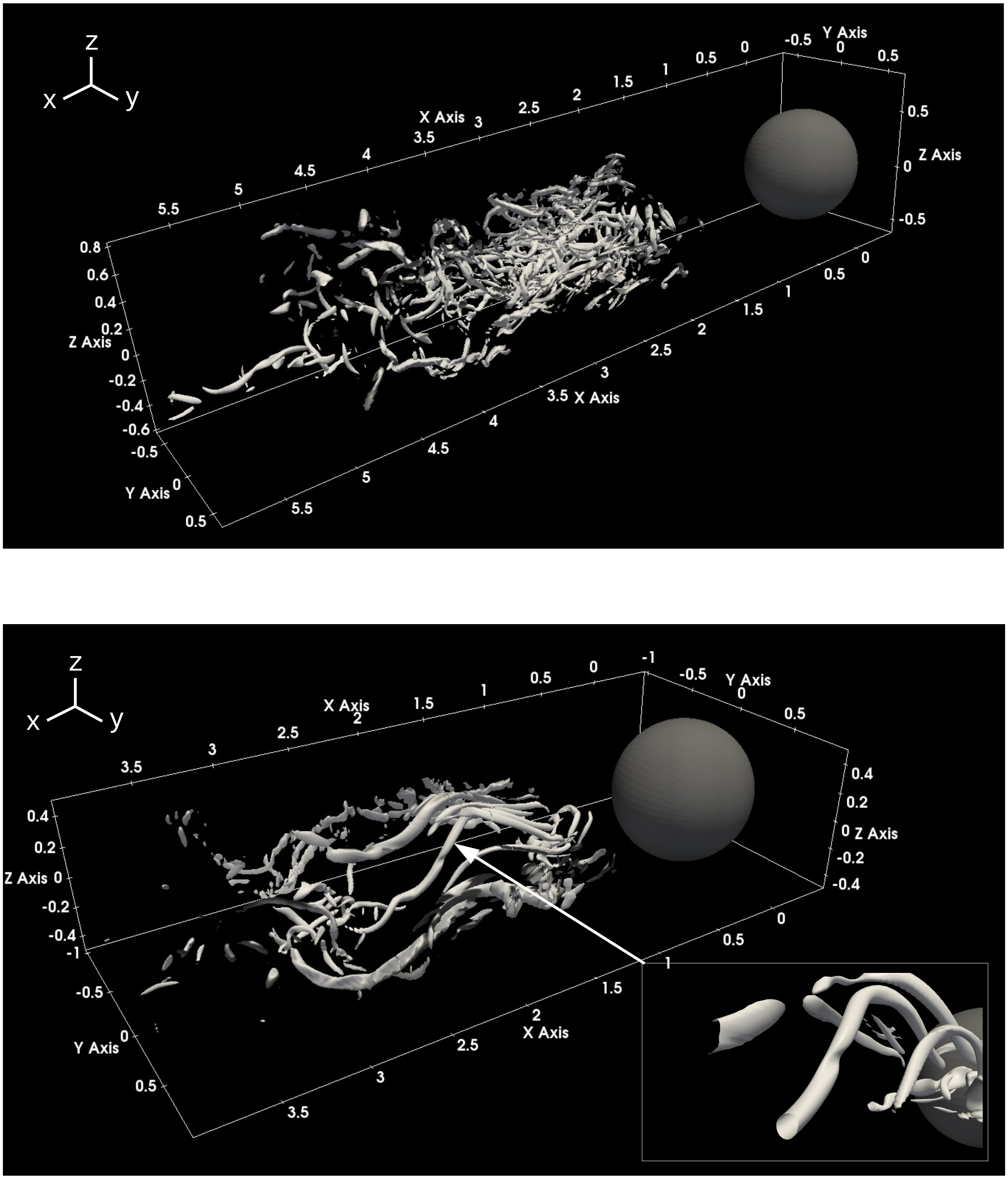

Figure 3.2: Iso-surface of Q criterion at Q = 50 for $Fr = \infty$ (top) and $Fr = 1$ (bottom). Inset on right panel shows the circular cross-section of the vortex tube.

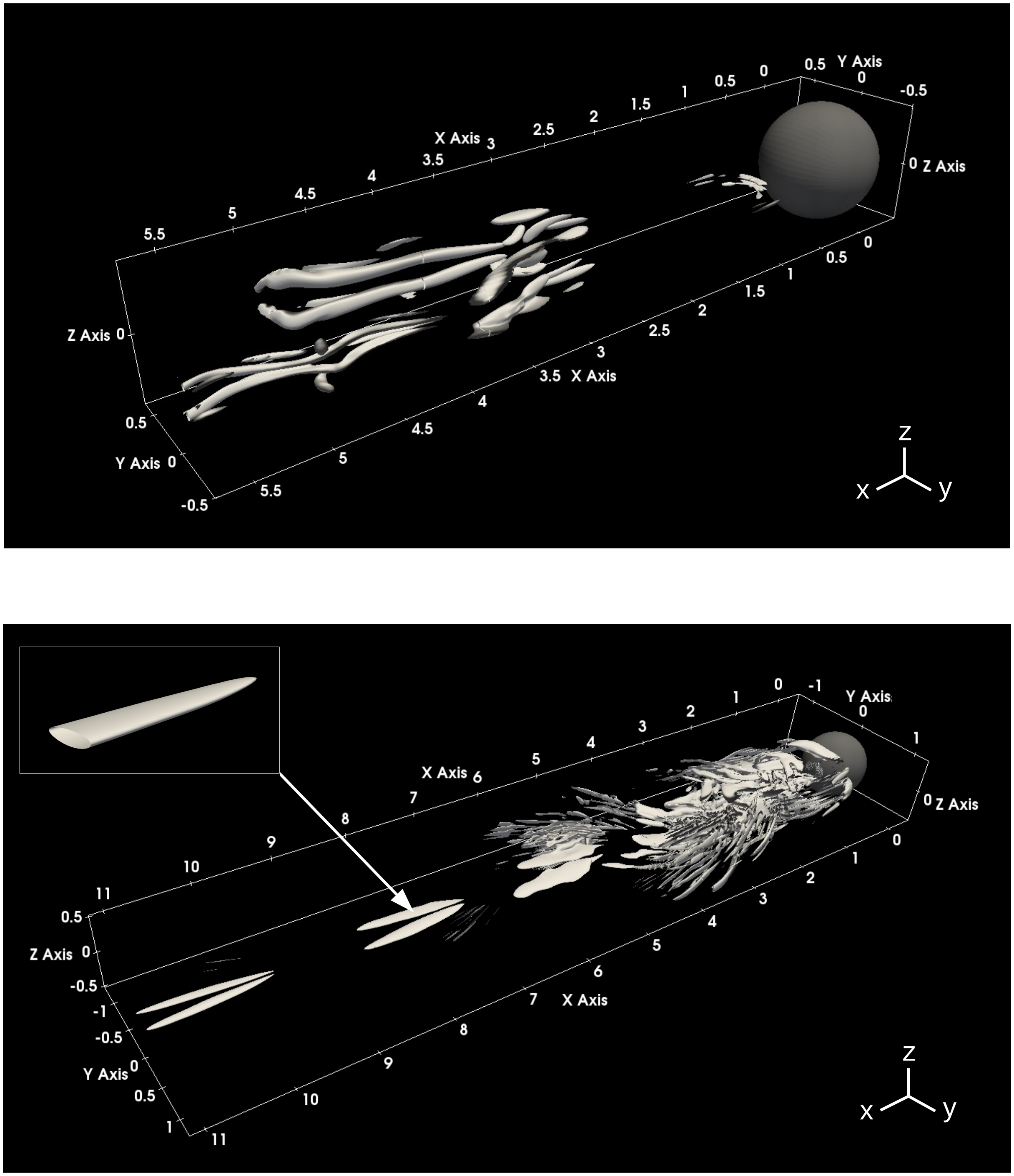

Figure 3.3: Iso-surface of Q criterion at Q = 5 for $Fr = 0.5$ (top) and for $Fr = 0.125$ (bottom). Inset on right shows the elliptical cross-section of the vortex tube in the strongly stratified regime.

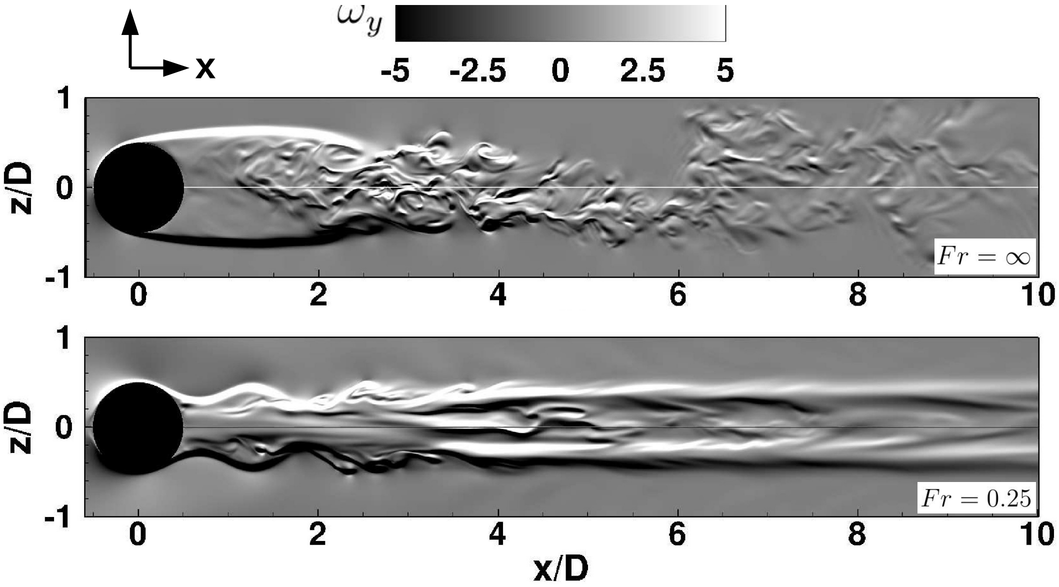

Figure 3.4: Side view azimuthal vorticity (ω_y) for $Fr = \infty$ (top) and $Fr = 0.25$ (bottom).

exhibit vertical undulations impressed by a steady lee wave pattern but little turbulence. The middle layer contains horizontal strips of vorticity that are thin in the vertical. The isosurface of Q at $Fr = 0.25$ is similar to that of $Fr = 0.125$ and is not shown here.

The quasi-2D regime is a feature of the far wake, appearing at $x/D \approx 1000$ or $Nt \approx 250$ in the moderately stratified $Fr = 4$ wake simulated by Brucker & Sarkar (2010) in a temporal flow model. When the stratification is very high, pancake vortices emerge in the near wake. Isosurface of Q = 0.25 in the perspective view of figure 3.5 (top) reveals two types of organized structures, both are thin in the vertical. Pancake vortices which take the form of discs are clear and the first pancake eddy is seen in the perspective view of the top panel at $x/D \approx 6$ which corresponds to $Nt = 6/Fr = 240$ which is close to the value of $Nt \approx 250$ quoted by Brucker & Sarkar (2010). While the pancake vortices are located off the center line, there are "surfboard" structures sequentially located closer to the middle. The side view (figure 3.5 middle) shows that, while the pancakes are located on the horizontal center plane, the surfboard-like structures are not horizontally oriented

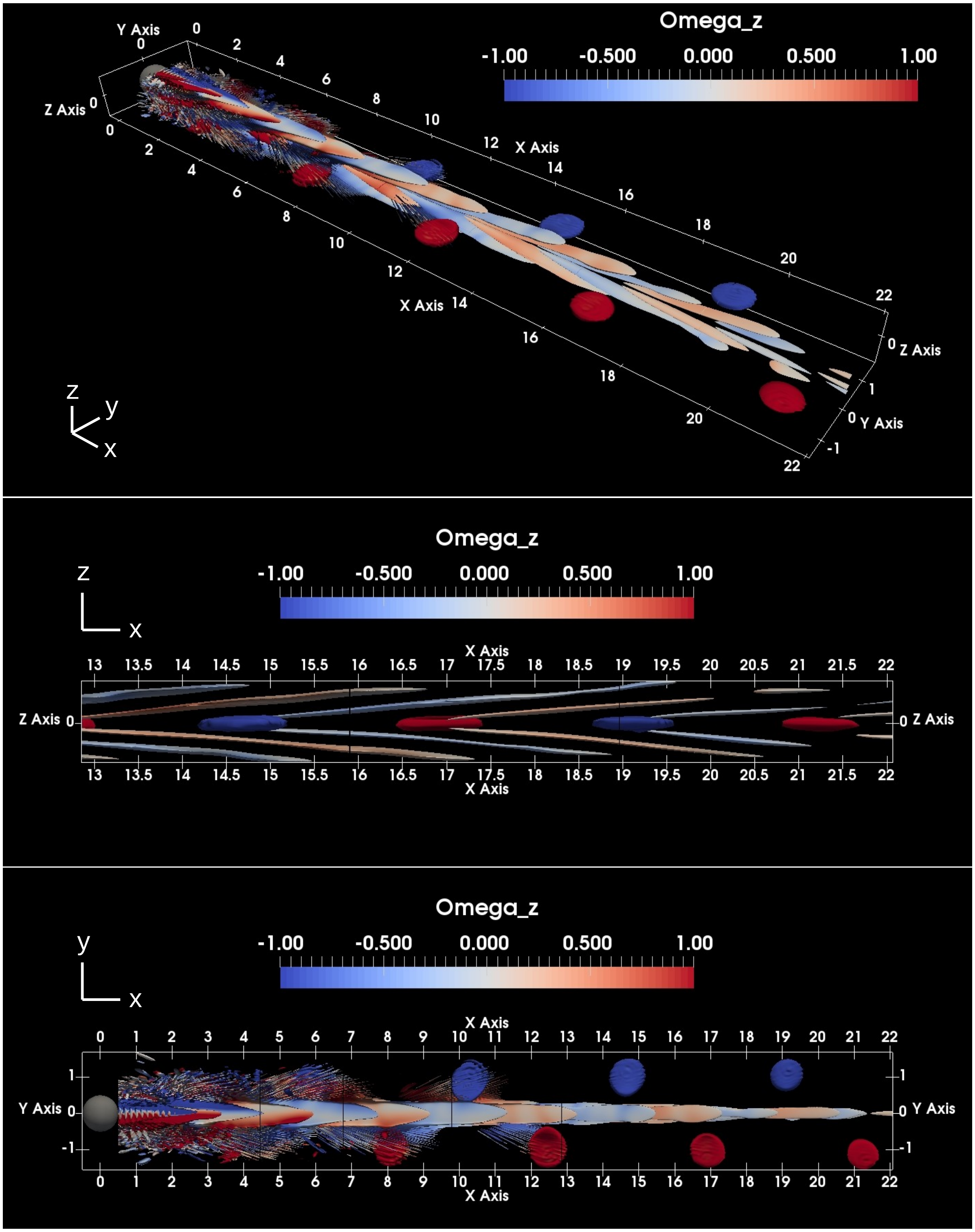

Figure 3.5: Coherent structures in a strongly stratified wake ($Fr = 0.025$) visualized with the isosurface of Q = 0.25. Top panel is a perspective of the wake with the sphere at the upper left corner. Middle panel is a side view (flow from left to right) and bottom panel is a top view.

and their leading edges are located at the same x/D location as of the pancake eddies. In the side view, each surfboard pair appears as a V with the vertex of the V coincident with the pancake. An average distance between the pancake eddies is $x/D = 4.41$ according to figure 3.5 (bottom). The advection velocity of a pancake is obtained by tracking an eddy through time as shown in Figure 3.6. Figure 3.7 (left) reveals an advection velocity of 0.846. The spacing between two subsequent pancake eddies and this estimate of advection velocity allows conversion to temporal frequency of the pancake eddy, leading to a Strouhal number of $St = fD/U = 0.192$. The primary peak in the streamwise and spanwise velocities power spectra (figure 3.7 right panel) is at $St \approx 0.2$. Therefore, the origin of these pancake eddies is shedding of boundary layer vorticity from the sides of the sphere (similar to the Karman vortex street of a cylinder). This frequency is close to the shedding frequency of flow past a cylinder at ($St = 0.208$) reported in Parnaudeau *et al.* (2008). The surfboard structures are shed from the sphere with the same frequency as of the pancakes. Inspection of the flow near the sphere suggests that the surfboards are an interaction of the top and bottom separated boundary layers with the horizontal vortex shedding.

Another kinematic aspect of the pancakes and of the surfboards apart from their convective translation is their rotational direction. The isosurface of Q is colored with vertical vorticity. The pancake disks originate from quasi 2D shedding of the boundary layer in the horizontal center plane. The shedding occurs from alternate sides of the sphere and the sign of the vertical vorticity of a pancake disk depends on the side of the centerline that it occupies. Two surfboard structures that form a ‘V’ in figure 3.5 (middle) have the same orientation of vertical vorticity as the pancake at the vertex of the V suggesting continuity of vortex lines at the leading edge of the V. The vertical vorticity amplitude of these surfboards is, however, smaller than that of the pancake disks. Overall, the distribution of vorticity is indicative of a sinuous instability mode.

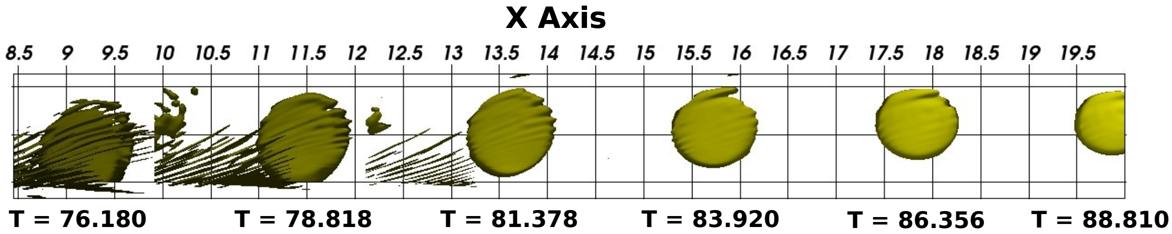

Figure 3.6: Location of a pancake eddy for $Fr = 0.025$ versus time.

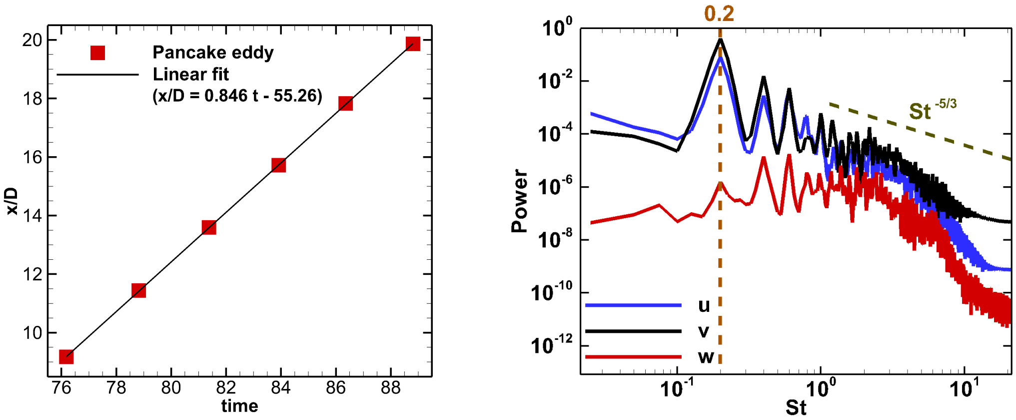

Figure 3.7: Location of a pancake eddy vs time (left) and power spectra of velocity components for $Fr = 0.025$ at $x/D = 2.19$, $y/D = 0.51$ and $z = 0$ (right).

3.5.1.2 Separation

While there are quantitative changes in how the incoming flow goes past the sphere under different levels of stratification, the cases of $Fr = 0.5$ and 0.125 shown in Figure 3.8 are sufficient to illustrate the qualitative changes induced by buoyancy on the flow at the sphere and its separation. At moderate Fr, the incoming flow has enough kinetic energy to go above and below the sphere which can be seen from the smooth and continuous isosurface of Q at $Fr = 0.5$. There is a difference with respect to the axisymmetric separation in the unstratified case. Stratification delays separation at the top and bottom of the sphere with respect to its sides. Due to conversion of stored potential energy to kinetic energy, fluid at the top and bottom regions gains momentum which helps the boundary layer overcome the adverse pressure gradient and remain attached to the surface further downstream than

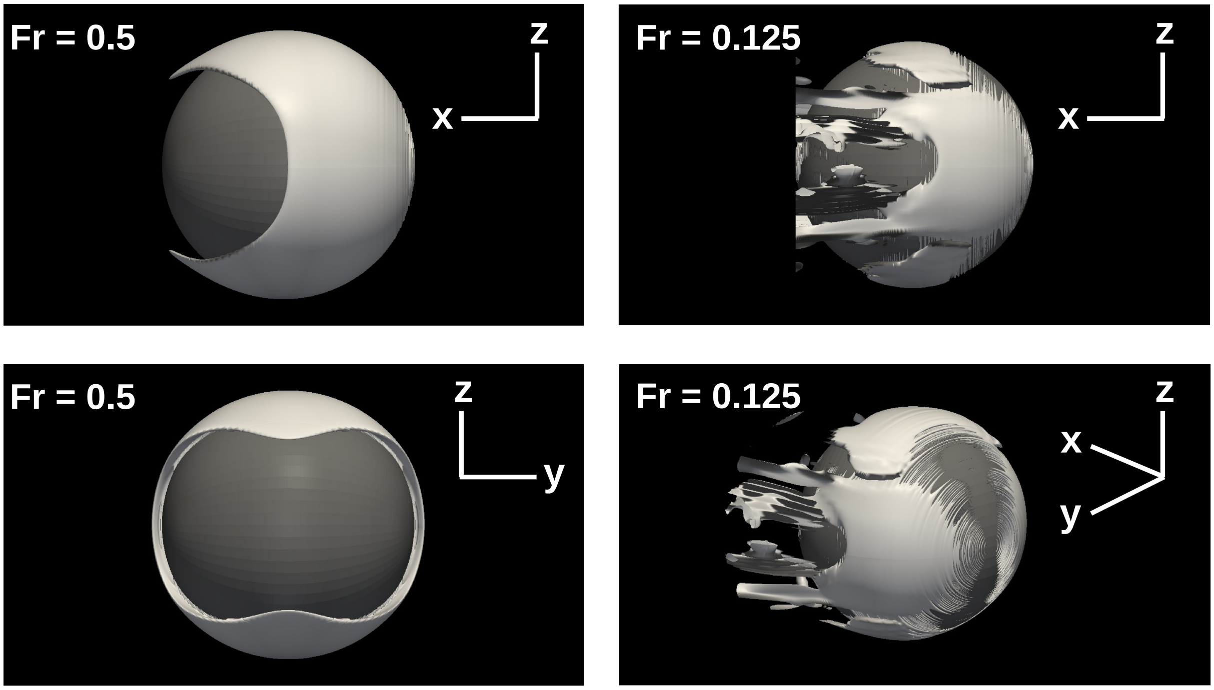

Figure 3.8: Isosurface of Q criterion used to examine flow separation.

in the horizontal plane. This results in the delay of separation in the vertical plane. The separation line viewed from the rear (bottom-left panel of Figure 3.8) has a bow-tie shape. At sufficiently low Fr, there is another qualitative change: flow blocking, i.e. the incoming flow does not have enough kinetic energy to go past the top and bottom points of the sphere. Therefore, the flow is forced to go around the sphere for $Fr = 0.125$ as shown by the absence of Q isosurface in the central region on the frontward-facing surface of the sphere (Figure 3.8, bottom right panel). The boundary layer at $Fr = 0.125$ is shed from the sides of the sphere (Figure 3.8, top and bottom right panels)

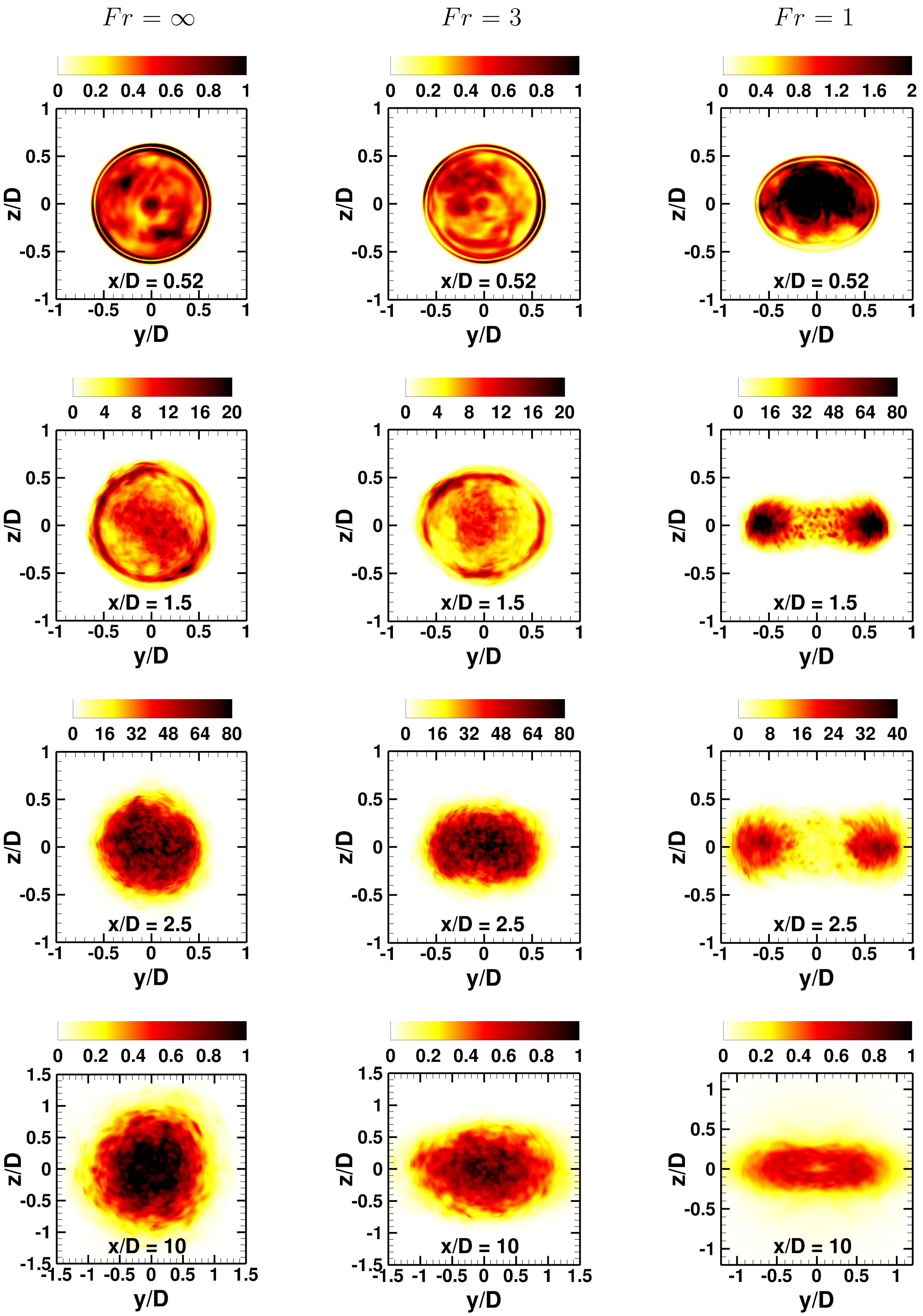

Figure 3.9: Enstrophy, $\overline{\omega_i'\omega_i'}/2$, plotted over a transverse cross-section at various streamwise locations. Cases with $Fr = \infty$, 3, and 1 are shown.

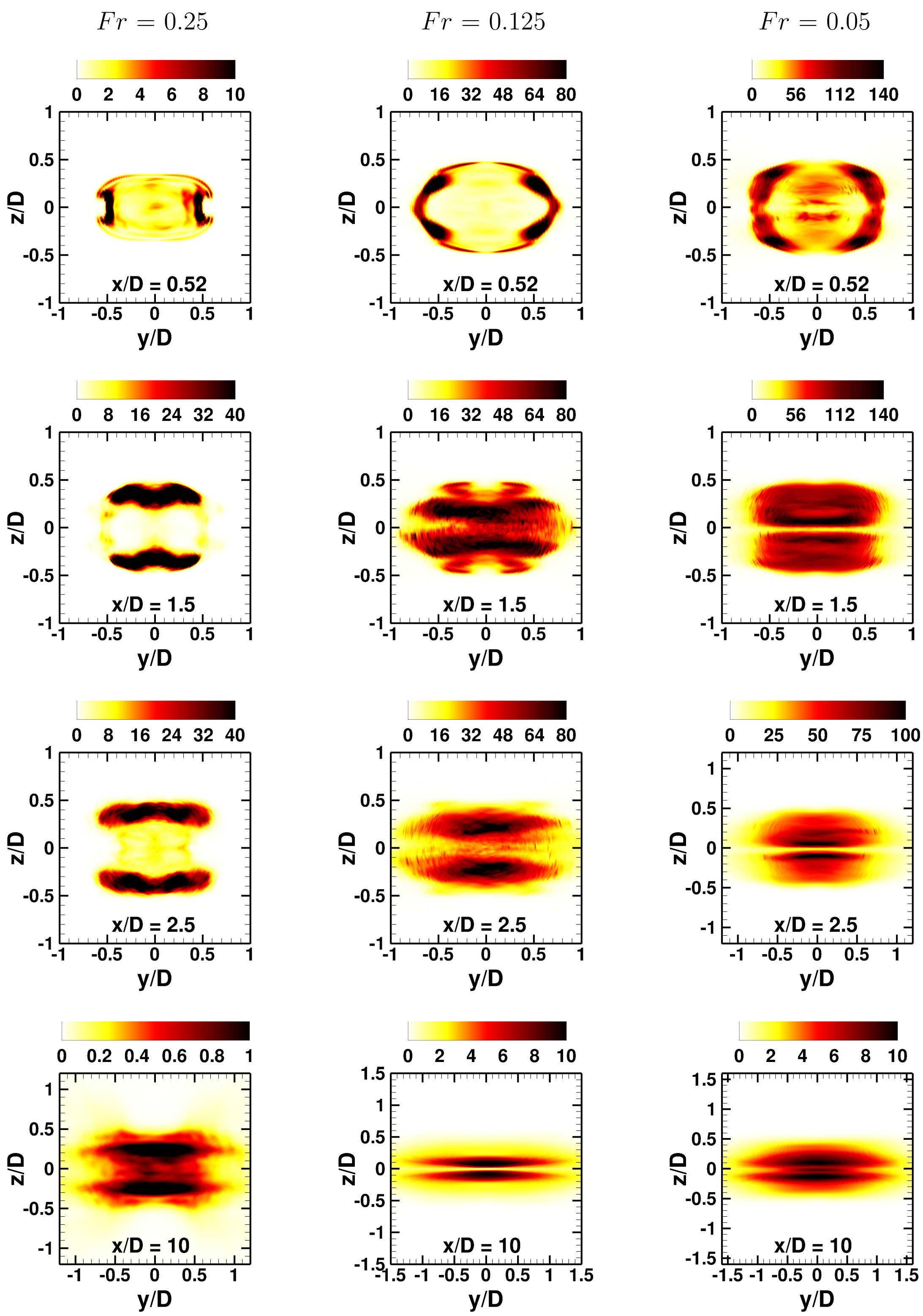

$Fr = 0.25$ $Fr = 0.125$ $Fr = 0.05$

Figure 3.10: Enstrophy, $\overline{\omega_i'\omega_i'}/2$, plotted over a transverse cross-section at various streamwise locations. Cases with $Fr = 0.25$, 0.125, and 0.05 are shown.

3.5.1.3 Spatial distribution of enstrophy variance

Figure 3.9 shows the spatial distribution of enstrophy at different downstream locations for Fr = ∞, 3, and 1. Beyond $x/D = 2.5$, the enstrophy in the core of the wake tends to decrease with decreasing Fr until $Fr = 0.5$ (not plotted) where the enstrophy is rather small, about 1 % of that at $Fr = \infty$. The distribution of enstrophy also changes among cases. Consider $x/D = 0.52$ (top panel). For $Fr = \infty$, there is a thin circular ring of high enstrophy associated with the separating boundary layer, also seen as a sequence of vortex rings in the visualization of Q (figure 3.1). The separating boundary layer forms an unstable ring-like shear layer that has enhanced enstrophy. As stratification increases (Fr decreases), the boundary of the region with relatively high enstrophy starts distorting from a circle to an ellipse. This non-circular cross-section very close to the sphere is consistent with the previous discussion of boundary layer separation occurring at different angles as measured from the sphere forward stagnation point. At $x/D = 0.52$, the $Fr = 1$ case shows the highest enstrophy among the three cases which can also be surmised from the isosurface of Q = 50 where intense swirling vortex tubes move slightly closer to the sphere as compared to $Fr = \infty$ in figure 3.2.

The fluctuating enstrophy increases moving downstream to $x/D = 1.5$. While peak enstrophy still resides at the periphery, there is significant enstrophy in the core associated with the recirculating flow and unsteady, flapping shear layer. Stratification causes downward motion behind the sphere keeping relatively high enstrophy closer to the sphere. Moving downstream, the buoyancy-induced anisotropy of cross-sectional enstrophy becomes more pronounced. At $x/D = 1.5$, the $Fr = 1$ cases loses the signature of the vortex ring and, instead, has a dumbbell shape with two local peaks, one on each side of the centerline. These two blobs of enstrophy are approximately 4 times larger in magnitude compared with Fr = ∞ and 3. At $x/D = 2.5$, the enstrophy increases for $Fr = \infty$ and

$Fr = 3$ while it fades for $Fr = 1$. By $x/D = 10$ (bottom panel), the two separated peaks of enstrophy are no longer prominent in the $Fr = 1$ wake. Although the enstrophy increases rapidly near the body for $Fr = 1$, stratification at this level suppresses small-scale turbulence after $x/D = 1.5$ according to figure 3.9.

Figure 3.10 shows cross-sectional enstrophy at low Fr of 0.25, 0.125, and 0.05. There is a striking increase of enstrophy in these low-Fr cases relative to the moderate-Fr cases of figure 3.9. This implies that small scale fluctuations reappear when Fr decreases beyond 0.25. Furthermore, the distribution of enstrophy is also different in this low-Fr regime relative to that at higher Fr. The flow separates from the sides of the sphere leading to intensified vertical side lobes of vorticity at $x/D = 0.52$. The separated shear layer responds to stratification by developing instabilities with small vertical scale as was seen in the Q-visualizations and also flaps unsteadily (more so in the $Fr = 0.125$ and 0.05 cases) in the horizontal plane. As a result the enstrophy variance takes the form of a horizontally-oriented triple layer: there are two outer layers with high enstrophy and a central layer with low enstrophy. The aspect ratio (horizontal to vertical) of these layers becomes progressively larger with increasing Fr.

3.5.2 Area-integrated values of enstrophy and its components

The enstrophy increases dramatically, by almost two orders of magnitude. The enstrophy integrated over the y-z cross-section is shown in figure 3.11 for different Fr. In all cases the enstrophy increases, reaches a maximum close to the sphere surface, and then decays. In the low- or moderate-stratification regime with $Fr \geq O(1)$, the effect of buoyancy is to reduce enstrophy. The onset of the stratification effect scales as Nx/D so that the deviation of enstrophy relative to the unstratified case in the $Fr = 3$ wake occurs further downstream than in the $Fr = 1$ case. The value of $Fr = 0.5$ appears to be a critical Fr where the integrated enstrophy in the near wake ($x/D < 20$) is the smallest among all

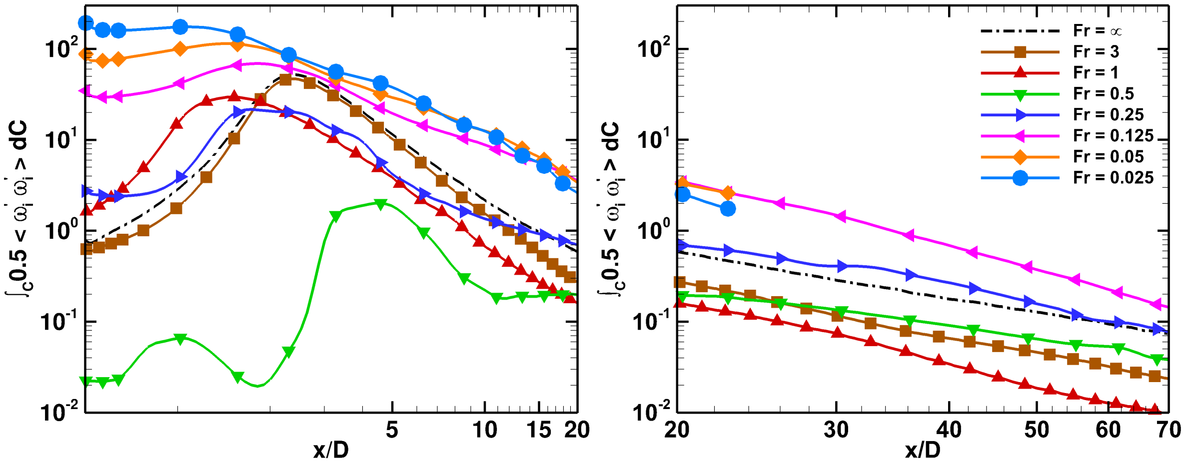

Figure 3.11: Streamwise variation of area-integrated enstrophy.

cases.

There is a qualitative change in the stratification effect on enstrophy when Fr decreases below 0.5, namely, the integrated enstrophy near the body ($x/D < 2$) monotonically increases with decreasing Fr. As discussed previously, the boundary layer sheds in a two-dimensional manner in this low-Fr regime; furthermore, vortices are shed unsteadily in the horizontal plane from various vertical locations, develop instabilities with small vertical scale, U/N, and also flap unsteadily in the horizontal plane. These aspects of unsteady motion create a wide range of scales of motion explaining why the enstrophy near the body increases again once $Fr < 0.5$.

The enstrophy near the body ($x/D < 2$) in the low-Fr cases with $Fr \leq 0.125$ exceeds the corresponding values in the unstratified case substantially, by 1-2 orders of magnitude. There is a rapid rise of enstrophy in the unstratified case which brings its value close to that in the low-Fr regime soon after. However, the relatively rapid spread of the unstratified wake thickness causes a corresponding decrease in enstrophy so that, for $10 < x/D < 70$, the unstratified wake has lower enstrophy than these low-Fr cases. This is in contrast to the situation in the $Fr \geq O(1)$ regime where the unstratified wake has larger enstrophy for $10 < x/D < 70$.

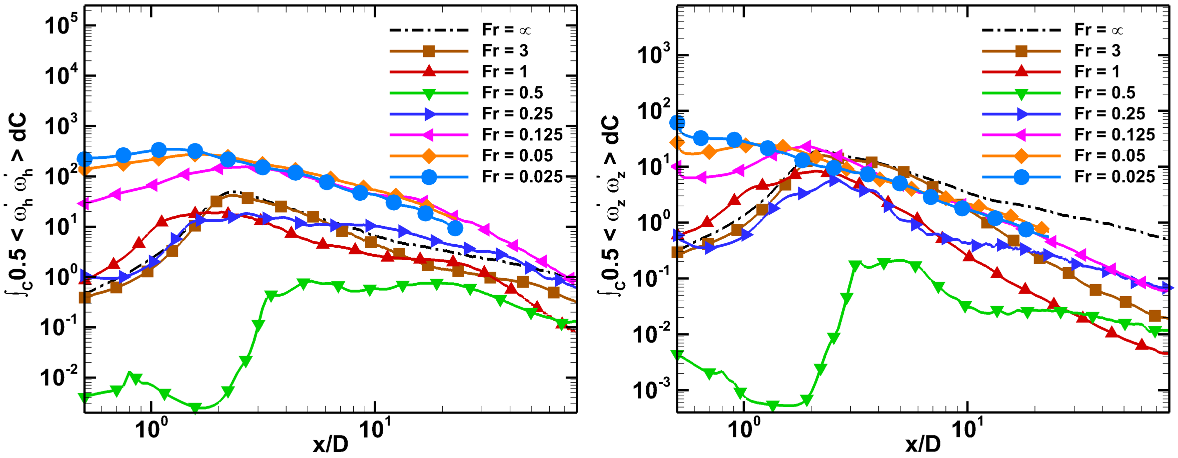

Figure 3.12: Partition of area-integrated enstrophy into: (a) horizontal component, and (b) vertical component.

Figure 3.12 shows decomposition of area-integrated fluctuating enstrophy into vertical (ω_z'), and horizontal (ω_h') components. Since, ω_x' and ω_y' components behave similarly, both contributions are lumped together in that of ω_h'. The behavior of the unstratified case (black dash-dot line) shows that there is little difference between the evolution of horizontal and vertical components. It was shown in figure 3.11 that the low-Fr cases with $Fr \leq 0.125$ have larger enstrophy relative to the unstratified case. This remains true for ω_h', but only very near the body ($x/D < 2.5$) in the case of ω_z'. The reason for the similar behavior of ω_z' and ω_h' for $x/D < 2.5$ is that vortex shedding from the side of the sphere (observed in figure 3.9 and figure 3.10) and subsequent instabilities of the shed vorticity layers increase all components of fluctuating vorticity for $x/D < 2.5$. However the stabilizing effect of buoyancy acts further downstream so that the contribution of the vertical component in all stratified wake simulations tends to decrease faster than the unstratified case at $x/D \approx 4$.

3.5.3 Enstrophy mechanisms

The vortex dynamics is analyzed by means of equation (3.13) below for the enstrophy variance. Each term is computed at statistical steady-state and the temporal derivative term thus vanishes. The interesting aspect of this equation is whether each term behaves as a source or as a sink of enstrophy. At sufficiently high Re, the dominant source term for the enstrophy equation is stretching by turbulent vorticity ($S1$) and the dominant sink term is dissipation ($DISSIP$), Tennekes & Lumley (1972). Vortex stretching underpins the energy cascade from large to small scales. The strongly positive values of $S1$ in figure 3.13 implies that stretching outweighs compression of vortex lines and the net effect of the strain field is to create enstrophy, Tennekes & Lumley (1972).

Consider the unstratified case first. The dominance of stretching and dissipation plotted in figures 3.13 and 3.14, respectively, is clear. Among the three stretching terms, stretching by fluctuating strain ($S1$) is dominant, stretching by mean strain ($S2$) is substantial while stretching of mean vorticity by fluctuating strain ($S3$) (figure 3.16, right) is the smallest. Recall that, although there were intense vortical structures (Q = 50) in figure 3.2 between $1.5 < x/D < 5$, they were absent near the sphere for $x/D < 1.5$. It is the large positive value of the vortex stretching terms ($S1$ and $S2$) in $1.5 < x/D < 5$ that enables the formation of these large-Q structures. Viscous dissipation ($DISSIP$) is the dominant sink for enstrophy while advection by mean ($ADVEC$) tends to redistribute enstrophy from the region near peak enstrophy. The other terms are at least an order of magnitude less than $S1$, $S2$, $ADVEC$, $DISSIP$ as well described by the order of magnitude analysis of Tennekes & Lumley (1972).

$$\begin{aligned}\frac{\partial}{\partial t}\left(\frac{1}{2}\overline{\omega_i'\omega_i'}\right) = &-\overline{u}_j\frac{\partial}{\partial x_j}\left(\frac{1}{2}\overline{\omega_i'\omega_i'}\right) - \overline{u_j'\omega_i'}\frac{\partial\overline{\omega}_i}{\partial x_j} - \frac{1}{2}\frac{\partial}{\partial x_j}\left(\overline{u_j'\omega_i'\omega_i'}\right)\\ &+ \overline{\omega_i'\omega_j's_{ij}'} + \overline{\omega_i'\omega_j'}\;\overline{S}_{ij} + \overline{\omega}_j\overline{\omega_i's_{ij}'}\\ &+ \frac{1}{Re}\frac{\partial^2}{\partial x_j\partial x_j}\left(\frac{1}{2}\overline{\omega_i'\omega_i'}\right) - \frac{1}{Re}\overline{\frac{\partial\omega_i'}{\partial x_j}\frac{\partial\omega_i'}{\partial x_j}} - \frac{\delta_{k3}}{Fr^2}\varepsilon_{ijk}\overline{\omega_i'\frac{\partial\rho'}{\partial x_j}}\end{aligned} \tag{3.13}$$

The physical meaning of each term is as follows:

$\frac{\partial}{\partial t}\left(\frac{1}{2}\overline{\omega_i'\omega_i'}\right)$: Rate of change of fluctuating enstrophy (DDT)
$-\overline{u}_j\frac{\partial}{\partial x_j}\left(\frac{1}{2}\overline{\omega_i'\omega_i'}\right)$: Advection by mean ($ADVEC$)
$-\overline{u_j'\omega_i'}\frac{\partial\overline{\omega}_i}{\partial x_j}$: Production by mean gradient of vorticity ($PROD$)
$-\frac{1}{2}\frac{\partial}{\partial x_j}\left(\overline{u_j'\omega_i'\omega_i'}\right)$: Diffusion by turbulence ($TDIFF$)
$\overline{\omega_i'\omega_j's_{ij}'}$: Stretching/tilting of vorticity fluctuation by fluctuating strain ($S1$)
$\overline{\omega_i'\omega_j'}\;\overline{S}_{ij}$: Stretching/tilting of vorticity fluctuation by mean strain ($S2$)
$\overline{\omega}_j\overline{\omega_i's_{ij}'}$: Stretching/tilting of mean vorticity by fluctuating strain ($S3$)
$\frac{1}{Re}\frac{\partial^2}{\partial x_j\partial x_j}\left(\frac{1}{2}\overline{\omega_i'\omega_i'}\right)$: Diffusion by viscosity ($VDIFF$)
$-\frac{1}{Re}\overline{\frac{\partial\omega_i'}{\partial x_j}\frac{\partial\omega_i'}{\partial x_j}}$: Dissipation ($DISSIP$)
$-\frac{\delta_{k3}}{Fr^2}\varepsilon_{ijk}\overline{\omega_i'\frac{\partial\rho'}{\partial x_j}}$: Baroclinic torque (BT)

Buoyancy significantly affects the distribution and magnitude of enstrophy as has been discussed in previous sections, e.g. section 3.5.2 shows that area-integrated enstrophy generally decreases with increasing stratification in moderately stratified wakes with $Fr = O(1)$ and generally increases with increasing stratification for highly stratified

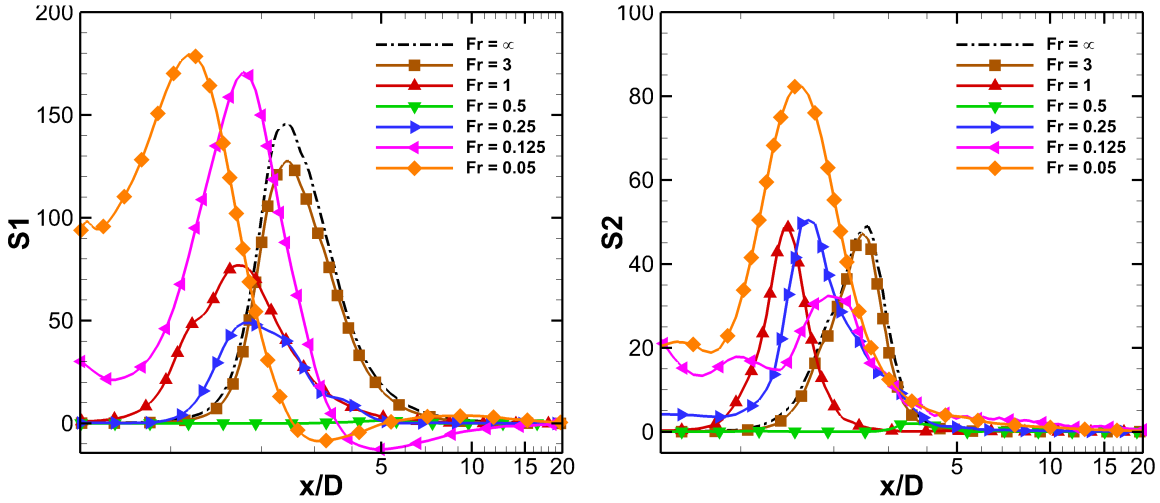

Figure 3.13: Cross-sectional integration of stretching term S1 (left) and S2 (right).

wakes with $Fr \leq 0.125$. Quantification of equation (3.13) allows examination of the underlying reason for the stratification effect observed in the simulations. Surprisingly, the area-integrated baroclinic torque (BT) is found to be relatively small (figure 3.16, left) and not the primary reason. Rather it is the implicit effect of buoyancy on vortex stretching as elaborated below.

Figure 3.13 shows that vortex stretching tends to decrease when the stratification increases as Fr is reduced to $O(1)$ values. In accordance with integrated enstrophy in figure 3.11, $Fr = 0.5$ is the critical Fr number beyond which a further reduction of Fr increases the vortex stretching term. $Fr = 0.125$ and $Fr = 0.05$ wakes experience higher peak in stretching by turbulent strain compared to the unstratified case. This increase is also observed in the stretching by the mean strain where $S2$ increases when $Fr < 0.5$. Reactivated velocity fluctuations and high velocity gradient in the vertical direction (the mean flow is reorganized into multiple two-dimensional layers) combine to increase $S2$. It is interesting to note that, while integrated enstrophy and their components shown in figure 3.11 and 3.12 for $Fr = 0.25$ and 0.125 are larger than that of unstratified wake until the far end of the downstream domain, vortex stretching remains large only closer

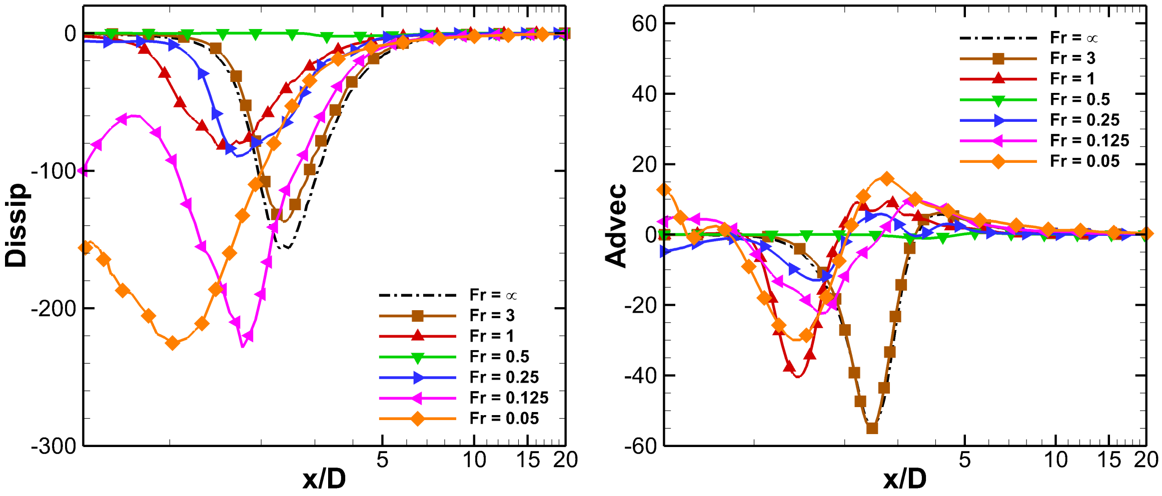

Figure 3.14: Cross-sectional integration of dissipation (left) and advection(right).

to the sphere and become less than unstratified stretching by $x/D \approx 3$. Regardless of the numerical approach one uses (LES,RANS) away from the body, it is thus imperative that the model accounts for motions near the sphere in these low-Fr wakes to capture the near-sphere enhancement of enstrophy that then lasts far downstream.

The stratified cases with $Fr \leq 0.125$ experience stronger vortex stretching compared with the unstratified case and stratified case at $Fr \geq 0.25$. The peaks of vortex stretching lie in the vicinity of highly rotational coherent vortices which shift upstream in the low Fr cases. Thus, as stratification increases, enstrophy is produced via stretching mechanism closer to the sphere. Even with relatively high mean strain in the near wake compared to late wake, fluctuating strain still exceeds the mean strain resulting in the higher value of $S1$ compared to $S2$ in all cases.

While stretching and tilting by mean and fluctuating strain act mainly as the source, advection and dissipation balance them by being a transport and a sink of the enstrophy. Similar to the unstratified case, small scale dissipation remains the primary sink in the fluctuating enstrophy equation while mean advection acts secondarily. Unlike advection by mean flow, turbulent transport and production increase enstrophy near the sphere

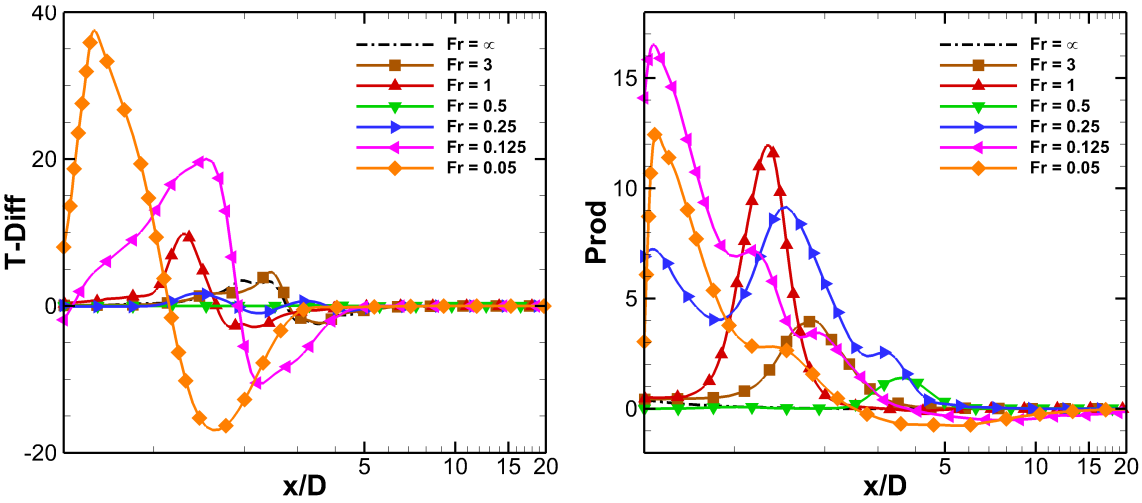

Figure 3.15: Cross-sectional integration of turbulent diffusion (left) and production (right).

and decrease enstrophy further downstream as shown in figure 3.15. Both transport and production terms are larger in magnitude in the low-Fr regime. Stretching, $S3$, and viscous diffusion term, $VDiff$ (not shown here) are two orders of magnitude smaller than $S1$ and do not significantly alter the enstrophy field.

3.6 Summary and Conclusions

DNS of flow past a sphere at Re = 3700 has been carried out in moderate-to-highly stratified cases and results with eight stratification levels of Fr = ∞, 3, 1, 0.5, 0.25, 0.125, 0.05, and 0.025 are reported; here, the unstratified case corresponds to $Fr = \infty$. Vortex dynamics is investigated by means of visualization of instantaneous vortical structures with the Q criterion, spatial distribution and magnitude of enstrophy ($\overline{\omega_i'\omega_i'}/2$), and computation of terms in the enstrophy transport equation.

The Q criterion enables three-dimensional visualization of vortical structures. In the unstratified case, circular vortex rings are shed from the sphere which then break down into small structures after approximately one and a half times the sphere diameter. These small

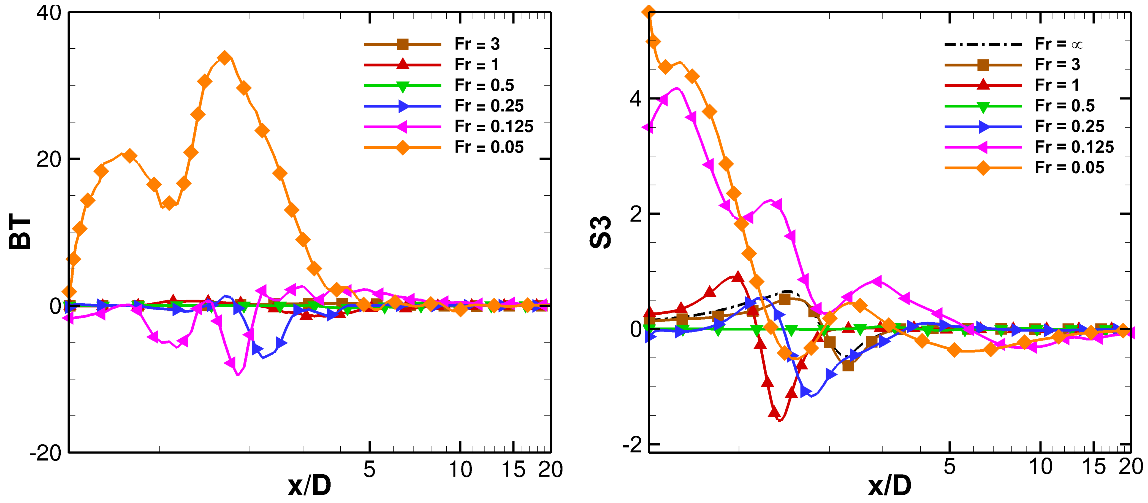

Figure 3.16: Cross-sectional integration of baroclinic torque (left) and stretching term S3 (right).

structures in the unstratified case are tube-like and show no preference in their orientation. Highly rotational vortex tubes are seen in the $1.5 < x/D < 5$ region behind the sphere and their rotational strength gradually decreases downstream. Moderate stratification, $Fr = O(1)$, preferentially orients vortex tubes in the streamwise direction but does not change their tube-like shape. At $0.25 < Fr < 1$, the lee wave impresses its undulation on the vortical structures.

High stratification, $Fr \leq 0.125$, significantly changes both the shape and orientation of the vortical structures. The cross-section of vortex tubes are no longer circular but flattened. The orientation of the vortex tubes lies in the horizontal plane. At $Fr = 0.025$, isosurface of Q shows distinct pancake eddies and inclined surfboard structures, both structures being thin in the vertical. The pancake eddies are disc-like structures located in the central horizontal plane that occur alternately on each side with an offset from the center line, and have an alternating sign of vertical vorticity. The surfboard structures are located in the middle, are inclined with the horizontal, and form successive V-shaped structures. The pancakes are regularly spaced with distance between two consecutive pancake eddies on the same side approximately $5D$ corresponding to the energy spectrum peak at Strouhal number of 0.2 associated with vortex shedding. Surfboard structures are shed with the same frequency as the pancake eddies. Thus, pancake eddies that occur in the near wake when the stratification is high are associated with the dominant vortex shedding mode at $Re = 3700$. The vorticity pattern is akin to that of a sinuous mode. The behavior at higher Re or at moderate-to-low stratification ($Fr \geq O(1)$) requires further exploration.

The distribution of enstrophy ($\overline{\omega_i'\omega_i'}/2$) across the wake cross-section is isotropic in the unstratified case. Stratification distorts this distribution from circular to elliptical, close to the sphere. The enstrophy magnitude decreases with increasing stratification until Fr of 0.5. In contrast, there is a rapid increase of enstrophy with increasing stratification when Fr is decreased to 0.125 and beyond. At $Fr = 0.25$, three distinct horizontal layers are found where relatively low enstrophy is sandwiched between upper and lower layers with high enstrophy. With increasing stratification, these three layers are vertically located closer to each other leaving a small thin layer in the middle.

The enstrophy equation shows that the dominant balance in the unstratified wake is between vortex stretching and dissipation with secondary contributions from advection and turbulent diffusion. In the stratified wake, the dominant balance remains between vortex stretching and dissipation with the contribution of the baroclinic term being secondary. Thus, the implicit stratification effect on vortex stretching is responsible for the changes in enstrophy with stratification observed in the simulations. In particular, stratified wakes with $Fr < 0.125$ have large vortex stretching in the region near the body that is associated with unsteady and intermittent shedding of the boundary layer from various vertical locations at the sides of the sphere. The vortex stretching in the region $x/D < 2$ is sufficiently large so that the enstrophy remains larger than in the unstratified case far downstream. The implication is that it is important to resolve the near-body flow for low-Fr wakes in order to obtain accurate results for the far wake. Simulations will have to be continued into the quasi 2D regime for $Fr \geq O(1)$ to investigate the persistence of near-body flow characteristics.

The content of Chapter 3, in full, is a reprint of the material as it appears in Chongsiripinyo K., Pal A., and Sarkar S., “On the vortex dynamics of flow past a sphere at Re=3700 in a uniformly stratified fluid”, *Phys. Fluids.*, 29(2), 020704, 2017. The dissertation author was the primary researcher and author of this paper.

Chapter 4

Effect of stratification on the turbulent wake behind a sphere at Re = 10,000

4.1 Abstract

Large eddy simulation of flow past a sphere in a density-stratified fluid is performed at a Reynolds number of $Re = U_\infty D/\nu =$ 10,000 and $Fr = U_\infty/ND = \infty$, 3, and 1 where $Fr = \infty$ refers to the unstratified case. Here, U_∞, D, and N are the free-stream velocity, sphere diameter, and constant background buoyancy frequency, respectively. The choice of $Fr = O(1)$ allows investigation of the turbulent wake under conditions where the buoyancy time scale, $1/N$, is comparable to the mean flow time scale, D/U_∞. Visualizations in the form of Q-criterion and azimuthal vorticity show that stratification introduces qualitative changes in the near wake structure as well as the helical mode instability. The centerline defect velocity, U_0, in the unstratified wake decays according to the power law, $U_0 \propto x^{-m}$, with $m = 1$ instead of the classical value of $m = 2/3$. In the stratified wakes, U_0 exhibits

an "oscillatory modulation" owing to the lee-wave pattern created by the sphere. As a result, U_0 increases in the region $\pi Fr \leqslant x/D \leqslant 2\pi Fr$ instead of the usual decrease. Further downstream, there is an overall decrease of U_0 but the exponent m in the power law, $U_0 \propto x^{-m}$, is reduced to $m = 0.4$. The turbulent kinetic energy (*t.k.e.*) budget is quantified to assess the influence of stratification. The relative roles of advection, production, dissipation, transport and buoyancy flux are found to be altered over the entire wake at $Fr = 1$ and in the intermediate and far wake at $Fr = 3$.

4.2 Introduction

Turbulent wakes under stratification are ubiquitous, e.g. in flows past marine swimmers, underwater submersibles, underwater topography, islands and mountains. In the early years, stratified wakes were studied primarily using experimental methods. Early experiments, as reviewed in Lin & Pao (1979), showed that stratification suppresses vertical motion, promotes downstream horizontal coherent eddies, and enables propagation of internal gravity waves into the far field. With better experimental instruments and advances in numerical simulation, more accurate qualitative and quantitative results have been obtained. Chomaz *et al.* (1993) experimentally showed that stratified wakes can be divided into four different regimes based on $Fr = U/ND$. For $Fr < 0.4$, the wake corresponds to triple-layer flow with two lee waves surrounding a layer of two-dimensional motion. For Fr between 0.4 and 0.75, the saturated lee wave suppresses the separation region or splits it into two. When Fr is between 0.75 and 2, the buoyancy effect on the near wake progressively decreases in importance and, by $Fr > 2.25$, the near wake is similar to the homogeneous case. A stratified wake at high Fr ($Fr > O(1)$) exhibits three distinct regions. The first region is the near wake (NW) where the wake spreads uniformly in all directions and turbulence behaves as it does in a homogeneous fluid. It is followed by a second non-equilibrium (NEQ) regime identified by Spedding (1997) where there is an onset of buoyancy effects including conversion of stored potential energy to kinetic energy and anisotropy between horizontal and vertical motions. The third region (Q2D) is characterized by the existence of vertically suppressed two-dimensional eddies, so called “pancake vortices”.

Recently Pal *et al.* (2016) and Pal *et al.* (2017) performed DNS of stratified flow past a sphere at $Re = 3700$ over a wide range of stratifications that encompass the $Fr < O(1)$ regime, the $Fr = O(1)$ regime and the lower boundary of the $Fr > O(1)$ regime. Unlike previous DNS/LES of stratified wakes that used a temporal flow model (Brucker & Sarkar, 2010; Diamessis *et al.*, 2011), the body was included in these simulations. Though computationally expensive owing to resolution of the boundary layer, the simulation led to new results regarding the near and intermediate wake. It was found that the body-generated lee waves cause oscillatory modulation of the mean defect velocity. Also, the flow enters a new regime of horizontal vortex shedding and turbulence when Fr smaller than about 0.25.

The objective of the present paper is to examine stratified and unstratified flow past a sphere at a higher $Re = 10^4$ and contrast the results with our knowledge of the $Re = 3700$ wake. We address the following questions. Do decay rates of centerline defect velocity change at higher Re? Do oscillatory modulations persist at the higher Re? What qualitative and quantitative changes occur in the turbulent kinetic energy budget?

4.3 Equations

A sphere of diameter D is immersed in a stream with velocity U. The background is density-stratified with a constant vertical density gradient, $d\rho_b/dx_3$, and buoyancy frequency N that is defined by $N^2 = -(g/\rho_o)d\rho_b/dx_3$ with ρ_0 a reference density that is representative of the background. The filtered Navier-Stokes equations under the Boussinesq approximation for density effects are solved along with an advection-diffusion equation for the filtered density. A dynamic eddy viscosity model is utilized. The following system of non-dimensional governing equations is numerically solved.

Continuity:

$$\frac{\partial u_i}{\partial x_i} = 0, \tag{4.1}$$

Momentum:

$$\frac{\partial u_i}{\partial t} + u_j \frac{\partial u_i}{\partial x_j} = -\frac{\partial p}{\partial x_i} + \frac{1}{Re}\frac{\partial}{\partial x_j}\left[(1 + \frac{\nu_{sgs}}{\nu})\frac{\partial u_i}{\partial x_j}\right] - \frac{1}{Fr^2}\rho_d \delta_{i3}, \tag{4.2}$$

Density:

$$\frac{\partial \rho}{\partial t} + u_j \frac{\partial \rho}{\partial x_j} = \frac{1}{Re}\frac{\partial}{\partial x_j}\left[(1 + \frac{\nu_{sgs}}{\nu})\frac{\partial \rho}{\partial x_j}\right]. \tag{4.3}$$

In Eq. (A.39), ρ_d is the deviation of the density from the background density, $\rho_b(x_3)$. Here, ν is the constant kinematic viscosity and κ is the constant diffusivity of density while ν_{sgs} and κ_{sgs} are the subgrid transport coefficients introduced by the LES model. The fluid has molecular Prandtl number, $Pr = \nu/\kappa = 1$, and the subgrid $Pr_{sgs} = \nu_{sgs}/\kappa_{sgs}$ is assumed to be unity leading to the simplified form of the RHS of Eq. (A.40). The Froude number, $Fr = U/ND$, and the Reynolds number, $Re = UD/\nu$, are the primary non-dimensional parameters. In the following discussion, all variables discussed are non-dimensional unless otherwise noted. Subgrid viscosity, ν_{sgs}, is obtained using the dynamic eddy viscosity model of Germano *et al.* (1991). The coefficient C, as in $\nu_{sgs} = C\overline{\Delta}^2|\overline{S}|$, is dynamically computed using a method of Lilly (1992). C is dynamically averaged along flow trajectories with an exponential weighting function chosen to give more weight to recent times in flow history.

4.4 Numerical methods

Governing equations (A.38)–(A.40) are solved numerically in a cylindrical coordinate system on a staggered grid. The sphere is represented by the immersed boundary method of Balaras (2004); Yang & Balaras (2006). The equations are marched using a combination of explicit and implicit schemes. Implicit marching by the second order Crank-Nicolson (CN) scheme is performed for the terms in the azimuthal direction to alleviate stiffness of the discretized system. The remaining terms are marched explicitly using a third-order Runge-Kutta (RK3) scheme. A periodic boundary condition in the azimuthal direction transforms the discretized Poisson equation into inversion of a pentadiagonal matrix. The pentadiagonal matrix system is solved using a direct solver, Rossi & Toivanen (1999). Inflow and convective outflow boundary conditions are applied at the inlet and outlet of the domain. In order to control spurious reflections from internal waves and other disturbances propagating out of the domain, sponge regions are employed near the free stream and inlet boundaries where the following relaxation terms are added to the governing equations:

$$-\phi(x_i)[u_i(x_i,t) - U_i], \qquad -\phi(x_i)[\rho(x_i,t) - \rho_\infty(x_3)]\,. \tag{4.4}$$

The sponge layer takes the form of a Rayleigh damping function which is designed in such a way so as to gradually relax the velocities and density to their respective values at the boundaries. Here U_i is the freestream velocity and $\rho_\infty(x_3)$ is the density of the stratified background. This is accomplished by adding the explicit damping terms of equation (4.4) to the right hand side of equation (A.39) and (A.40). The variable $\phi(x_i)$ is constructed such that it increases quadratically from $\phi = 0$ to $\phi = 1$ over a sponge region of thickness 10 grid points at the inflow and at the freestream boundaries.

4.5 Parameters

All simulations are performed with $Re = UD/\nu = 10^4$. Three cases are investigated with $Fr = \infty$ (unstratified), $Fr = 3$, and $Fr = 1$. The choice of $Re = 10^4$ allows for validation against the LES of Rodríguez *et al.* (2013), Yun *et al.* (2006), and Constantinescu & Squires (2004). Domain sizes in the upstream, downstream, and radial directions are $L_x^-/D = 40.16$, $L_x^+/D = 80.62$, and $L_r/D = 59.84$, respectively. The sphere center is at $(x/D, r/D) = (0, 0)$. In comparison to the unstratified flow past a sphere of Rodríguez *et al.* (2013), the domain sizes in the radial and upstream directions are enlarged to allow free propagation of internal gravity waves induced by stratification. While this is not necessary for the unstratified case, the same domain size is kept for consistency. The number of grid points in the streamwise, radial, and azimuthal directions are $N_x = 6144$, $N_r = 918$, and $N_\theta = 128$ giving a total number of grid points of approximately 720 million. Grid stretching is used in the radial and streamwise directions to concentrate points near the sphere surface in order to resolve the laminar boundary layer. To compute statistics, temporal averaging of data is performed over 100 non-dimensionalized time units or approximately one flow-through time unit after statistical steady-state. Each simulation uses 512 processors with approximately 1700 hours of wall clock time. The computations utilize a Cray XC40 system with Intel Xeon E5-2698v3 (Haswell-EP) processors clocked at 2.3 GHz.

4.6 Validations

Validation of the unstratified case is performed by examination of the distributions of mean pressure coefficient and mean skin friction coefficient on the body, mean separation angle, drag coefficient and shedding frequency. Computation of the mean is done by

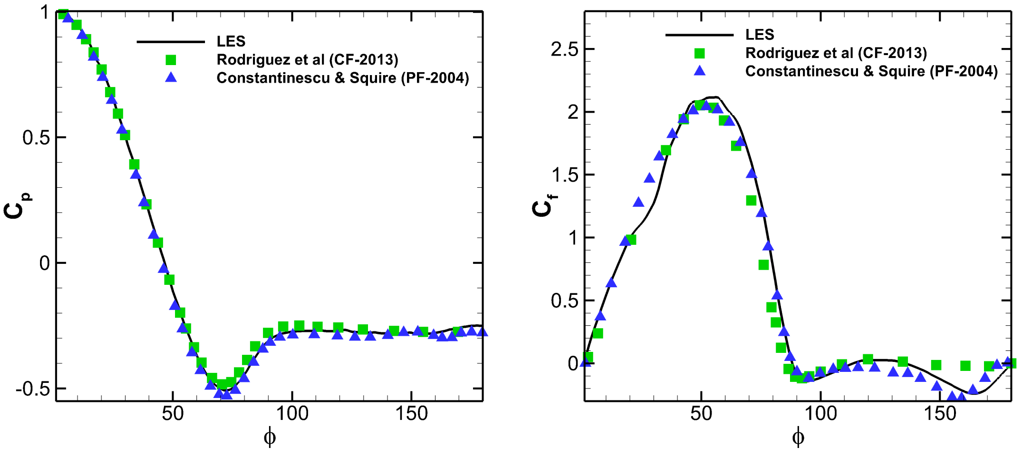

Figure 4.1: Temporal-azimuthal average of pressure coefficient and shear stress on the sphere.

Table 4.1: Comparision of near field statistics.

Studies	St	ϕ_s	C_d	C_{pb}
Present LES	0.199	88.1	0.407	-0.251
Rodríguez *et al.* (2013)	0.195	84.7	0.402	-0.272
Yun *et al.* (2006)	0.17	90	0.393	-0.274
Constantinescu & Squires (2004)	0.195	84	0.393	

averaging both in time and in the azimuthal direction. These results are compared with previous results (Rodríguez *et al.*, 2013; Constantinescu & Squires, 2004). Figure 4.1 shows that pressure and skin friction coefficients are well captured in our simulation. The variable ϕ in the figure denotes the angle from the forward stagnation point of the sphere, $\phi = 0$. Mean separation angle, ϕ_s, is determined by the position, ϕ, where mean $C_f = 0$. The minimum value of C_p, located at $\phi = 72^o$, marks the onset of an adverse pressure gradient. The rise in C_p beyond $\phi = 72^o$ indicative of this adverse gradient contributes to a continuous decrease in C_f until the flow detaches from the surface at separation angle of $\phi_s = 88.1^o$.

4.7 Visualizations

Three-dimensional visualization of instantaneous vortical structures in the wake is done using the Q-criterion of Hunt *et al.* (1988), $Q = 0.5(|\mathbf{\Omega}|^2 - |\mathbf{S}|^2)$ where $\Omega_{ij} = 0.5\left(\partial u_i/\partial x_j - \partial u_j/\partial x_i\right)$ and $S_{ij} = 0.5\left(\partial u_i/\partial x_j + \partial u_j/\partial x_i\right)$. Figure 4.2 shows isosurface of $Q = 2$, 1, and 0.5 for $Fr = \infty$, 3, and 1, respectively. The reduction of isosurface Q-level with increasing Fr is required to enable sufficient downstream extent of the wake-structure visualization. Regions with intensified fluid element rotation are signified by a large positive value of Q where the rate of rotation tensor, Ω_{ij}, exceeds the rate of strain tensor, S_{ij}. For the unstratified case in the range, $0.5 \leqslant x/D \leqslant 1$, axisymmetric vortex rings are shed from the sphere. Helical orientation of the unstratified wake previously observed by Yun *et al.* (2006) is apparent in Figure 4.2 (top). Visualization of the isosurfaces at different times confirms that helical structures do not rotate around the streamwise axis as they travel downstream but rather simply translate downstream as stated in Yun *et al.* (2006). At $Fr = 3$ and especially $Fr = 1$, the vortex rings are distorted into ellipsoids with the major axis in the spanwise, y, direction. The suppression of vertical motion is, thus, immediate for $Fr = O(1)$ wakes and influences how the incoming freestream travels around the sphere. In their results for stratified flow past a sphere at $(Re, Fr) = (3700, 0.5)$, Chongsiripinyo *et al.* (2017) visualized blocking in front of a sphere, i.e there is insufficient kinetic energy to vertically displace incoming fluid over the poles of the sphere. The incoming fluid is, thus, forced to travel horizontally around the sphere when $Fr < O(1)$.

Besides the helical orientation in the unstratified case, a wavy orientation is present at $Fr = 3$ but only in the horizontal plane while this feature disappears for $Fr = 1$. The number density of vortical structures in all cases decrease downstream. Chongsiripinyo *et al.* (2017) investigated dynamics of vortical structures by means of the enstrophy budget. Their results show that stretching/tilting of vorticity fluctuation by fluctuating strain,

$\overline{\omega_i'\omega_j's_{ij}'}$, is primarily responsible for the high density of vortical structures in a small region behind the sphere $1.5 < x/D < 5$.

Figure 4.3 and 4.4 show contours of instantaneous spanwise vorticity in the vertical center plane ($y = 0$) for $-1 < x/D < 10$ and $10 < x/D < 40$. For the unstratified case, given that the present $Re = 10^4$ is much smaller than the critical Reynolds number, $Re \sim 3 \times 10^5$, the entire boundary layer remains laminar from the forward stagnation point until separation. The separated shear layer breaks down into small scale motions via Kelvin-Helmholtz (KH) instabilities at the separated shear layer for both $Fr = \infty$ and 3. At $Fr = 1$, the separated shear layers initially conform with lee waves that have higher amplitude than those at $Fr = 3$; consequently, the shear layers bend toward the centerline. The location where the shear layers plunge at the centerline is also where production of $t.k.e$ achieves its maximum. The $t.k.e.$ budget is explained in a subsequent section. Figure 4.4 shows not only the apparent vertical suppression but also the gradual disappearance of small-scale eddies as stratification increases. Internal gravity waves emitted from the wakes are also detected in both stratified cases.

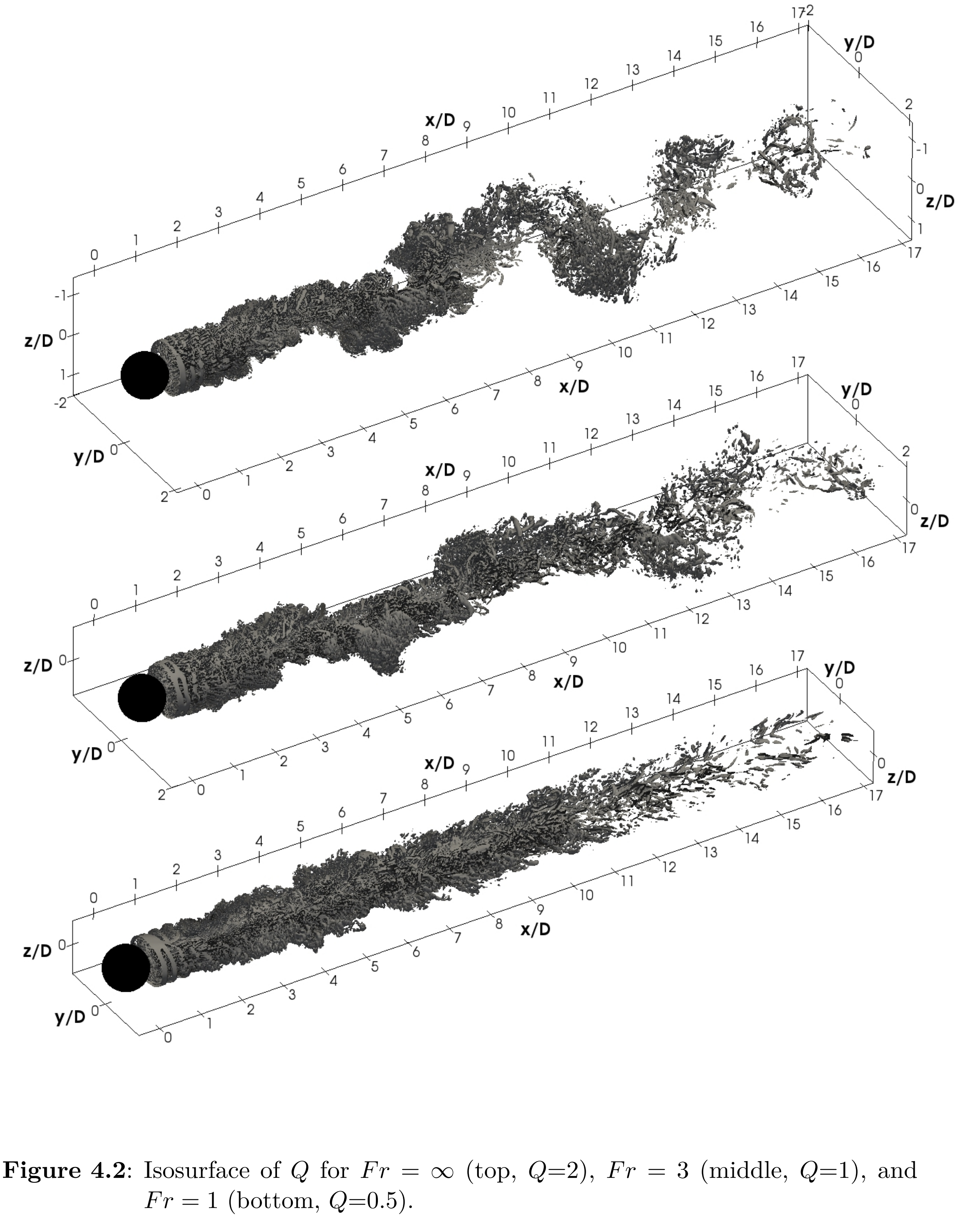

Figure 4.2: Isosurface of Q for $Fr = \infty$ (top, Q=2), $Fr = 3$ (middle, Q=1), and $Fr = 1$ (bottom, Q=0.5).

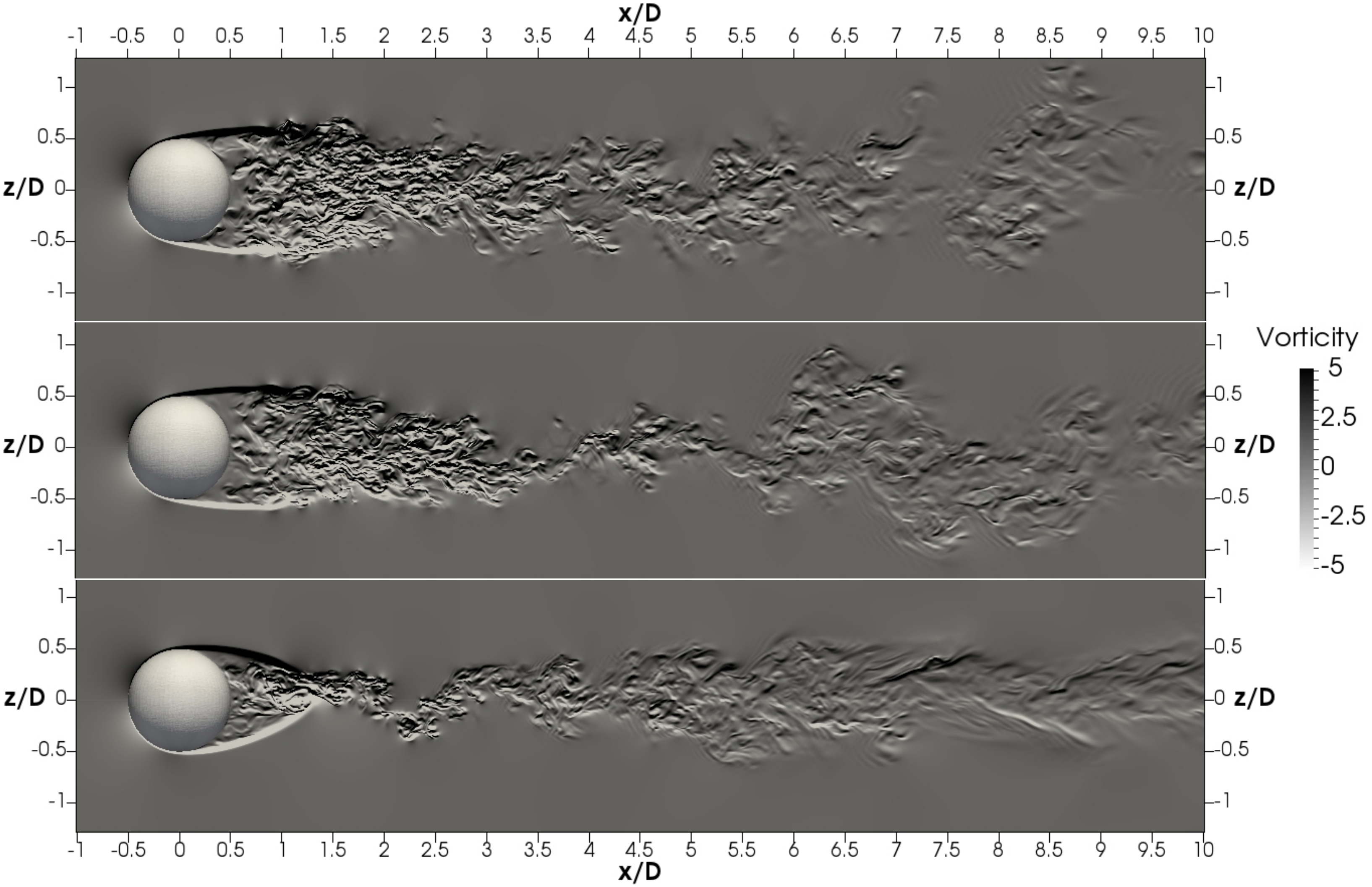

Figure 4.3: Spanwise vorticity contour in the near wake ($-1 < x/D < 10$) on a vertical plane for $Fr = \infty$ (top), $Fr = 3$ (middle), and $Fr = 1$ (bottom).

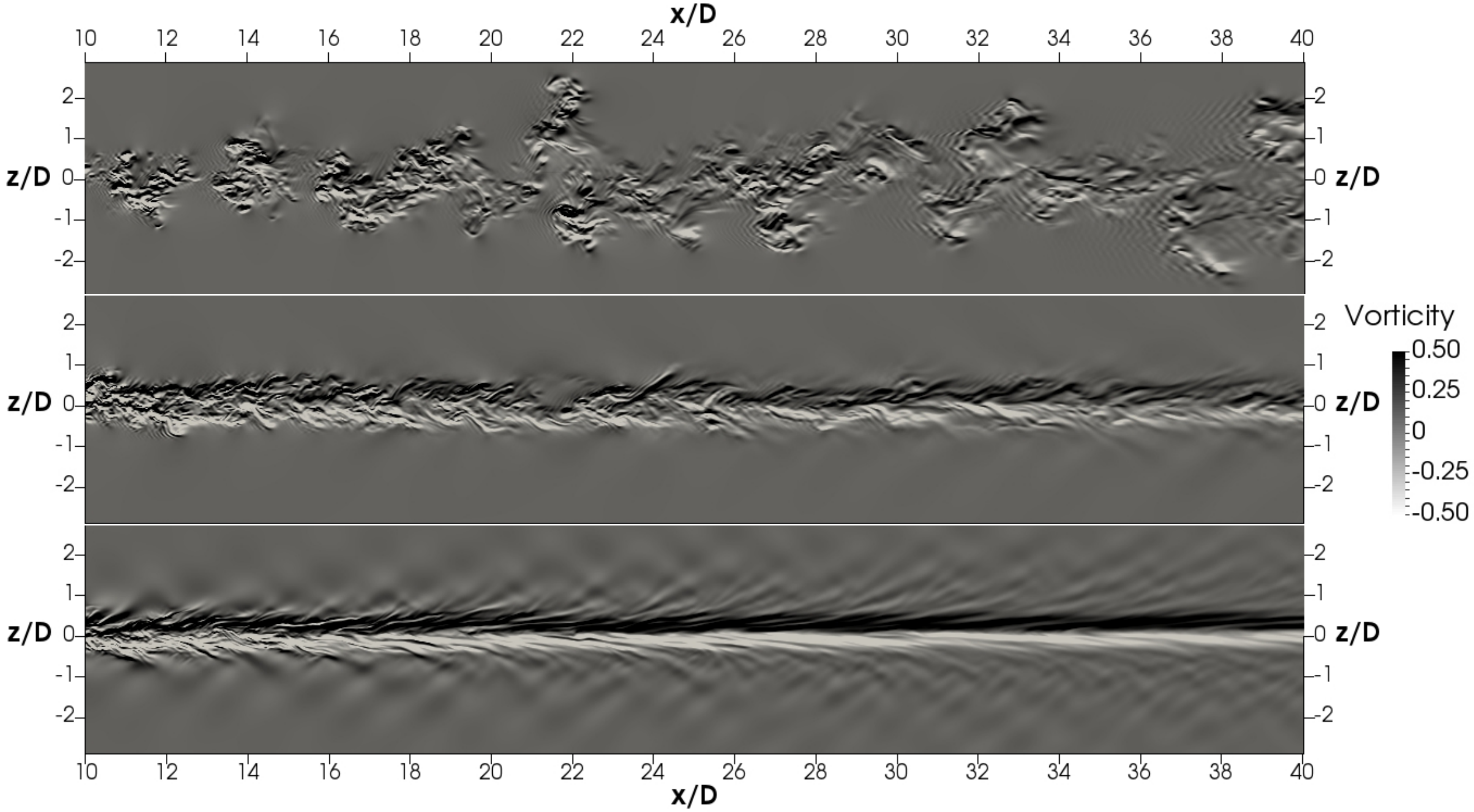

Figure 4.4: Spanwise vorticity contour in the intermediate ($10 < x/D < 40$) for $Fr = \infty$ (top), $Fr = 3$ (middle), and $Fr = 1$ (bottom).

4.8 Defect velocity

Figure 4.5 shows the temporal mean streamwise defect velocity at the centerline. There is an initial rise of defect velocity for all cases close to the sphere in the recirculation zone. For the unstratified case, after the peak, the defect velocity monotonically decreases and approaches an approximate constant decay rate of $(x/D)^{-1}$. This $(x/D)^{-1}$ power law is also observed in an unstratified flow past a sphere at lower $Re = 3700$ in Pal *et al.* (2017). The equilibrium similarity analysis of axisymmetric wakes from George (1989) has shown that the $(x/D)^{-1}$ decay rate of defect velocity can be derived from the low Re dissipation scaling, $D_0 \sim \nu u_0^2/\delta^2$, where u_0 and δ are the characteristic velocity and length scale, respectively. However, this dissipation scaling is not valid in high-Re flow with fully developed turbulence. Recently, Nedić *et al.* (2013) introduced a modified dissipation scaling, $D_0 \sim (U_\infty l/\nu)^m (u_0\delta/\nu)^{-n} u_0^3/\delta$ where l is the size of the wake generator. By setting $m = n = 1$, they obtain $U_0 \sim (x/D)^{-1}$ which, in contrast to George (1989), is independent of global Reynolds number $Re_G = U_\infty l/\nu$.

Centerline defect velocities in stratified cases behave differently from their unstratified counterpart. Distributions of the defect velocities over the streamwise centerline for both stratified cases contain information imposed by the body and the buoyancy frequency. Both velocities reach their first minimum at half of their buoyancy period, $x/D = \pi Fr$, away from the sphere center. Downstream of the first minimum, the defect velocity, U_0, increases and reaches a peak at one full buoyancy period, $x/D = 2\pi Fr$. Bonnier & Eiff (2002) used hot-film measurement and identified a region known as "accelerated collapse" which is characterized by an increase in defect velocity until achieving a so-called transition region where the defect velocity starts to decrease again. The "accelerated collapse" is better termed "oscillatory modulation" and the initial increase of U_0 occurs in the region $\pi Fr \leqslant x/D \leqslant 2\pi Fr$. In fact, the defect velocities in both stratified cases continue to

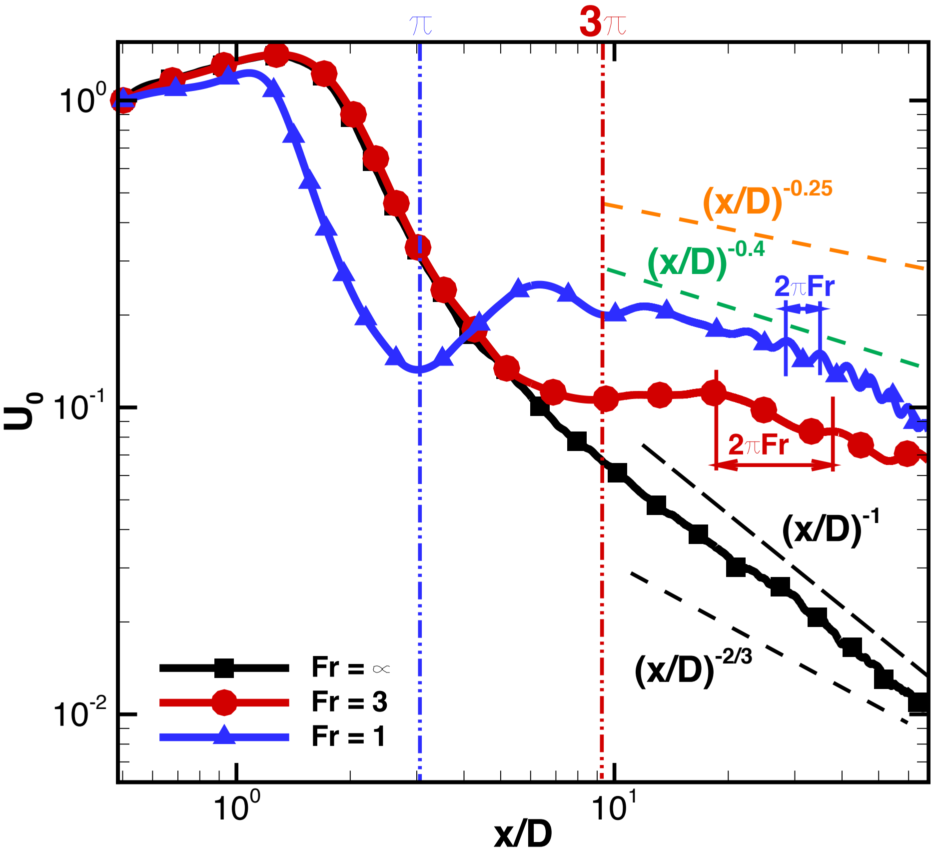

Figure 4.5: Centerline mean streamwise defect velocity.

alternately increase and decrease further downstream in response to the steady lee-wave pattern created by the sphere. These oscillatory modulations especially those downstream are also visible for lower $Re = 3700$ as in Pal *et al.* (2017). Beyond $x/D = 2\pi Fr$, the defect velocities decay with an overall trend $U_0 \propto x^{-m}$ where $m \simeq 0.4$. Bonnier & Eiff (2002) report $m = 0.38$ in their stratified flow past a sphere experiments with $(Fr = U/ND, Re) = (1.5, 3400); (3, 6900); (5, 11500)$. The fact that the decay rate of defect velocity in the stratified wakes is smaller than that of the unstratified wake implies that stratified wakes live longer in the mean.

4.9 Turbulent kinetic energy

The evolution of turbulent kinetic energy is given below. This *t.k.e.* budget details the energy dynamics from the fluctuating flow components. It is used to quantify and analyze the relative roles of advection, production, dissipation, transport, and buoyancy flux. The $t.k.e. = \langle u_i' u_i' \rangle /2$ is denoted as K from here on.

$$\frac{\partial K}{\partial t} = A + P + \epsilon + T + B. \tag{4.5}$$

A and P are advection and production terms defined as

$$A = -\langle u_j \rangle \frac{\partial K}{\partial x_j}, \qquad P = -\langle u_i' u_j' \rangle \frac{\partial \langle u_i \rangle}{\partial x_j}. \tag{4.6}$$

ϵ, the turbulent dissipation rate and B, the buoyancy flux, are defined as follows.

$$\epsilon = -\frac{1}{Re} \left\langle (1 + \frac{\nu_{sgs}}{\nu}) \frac{\partial u_i'}{\partial x_j} \frac{\partial u_i'}{\partial x_j} \right\rangle, \qquad B = -\frac{1}{Fr^2} \langle \rho_d' u_z' \rangle. \tag{4.7}$$

T is the transport of K defined as

$$\begin{aligned} T = & -\frac{1}{2} \frac{\partial}{\partial x_i} \langle u_i' u_j' u_j' \rangle - \frac{\partial \langle p' u_i' \rangle}{\partial x_i} \\ & + \frac{1}{2Re} \left\langle \frac{\partial}{\partial x_j} \left((1 + \frac{\nu_{sgs}}{\nu}) \frac{\partial (u_i' u_i')}{\partial x_j} \right) \right\rangle \\ & + \frac{1}{Re} \left\langle u_i' \frac{\partial u_j'}{\partial x_i} \frac{\partial (\nu_{sgs}/\nu)}{\partial x_j} \right\rangle . \end{aligned} \tag{4.8}$$

The cross-sectional area integrated terms in the turbulent kinetic energy budget are shown in Figure 4.7. For simplification, we divide the streamwise domain into 3 regions, $0.7 < x/D \leqslant 10$, $10 < x/D \leqslant 40$, and $40 < x/D \leqslant 70$ referred to as near, intermediate, and far wake, respectively. Note that this nomenclature is consistent with unstratified-wake

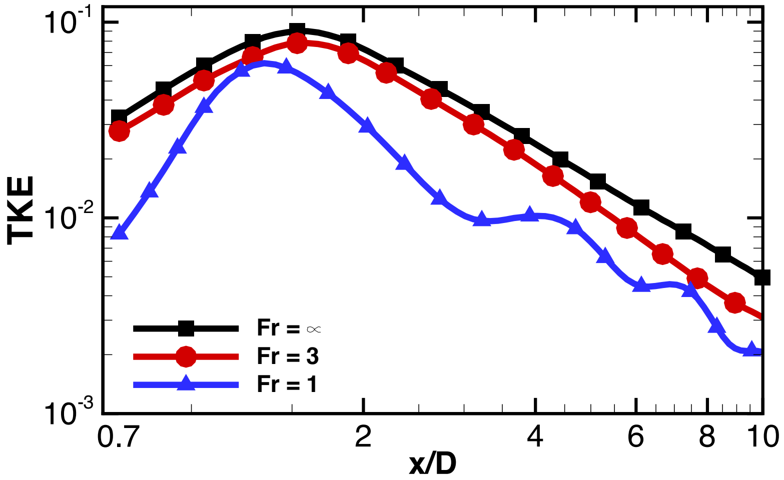

Figure 4.6: Area integrated turbulent kinetic energy.

literature and does not correspond to regimes based on buoyancy frequency.

The near-wake evolution of $t.k.e.$ (left column of Figure 4.7) reveals that the generation, destruction, and transport of $t.k.e.$ are relatively large close to the sphere, $0.7 \leqslant x/D \leqslant 5$. Both production and dissipation reach their peaks at approximately the same location of $x/D \simeq 1.5$. Integrated advection is initially negative in the vicinity of the recirculation region and, further downstream, is positive acting as a local source. The transport term, unlike in simulations of stratified flow past a sphere at lower $Re = 3700$ by Pal *et al.* (2017), is no longer negligible for the entire downstream domain regardless of Fr. Chomaz *et al.* (1993) points out that for $Fr > 2.25$, the near-wake is similar to the homogeneous case. Consistent with Chomaz *et al.* (1993), quantitative changes relative to the unstratified counterpart are largely insignificant in the $Fr = 3$ near-wake budget.

The near-wake balance of $t.k.e.$ is significantly altered at $Fr = 1$. The peak production is approximately 50% larger but large P spans a shorter streamwise distance so that the $t.k.e.$ shown in Figure 5.5 is smaller than in the unstratified case. The dissipation is significantly reduced so that at the point of maximum production, $P/\epsilon \simeq 6$ compared to the unstratified-wake value of 2. There is a significant increase in advection. The maxima of production and advection occur at approximately the same location where the upper and lower separated shear layers plunge toward the centerline as observed in Figure 4.3. While the buoyancy term is negligible in the near wake of the $Fr = 3$ case, it is significant in the $Fr = 1$ case. B has an oscillatory signature that persists for the entire downstream domain. Note that since lee waves are introduced by a wake generator, a simulation using a temporal flow model, as in Brucker & Sarkar (2010), is unable to capture these oscillatory modulations in U_0, P and B. Buoyancy flux, B, as well as turbulent production, P, cross zero at $x/D = \pi$, the same location where the mean streamwise centerline defect velocity reaches its first local minimum. Thereafter, over the entire downstream region, both B and P show oscillations with wavelength of $2\pi Fr$. At $Fr = 3$, B and P also cross zero but in the intermediate wake and also exhibit oscillatory behavior. It appears that, in $Fr = O(1)$ wakes, the turbulent production crosses zero at $x/D \approx \pi Fr$ and, thereafter, both P and B exhibit an oscillatory modulation with spatial period of $2\pi Fr$.

The middle column of Figure 4.7 depicts the intermediate-wake region. In the unstratified case, production becomes small relative to the other terms and the flow evolves as freely decaying turbulence. Although shear production is also small in the stratified wakes, there are clear differences in the behavior of the different terms in the *t.k.e.* balance. At $Fr = 3$, advection decreases by an approximate factor of two while the transport term becomes smaller by an even larger proportion. In addition, oscillatory modulations of buoyancy and production are visible. Dissipation is the only term which does not show the oscillatory signature but monotonically decays. This is because the small spatial scales responsible for turbulent dissipation also have a small time scale, much smaller than the buoyancy time scale of $1/N$. Beyond $x/D \approx 15$, buoyancy and transport dominate the $Fr = 1$ budget and balance one another.

Budget distributions are distinctive for all three simulated stratifications in the far wake as shown in Figure 4.7 (right column). The budget for the unstratified case remains similar to that of the intermediate wake where production is relatively small suggesting that the wake continues to behave as freely-decaying turbulence. In addition, advection is balanced by transport and dissipation. For $Fr = 3$, all terms are of the same order of magnitude. For both stratified cases, production has order of magnitude $O(10^{-5})$, two order of magnitude larger than in the unstratified case with $O(10^{-7})$. The dissipation takes similar values in the $Fr = 3$ and 1 wakes. At $Fr = 1$, buoyancy and transport remain dominant. This is contrary to the *t.k.e.* budget for $Fr = 1$ at lower $Re = 3700$ presented in Pal *et al.* (2017) where the buoyancy term is balanced by the advection term in the far-wake.

The content of Chapter 4, in full, is a reprint of the material as it appears in Chongsiripinyo K. and Sarkar S., "Effect of stratification on the turbulent wake behind a sphere at Re=10,000", *10th International Symposium on Turbulence and Shear Flow Phenomena (TSFP10)*, Chicago, USA, 2017. The dissertation author was the primary researcher and author of this paper.

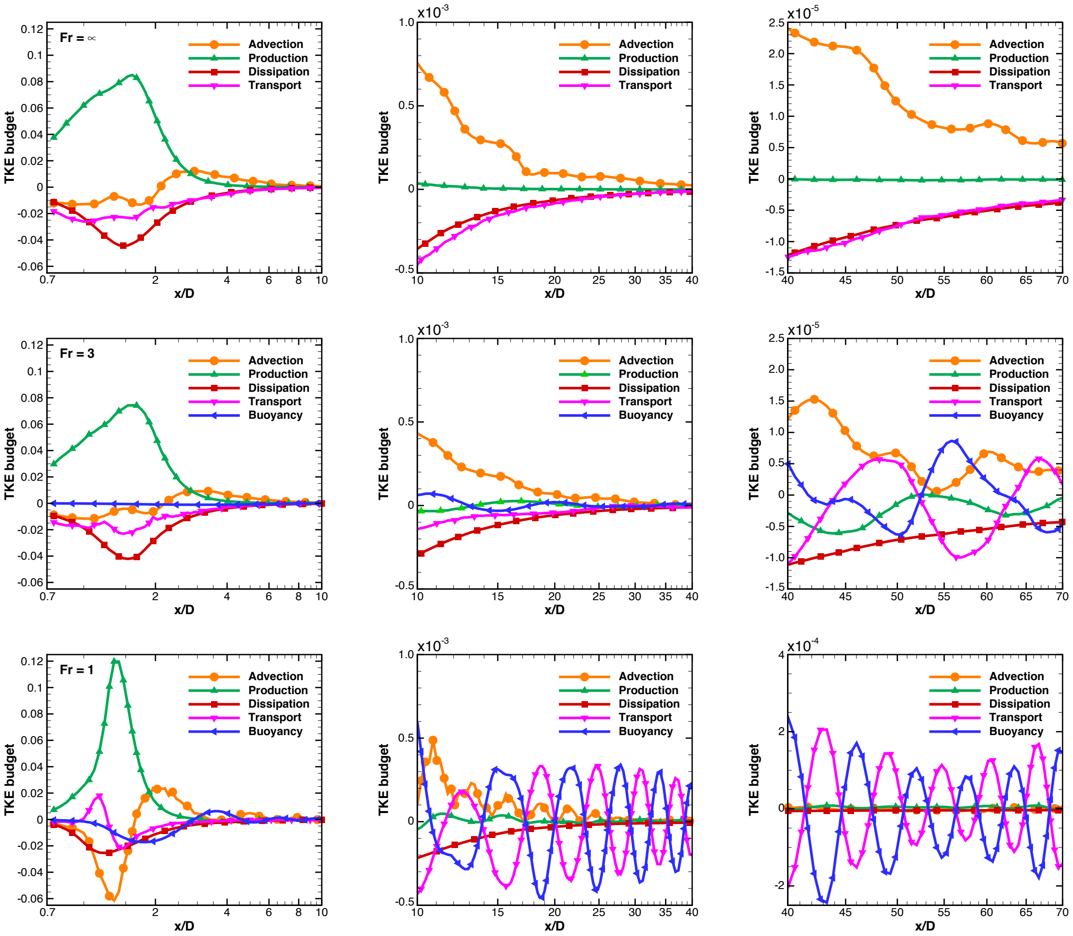

Figure 4.7: Terms in the $t.k.e.$ budget for $Fr = \infty$ (top row), $Fr = 3$ (middle row), and $Fr = 1$ (bottom row) in the near-wake region $0.7 < x/D \leqslant 10$ (left column), the intermediate-wake region $10 < x/D \leqslant 40$ (middle column), and the far-wake region $40 < x/D \leqslant 70$ (right column).

Chapter 5

Scaling laws in the axisymmetric wake of a sphere

5.1 Introduction

An axisymmetric turbulent wake is often assumed to be self-similar when the streamwise location x is sufficiently far from the wake generator. Thus, profiles of the single-point statistics have the local wake width, $\delta(x)$, and the centerline streamwise mean defect velocity, $U_0(x)$, as the characteristic length and velocity scales. Under self-similarity, the evolution of the scaling parameters, U_0 and δ, is described by power laws: $U_0/U_\infty \propto x^m$ and $\delta/D \propto x^n$ where D is a characteristic length scale of the body. The power-law coefficients m and n were found theoretically (George, 1989) to be $(m_L, n_L) = (-1, 1/2)$ and $(m_H, n_H) = (-2/3, 1/3)$ for low-Re and high-Re regimes, respectively. According to Johansson *et al.* (2003), the high-Re regime should apply only after the initial transient has decayed so that u'/U_0 becomes constant and only as long as the *local* Reynolds number is sufficiently large, $Re_l = U_0\delta/\nu > 500$. The decrease in *local* Reynolds number as one travels downstream distinguishes the turbulent axisymmetric wake from other free shear flow. There may be a transition from the high to low-Re scaling at large x where Re_l is sufficiently small. It is worth noting that the dissipation is taken to scale as $\epsilon \sim U_0^3/\delta$ at high Re while $\epsilon \sim \nu U_0^2/\delta^2$ at low Re. Recently, Nedić *et al.* (2013) have found that the axisymmetric wake of high-drag, irregularly shaped plates exhibit $(m, n) = (-1, 1/2)$ while flow past a regular circular disk and a square plate leads to a wake with the classical high-Re scaling of $(m, n) = (-2/3, 1/3)$. The Reynolds number was not small in the experiments of Nedić *et al.* (2013) and, different from George (1989), a nonequilibrium (NEQ) dissipation law is proposed by Nedić *et al.* (2013) to explain their finding of the anomalous $(m, n) = (-1, 1/2)$ scaling.

In the present work, we consider another canonical wake generator, a sphere, that gives rise to an axisymmetric wake. Numerical simulations are conducted with the objective of characterizing the power laws and discussed in the context of the previous work on this topic.

5.2 Numerical approach

The incompressible Navier-Stokes equations along with the continuity equation are numerically solved in a cylindrical coordinate system.The sphere is represented by the immersed boundary method (Balaras, 2004; Yang & Balaras, 2006). The equations are marched using a combination of explicit (third-order Runge-Kutta) and implicit (Crank-Nicolson) schemes. Periodicity allows Fourier transformation of the Poisson equation in the azimuthal direction and the resulting equation for the Fourier modes is solved using a direct solver. Velocity boundary conditions (BCs) are Dirichlet, convective outflow, and free-stream at the inlet, outlet and outer radial directions, respectively. The dynamic eddy viscosity model is utilized for the $Re = 10^4$ (LES) case. Table 5.1 lists the computational parameters. The values of C_p and C_f at the body have been validated previously for both

Table 5.1: Computational domains. L_x^- and L_x^+ refer to domain upstream and downstream lengths. N is number of grid points.

Re	L_r/D	L_θ	L_x^-	L_x^+	N_r	N_θ	N_x	$N_{total}(\cdot 10^6)$
3700 (DNS)	16	2π	23	80	632	128	4608	372.77
10^4 (LES)	59	2π	40	80	918	128	6144	721.94

$Re = 3700$ (Pal *et al.*, 2017) and $Re = 10^4$ (Chongsiripinyo & Sarkar, 2017).

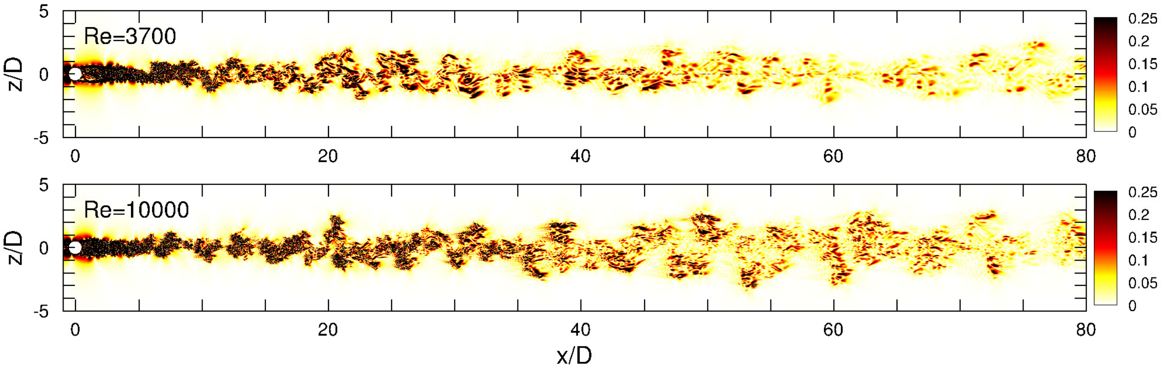

Figure 5.1: Contours of azimuthal vorticity magnitude. z/D is cross-stream direction normalized by sphere diameter.

5.3 Decay of turbulent wake

Figure 5.2 and 5.3 show the present simulation results of $U_0(x)$ and $\delta(x)$, respectively, along with previous results of the sphere wake. At $Re = 10,000$, the recirculation region is shorter than at $Re = 3700$. Further downstream, both cases exhibit a power law close to $U_0 \propto x^{-1}$. The literature shows different combinations of power-law exponents. At $Re = 50,000$, the temporally evolving model of Brucker & Sarkar (2010) exhibits $(m, n) = (-2/3, 1/3)$. Note that the temporal model uses synthetic initial turbulence that does not contain the large scale helical structures that arise from shedding of the sphere boundary layer (Yun *et al.*, 2006; Chongsiripinyo *et al.*, 2017). A laboratory experiment at similar $Re = 65,000$ (Gibson *et al.*, 1968) in figure 5.2 exhibits a power-law decay of U_0 at

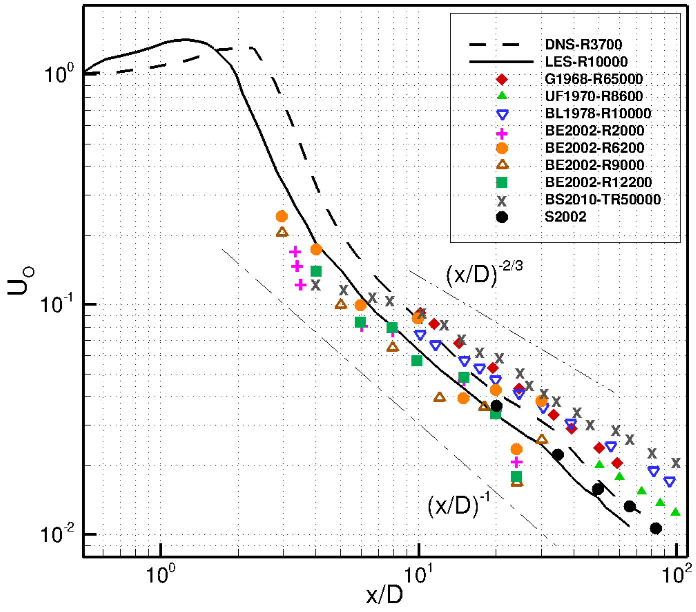

Figure 5.2: Centerline streamwise mean defect velocity. Legends are as follows: G1968, Gibson *et al.* (1968); UF1970, Uberoi & Freymuth (1970); BL1978, Bevilaqua & Lykoudis (1978); BE2002, Bonnier & Eiff (2002); BS2010, Brucker & Sarkar (2010); S2002, Spedding (2002).

least during $10 < x/D < 60$. This decay rate is, however, neither $m = -1$ nor $m = -2/3$. Let us turn to sphere wakes at lower Re. The laboratory experiment of Bevilaqua & Lykoudis (1978) at $Re = 10,000$ exhibits $(m, n) = (-2/3, 1/3)$. In contrast, the wakes spanning $Re = 2000 - 12,000$ studied by Bonnier & Eiff (2002) show behavior closer to $(m, n) = (-1, 1/2)$.

The evolution of local $Re_l = U_0\delta/\nu$ is shown in figure 5.4. If the criterion (Johansson *et al.*, 2003) of $Re_l = U_O\delta/\nu > 500$ for the high-Re regime is true, it can be inferred from figure 5.4 that the present simulations at $Re = 3700$ and $10,000$ do not fall into the high-Re regime and, therefore, $m = -2/3$ and $n = 1/3$ would not be expected. Note that the experiment of Bevilaqua & Lykoudis (1978) contradicts the criterion of Johansson *et al.* (2003) since their $Re = 10,000$ wake exhibits $(m, n) = (-2/3, 1/3)$ despite that fact that $Re_l < 500$.

The evolution of centerline t.k.e (K) is shown in Figure 5.5. The $x^{-3/2}$ power law

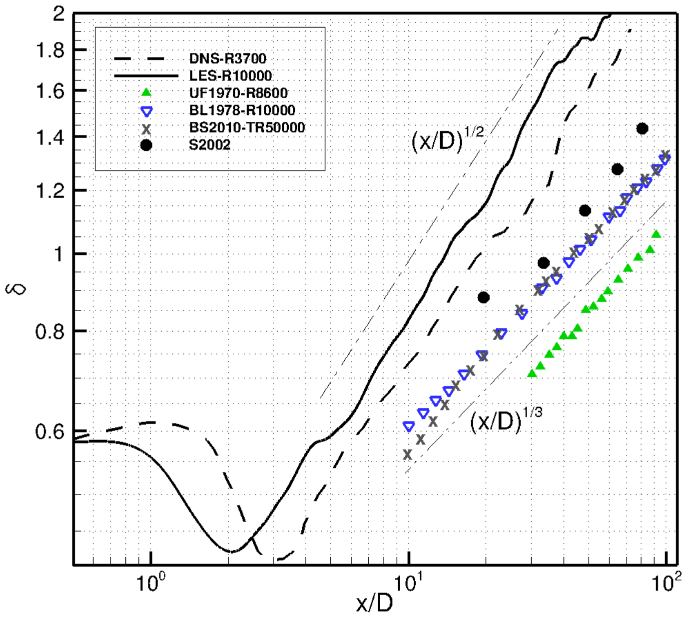

Figure 5.3: Wake half width, L_v (or δ). The dashed-dotted line is $\delta \propto (x/D)^{1/2}$ and the dashed-dotted-dotted line is $\delta \propto (x/D)^{1/3}$. The legend is the same as figure 5.2.

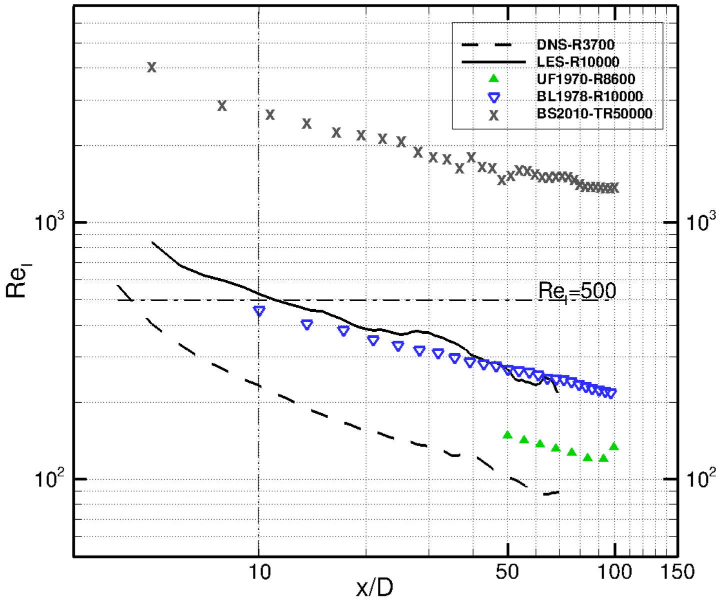

Figure 5.4: Local Reynolds number, $Re_l = U_0\delta/\nu$.

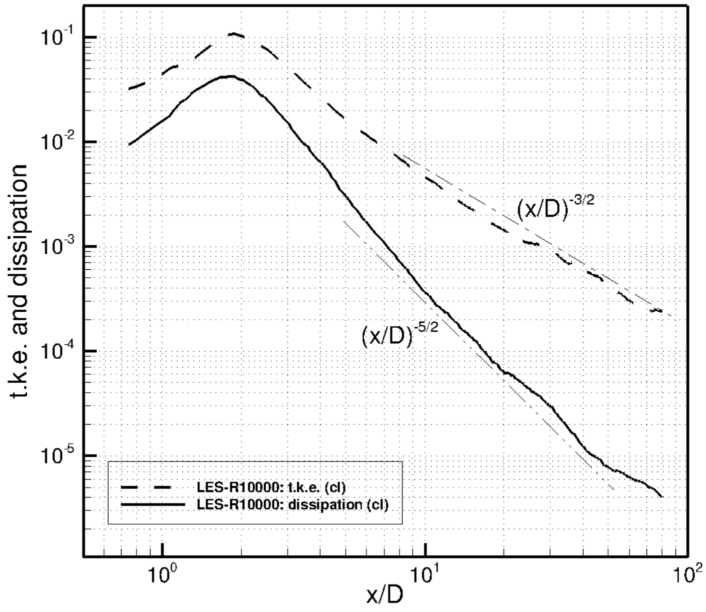

Figure 5.5: Turbulent kinetic energy, t.k.e (or K) and dissipation, ε, at the centerline for the $Re = 10,000$ LES. The dashed-dotted line is $K \sim (x/D)^{-3/2}$ and the dashed-dotted-dotted line is $\epsilon \sim (x/D)^{-5/2}$.

of K translates to a $u' \propto x^{-3/4}$ scaling for the turbulence velocity scale of $u' = \sqrt{K}$. The streamwise velocity fluctuation (not shown) also shows a $-3/4$ decay exponent. It is worth noting that u' does not vary at the same rate as U_0.

The turbulent kinetic energy (Figure 5.5) follows $x^{-5/2}$. The classical high-Re scaling of $\varepsilon \sim U_0^3/\delta$ leads to an exponent of $-7/2$ while the low-Re scaling of $\varepsilon \sim \nu U_0^2/\delta^2$ introduced by George (1989) leads to an exponent of -3. Both of these scaling laws lead to steeper decay of ε than the $-5/2$ behavior found in the simulations. We can alternatively use u' as the velocity scale instead of U_0 in the dissipation estimate. The low-Re scaling of $\varepsilon \sim \nu u'^2/\delta^2$ leads to $\varepsilon \propto x^{-5/2}$ which is in agreement with the LES result. Thus, one explanation of the behavior of ε in the simulations is low-Re.

The energy spectrum in the LES at $Re = 10,000$ has a decade of broad-band fluctuations (not $k^{-5/3}$ but similarly steep) in the intermediate wake where the wake power laws with $(m, n) = (-1, 1/2)$ are already established. We, therefore, explore the

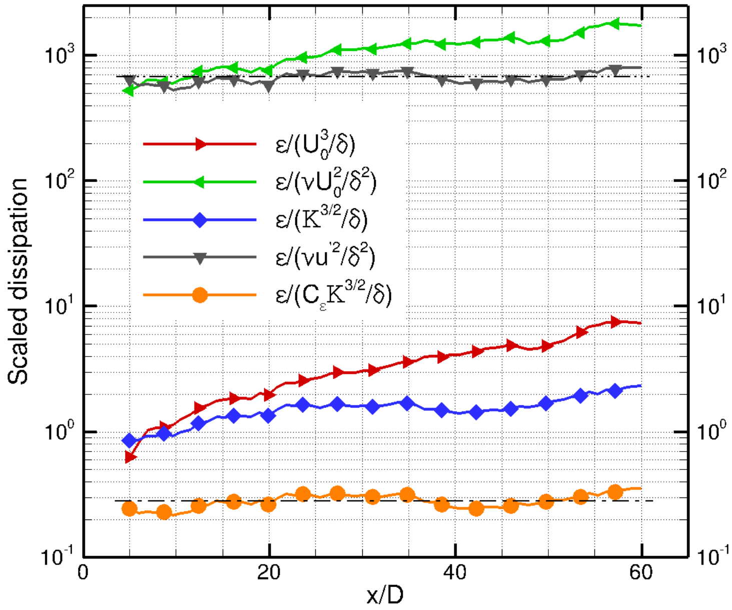

Figure 5.6: Scalings of dissipation for the $Re = 10{,}000$ case. The classical high-Re scaling: $\varepsilon \sim U_0^3/\delta$; the classical low-$Re$ scaling: $\varepsilon \sim \nu U_0^2/\delta^2$; the classical inviscid estimate: $\epsilon \sim K^{3/2}/\delta$; the modified low-$Re$ scaling: $\varepsilon \sim \nu u'^2/\delta^2$; and the NEQ scaling: $\epsilon = C_\epsilon K^{3/2}/\delta$ with $C_\epsilon = (Re_G/Re_l)^{1/2}$.

implications of the high-Re NEQ dissipation (*ansatz* Nedić *et al.* (2013); Vassilicos (2015)) and find that NEQ dissipation provides an alternate explanation for the ε power law found in the simulations. According to the NEQ dissipation formulation, the coefficient C_ϵ in $\epsilon = C_\epsilon K^{3/2}/\delta$ is no longer a universal constant but takes the form $C_\epsilon = Re_G^m/Re_l^n$. Here Re_G is a global Reynolds number characteristic of the inflow and is taken to be $Re_G = UD/\nu$, the sphere Reynolds number.

By taking the decay rates of centerline dissipation and t.k.e., shown in figure 5.5, along with the growth rate of wake dimensions in figure 5.3, it follows that $C_\epsilon = \epsilon K^{-3/2}\delta$ varies as $x^{1/4}$ which contradicts the classical Kolmogorov theory of constant C_ϵ. However, the decay of defect velocity as in figure 5.2 along with the growth rate in figure 5.3 gives $C_\epsilon = Re_G^m/Re_l^n \propto x^{1/4}$ if we choose $m = n = 0.5$. This is in agreement with the simulation result of $\epsilon K^{-3/2}\delta$. Note, Dairay *et al.* (2015) reports m=n=0.5 to be effective at $55 < x/L_b < 100$, where L_b is their equivalent wake generator length scale. Thus, the new non-equilibrium dissipation law in which C_ϵ as in $\epsilon = C_\epsilon K^{3/2}/\delta$ is not a constant but takes the value $C_\epsilon = (Re_G/Re_l)^{1/2}$ provides an alternative explanation. Figure 5.6 shows the evolution of centerline ε normalized according to different theoretical scaling laws. It can be seen that both the modified low-Re and the NEQ dissipation theory are successful in explaining the power law for ε found in the $Re = 10,000$ simulation.

The content of Chapter 5, in full, is a reprint of the material as it appears in Chongsiripinyo K., Pal A., and Sarkar S., "Scaling laws in the axisymmetric wake of a sphere", *Direct and Large-Eddy Simulation XI* (ERCOFTAC Series), pp. 439-444, 2019, Springer. The dissertation author was the primary researcher and author of this paper.

Chapter 6

Decay of turbulent wakes behind a disk in homogeneous and stratified fluids

6.1 Abstract

The primary objective of the present work is to investigate buoyancy effects in a turbulent bluff-body wake that evolves at relatively high Reynolds number in a stratified fluid. Large-eddy simulations (LES) with high resolution are conducted for the flow past a disk at $Re = U_b L_b/\nu$=50,000 and at $Fr = U_b/NL_b = \infty$, 50, 10, 2; here, U_b is the free-stream velocity, L_b is the disk diameter, ν is the fluid kinematic viscosity, and N is the buoyancy frequency. Unlike most other numerical studies of stratified wakes that use a temporal model, body-inclusive spatially-evolving simulations are performed.

In the axisymmetric wake in a homogeneous fluid, it is found that the mean streamwise velocity deficit (U_0) decays in two stages; $U_0 \propto x^{-0.9}$ during $10 < x/L_b < 65$ followed by $U_0 \gtrsim x^{-2/3}$. Consequently, none of the simulated stratified wakes is able to

exhibit the classical 2/3 decay exponent of U_0 in the interval before buoyancy effects set in. The turbulent characteristic velocity, taken as $K^{1/2}$ with K the turbulent kinetic energy (TKE), satisfies $K^{1/2} \underset{\sim}{\propto} x^{-2/3}$ after $x/L_b \approx 10$.

Turbulent wakes are affected by stratification within approximately one buoyancy time scale ($Nt_b \approx 1$) after which, provided that $Re_h Fr_h^2 \geq 1$, we find 3 regimes: weakly stratified turbulence (WST), intermediately stratified turbulence (IST), and strongly stratified turbulence (SST). The regime boundaries are delineated by the turbulent horizontal Froude number $Fr_h = u_h'/NL_{Hk}$; here, u_h' and L_{Hk} are r.m.s horizontal velocity and TKE-based horizontal wake width. WST begins when Fr_h decreases to $O(1)$, spans $1 \lesssim Nt_b \lesssim 5$ and, while the mean flow is strongly affected by buoyancy in WST, turbulence is not. Thus, while the mean flow transitions into the so-called non-equilibrium (NEQ) regime, turbulence remains approximately isotropic in WST. The next stage of IST, identified by progressively increasing turbulence anisotropy, commences at $Nt_b \approx 5$ once Fr_h decreases to $O(0.1)$. During IST, the mean flow has arrived into the NEQ regime with a constant decay exponent, $U_0 \propto x^{-0.18}$, but turbulence is still in transition. The exponent of 0.18 for the disk wake is smaller than the approximately 0.25 exponent found for the stratified sphere wake. When Fr_h decreases by another order of magnitude to $Fr_h \sim O(0.01)$, the wake transitions into the third regime of SST that is identified based on the asymptote of turbulent vertical Froude number ($Fr_v = u_h'/Nl_v$) to a $O(1)$ constant. During SST that commences at $Nt_b \approx 20$, turbulence is strongly anisotropic ($u_z' \ll u_h'$), and, both u_h' and U_0 satisfy $x^{-0.18}$ decay signifying the arrival of the NEQ regime for both turbulence and mean flow. Turbulence is patchy and temporal spectra are broadband in the SST wake.

Energy budgets reveal that stratification has a direct and positive influence on the prolongation of wake life. During the WST/early-IST stage, energy budgets show that the mean buoyancy flux acts to augment the MKE before the additional augmentation by reduced turbulent production. On the other hand, during WST/early-IST, the decay of

TKE is faster than the unstratified case because of negative buoyancy flux (a sink that serves to increase turbulent potential energy) and increased dissipation and, additionally, also by the reduced production. In the late-IST/early-SST stages, production is enhanced and, additionally, there is injection from turbulent potential energy so that the TKE decay slows down. Only in the SST stage, when NEQ is realized for both the mean and turbulence, the turbulent buoyancy flux becomes negative again, acting as a sink of TKE.

6.2 Introduction and objectives

Canonical shear flows such as wakes, jets, shear layers and boundary layers have received much attention because they are relatively simple examples that serve as building blocks for more complex flows. The wake in a density-stratified background is such a canonical flow whose importance stems from engineering, biological and geophysical applications such as underwater submersibles, aerial vehicles, marine swimmers, wind turbines, and flows past topographic features on land and under water. Our interest is in the wake of ocean submersibles that inevitably operate in a density-stratified background. Such wakes are almost always turbulent with a Reynolds number ($Re = U_b L_b/\nu$) that is large, e.g. $Re \sim O(10^4 - 10^7)$, and is subject to stratification whose strength is measured by a Froude number, $Fr = U_b/NL_b$, that takes values of $O(1 - 10^2)$.

Turbulent wakes of axisymmetric bodies, when subject to stratification, are non-axisymmetric, inhomogeneous, and multistage. Axisymmetry is broken as a result of gravity-suppressed vertical motion. Wake turbulence is inhomogeneous due to the spatial variation from the wake core to the wake boundary as well as streamwise (x) evolution. As the wake evolves in x, the relative strength of stratification increases even for constant N, since the 'local Froude number' ($Fr_H = U_0/NL_H$) based on a local wake size (L_H) continually decreases. Therefore, the wake evolution is multistage as was first categorized by Spedding

(1997), who experimentally measured U_0 behind a towed sphere in a salt-stratified tank, and identified three-dimensional (3D), non-equilibrium (NEQ), and quasi-two-dimensional (Q2D) stages in the evolution of U_0. Later, Meunier *et al.* (2006) pointed to a viscous-three-dimensional (V3D) regime, a final stage of the evolution. While subsequent studies have confirmed the existence of these stages, quantitative results regarding regime characteristics and the transition points between successive regimes are not strictly consistent, and the applicability of these regimes to turbulence statistics is unclear.

During the initial 3D stage, a stratified wake shows little effect of buoyancy and unstratified wake laws apply. For a high-Re unstratified wake, classical theory (Tennekes & Lumley, 1972; Townsend, 1976) offers the power law, $U_0 \propto x^{-2/3}$, for the far wake. Later, George (1989) proposed that $U_0 \propto x^{-1}$ applies to a low-Re wake. While these two scalings have been "found" in early experiments and numerical simulations (see review by Johansson *et al.* (2003)), their universality is not clear. Evidence of axisymmetric wakes with power laws that do not conform to $U_0 \propto x^{-2/3}$ has accumulated, e.g. Bonnier & Eiff (2002); Nedić *et al.* (2013); de Stadler *et al.* (2014); Dairay *et al.* (2015); Pal *et al.* (2017); Chongsiripinyo & Sarkar (2017). Nedić *et al.* (2013) suggested that this contradiction can be explained if the inviscid dissipation estimate $\varepsilon \sim u'^3/l$, that is consistent with classical similarity analysis as applied to the TKE equation, is modified. Here, u' is the r.m.s streamwise velocity fluctuation and l is taken to be the wake width. It is also worth nothing that a proportionality $u' \sim U_0$ is assumed in the classical analysis. An alternative to the inviscid estimate is $\varepsilon = C_\varepsilon u'^3/l$ where $C_\varepsilon \sim Re^m_{Global}/Re^n_{Local}$, as discussed by Vassilicos (2015); here, Re_{Global} is a global Reynolds number based on inlet conditions, and Re_{Local} is a local Reynolds number based on local velocity and length scales. This 'non-equilibrium' dissipation scaling has been tested in a variety of turbulent flows, e.g. decay of fractal-generated turbulence (Seoud & Vassilicos, 2007), fractal-plate turbulent wake (Nedić *et al.*, 2013; Dairay *et al.*, 2015), and a sphere wake (Chongsiripinyo *et al.*, 2019).

Following the 3D regime in stratified wakes is the NEQ regime. Here, the decay of U_0 slows down substantially and is close to $U_0 \propto x^{-0.25}$ (Spedding, 1997) in sphere-wake experiments. This is the regime whose dynamics allows a stratified wake to 'survive longer' than its unstratified counterpart. Brucker & Sarkar (2010) attributed the slower decay of U_0 to the reduction of the mean-to-turbulence energy transfer by production, $P = -\langle u_x' u_z' \rangle \partial_z \langle u_x \rangle$, an effect that was attributed to buoyancy-induced reduction of the correlation between u_x' and u_z'. Following NEQ, the wake enters into the Q2D regime where $u_h' \gg u_z'$ (hence the 'two-dimensional' attribute). According to Spedding (1997), the Q2D regime exhibits an increase in wake decay to $U_0 \propto x^{-3/4}$, and the NEQ-to-Q2D transition takes place at $Nt_b = 50$, where $t_b = x/U_b$. It is worth noting that later studies, e.g. Brucker & Sarkar (2010); Diamessis *et al.* (2011), find that the span of the NEQ regime increases with Re. The other distinct characteristic of the Q2D wake is the presence of horizontally large but vertically-thin 'pancake eddies' at large Nt_b, e.g. at $Nt_b \approx 250$ in the simulations of Brucker & Sarkar (2010); Chongsiripinyo *et al.* (2017).

The evolution of stratified wakes through each regime has becoming clearer owing to previous work. However, much of our later understanding derives from simulations that utilize the so-called temporal model, e.g. Gourlay *et al.* (2001); Dommermuth *et al.* (2002); Diamessis *et al.* (2005); Brucker & Sarkar (2010); Diamessis *et al.* (2011); de Stadler & Sarkar (2012); Abdilghanie & Diamessis (2013); Redford *et al.* (2015) among others. The temporal model invokes the Galilean transformation that relates time $T = x/U$ in the reference frame (implicitly moves with the body velocity U) of the simulation to distance (x) from the wake generator in the laboratory frame.

The temporal model has proved important to track wakes over a long time (equivalently, streamwise distance) and into the Q2D regime. However, temporal-model simulations are sensitive to the choice of initial conditions. Redford *et al.* (2012) found that the early and intermediate evolution of the axisymmetric wake in the temporal model depends on not only whether coherent vortex rings are initially introduced, but also on their relative spacing. For example both of the power-law exponents, $U_0 \propto x^{-1}$ and $x^{-2/3}$, were found to arise from two initial conditions that differ by the presence of coherent vortex rings. Interestingly, Redford *et al.* (2015) found the canonical rate of decay $U_0 \propto x^{-2/3}$ despite the statistics not being fully self-similar. To the best of our knowledge, the early/intermediate development of case VR (with vortex rings) from Redford *et al.* (2015) is the only simulation utilizing the temporal-model approximation that produces $U_0 \propto x^{-1}$.

Body-inclusive simulations naturally capture flow separation and vortex shedding from the body and, importantly, avoid the uncertainty introduced by assumed initial conditions in the temporal model. The disadvantage, however, is the high computational cost of boundary-layer resolution so that a long domain that captures all the three regimes (3D, NEQ, Q2D) becomes infeasible for a high-Fr wake. A work-around is to continue a body-inclusive simulation with separate simulations, e.g. a temporal model (Pasquetti, 2011) or a spatially-evolving model (VanDine *et al.*, 2018).

Body-inclusive simulations of stratified turbulent wakes are of recent origin, e.g. a $Re = 10^3$ sphere by Orr *et al.* (2015) and $Re = 3700$ sphere wakes at $Fr < O(1)$ (Pal *et al.*, 2016; Chongsiripinyo *et al.*, 2017) and $Fr = O(1)$ (Pal *et al.*, 2017). These simulations have captured vortex-shedding modes (Orr *et al.*, 2015), oscillatory modulation of the wake by body-generated lee waves (Pal *et al.*, 2017), the re-energization of fluctuations at low Fr (Pal *et al.*, 2016), and the associated change in vortex dynamics (Chongsiripinyo *et al.*, 2017).

Stratified wakes are inhomogeneous turbulent flows with mean shear that are subject to stratification. There has been much work, e.g. Lilly (1983); Billant & Chomaz (2001); Riley & deBruynKops (2003); Brethouwer *et al.* (2007); Kimura & Herring (2012); Maffioli & Davidson (2016); de Bruyn Kops & Riley (2019) in the related problem of fluctuations that evolve without mean shear in a stratified fluid. The interest is in the behavior of 'stratified turbulence' defined as fluctuations that have low values of Froude number (e.g. Fr_h defined by Eq. (6.7) is < 1) but the Reynolds number is not low (e.g. Re_b defined by Eq. (6.6) is > 1).

A limitation of the previous body inclusive simulations is that $Re = O(10^3)$ was not sufficiently large to have a developed region of stratified turbulence with fluctuations at low Froude number and high Reynolds number. Furthermore, wakes with high Fr ($> O(10)$) were not simulated. We are therefore motivated to simulate wakes at a higher $Re = 5 \times 10^4$ and over a wide range of stratifications, $\{Fr = 2, 10, 50, \infty\}$. We will explore links between the findings in our simulations and those in the general topic of stratified turbulence. Furthermore, we consider a disk rather than a sphere to broaden the stratified-wake literature. The unstratified $Fr = \infty$ case allows examination of power laws at a higher Re than in prior simulations and assess the possibility of non-canonical power laws for U_0 and L.

The primary objective of the present study is to improve our understanding of the evolution of relatively high-Re stratified wakes. In particular: What are the power laws that are satisfied by characteristic velocities/lengthscales as the wake progresses? Are there differences between the progression of mean and r.m.s turbulence as they react to stratification? How does the evolution of wake turbulence relate to the broader area of stratified turbulence decay? Lastly, what are the reasons underlying the slower decay of the wake in the NEQ regime?

The numerical setup and the parameters of the simulated cases are given in section 6.3. Definitions used in the analysis and interpretation of results are given in section 6.4. Presentation of the results begins with section 6.5 which introduces the effect of stratification by visual contrasts among the different cases. Section 6.6 reports on the evolution of centerline values of the mean and the three r.m.s components for each of the cases, separately. Section 6.7 presents a consolidated picture of all stratified cases in phase space. We discuss links with previous work on regimes (characterization and transitions) of stratified wakes and stratified turbulence in both sections 6.6 and 6.7. Section 6.8 concerns the evolution of two distinct wake sizes; one is derived from profiles of U_0 and the other is based on TKE. Section 6.9 discusses the evolution of area-integrated kinetic and potential energy in stratified wakes and contrasts with the unstratified wake. Section 6.10 delves deeper into the evolution of MKE and TKE through their budgets. Section 6.11 discusses possible scaling laws for the dissipation (ε) of TKE. We end with a summary and conclusions in section 6.12.

6.3 Numerical simulations

The questions above exclude the possibility of utilizing temporal-evolving simulation where a wake-like initial condition is always required. We address the questions introduced in section 6.2 with large-eddy simulations (LES) of flow past a circular solid disk placed perpendicular to the uniform free stream. The background is taken to have a uniform stratification. These body-inclusive simulations of flow into the far wake (up to $x/D = 125$) are at a relatively high Re of 50,000 and computationally intensive because of the necessity of resolving the separated flow at the body and the turbulent recirculation region. The following non-dimensional filtered Navier-Stokes equations under the Boussinesq assumption for density effects along with the filtered advection-diffusion equation for density are numerically solved:

$$\text{Continuity}: \partial_i u_i = 0, \tag{6.1}$$

$$\text{Momentum}: \partial_t u_i + u_j \partial_j u_i = -\partial_i p + Re^{-1} \partial_j \left[(1 + \nu_s/\nu) \partial_j u_i \right] - Fr^{-2} \rho_d \delta_{i3}, \tag{6.2}$$

$$\text{Density}: \partial_t \rho + u_j \partial_j \rho = (RePr)^{-1} \partial_j \left[(1 + \kappa_s/\kappa) \partial_j \rho \right]. \tag{6.3}$$

The symbol ∂_i denotes a spatial derivative with respect to x_i where $i = 1, 2$, and 3 refer to streamwise (x), lateral (y), and vertical (z) directions with u_x, u_y, and u_z the corresponding velocities, respectively. The governing equations are non-dimensionalized with the following parameters: the background free-stream velocity (U_b), the disk diameter referred as the body length scale (L_b), advection time (L_b/U_b), dynamic pressure ($\rho_0 U_b^2$), and characteristic change in background density deviation across the body ($-L_b \partial_3 \rho_b$). Under the Boussinesq approximation, the density deviation from its equilibrium alters the momentum equation only through the last term on the RHS of Eq. (6.2). Here δ_{i3} is the Dirac-delta function. The density is decomposed into a constant reference density (ρ_0), the linearly varying deviation of the background $\rho_b(x_3)$ and the flow-induced deviation, $\rho_d(x_i, t)$, as follows

$$\text{Density decomposition} : \rho(x_i, t) = \rho_0 + \rho_b(x_3) + \rho_d(x_i, t). \tag{6.4}$$

Note that $\rho_d(x_i, t) = \langle \rho_d(x_i, t) \rangle + \rho'_d(x_i, t)$; where $\langle \rho_d(x_i, t) \rangle$ is not necessarily zero but takes a value of $\partial_n \langle \rho_d(x_i, t) \rangle = -\partial_n \rho_b(x_3)$ at a solid surface; n is a surface normal direction. Background density and static linear variation are absorbed into the modified pressure. The body Reynolds number is $Re = U_b L_b / \nu$ where U_b is the free-stream velocity, L_b is the characteristic length taken to be the disk diameter, and ν is the fluid kinematic viscosity. The body Froude number $Fr = U_b / N L_b$ is the ratio of buoyancy time scale to the characteristic advection time scale, L_b/U_b; here, N is the constant buoyancy frequency defined by $N^2 = -(g/\rho_o) \partial_3 \rho_b$. The background is stably stratified if $\partial_3 \rho_b$ is negative, as is the case here. The disk thickness of $0.01 L_b$ is small. The Prandtl number, $Pr = \nu/\kappa$, that is the ratio of velocity and density (temperature) diffusivities is assumed to be unity. Additional variables from small unresolved scales are subgrid kinematic viscosity, ν_s, and density diffusivity, κ_s. The Prandtl number based on these subgrid variables is also assumed to be unity. The study of the Prandtl number effects in a stratified wake can be found in de Stadler *et al.* (2010).

Since the turbulent wake under weak-to-intermediate stratification is quasi-axisymmetric in the 3D and in the early NEQ regimes, a cylindrical coordinate system is employed. The choice of cylindrical coordinates allows efficient distribution of grid points especially from the core to the wake periphery. Spatial numerical derivatives are obtained with second-order accurate central differences while temporal marching is done with a fractional-step method that combines a third-order Runge-Kutta explicit scheme with the second order Crank-Nicolson implicit scheme. To alleviate stiffness of the discretized system, especially near the coordinate streamwise axis, implicit marching is performed for viscous and advection terms (both velocities and density) that involve spatial discretization in the azimuthal direction. In the fractional-step method, the Poisson equation is formed by taking the divergence of the momentum equation for predicted velocity. The periodic boundary condition in the azimuthal direction transforms the discretized Poisson equation into inversion of a pentadiagonal matrix. The pentadiagonal matrix system is then inverted using a direct solver (Rossi & Toivanen, 1999). The disk is represented by the immersed boundary method of Balaras (2004); Yang & Balaras (2006). Kinematic subgrid viscosity, ν_s, is obtained using the eddy viscosity model of Germano *et al.* (1991), a variant of the dynamic Smagorinsky model (Smagorinsky, 1963). The coefficient C, as in $\nu_t = C\widetilde{\Delta}^2|\widetilde{S}|$ where $\widetilde{\Delta}^3 = V$ is a measure of the local cell volume and $|\widetilde{S}|$ is the instantaneous strain rate magnitude of filtered velocity, is dynamically computed using a method of Lilly (1992) that takes the cumulative average of C along flow trajectories with an exponential weighting function chosen to give more weight to recent times in flow history. Boundary conditions at the inlet and outlet of the domain are Dirichlet inflow and Orlanski-type convective outflow, $\partial_t\phi + C\partial_1\phi = 0$. The magnitude of convective velocity, C, is set at U_b. Note that a localized mean value of C as an alternative to U_b is tested with negligible consequence. Neumann

Table 6.1: Physical and numerical parameters used in the simulations. N_r, N_θ, and N_x are the number of nodes in the radial, azimuthal, and streamwise direction, respectively. Note that all lengths are normalized by diameter, L_b, of the disk.

Case.#	Re	Fr	Pr	N_r	N_θ	N_x	L_r	L_θ	L_x
UNS	50,000	∞	1	364	256	4608	15.14	2π	125.51
F02	50,000	2	1	529	256	4608	80.00	2π	125.51
F10	50,000	10	1	529	256	4608	80.00	2π	125.51
F50	50,000	50	1	529	256	4608	80.00	2π	125.51

condition is used at the outer radial boundary. Unlike Pal *et al.* (2017) and Chongsiripinyo & Sarkar (2017) who use a “sponge” region to absorb internal gravity wave, the domain’s radial extent in this present study is enlarged to $80L_b$ allowing free propagation of internal gravity waves while minimizing reflection from the boundary without artificially adjusting the farfield to a background state.

Parameters of the simulations are given in table 6.1. The distribution of the computational grid is optimized on the basis of the unstratified case where the turbulent dissipation rate is known to decays as $\varepsilon \propto x^{-m}$, $m \leq 5/2$, in the self-similar solution (George, 1989), thus leading to an estimate of the Kolmogorov length. The streamwise-dependent radial distribution of ε is estimated from the DNS of Dairay *et al.* (2015) and LES of Chongsiripinyo & Sarkar (2017). The resulting number of grid points for the weakly stratified cases is 624 millions cells. In the unstratified wake, $\Delta x/\eta$ is at worst ≈ 17 near the centerline at $x/L_b \approx 2.5$; η is the Kolmogorov scale calculated directly from the turbulent dissipation rate by $\eta = (Re^3\varepsilon)^{-1/4}$. Beyond about $x/L_b = 10$, the centerline $\Delta x/\eta$ is smaller than 10 and gradually decreases to about 6 at $x/L_b = 125$. The distribution of $\Delta x/\eta$ and $\Delta r/\eta$ are given in figure 6.1. The approximate time step for all the cases lies between $2 - 9 \cdot 10^{-4} L_b/U_b$. Statistics are collected over $\Delta t/(U_b^{-1}L_b) \in (200 - 250)$ during a statistically steady state determined by convergence of moving-window averages

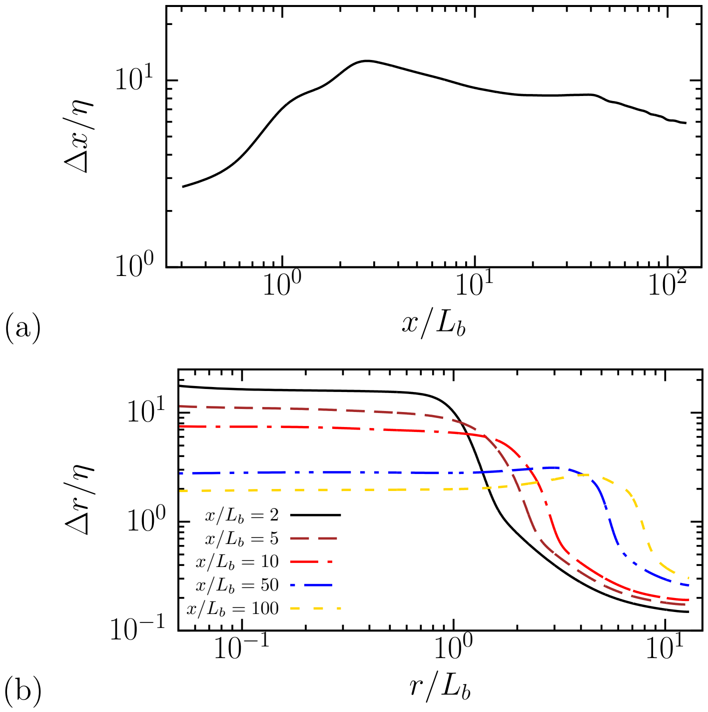

Figure 6.1: Grid quality: (a) Streamwise variation of nondimensional streamwise grid spacing, and (b) Radial profiles of nondimensional radial grid spacing. Kolmogorov length scale, $\eta = (\nu^3/\varepsilon_k)^{1/4}$, is computed using the turbulent dissipation rate of the unstratified wake.

of centerline streamwise and radial velocities at $x/L_b = 100$. The steady state is reached after initial transient that typically takes two to three flow through times ($300L_b/U_b$). For the unstratified case, we use an averaging time of $500L_b/U_b$. The CPU usage, between 750,000 and 10^6 core hours distributed over 512 cores for each case, is large because of the long integration time. The averaged drag coefficient in the unstratified case is found to be $C_d = 1.145$ comparable to the value of $C_d = 1.12$ in Fail *et al.* (1959).

6.4 Analysis and interpretation

6.4.1 Statistics

The ensemble, collected once statistical steady state is reached, is Reynolds decomposed, $\phi = \langle\phi\rangle + \phi'$, where ϕ is an instantaneous realization. Representing an ensemble average, the angle bracket $\langle\cdot\rangle$ denotes an appropriate averaging operator and performs averaging in all applicable homogeneous directions wherever applicable. Simulated in a spatially-evolving domain, the turbulent wake in a homogeneous fluid is statistically-homogeneous in time and in the azimuthal direction. The stratified wake is statistically homogeneous in time and is statistically-symmetric across vertical and horizontal center planes, $\langle\phi\rangle(x, y, z)=\langle\phi\rangle(x, \pm y, \pm z)$. The other type of statistic is obtained from cross-wake area integration indicated by braces $\{\cdot\}$,

$$\{\phi\}(x) = \int\limits_{0}^{2L_k(x,\theta)} \phi(x, r, \theta)dC, \tag{6.5}$$

where the wake width (L_k) is described in section 6.4.2. In order to include only wake turbulence and exclude internal wave contributions, a small integral number ($2L_K$) of wake widths is chosen for the radial limits of the integral. Lee waves, especially at intermediate stratification, generated by a wake generator can propagate considerably into the far field and we prefer to exclude the far field in the area integral.

6.4.2 Mean and turbulent lengthscales

In a homogeneous fluid, an axisymmetric half-length L measures an azimuthally-averaged distance from the centerline to a position where the streamwise mean velocity deficit is reduced to half of its centerline value, $U_0|_{r=L} = U_0|_{r=0}/2$. The other half-length,

L_k, is based on profiles of the turbulent kinetic energy (TKE), $K = \langle u_i' u_i' \rangle/2$ as opposed to U_0, taking $K|_{r=L_k} = K|_{r=0}/2$. In a stratified fluid, horizontal and vertical length scales are defined separately but again based on U_0 and K profiles, and denoted as

$$L_H, \quad L_V, \quad L_{Hk}, \quad L_{Vk}\,.$$

Here, the horizontal width (L_H) and vertical height (L_V) represent half lengths in the lateral (y) and in the vertical (z) direction based on U_0, while L_{Hk} and L_{Vk} are derived from profiles of the TKE. Since U_0 and K are obtained from the $\langle\cdot\rangle$ operator, a half length is calculated based on an appropriately-averaged ensemble. Note that at steady state of all cases, although instantaneous wakes can meander around a mean position, the centerline peak values of U_0 and K remain close to the axis of the cylindrical grid.

The turbulent integral length scale is not easy to calculate in a spatially-evolving stratified wake where spatial homogeneity is absent. We use the wake width (L_{Hk}) as a surrogate for the horizontal integral length scale. The turbulent vertical length scale, l_v, is calculated along the centerline and its method of calculation is adopted from Riley & deBruynKops (2003) as $l_v^2 = \langle u_x'^2 + u_y'^2 \rangle / \langle (\partial_z u_x')^2 + (\partial_z u_y')^2 \rangle$.

6.4.3 Reynolds numbers and Froude numbers

The buoyancy Reynolds number (Re_b), the horizontal-motion Reynolds number (Re_h), and the microscale Reynolds number (Re_λ) are defined as follows:

$$Re_b = \frac{\varepsilon_k}{\nu N^2}, \quad Re_h = \frac{u_h' L_{Hk}}{\nu}, \quad Re_\lambda = \frac{u_x' \lambda}{\nu}, \tag{6.6}$$

where $u_h' = (u_x'^2 + u_y'^2)^{1/2}$ is the rms horizontal velocity and λ is the Taylor microscale defined by $\lambda^2 = 15\nu u_x'^2/\varepsilon_k$. The mean vertical Froude number (Fr_V), the mean horizontal

Froude number (Fr_H), the turbulent vertical Froude number (Fr_v) and the turbulent horizontal Froude number (Fr_h) are defined as follows:

$$Fr_V = \frac{U_0}{NL_V}, \quad Fr_H = \frac{U_0}{NL_H}, \quad Fr_v = \frac{u'_h}{Nl_v}, \quad Fr_h = \frac{u'_h}{NL_{Hk}}. \tag{6.7}$$

6.5 Visualization

Before diving into the detailed analysis of wake statistics, we begin with a visualization that contrasts flow structures of the stratified wakes with those under unstratified conditions. Snapshots of the streamwise velocity (u_x) for the $Fr = \infty$, 10, and 2 wakes are shown in figure 6.2, 6.3, and 6.4, respectively. The body moving through the background leaves its imprint that grows and lasts for a long distance, with its visual presentation being strongly dependent on the strength of stratification. When the stratification is weak ($Fr = 10$), the near wake remains relatively unchanged relative to $Fr = \infty$ but the anisotropy between vertical and horizontal cuts is readily apparent in the intermediate and far wake. When the stratification is strong ($Fr = 2$), the wake quickly responds to the background stratification; even the near wake is vertically contracted and the intermediate/far wake is more coherent than at $Fr = \infty$. As buoyancy forces become relatively stronger characterized by the decreased local Froude number; the far-field $Fr = 10$ wake behaves similarly to the near-field $Fr = 2$ wake, horizontally wide but vertically thin. In fact, they are qualitatively in-sync if we compare the two at a normalized distance, i.e., $(x/L_b)Fr^{-1} = Nt_b$. This aspect will be quantitatively elaborated in sections 6.6 and 6.7. As vertical motions become progressively suppressed, the wakes become increasingly two-dimensional, with the appearance of horizontal waviness that drives the formation of large-scale horizontal but vertically thin ‘pancake’ eddies that will emerge later in the Q2D regime.

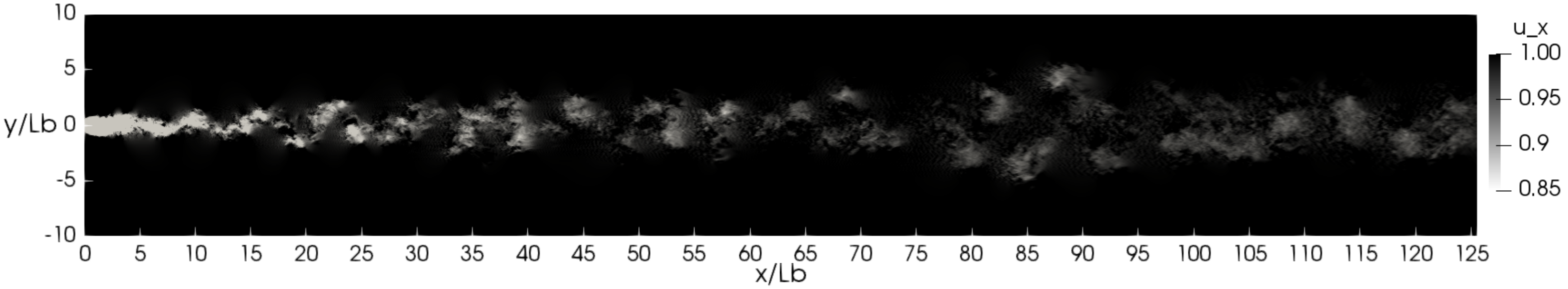

Figure 6.2: Snapshot of the streamwise velocity for the unstratified wake.

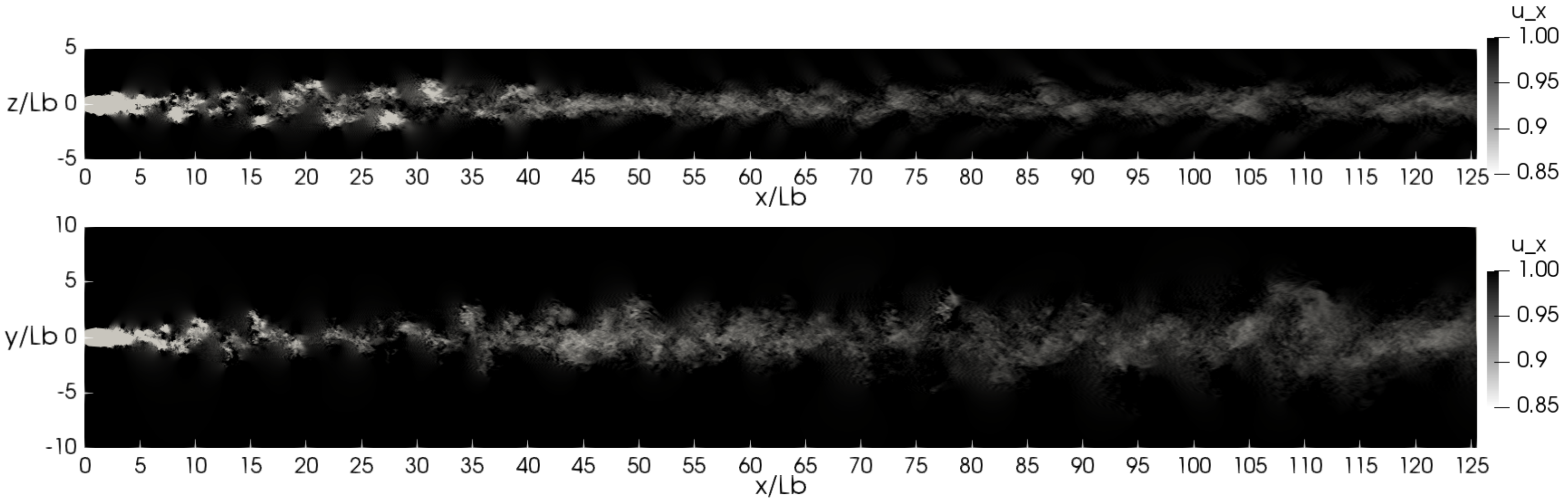

Figure 6.3: Case F10. Snapshot of the streamwise velocity in a vertical cut (top) and in a horizontal cut (bottom).

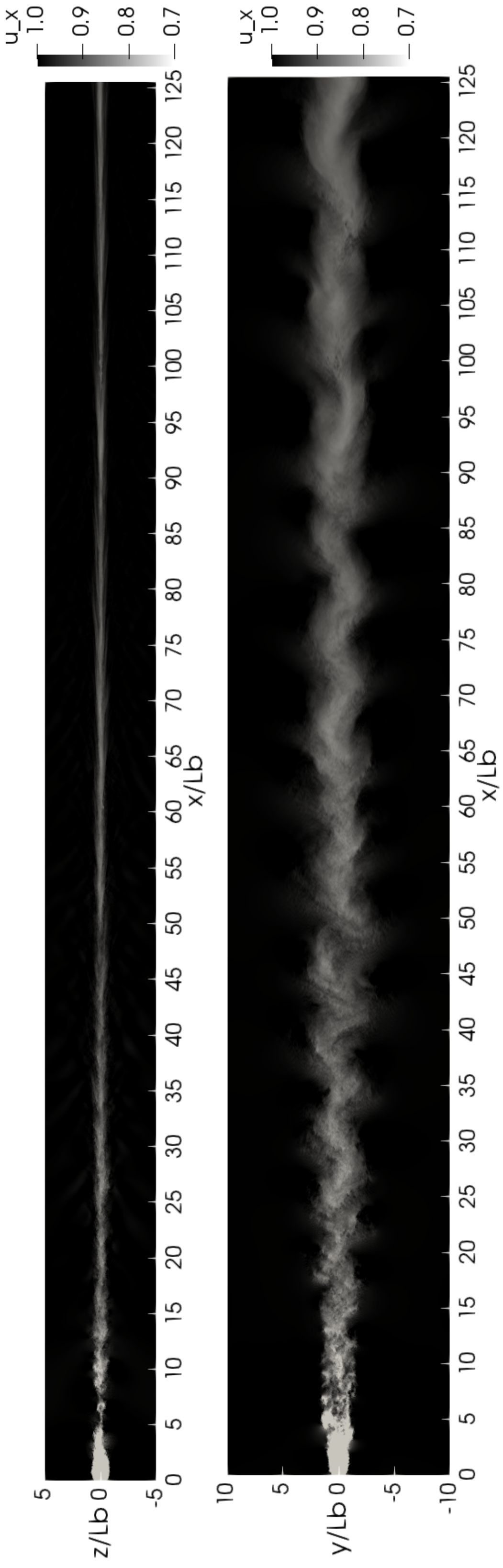

Figure 6.4: Case F02. Caption as in figure 6.3.

6.6 Evolution of mean deficit velocity and turbulence intensities

Centerline values of mean streamwise velocity deficit (U_0) and root mean square (r.m.s) velocity fluctuations in streamwise (u'_x), spanwise (u'_y) and vertical (u'_z) directions are shown in figure 6.5 for the unstratified wake. The initial increase of U_0 in the recirculation zone to exceed the freestream velocity (U_b) is accompanied by an increase in all r.m.s components signifying the establishment of turbulence. R.m.s fluctuations peak at $x/L_b \approx 2.5$ which lies in the recirculation region. U_0/U_b decays over $2 \leq x/L_b \leq 10$ with a rate that gradually decreases with increasing x. The subsequent evolution of U_0 in figure 6.5 reveals a break in slopes at $x/L_b \approx 65$ that separates two stages with different power-law exponents. The first stage of $10 < x/L_b < 65$ exhibits approximately $U_0 \propto x^{-0.9}$ while the second stage of $65 < x/L_b < 125$ satisfies $U_0 \propto x^{-0.6}$, close to the classical $U_0 \propto x^{-2/3}$ behavior. A similar transition between two different power laws was found by Dairay *et al.* (2015) in the axisymmetric wake of a fractal plate. They identified $U_0 \propto x^{-1}$ (an exponent of -0.94 in their $Re = 5000$ DNS and -1.03 in their $Re = 50,000$ experiment) for $10 < x/L_b < 50$ that transitions to a different power law reported as $U_0 \propto x^{-0.81}$ in the $Re = 5000$ DNS. The evolution of U_0 showed behavior close to x^{-1} scaling in our previous simulations of sphere wakes: DNS at $Re = 3700$ by Pal *et al.* (2017) and LES at $Re = 10,000$ by Chongsiripinyo *et al.* (2019). Although it is tempting to attribute the x^{-1} power law of U_0 to low-Re viscous decay (e.g George (1989)), that is not the case. As we will show later during the analysis of mean kinetic energy (MKE), the turbulent production that acts as a sink of MKE is much larger in magnitude than the viscous dissipation term in the MKE equation. Furthermore, the microscale Reynolds number that varies between $Re_\lambda = 200$ at $x/D = 10$ and $Re_\lambda = 120$ at $x/D = 100$ is not small.

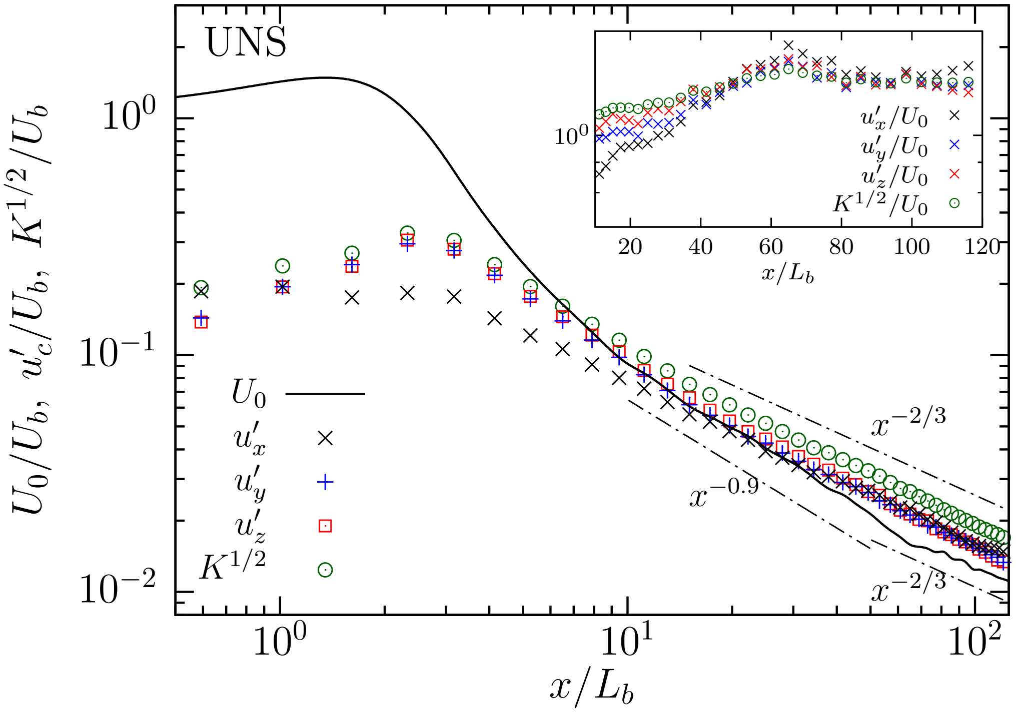

Figure 6.5: Unstratified wake. Evolution of centerline values of mean streamwise velocity deficit (U_0), r.m.s velocity fluctuation (u'_x, u'_y, u'_z), and turbulent velocity ($K^{1/2}$). The inset shows the evolution of turbulence velocity quantities normalized with the local $U_0(x)$.

In contrast to U_0, the evolution of the turbulent velocity scale ($K^{1/2}$) does not break into two separate power laws. The decay of $K^{1/2}$ (green circles in figure 6.5) is found to be $K^{1/2} \propto x^{-0.71}$, close to $x^{-2/3}$ from $x/L_b = 10$ to the end of the computational domain. Thus, the mean velocity scale in the intermediate wake ($10 < x/L_b < 65$) decays with a different power law exponent (-0.9 as shown in figure 6.5) than the exponent satisfied by the turbulence velocity scale. Similarity theory for the turbulent wake (e.g. Tennekes & Lumley (1972)) assumes the same velocity scale for both mean and turbulence. In the present simulation, it is only beyond $x/L_b = 65$ that the power law exponents for U_0 and $K^{1/2}$ become similar and close to the classical value of $-2/3$. Near-wake turbulence is found to be anisotropic with u'_x substantially smaller than u'_y and u'_z near the body; however, the r.m.s velocity components (inset of figure 6.5) become more isotropic for $x/D > 40$.

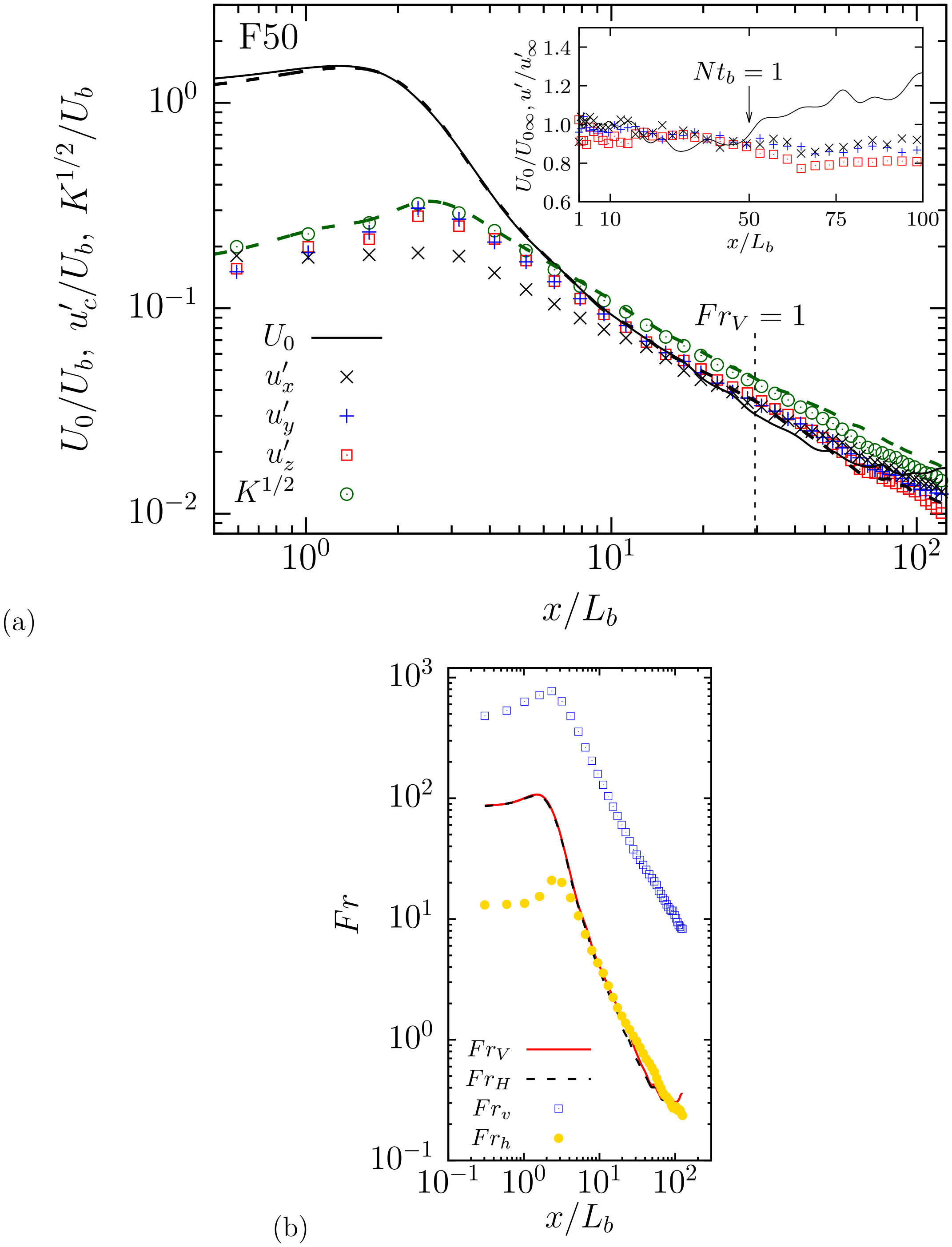

Figure 6.6: Case F50. (a) Evolution of U_0, u', and $K^{1/2}$. Inset shows quantities normalized by the corresponding unstratified-wake value (symbols and black solid line are as in the main figure). (b) Evolution of different Froude numbers defined by Eq. 6.7.

The evolution of U_0 in case F50 (figure 6.6) shows little deviation from the UNS case until $x/L_b \simeq 50$ or $Nt_b \simeq 1$, consistent with theoretical arguments (e.g. Riley & Lelong (2000)) that it takes a time interval of $Nt \sim 1$ for buoyancy forces to become comparable to inertial forces in a flow that originates with weak buoyancy effects. The inset emphasizes the importance of $Nt_b = 1$ by showing that $U_0/U_{0\infty}$ abruptly increases at $Nt_b \approx 1$; here, $U_{0\infty}$ denotes the centerline deficit in the UNS case. The inset also shows that stratification increases the rate of decay of U_0 as early as $x/L_b = 10$ or $Nt_b = 0.2$ (observe that $U_0/U_{0\infty}$ starts decreasing around $x/L_b = 10$). Thus, there is a mild effect of buoyancy in the weakly stratified wake before $Nt_b = 1$. Buoyancy increases the decay rate of $K^{1/2}$ (green circles) relative to the unstratified case (dashed green line). The inset shows that all three turbulence components in F50 are reduced with respect to UNS, but the difference relative to UNS is smaller than that in U_0. The delay in the turbulence response to stratification in comparison to the mean velocity deficit will be more apparent in the F10 case and the reason for this delay will be made clear in the discussion of the F02 case.

The evolution of Froude numbers based on mean and r.m.s components is shown in figure 6.6 (b). We defer discussion of Froude numbers to later in this section after introducing the results regarding the velocity in the F02 case.

In the F10 case (figure 6.7), buoyancy forces become comparable with inertial forces at a location closer to the body relative to F50 but at a similar value of Nt_b. U_0 deviates from the unstratified case at $x/L_b \approx 10$ (equivalently, $Nt_b \approx 1$) and, as emphasized by the inset, $U_0/U_{0\infty}$ increases sharply at $x/L_b \approx 10$. There is a strong effect of buoyancy on r.m.s velocity fluctuations but it is delayed until $x/L_b \approx 50$ when, as shown by the inset, r.m.s of the horizontal components increase while the vertical r.m.s decreases relative to UNS. It is clear that the stratified wake exhibits a regime between $Nt_b \approx 1$ and $Nt_b \approx 5$ wherein the effect of buoyancy on the mean velocity is much stronger than that on turbulence. Beyond $Nt_b \approx 5$, the Reynolds stresses deviate strongly from isotropy towards a “pancake” with

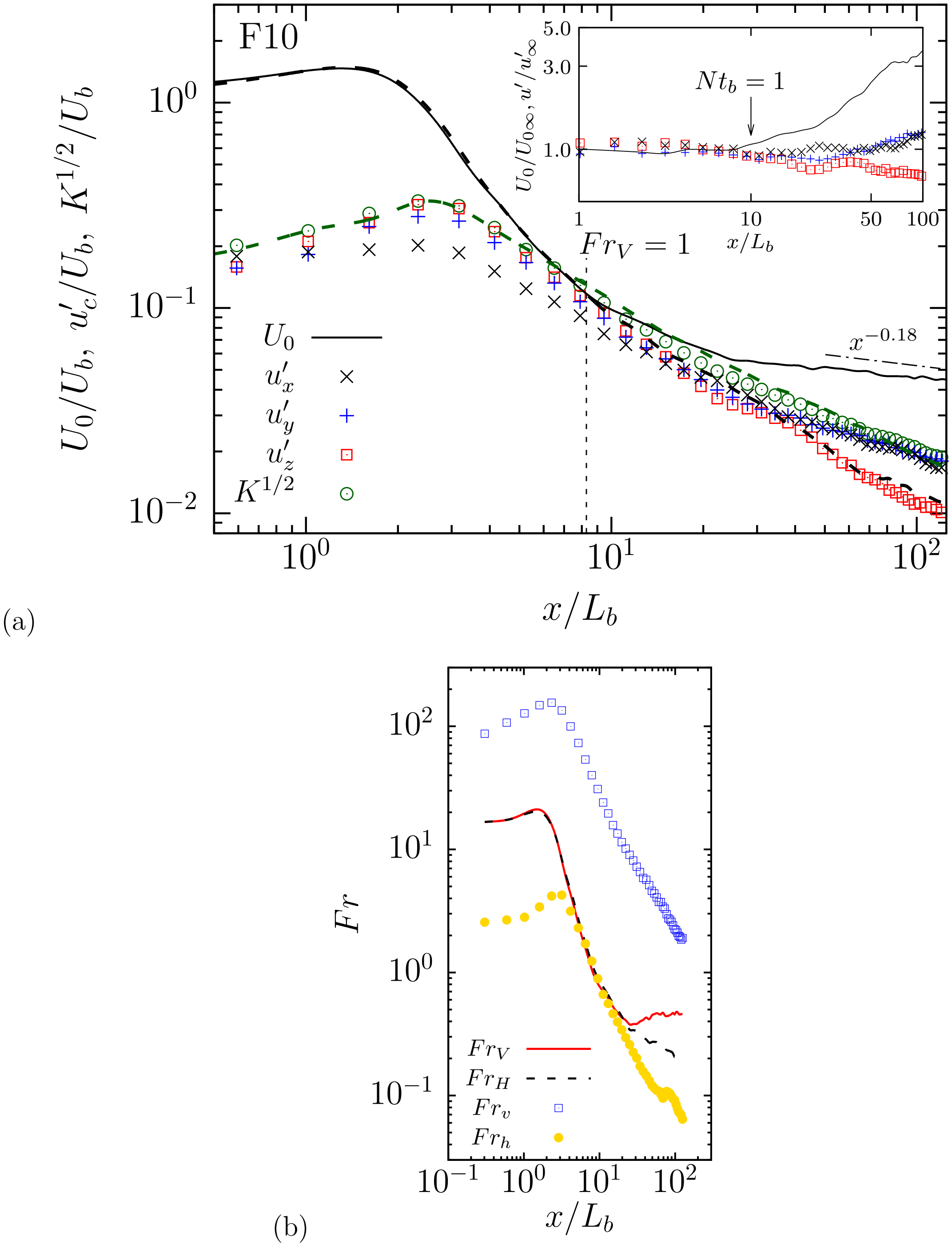

Figure 6.7: Case F10. Caption as in figure 6.6.

$u'_x \approx u'_y \gg u'_z$.

The behavior of $Fr = O(1)$ wakes is quite different in the near and intermediate wake from the $Fr \geq O(10)$ cases that have been discussed so far. Consider U_0 at $Fr = 2$ (case F02) in figure 6.8 (a) together with the evolution of Froude numbers in figure 6.8 (b). The mean recirculation region (has negative velocity and deficit velocity $U_0 > 1$) is shorter because the incoming fluid that is vertically displaced by the body has sufficient buoyancy so that it plunges back in the separated flow towards the centerline. In contrast to F10 and F50, there is a region after the recirculation region where U_0 increases instead of decreasing. There is a local minimum of U_0 at $Nt_b \simeq \pi$, i.e., a half lee-wave period behind the disk; subsequently, U_0 increases and reaches a local maximum at $Nt_b \simeq 2\pi$. This behavior is the manifestation of the lee-wave induced 'oscillatory modulation' of U_0 reported in the DNS of the $Re = 3700$ sphere wake by Pal *et al.* (2017). In the NEQ regime, U_0 is found to decay with a rate that is close to $x^{-0.18}$. The rate of decay is smaller than the $U_0 \propto x^{-0.25}$ behavior in the sphere wake experiments of Spedding (1997).

We now turn to the Froude numbers. Consider $Fr_V = U_0/NL_V$ based on mean wake deficit velocity. The value of Fr_V (red curve in figure 6.8 (b)) reaches 1 at $x/D \approx 5$, a location at which U_0 commences a rapid deviation from the unstratified result. Fr_V remains close to unity further downstream. Interestingly, in the F10 (figure 6.7 (b)) and F50 (figure 6.6 (b)) cases too, Fr_V decreases to O(1) before U_0 commences to deviate from unstratified behavior and plateaus at an O(1) value further downstream.

The role of Froude number, Fr_v (based on fluctuation rather than mean-flow statistics), in the evolution of r.m.s turbulence is analogous to that of Fr_V in the evolution of the mean flow. When Fr_v decreases to O(1) ($x/L_b \approx 20$), the evolution of r.m.s turbulence deviates strongly from unstratified behavior since buoyancy becomes comparable to inertial forces in the inertial-range turbulent motions. The F02 case (figure 6.8 (a)) has a distinguished region between $x/L_b = 5$ and $x/L_b = 20$ where $Fr_V = O(1)$ so that the

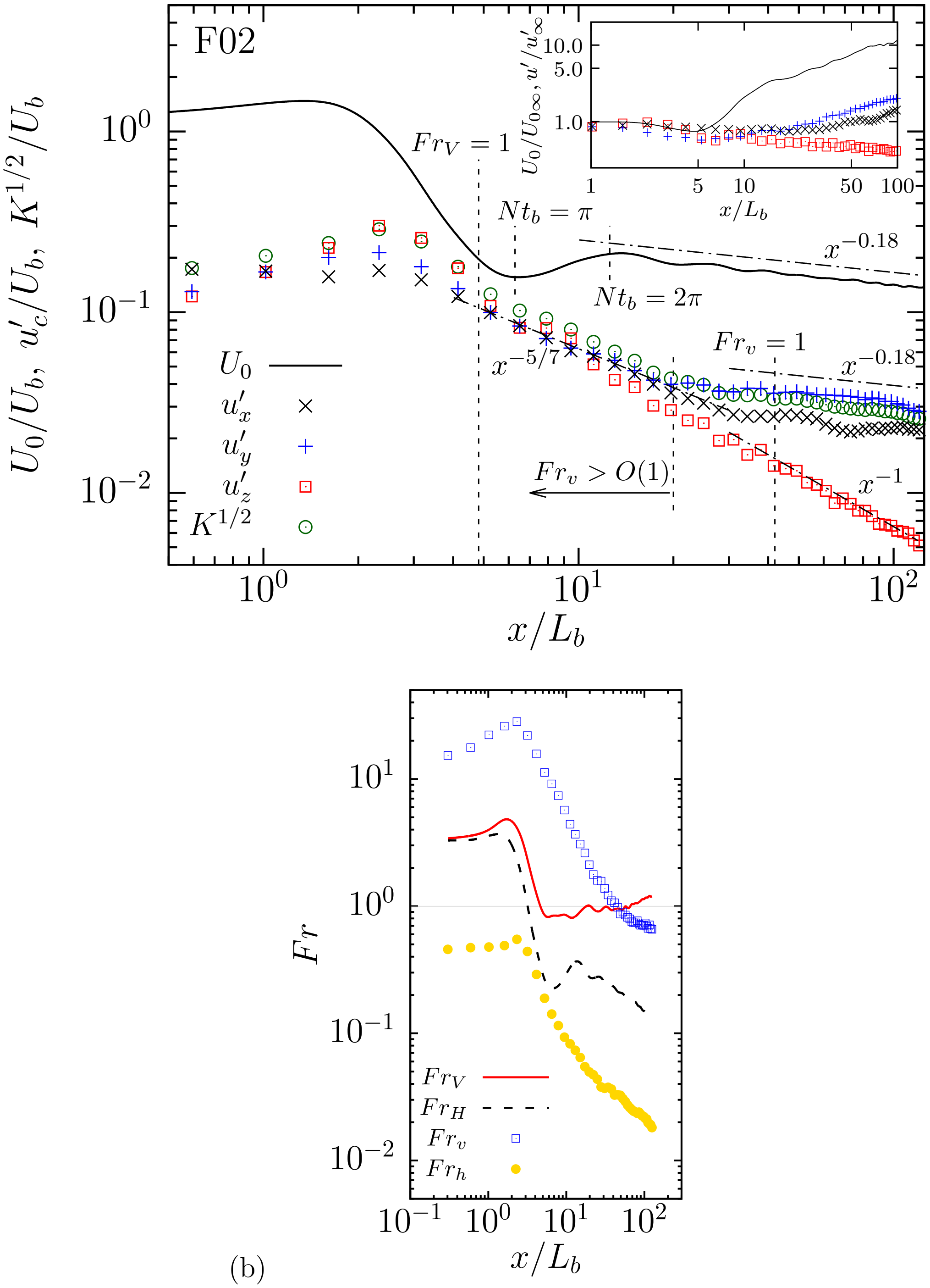

(a)

(b)

Figure 6.8: Case F02. Caption as in figure 6.6 but excludes U_0 and $K^{1/2}$ of the UNS case.

mean is strongly affected by buoyancy and $Fr_v > O(1)$ so that r.m.s turbulence is not. Since the Reynolds number (both Re_λ and Re_b) is sufficiently high in this distinguished region between $x/L_b = 5$ and 20 that has $Fr_v > O(1)$, the decay of turbulence is close to the classical Kolmogorov decay law for unstratified turbulence, $u^2 \propto t^{-10/7}$, as can be seen by comparing the evolution of $K^{1/2}$ with the $x^{-5/7}$ line in figure 6.8 (a). Despite the weak effect of buoyancy on turbulence, U_0 in this same distinguished region exhibits strong buoyancy effects since Fr_V has decreased to O(1). In the vicinity of $Fr_v \simeq 1$ and beyond, the decay rates of u'_h and $K^{1/2}$ are reduced with respect to their unstratified counterparts. Once their decay has "settled" in the NEQ regime, it is found that $K^{1/2} \propto x^{-0.18}$, i.e., turbulence and mean evolve with the same power law. This can be regarded as the official arrival of the NEQ regime. u'_z continues to monotonically decrease with an approximate power-law decay of $u'_z \propto x^{-1}$ agreeing with the t^{-1} scaling observed in the experiment of Lin & Pao (1979) and close to the $t^{-1.08}$ scaling observed in the numerical simulation of Brucker & Sarkar (2010). Notice that $u'_y > u'_x$ in the late wake, a result that is consistent with coherent vortex patches that are located laterally off-centerline.

6.7 Turbulence in phase space

The $Fr_h - Re_h Fr_h^2$ phase presents a consolidated view of the progression of wake turbulence under the influence of stratification. The phase-space map (Figure 6.9) of wake evolution shows the progression of each of the simulated cases through different stages which, as elaborated below, exhibit qualitatively different effects of buoyancy. Decreasing Fr_h implies an increasing effect of buoyancy. Large scales of motion are preferentially affected by buoyancy and, as Fr_h decreases, the largest scale affected by buoyancy also decreases. The quantity $Re_h Fr_h^2$ has been introduced by Billant & Chomaz (2001) as a parameter that must be > 1 to prevent viscous effects from directly affecting turbulent motions, and Riley & deBruynKops (2003) relates $Re_h Fr_h^2$ to an inverse Richardson number of fluctuating motions so that $Re_h Fr_h^2 > 1$ implies the possibility of local shear instability. $Re_h Fr_h^2$ can be related to the buoyancy Reynolds number, denoted by Re_b, via the inviscid estimate dissipation scaling, $\varepsilon_k \sim u_h'^3/L_{Hk}$. Re_b can be expressed as a ratio of inertial and viscous forces,

$$Re_b = \frac{u_o l_o}{\nu}; \quad u_o = \left(\frac{\varepsilon_k}{N}\right)^{1/2}, \quad l_o = \left(\frac{\varepsilon_k}{N^3}\right)^{1/2}, \tag{6.8}$$

i. e. the Reynolds number of Ozmidov-scale eddies. Eddies with size less than the Ozmidov length, l_o, are not restrained from overturning by buoyancy. Since $Re_b = (l_o/\eta)^{4/3}$ where $\eta = (\nu^3/\varepsilon_k)^{1/4}$ is the Kolmogorov scale, it follows that when $Re_b \gg 1$ there is a large scale separation between the Ozmidov and the Kolmogorov scales which is necessary for the presence of an inertial subrange that is unaffected by either buoyancy or viscous forces. The turbulent horizontal Froude number, $Fr_h = u_h'/NL_{Hk}$, is the ratio of the buoyancy timescale (N^{-1}) to the turbulent horizontal timescale (L_{Hk}/u_h'), and is a measure of the strength of buoyancy effects on the energy-containing scales; a decrease in Fr_h implies an increase in the relative strength of buoyancy. Fr_h can also be interpreted based on length scales using $\varepsilon_k \sim u_h'^3/L_{Hk}$ that leads to $Fr_h = (l_o/L_{Hk})^{2/3}$.

The $Fr_h - Re_h Fr_h^2$ phase portrait serves to distinguish among the different manifestations of the influence of buoyancy as the wake evolves through progressively decreasing values of both Fr_h and $Re_h Fr_h^2$. As Fr_h decreases, the lower bound (l_o) on the length scale of buoyancy-affected motions decreases. As $Re_h Fr_h^2$ decreases, the scale separation between l_o and η decreases so that, for a given Fr_h, the parameter $Re_h Fr_h^2$ is a measure of the range of scales that can support turbulent motions. The wake is found to pass from a state of weak buoyancy (WB) to stratified turbulence (ST) at $Fr_h = 1$ when the large-eddy lengthscale, L_{Hk}, becomes equal to the Ozmidov lengthscale, $l_o = (\varepsilon_k/N^3)^{1/2}$. Figure 6.10 (a) shows that $Fr_h = 1$ is achieved at about the first buoyancy adjustment period ($Nt_b = 1$) for all the simulated wakes. As was discussed in section 6.6, $U_0/U_{0\infty}$ is found to deviate

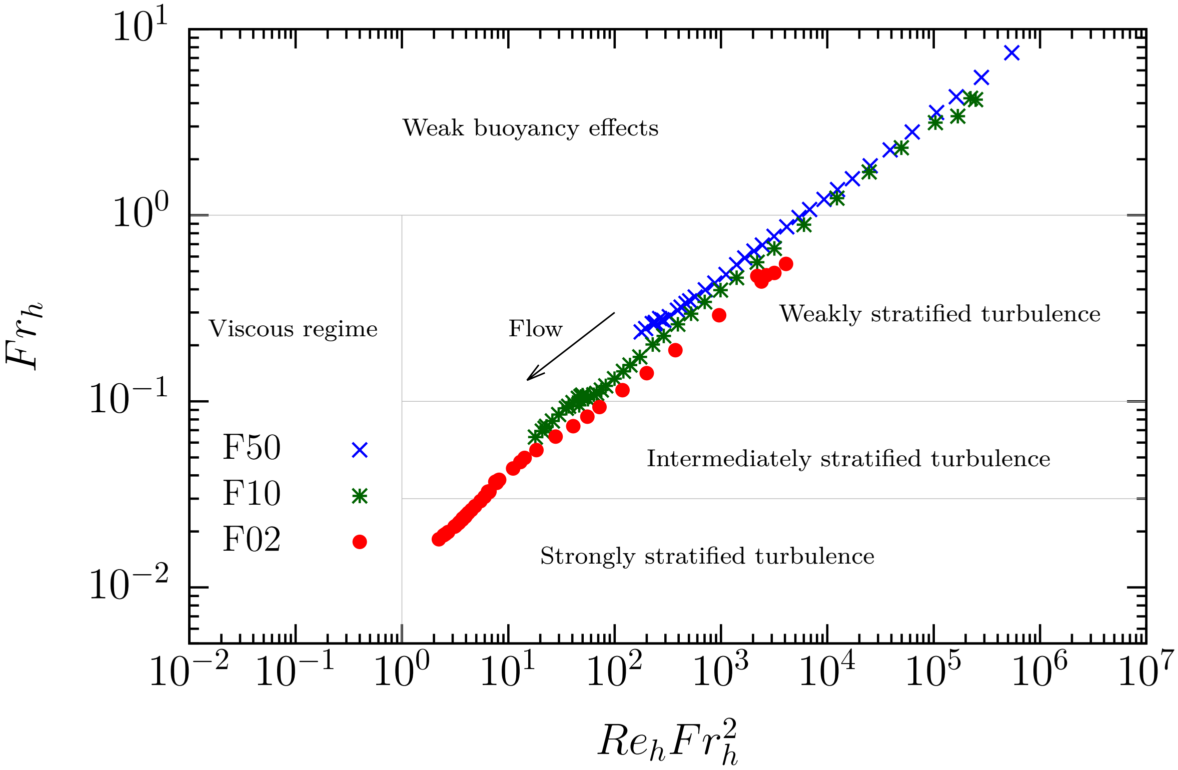

Figure 6.9: The trajectory of each of the simulated wakes in $Fr_h - Re_h Fr_h^2$ phase space computed using centerline values of Fr_h and $Re_h Fr_h^2$. Stratified turbulence ($Fr_h < 1$ and $Re_h Fr_h^2 > 1$) is divided into three regimes by the horizontal lines through $Fr_h = 0.1$ and 0.03.

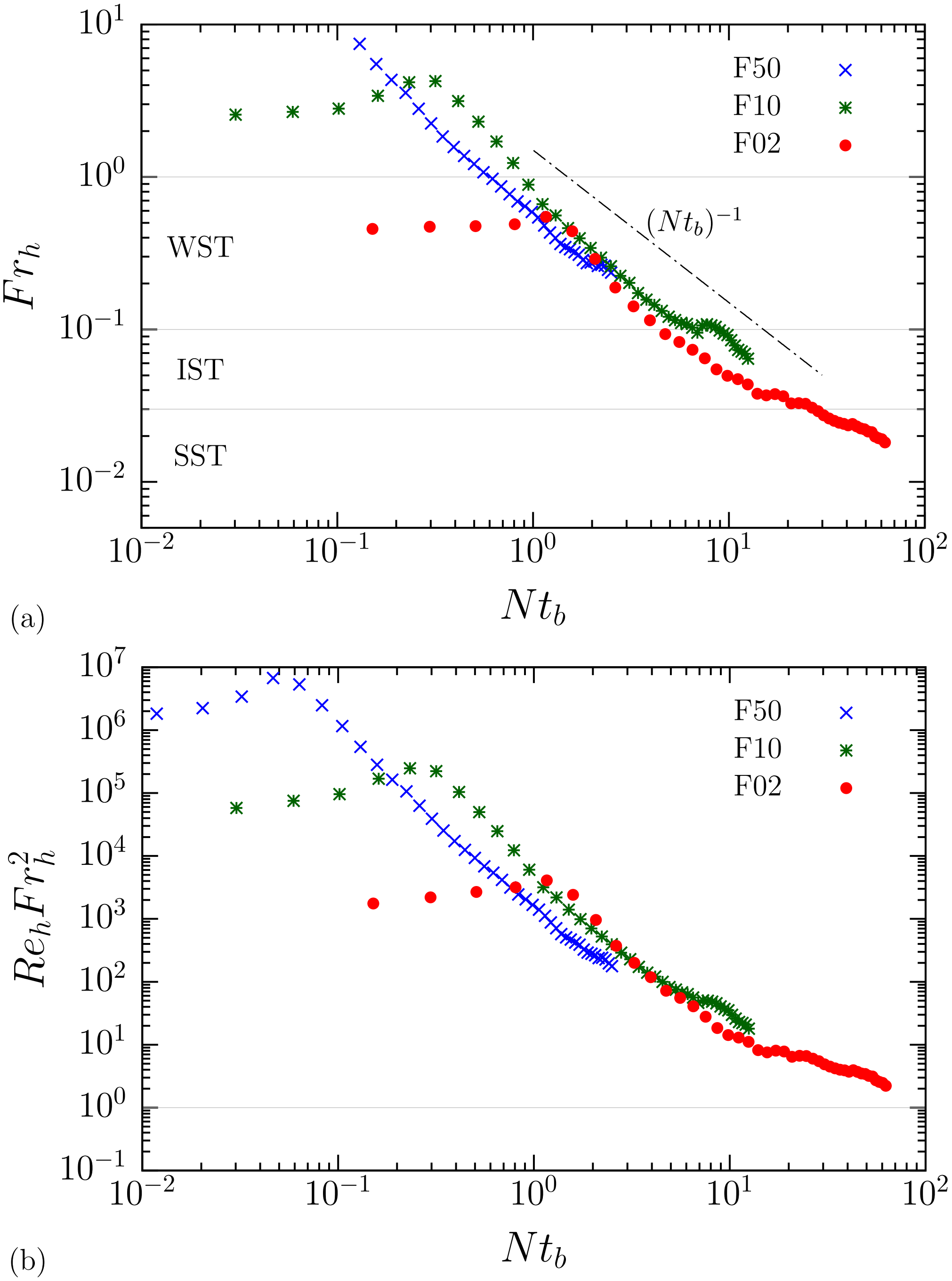

Figure 6.10: Evolution of phase-space parameters: (a) Fr_h, and (b) $Re_hFr_h^2$. The horizontal grey lines in (a) divide the wake into WST, IST, and SST regimes.

sharply from unity at $Nt_b \approx 1$ marking a point when buoyancy has begun to significantly affect the largest scales of the flow.

Stratified wake turbulence can be further subcategorized into 3 regimes: weakly stratified turbulence (WST), intermediately stratified turbulence (IST), and strongly stratified turbulence (SST) as marked in figure 6.9. In the WST stage, the effect of buoyancy on the mean flow is significant but its effect on turbulence is not. In particular, turbulence anisotropy is hardly affected in the WST regime. The value of Fr_h has to decrease from unity by almost an order of magnitude before there is a trend of increasing turbulence anisotropy associated with r.m.s in the horizontal progressively becoming larger than in the vertical. As discussed in section 6.6, turbulence anisotropy increases in both $Fr = 2$ and 10 wakes at $Fr_h \approx 0.1$. This suggests that WST transitions at $Fr_h \sim O(0.1)$ to a regime of intermediately stratified turbulence (IST) that is distinguished by progressively increasing turbulence anisotropy. The final stage of strongly stratified turbulence (SST) is based on Fr_h becoming $Fr_h \sim O(0.01)$. In particular, we consider SST to commence at $Fr_h = 0.03$, based on the value of $Fr_v = u'_h/Nl_v$ approaching an $O(1)$ constant. It is worth noting that $Fr_h = 0.03$ is close to the prediction of Lindborg (2006) that the critical horizontal Froude number $Fr_{h,crit} = 0.02$.

Figure 6.9 shows that the entry of stratified wakes into the three ST regimes depends on the Fr of the wake. The F50 trajectory enters WST relatively late and is not able to enter IST. Notice that Fr_h is however close to 0.1 (near the entry of IST) by the end of the computational domain and turbulence starts becoming anisotropic as seen in figure 6.6 (a). Both F10 and F02 trajectories access the IST regime with a sufficiently large $Re_h Fr_h^2 \approx 100$.Turbulence anisotropy progressively increases as the wake traverses the IST regime as shown by the divergence of u'_z from $K^{1/2}$ in figures 6.7 (a) and 6.8 (a). In the IST regime, the inertial force on the mean flow dynamically adjusts to balance the buoyancy force such that Fr_V becomes close to an $O(1)$ constant (see figure 6.7 (b) and 6.8

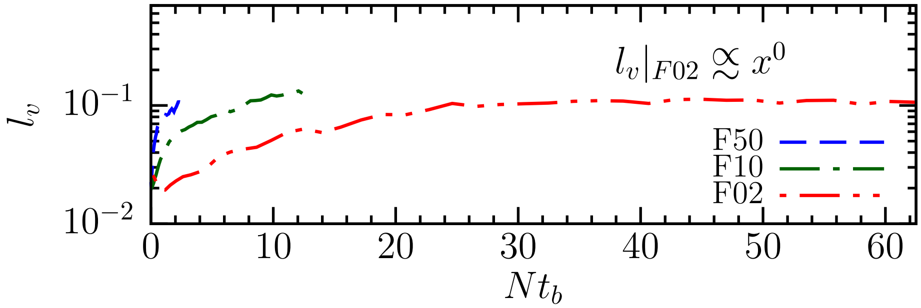

Figure 6.11: Turbulent vertical lengthscale, $l_v = u'_h/\partial_z u'_h$.

(b)). However, buoyancy becomes progressively stronger in the case of turbulent eddies as indicated by the continued decrease of Fr_v as the flow evolves. The $Fr = 2$ wake is able to cross the $Fr_h = 0.03$ boundary to access the SST regime and remains in the regime until the end of the simulation domain. Figure 6.8 (b) shows that $Fr_v = u'_h/Nl_v$ asymptotes to an $O(1)$ constant in the SST regime. Thus, stratification imposes a characteristic buoyancy length scale, $l_v = u'_h/N$, on small-scale turbulence in the SST regime. Since $l_v = u'_h/\partial_z u'_h$, it follows that vertical shear of the fluctuations asymptotes to $O(N)$. l_v becomes approximately constant in case F02 (Figure 6.11) when $Nt_b > 20$. The value of $Nt_b = 20$ also marks the entry of Case F02 into the SST regime as indicated by the crossing of $Fr_h \simeq 0.03$ at $Nt_b \approx 20$ by the F02 trajectory in figure 6.10.

Since $Re_h Fr_h^2 \sim O(10)$ as the F02 wake enters into the SST regime, figure 6.12 (a) reveals small-scale patchiness of turbulence displayed by a contour of instantaneous turbulent dissipation. While F02 turbulence has decayed in amplitude during the SST regime, figure 6.12 (b) shows that the power spectra of centerline streamwise velocity remains broadband during the SST regime. Figure 6.13 displays the three regimes of stratified turbulence. At F02, the SST spans a substantial streamwise distance (almost 85 body diameters from $x/L_b \approx 40$ to the end of the computational domain) indicating that the dynamics of strongly stratified flow is important to the evolution of high-Re wakes.

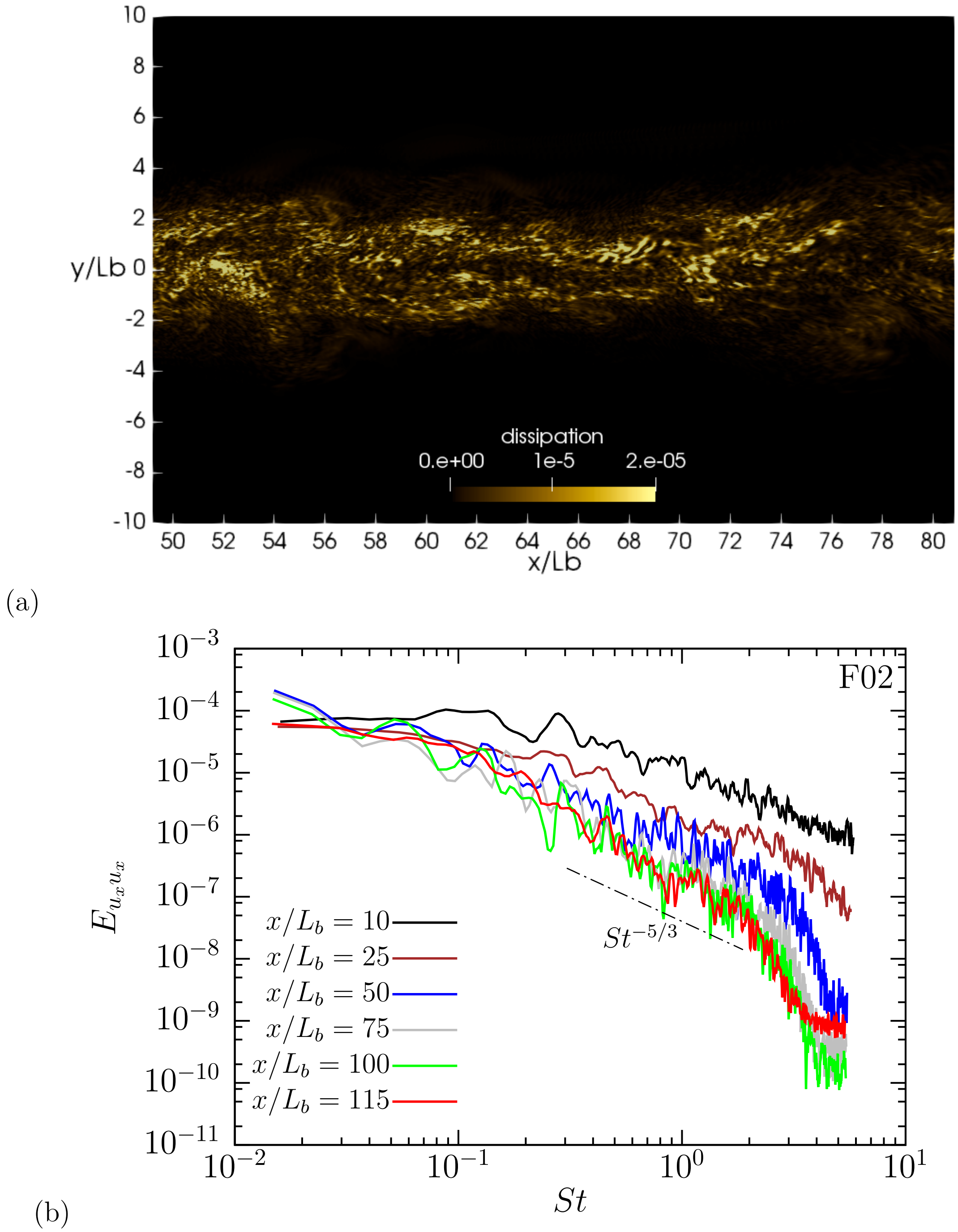

Figure 6.12: Case F02: (a) Snapshot of instantaneous field of dissipation rate fluctuation in the SST regime of the wake, shown on a horizontal plane, and (b) Power spectra of centerline streamwise velocity at multiple downstream locations.

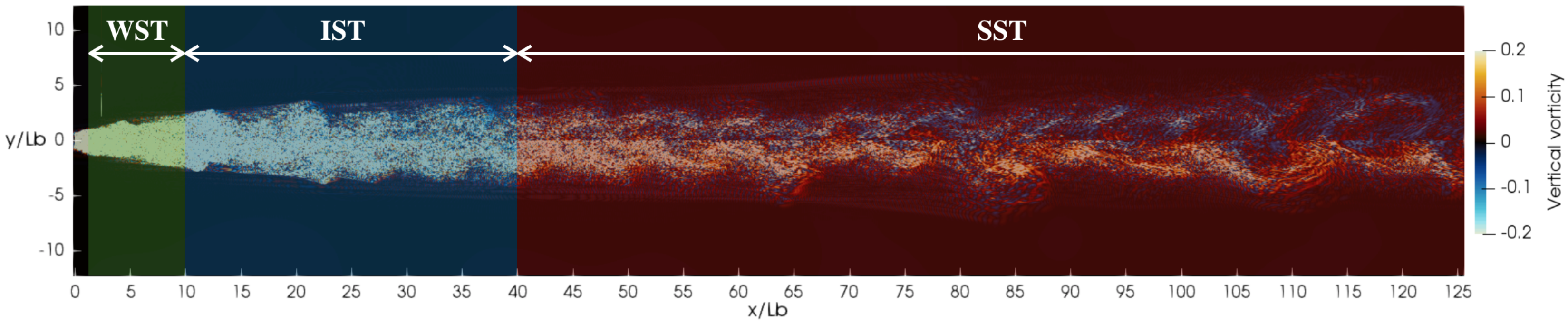

Figure 6.13: Subdivisions of stratified turbulence displayed on a horizontal-plane snapshot of F02 vertical vorticity. Weakly stratified turbulence (WST) in green, intermediately stratified turbulence (IST) in blue, and strongly stratified turbulence (SST) in red.

6.8 Wake lengthscales

The evolution of the geometrical dimensions of the wake is closely related to the decay of U_0 owing to conservation of momentum deficit.The horizontal (L_H) and vertical (L_V) wake extents derived from profiles of mean streamwise velocity deficit are shown in figure 6.14. The width and height of the unstratified case are identical by construction as they are obtained from additional azimuthal averaging. It is found that during the interval, $10 < x/L_b < 65$, the wake satisfies $L \propto x^{0.45}$ in accord with momentum-deficit conservation, $U_0 L^2 = const$ and the $U_0 \propto x^{-0.9}$ law found in that interval. During the interval, $65 < x/L_b < 125$, the wake length grows with an exponent $L \propto x^{0.29}$, close to $L \propto x^{1/3}$, the classical similarity law for L in the turbulent far wake.

Consider the wake length L_k, derived from profiles of TKE in the UNS case, and plotted in figure 6.15 (solid-black line). Unlike L which exhibits a breakpoint at $x/L_b \approx 65$, there is no corresponding breakpoint in the evolution of L_k. Rather, a least-squares power-law fit to L_k yields $L_k \propto x^{0.31}$ close to $x^{1/3}$ during the entire domain after $x/L_b > 10$. Therefore, it is a combination of quantities derived from turbulence ($K^{1/2}$ and L_k) and not those derived from the mean flow (U_0 and L) that appears to satisfy the classical high-Re similarity result.

We return to figure 6.14 and discuss how buoyancy sets in to create anisotropy between L_H and L_V in stratified wakes. For the weakly-stratified Fr=50 and 10 cases, both L_H and L_V behave in the near wake as expected with little to no variation compared to the UNS case. Further downstream, the growth of L_V reduces at $Nt_b \approx 1$ (recall that $Nt_b = Fr^{-1} x/L_b$). As far as we know, this is the first body-inclusive stratified wake simulation that finds a continuous decrease of vertical thickness. The horizontal width L_H, for both $Fr = 10$ and 50, deviate away from the UNS case before L_V does. Beyond $x/L_b = 10$ in the $Fr = 10$ wake, the growth of L_H is close to $L_H \propto x^{1/3}$ over a long interval until the end of the computational domain.

The wake dimensions in the $Fr = 2$ case are significantly different from the UNS case. L_H and L_V start deviating from the UNS case close behind the body indicating an absence of the '3D, unstratified' regime. The deviation is consistent with conservation of momentum deficit; L_H is enhanced to counteract the contraction of L_V as buoyancy returns vertically-displaced fluid towards its neutral equilibrium. After $x/L_b = 2$ that marks the end of the recirculation zone, L_H commences to increase with a rate slightly larger than that of the UNS case until $x/L_b = 5$ or $Nt_b = 2.5$ where the growth rate decreases. At $x/L_b \approx 2\pi$, where the mean wake enters into the next phase of the oscillatory modulation depicted by the rapid increment of L_V, the velocity deficit (U_0) increases and, as a consequence of conservation of momentum deficit, L_H decreases sharply to satisfy $U_0 L_H L_V \approx const$. This sharp lateral contraction of L_H leads to the F02 trajectory crossing its unstratified counterpart at $x/L_b = 10$. Beyond $x/L_b = 20$, the growth rate of L_H progressively approaches $L_H \propto x^{1/3}$. After the rapid growth of L_V over $2\pi < x/L_b < 4\pi$ ($\pi < Nt_b < 2\pi$), the oscillatory modulation remains visible, albeit with diminished amplitude, throughout the wake evolution until the end of the computational domain.

The $Fr = 2$ power-law exponents of L_H and L_V can, in fact, be inferred based on $Fr_V \to const.$ and the conservation of momentum. The proportionality $Fr_V \propto x^0$ implies that $L_V \propto U_0$. Invoking the conservation of streamwise momentum deficit where $U_0 L_V L_H \approx const$ and assuming that the shape of deficit profiles in the $y - z$ plane is characterized by the two lengths scales L_H and L_V, yields $L_H L_V^2 \approx const$ or $L_H \propto L_V^{-2}$. Since $U_0 \propto x^{-0.18}$ in the $Fr = 2$ wake, it directly follows that $L_V \propto x^{-0.18}$ and $L_H \propto x^{0.36}$, which are close to the present result.

The horizontal extent (figure 6.15 a) of the TKE profile become comparable to that of the UNS case, even in the NEQ regime, with a grow rate of $L_{Hk} \propto x^{1/3}$. In the vertical direction, the half-height (L_{Vk}) based on TKE decreases similar to L_V. For example, L_{Vk}

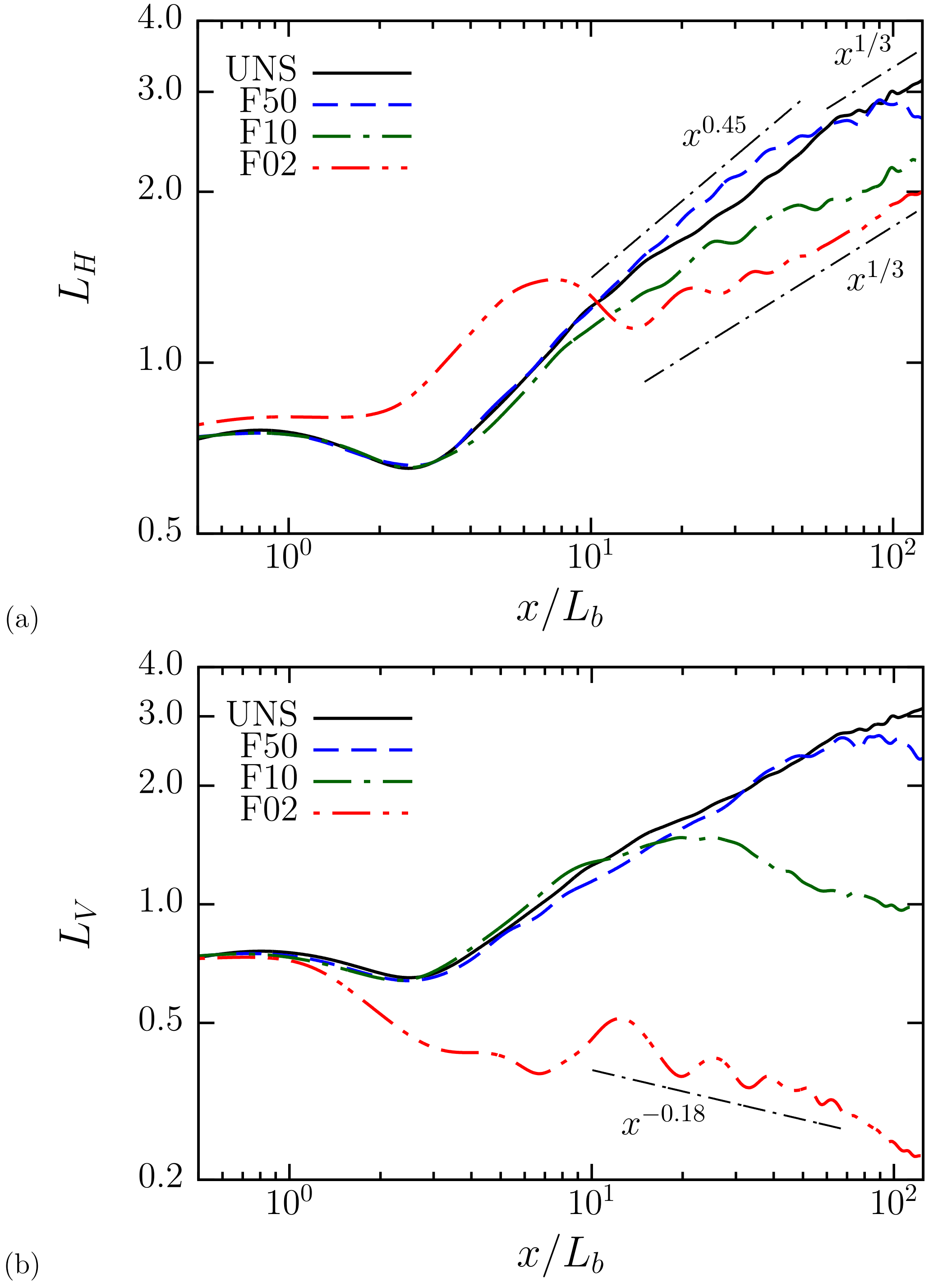

Figure 6.14: Wake dimensions based on the the velocity profile: (a) horizontal wake width (L_H), and vertical wake height (L_V).

at F10 begins to deviate away from the UNS case around $x/L_b = 10$ ($Nt_b = 1$), practically identical to where L_V deviates from its UNS counterpart. In case F02, once wake turbulence enters into the NEQ stage, it is found that $L_{Vk} \propto K^{1/2} (\propto x^{-0.18})$ in agreement with the predicted vertical length scaling of strongly stratified flow.

6.9 Histories of kinetic and potential energies

In section 6.6, we discussed buoyancy effects on centerline values of mean and r.m.s velocity. The evolution of area-integrated values of the kinetic and potential energy, each split into mean and turbulent constituents, is also of interest. Figure 6.16 shows the histories of area integrals, denoted by $\{\cdot\}$, of mean kinetic energy, $E_k^M = \langle u_d \rangle^2/2$, turbulent kinetic energy, $E_k^T = \langle u_i' u_i' \rangle/2$, mean available potential energy, $E_\rho^M = \gamma \langle \rho_d \rangle^2/2$ where $\gamma = g^2 \rho_0^{-2} N^{-2}$, and turbulent available potential energy, $E_\rho^T = \gamma \langle \rho'^2 \rangle/2$. The subscript '$d$' denotes deviation of velocity from background velocity $(U_b, 0, 0)$ or density from the linearly-varying background density.

Consider first the decay of E_k^M (figure 6.16 (a)). The decay of E_k^M in the stratified wakes slows down once the downstream location in each wake has reached the corresponding $Nt_b = 1$. The inset shows that E_k^M, when normalized by the corresponding UNS value, increases as approximately $x^{0.5}$ which can be explained as follows. If U_0, L_H, and L_V are the characteristic velocity and lateral wake lengthscales for the mean deficit velocity profile, then

$$\{E_k^M\} \sim U_0^2 L_V L_H \propto U_0 \, . \tag{6.9}$$

The second proportionality comes from invoking conservation of deficit momentum and, again, assuming that the shape of the deficit profile is characterized by L_H and L_V. Thus, $\{E_k^M\}/\{E_k^M\}_\infty \sim U_0/U_{0\infty}$, where $U_0/U_{0\infty} \gtrsim x^{-0.18}/x^{-2/3} \propto x^{0.49}$ which is close to the $x^{0.5}$

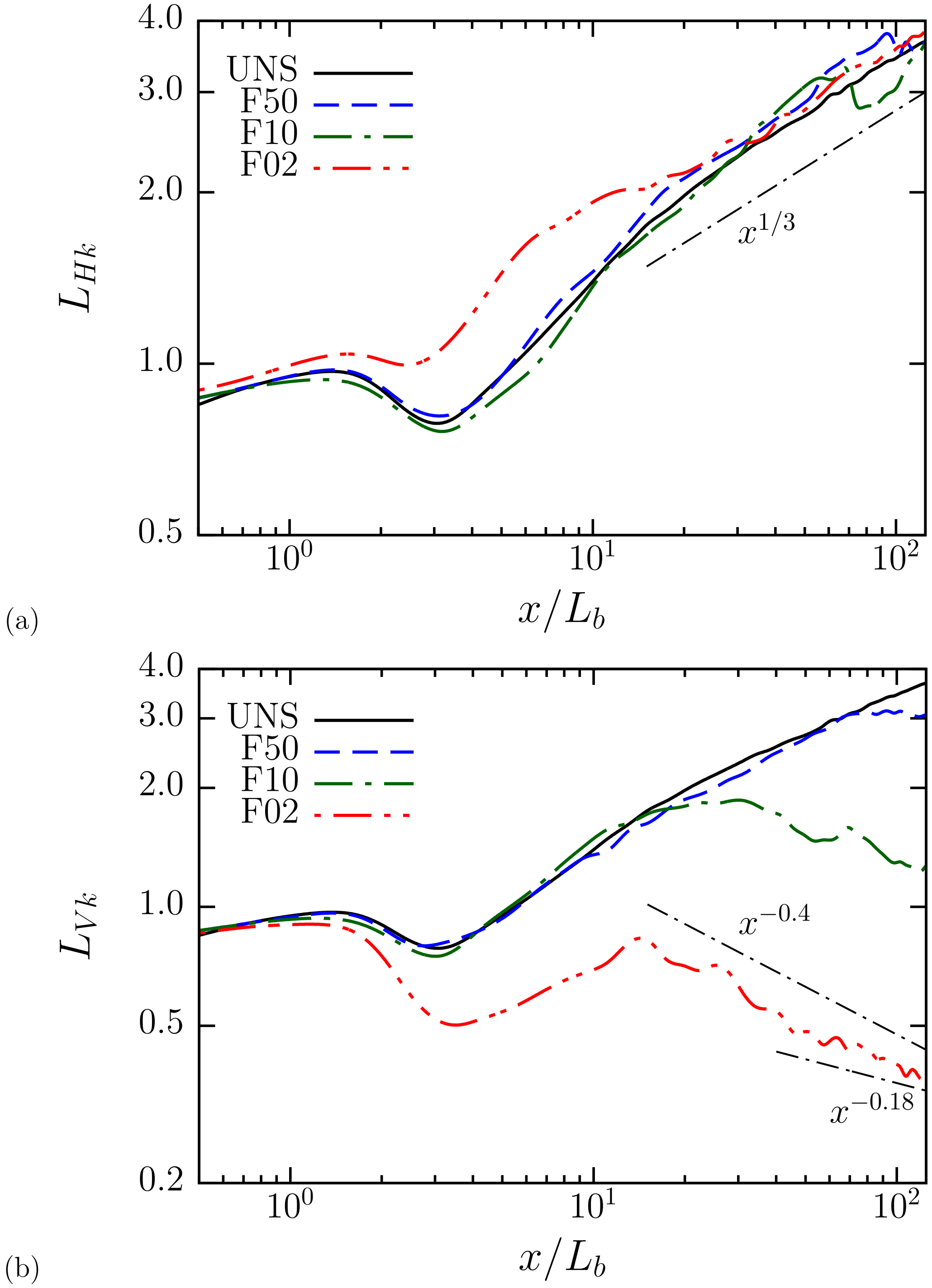

Figure 6.15: Wake dimensions based on the the profile of turbulent kinetic energy: (a) horizontal width (L_{Hk}), and (b) vertical height (L_{Vk})

scaling in the inset. Similarly, scaling E_k^T shows that

$$\{E_k^T\} \sim K L_V L_H \propto \frac{K}{U_0}. \tag{6.10}$$

In the WST regime, the evolution of K is unchanged while U_0 increases relative to the unstratified case, so that Eq. (6.10) implies that $\{E_k^T\}$ decreases relative to UNS once the stratified wakes enter the WST regime. This can be seen in figure 6.16 (b) where the $Fr = 10$ and 50 wakes access the WST regime at their corresponding $Nt_b \approx 1$, at which point they decrease faster than the UNS case. The inset shows that the reduction of the $\{E_k^T\}/\{E_k^M\}$ ratio relative to the unstratified case largely takes place in the WST and the early-IST regimes and reaches a plateau in the SST regime. In the unstratified case, the mean component becomes much smaller than the turbulent component. However, as inferred from the inset of figure 6.16 (b), the mean wake remains at long distance from the body in stratified cases even when the turbulence has decayed.

Consider the evolution of potential energies in figure 6.16 (c, d). $\{E_\rho^M\}$ is largest initially in the F02 wake where the the disk displaces fluid under the highest stratification of the cases simulated here. Subsequently, $\{E_\rho^M\}$ decreases with the decay rate being larger in the IST and SST regimes than in WST. Examination of the budget of $\{E_\rho^M\}$ (not shown) reveals that the dominant balance is between advection and the mean buoyancy flux, $B_k^M = -g\rho_0^{-1}\langle\rho_d\rangle\langle u_3\rangle$. The mean buoyancy flux in the F02 wake acts to transfer energy to the mean kinetic energy during the IST and SST regimes, leading to a sharp drop in E_ρ^M. By the end of the computational domain, $\{E_\rho^M\}$ in case F02 becomes smaller than in the other cases. The turbulent buoyancy flux, $B_k^T = -g\rho_0^{-1}\langle\rho' u_3'\rangle$, acts to transfer energy into the turbulent available potential energy (APE) leading to a decrease in the decay rate of $\{E_\rho^T\}$ during the SST phase of case F02.

The inset in the figure 6.16 (c) shows that, in the $Fr = 10$ and $Fr = 50$ wakes,

$\{E_\rho^M\}/\{E_k^M\}$ increases with downstream distance reaching $\approx O(0.1)$. On the other hand, the inset in the figure 6.16 (d) shows the turbulent kinetic and turbulent potential energies are more evenly partitioned with $\{E_\rho^T\}/\{E_k^T\} \approx O(1)$ over a substantial distance in the $Fr = 2$ and $Fr = 10$ wakes. This is a consequence of hydrostatic balance of vertical motion in buoyancy-dominated high-Re flow, where the vertical pressure gradient is balanced by buoyancy giving $\rho' \sim u_h'^2 \rho_0 / g l_v$ and, since $l_v \sim u_h'/N$, it follows that $\rho'^2 \propto (u_h' N)^2$ or $E_\rho^T \sim E_K^T$.

6.10 Budgets of mean and turbulent kinetic energies

The velocities, lengthscales, and energies discussed in the previous sections are statistical representations of mean flow and turbulence whose evolution is modified in stratified wakes. We further elaborate on the dynamical processes responsible for these modifications in stratified wakes by means of the evolutionary equations for MKE and TKE. The budget of MKE is written as

$$\partial_t E_k^M = -A_k^M - P_k - D_k^M - T_k^M + B_k^M, \tag{6.11}$$

where the advection, production, dissipation, transport, and buoyancy flux are defined as follows: $A_k^M = \langle u_j \rangle \partial_j E_k^M$, $P_k = -\langle u_i' u_j' \rangle \partial_j \langle u_i \rangle - \langle \tau_{ij}^s \rangle \partial_j \langle u_i \rangle$, $D_k^M = \nu \partial_j \langle u_i \rangle \partial_j \langle u_i \rangle + \nu \partial_j \langle u_i \rangle \partial_i \langle u_j \rangle$, $T_k^M = \partial_i \{ \langle p \rangle \langle u_{di} \rangle + \langle u_{dj} \rangle \langle u_i' u_j' \rangle \} - \nu \partial_{jj} E_k^M - \nu \partial_j \langle u_i \rangle \partial_i \langle u_j \rangle + \partial_j (\langle \tau_{ij}^s \rangle \langle u_{di} \rangle)$, and $B_k^M = -g \rho_0^{-1} \langle \rho_d \rangle \langle u_3 \rangle$. Similarly, the budget of TKE is written as

$$\partial_t E_k^T = -A_k^T + P_k - D_k^T - T_k^T + B_k^T, \tag{6.12}$$

where the advection, dissipation, transport, and buoyancy flux are defined as follows: $A_k^T = \langle u_j \rangle \partial_j E_k^T$, $D_k^T = \nu \langle \partial_j u_i' \partial_j u_i' \rangle + \nu \langle \partial_j u_i' \partial_i u_j' \rangle - \langle \tau_{ij}^s \partial_j u_i \rangle$, $T_k^T = \partial_i \{ \langle p' u_i' \rangle + \langle u_i' u_j' u_j' / 2 \rangle \} -$

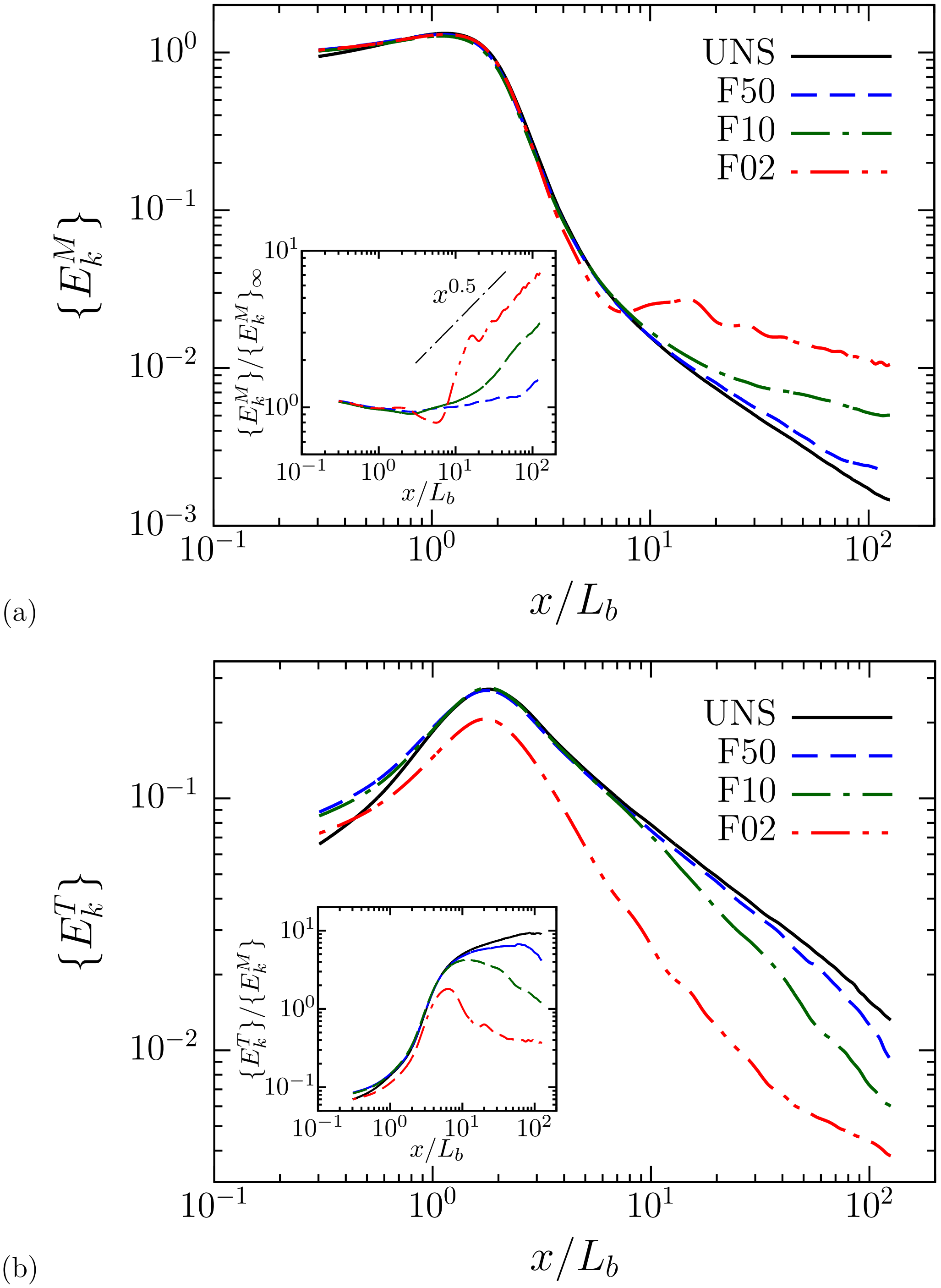

Figure 6.16: Histories of cross-wake integrals of kinetic and potential energies. (a) Mean kinetic energy, $\{E_k^M\}$. Inset compares $\{E_k^M\}$ with the UNS case, denoted $\{E_k^M\}_\infty$. (b) Turbulent kinetic energy, $\{E_k^T\}$. Inset shows ratio of turbulent to mean kinetic energy.

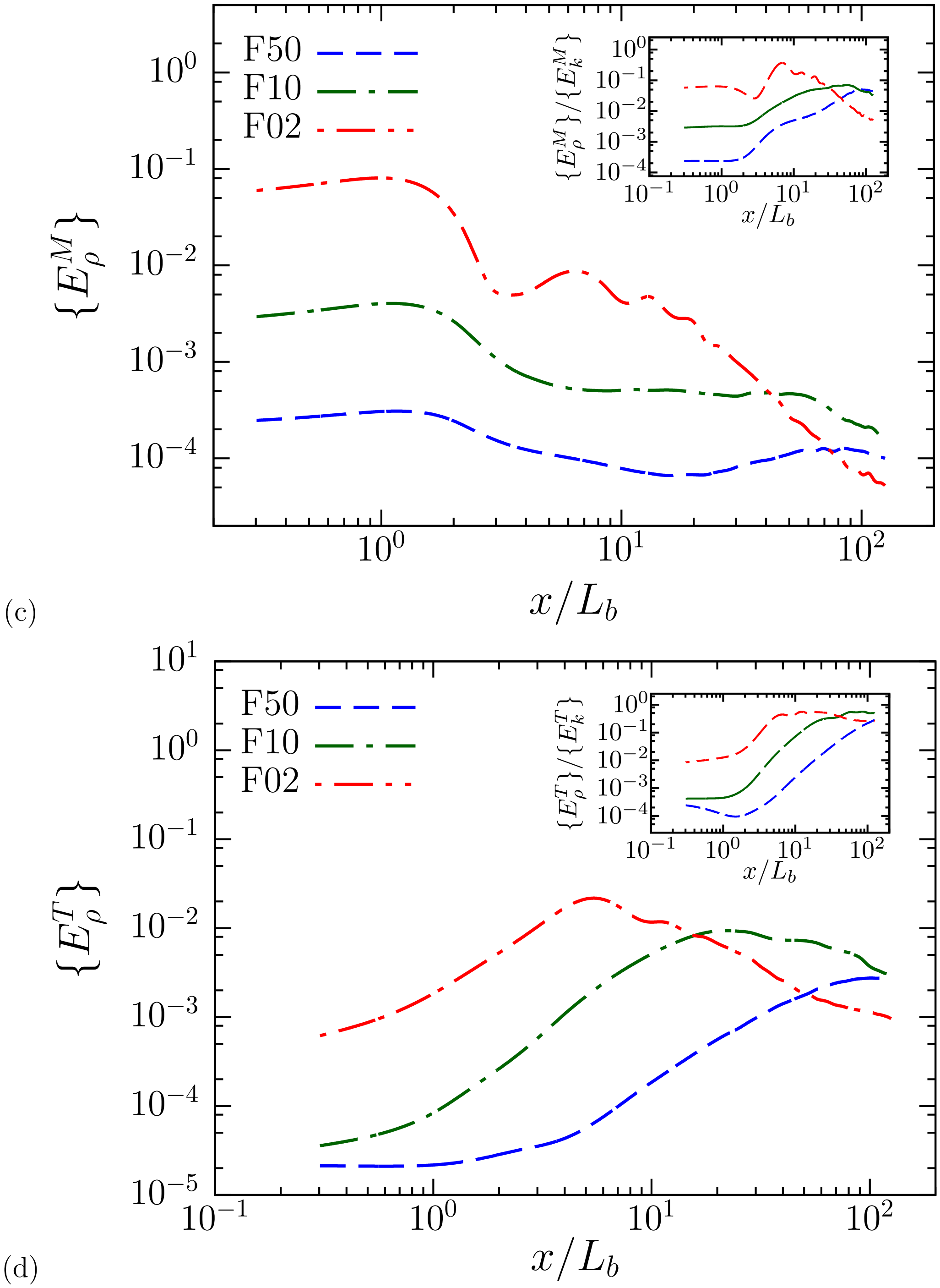

Figure 6.16: (Cont.) Histories of cross-wake integrals of kinetic and potential energies. (c) Mean potential energy, $\{E_\rho^M\}$. Inset compares mean potential energy to mean kinetic energy. (d) Turbulent potential energy, $\{E_\rho^T\}$. Inset shows ratio of turbulent potential to kinetic energies.

$\nu\partial_{jj}E_k^T - \nu\langle\partial_j u_i'\partial_i u_j'\rangle + \partial_j\langle\tau_{ij}'^s u_i'\rangle$, and $B_k^T = -g\rho_0^{-1}\langle\rho' u_3'\rangle$. The only additional term arising from the subgrid viscosity is $\left\langle u_i'\partial_j\tau_{ij}^s\right\rangle$, where $\tau_{ij}^s = 2\nu_s S_{ij}$ and $S_{ij} = (\partial_j\langle u_i\rangle + \partial_i\langle u_j\rangle)/2$. The contribution of this term is is found to be negligible.

We start by contrasting area-integrated kinetic energy budgets between the $Fr = 2$ and $Fr = \infty$ wakes. Terms in the MKE budget, Eq. (6.11), are plotted in figure 6.17 (a, c). The figure shows that the magnitude of $\{P_k\} \gg \{D_k^M\}$ (recall that $\{\cdot\}$ denotes an integral over cross-sectional area in the $y - z$ plane) indicating that the production of TKE is the primary sink of MKE. This is another manifestation of high-Re behavior of this flow; the close to x^{-1} scaling of U_0 in the UNS case cannot be attributed to a low-Re similarity result. The large pressure transport, $\{T_{k,p}^M\}$ in the insets, is a consequence of the relaxation of the flow from the low-pressure recirculation zone with increasing streamwise distance. While the $Fr = \infty$ pressure transport decreases significantly and becomes virtually negligible after the relaxation, the $Fr = 2$ pressure transport manifests wave-like behavior with a wave length of gravity lee waves, $\lambda \approx 2\pi Fr$, and progressively decreasing amplitude. This oscillatory modulation is observed in the behavior of every term in the MKE budget except the dissipation. The oscillations of the advection, $\{A_k^M\}$, and the pressure transport have opposing phase, and the wave length of the mean buoyancy flux, $\{B_k^M\}$, is $\lambda \approx \pi Fr$.

Terms in the TKE budget, Eq. (6.12), are plotted in figure 6.17 (b, d). Turbulence is established early on as shown by the large positive production, $\{P_k\}$, that exceeds the dissipation, $\{D_k^T\}$, in the region before $x/L_b \approx 5$. While the decay of TKE in the $Fr = \infty$ wake via $\{D_k^T\}$ is counteracted solely by $\{P_k\}$, the turbulent buoyancy flux, $\{B_k^T\}$, plays a role in stratified wakes, e.g. it is found in the $Fr = 2$ wake to be significant after $x/L_b = 5$. $\{B_k^T\}$ has an order of magnitude that is comparable to the production and the dissipation, and it is in phase with the advection term.

To help understand how MKE and TKE evolve, the production, buoyancy flux, and dissipation are normalized by the Lagrangian rate of change of their corresponding

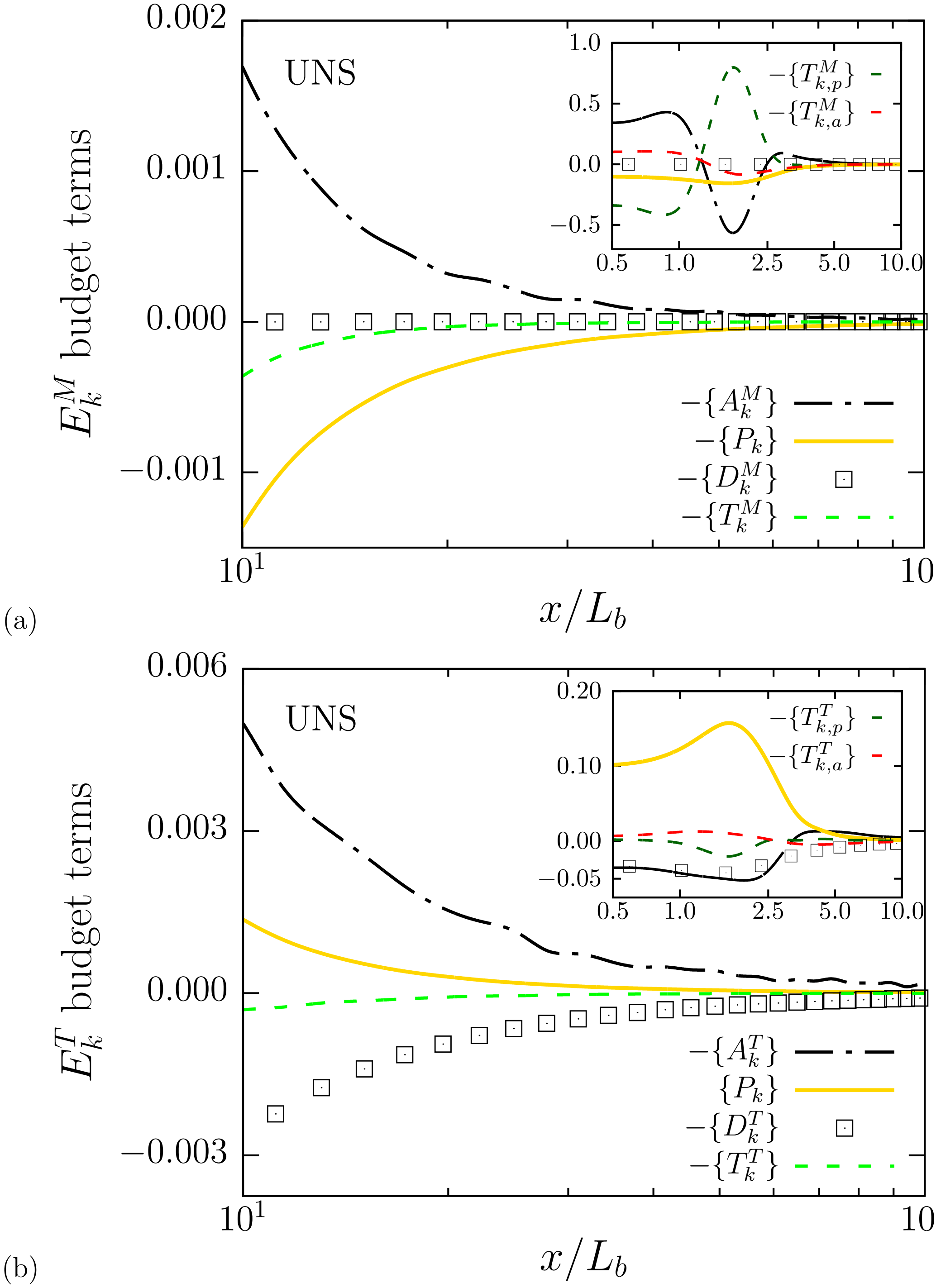

Figure 6.17: Terms in the MKE budget (top) and in the TKE budget (bottom) for the $Fr = \infty$ wake. Insets show budgets in the near-field $0.5 \leq x/L_b \leq 10$ while the main figure depicts the budgets in $10 \leq x/L_b \leq 100$.

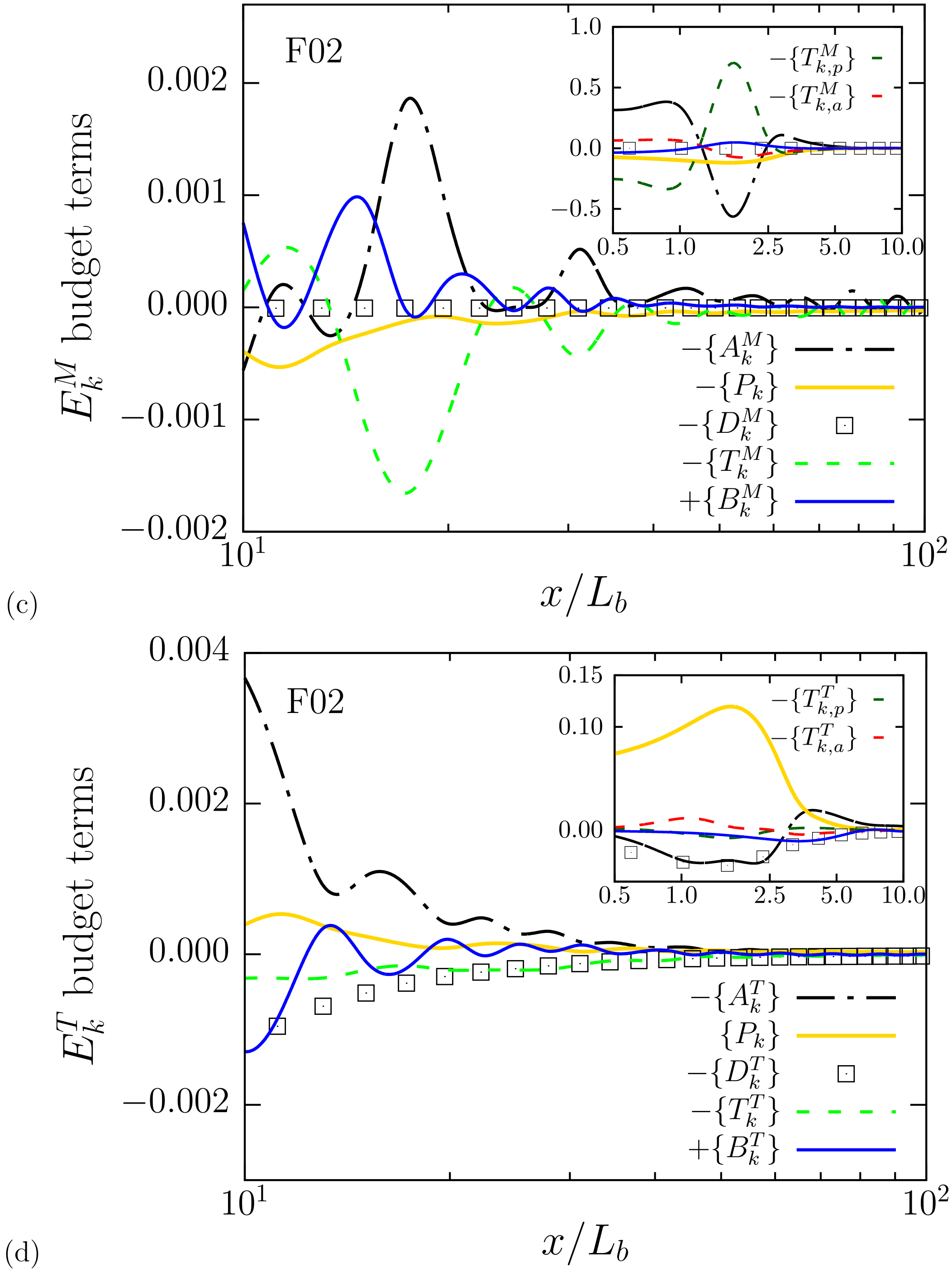

Figure 6.17: (Cont.) Terms in the MKE budget (top) and in the TKE budget (bottom) for the $Fr = 2$ wake. Insets show budgets in the near-field $0.5 \le x/L_b \le 10$ while the main figure depicts the budgets in $10 \le x/L_b \le 100$.

energy, taken to be $\delta_t E_k \sim O(E_k U_b/x)$, and plotted in Figure 6.18. It is clear that all the simulated wakes are, again, of the high-Re type until the end of the domain since the compensated production, $\{P_k\}_M = \{P_k\}/\{\delta_t E_k^M\}$, is a much larger sink for MKE than its dissipation counterpart, $\{D_k^M\}_M$. The inset in figure 6.18 (a) shows that the production is suppressed in the presence of stratification after $Nt_b \approx 1$ but not necessarily for the entire wake. Thus, $\{P_k\}/\{P_k\}_\infty$ is < 1 for the $Fr = 50$ and 10 wakes but becomes > 1 in the $Fr = 2$ wake beyond about $x/L_b = 60$. However regardless of the fact that the $Fr = 2$ production is promoted later in the $Fr = 2$ wake ($\{P_k\}_{F02}/\{P_k\}_\infty > 1$), the compensated production for all the stratified wakes remain relatively small at all time after $Nt_b \approx 1$ ($\{P_k\}_M < \{P_k\}_{M\infty}$). Figure 6.18 (c) shows that the mean buoyancy flux takes positive values indicating that energy is transferred from mean APE to MKE. Observe the $Fr = 2$ wake; the oscillatory modulation induces a huge jump in the mean buoyancy flux at $x/L_b \approx 2\pi$, the same location where the production is most suppressed. This relatively large B_k^M where $\{B_k^M\}_M|_{peak} \sim O(1)$ implies that B_k^M is an important contributor to E_k^M being larger in stratified wakes relative to their unstratified counterpart. Therefore, reduction in the decay rate of E_k^M in the stratified $Fr = 2$ wake has two reasons: (i) the early suppression of production, and (ii) the significant positive mean buoyancy flux.

TKE is reduced in stratified wakes as seen in figure 6.16 (b) and the reasons can be deduced from Figure 6.18 (right column). Interestingly, it is primarily the turbulent buoyancy flux (B_k^T) and, additionally, the dissipation of turbulent kinetic energy (D_k^T) that cause the initial reduction of E_k^T, and it is only later that the direct effect of reduced production sets in to further reduce the TKE. This is seen from compensated $\{B_k^T\}_T$ ($= \{B_k^T\}/\{\delta_t E_k^T\}$) that becomes strongly negative (implying that TKE is being used to stir the density field and generate TAPE) and $\{D_k^T\}_T$ that is increased prior to where $\{P_k\}_T$ significantly deviates from the unstratified counterpart. The result is evident in the $Fr = 2$ wake where $x/L_b = 5$ marks the location where buoyancy begins to significantly affect

$\{P_k\}_T$ while $\{B_k^T\}_T$ and $\{D_k^T\}_T$ have already been altered earlier in the wake.

Consider the F02 wake behavior in Figure 6.18 (right column). While the enhanced $\{D_k^T\}_T$ explains the enhanced decay rate of $\{E_K^T\}$ during $10 \leq x/L_b \leq 40$, $\{P_k\}_T$ progressively increases. $\{B_k^T\}_T$ is found to be partially positive with the peak $\{B_k^T\}_T \approx 0.5$ at $x/L_b \approx 30$. Thus, the reduction in the $\{E_k^T\}$ decay rate after $x/L_b \approx 40$ seen in the figure 6.16 (top-right) is the result of the increased $\{P_k\}_T$ along with the positive $\{B_k^T\}_T$ so that the combined source terms become comparable to $\{D_k^T\}_T$. Thus, turbulence in the $Fr = O(1)$ wakes is energized by the potential energy that was injected during the intermediate-wake period and not only the enhanced production. Later, the significant increased $\{P_k\}_T$ is sufficient to counteract with $\{D_k^T\}_T$ once $\{B_k^T\}_T$ has become negative so that the reduced decay rate of $\{E_k^T\}$ remains intact.

It is worth noting that (consider the $Fr = 2$ case) if the NEQ regime is characterized solely by the reduced decay rate of $\{E_k^M\}$ in figure 6.16 (a), the present result of partially positive B_k^T will be in contrast with the finding of Redford *et al.* (2015) for weakly-stratified wakes that B_k^T is a sink of E_k^T throughout the NEQ regime. However, as described in the section 6.6, the official arrival of the NEQ regime should be based on the reduced decay rate of $\{E_k^T\}$ in figure 6.16 (b), i.e. $Nt_b \approx 20$ or the entry into the SST regime. If we accept $Nt_b \approx 20$ as the official arrival of the wake (both mean and turbulence) into NEQ, then B_k^T behaves as a sink in the NEQ regime in agreement with Redford *et al.* (2015).

6.11 Dissipation

The evolution of turbulent dissipation (ε), characterized by centerline values, is discussed and possible scaling laws are explored in this section. The dissipation (ε_k) of TKE in lines and the dissipation (ε_ρ) of TPE in symbols are shown in figure 6.19. Given that the unstratified wake has high Re, classical theory suggests the scaling $\varepsilon \propto x^{-7/3}$,

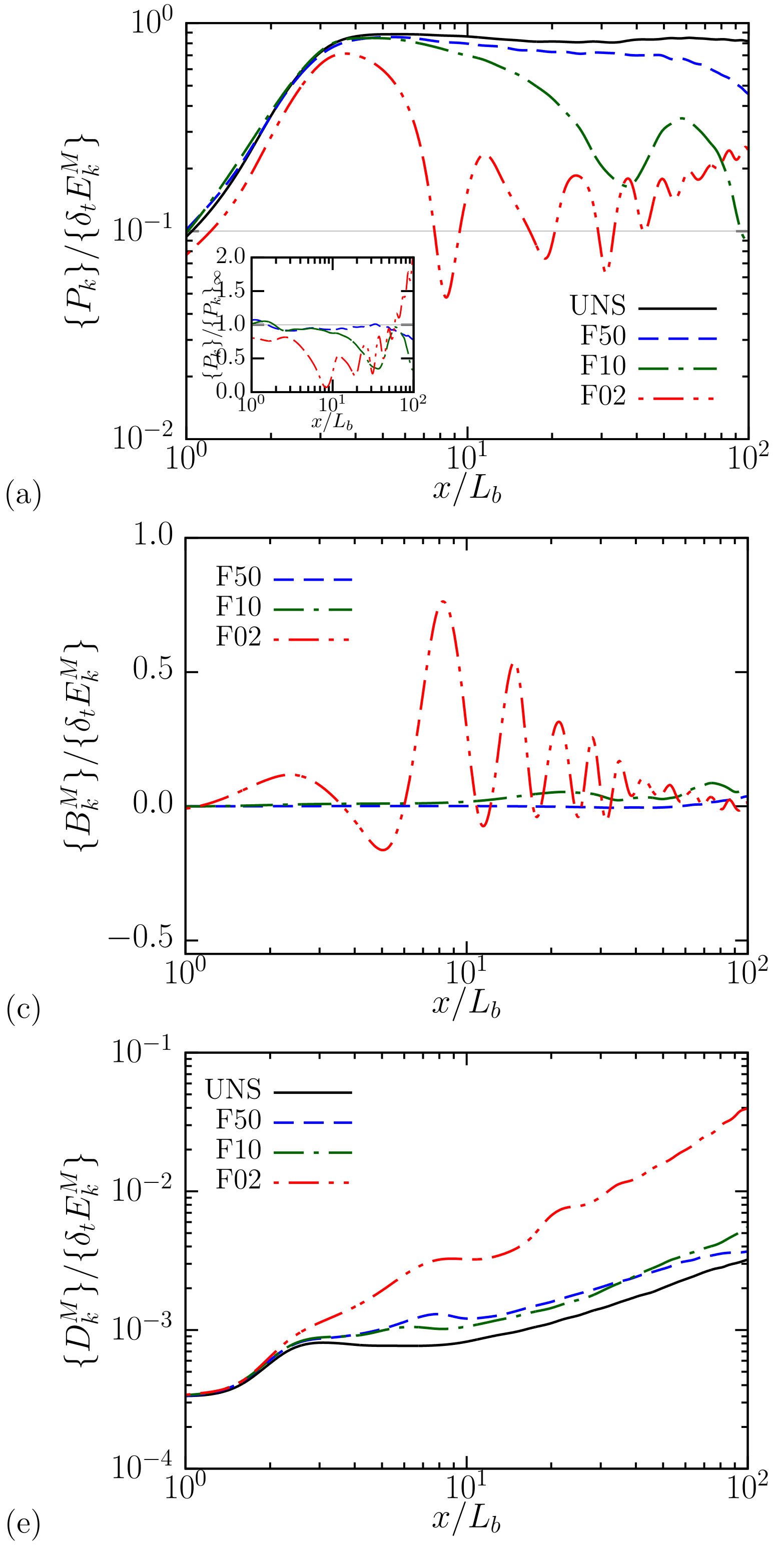

Figure 6.18: Ratio of cross-wake integrated budget terms for the evolutionary equation for E_K^M (a, c, e). The budget terms are normalized by the Lagrangian rate of change of their corresponding energy, $\delta_t\{E_k\} = \{E_k\}U_b/x$.

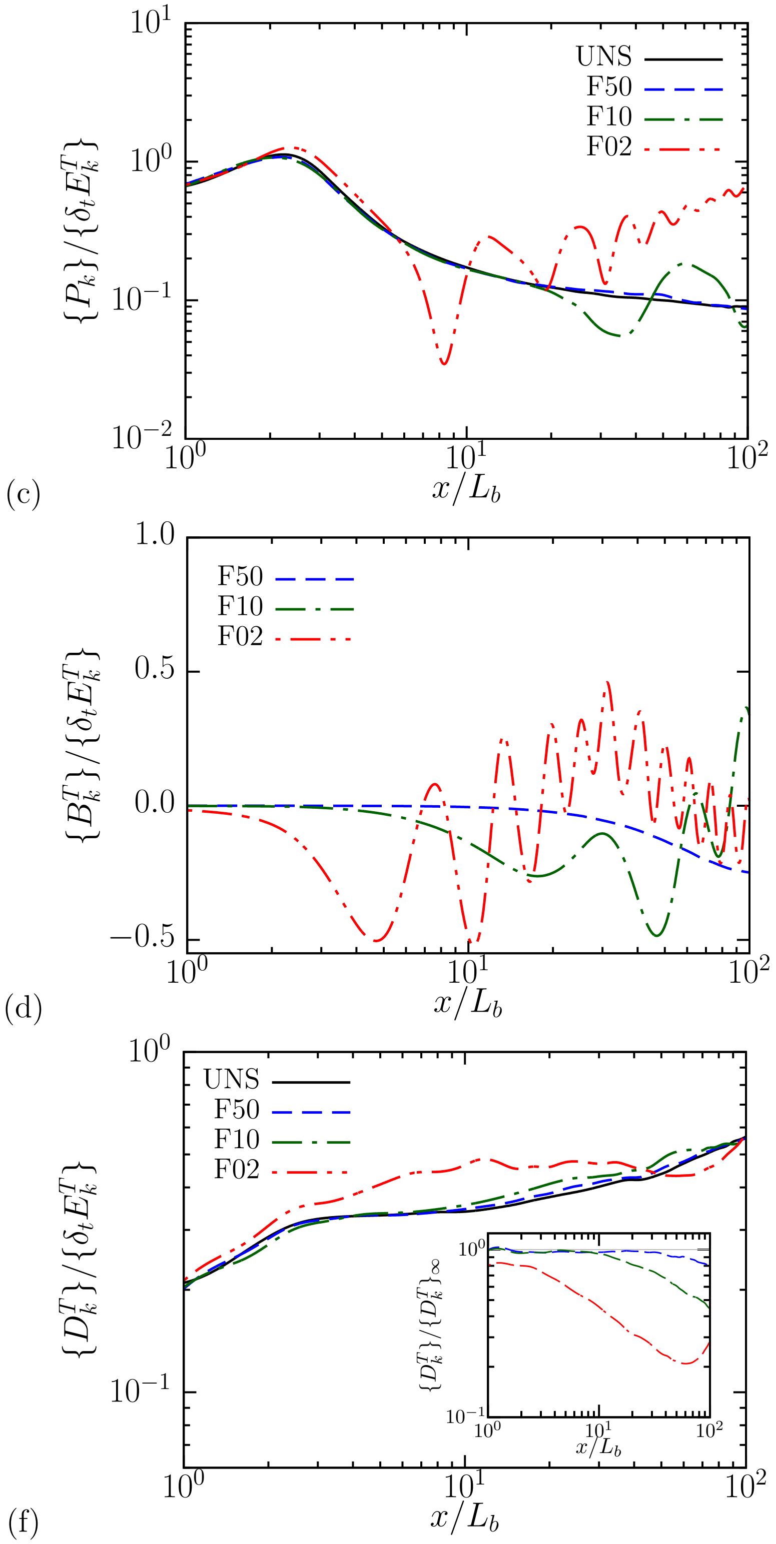

Figure 6.18: (Cont.) Ratio of cross-wake integrated budget terms for the evolutionary equation for E_K^T (b, d, f). The budget terms are normalized by the Lagrangian rate of change of their corresponding energy, $\delta_t\{E_k\} = \{E_k\}U_b/x$.

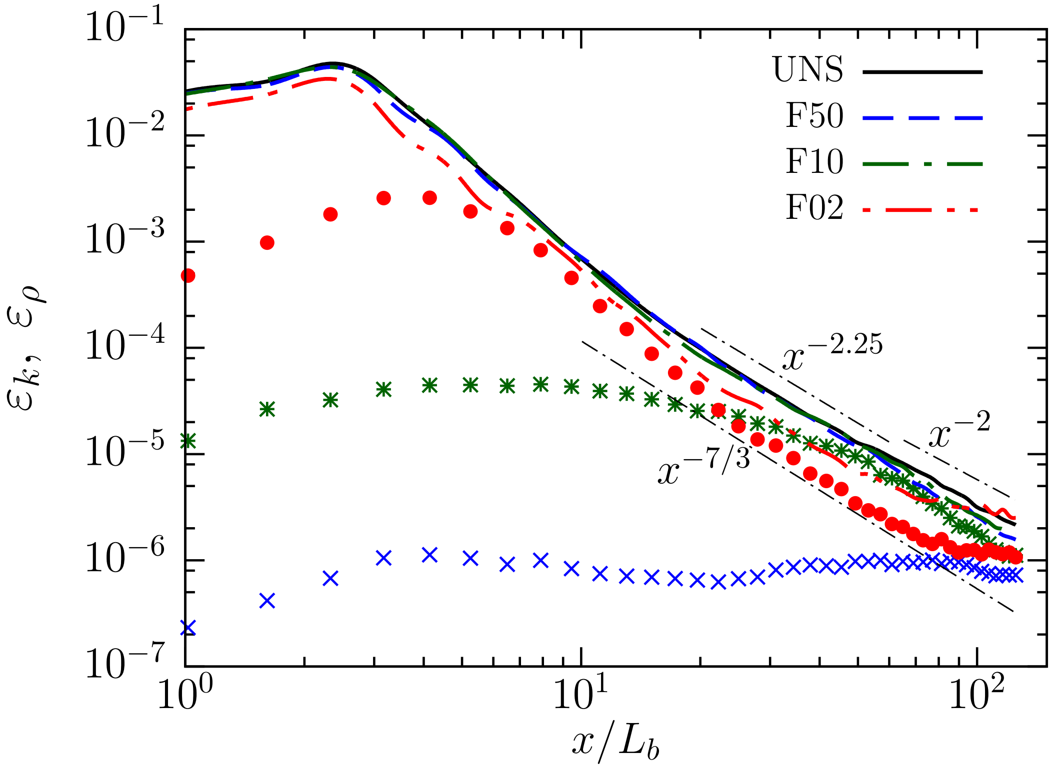

Figure 6.19: Evolution of centerline dissipation of turbulent kinetic energy (ε_k), shown in lines, and centerline dissipation of turbulent potential energy, shown in symbols.

which is a direct result from substituting the self-similarity solution $u' \propto x^{-2/3}$ and $l \propto x^{1/3}$ into the inviscid estimate $\varepsilon \sim u'^3/l$. To test the preceding inviscid scaling of ε, we take $u' = K^{1/2}$ and $l = L_k$ to be the half-width of the TKE profile. For the unstratified wake, however, power-law exponents obtained from the least-square fits, m as in $\varepsilon \propto x^m$, is found to be $m \approx -2.25$ followed by $m \approx -2$ (after a slope change at $x/L_b \approx 50$). Thus, ε power law in the unstratified case is not consistent with the u'^3/l scaling prediction of $x^{-2.44}$ that follows by the power-law exponents $u' = K^{1/2} \propto x^{-0.71}$ and $l = L_k \propto x^{0.31}$ found in the simulations as discussed in section 6.6. Note that, interestingly, $\varepsilon(U_0^3/L)^{-1} \approx$ const beyond $x/L_b \approx 65$.

Figure 6.20 (a) emphasizes the point that ε evolves differently from u'^3/l by showing that the scaled dissipation, $C_\varepsilon = \varepsilon(u'^3/l)^{-1}$ in green triangles, is not constant but increases with streamwise distance in the wake. This apparent contradiction between ε and u'^3/l was previously found in an experiment on turbulence generated by a fractal grid (Seoud & Vassilicos, 2007) where $C_\varepsilon \neq$ const despite an observed -5/3 inertial range in the energy spectrum. Vassilicos (2015) points to accumulating evidence in some turbulent shear flows that $C_\varepsilon = Re_{Global}^m/Re_{Local}^n (\neq \text{const})$ in a so-called 'nonequilibrium region' wherein the rate at which the turbulent kinetic energy cascades from large to small scales motion, u'^3/l (formed by a dimensional argument), is not strictly equal to the dissipation, ε, felt by the TKE. Our result shown in figure 6.20 (b) presents additional support that the centerline dissipation can reasonably be scaled by the form $(Re_{Global}^n/Re_{Local}^n)K^{3/2}/L$ where $Re_{Local} = U_0L/\nu$ at least beyond $x/L_b = 40$.

In stratified flows, the dissipation of turbulent kinetic and potential energy have often been suggested to scale using the inviscid estimate, with u' and l replaced by u'_h and l_h, i.e. $\varepsilon_{k,\rho} \sim u_h'^3/l_h$. This comes from the notion that the non-linear forward energy cascade is driven largely from the fluctuating energy present in horizontal motions. However, if the nonequilibrium region exists in the stratified wakes, we should expect that $\varepsilon_{k,\rho} = C_{\varepsilon_k,\varepsilon_\rho} u_h'^3/l_h$

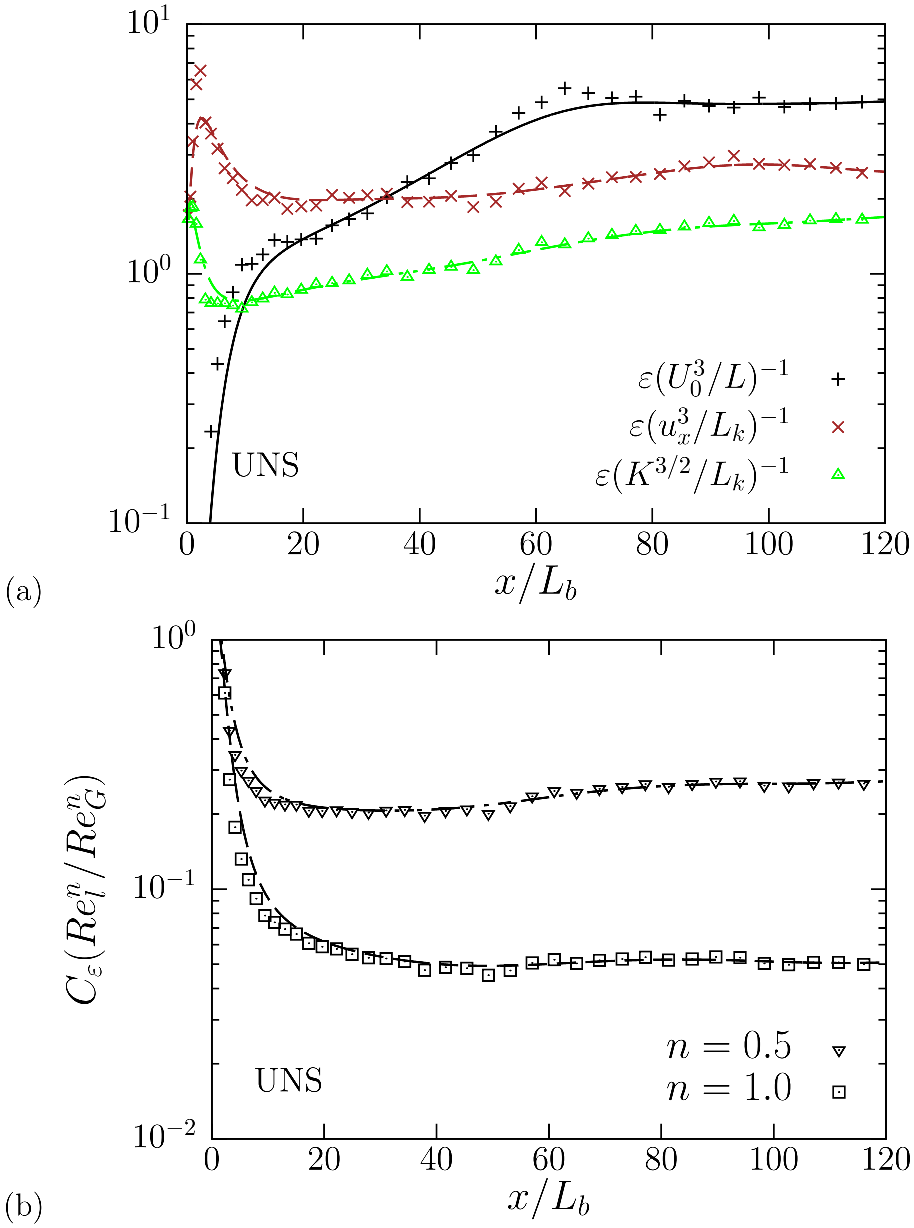

Figure 6.20: The $Fr = \infty$ wake: (a) Centerline scaled dissipation, C_ε, and (b) the product $C_\varepsilon(Re_l/Re_G)$. Lines approximate the simulation data (symbols) with Bézier splines.

where $C_{\varepsilon_k,\varepsilon_\rho} \neq$ const. While C_ε is found close to a constant in the homogeneous stratified turbulence of Maffioli & Davidson (2016), assessing this hypothesis can be difficult for localized turbulence such as in a core of the stratified wake where the lack of a homogeneous direction presents a challenge for the estimation of l_h. If $\varepsilon_k \sim u_h'^3/l_h$, $l_h \sim L_{Hk}$, and centerline estimates are employed, the decay rate of ε_k should reduce once the stratified wake has entered into the IST regime where the decay rate of u_h' is reduced. This is seen in figure 6.19 for the $Fr = 2$ wake but not for the $Fr = 10$ case. In the $Fr = 2, 10$ wakes, ε_ρ appears to decay like its ε_k counterpart but only after $Nt_b \gg 1$, i.e. after the initial adjustment between the APE of the displaced fluid and its KE is completed. Scaling of the $Fr = 2$ dissipation of TKE is presented in figure 6.21 (a). Similar to the $Fr = \infty$ wake, $\varepsilon_k \sim (U_0^3/L)$ after about $x/L_b \approx 65$. The scaling $\varepsilon_k \sim u_h'^2 N$ appears valid as the wake approaches the SST regime in which there is turbulence ($Re_b \gtrsim O(1)$) and it is largely controlled by buoyancy. As the $Fr = 2$ wake approaches toward the viscous regime, our result (not shown) reveals that ε_k is becomingly dominated by the components associated with the vertical shear of horizontal motions. This implies that the scaling $\varepsilon_k \sim \nu u_h'^2/l_v^2$, deduced from a dimensional argument, should become applicable. Indeed, $\varepsilon_k(\nu u_h'^2/l_v^2)^{-1}$ flattens in the downstream direction. The nonequilibrium dissipation scaling is shown in figure 6.21 (b). Unlike the unstratified wake, there is no evidence that the nonequilibrium dissipation scaling works for the simulated $Fr = 2$ wake.

6.12 Summary and conclusions

The present work is devoted to an examination of relatively high-Reynolds number turbulent wakes that evolve in stratified fluids. Body-inclusive LES of unstratified and stratified flows past a circular thin disk placed perpendicular to background stream are conducted. The wakes are simulated at a Reynolds number of Re=U_bL_b/ν=50,000 and

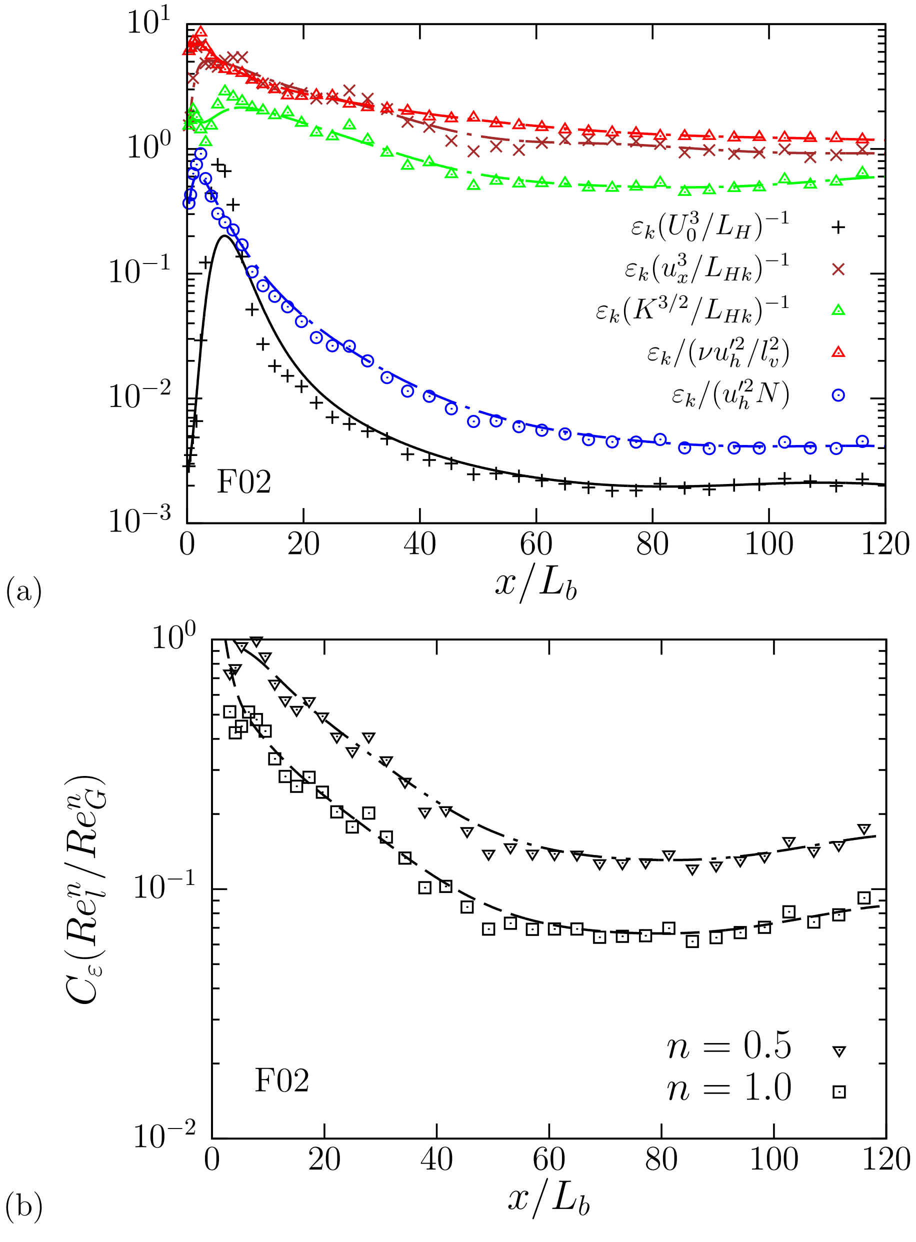

Figure 6.21: The $Fr = 2$ wake. Caption as in figure 6.20.

over a wide range of stratifications: $Fr{=}U_b/NL_b{=}\infty$, 50, 10, and 2.

In the axisymmetric wake at $Fr = \infty$, it is found that the centerline deficit velocity (U_0) does not always scale with the turbulence velocity scale ($K^{1/2}$) contrary to classical theory. The mean flow decays in two stages with a break in slopes at $x/L_b \approx 65$ but no such transition is found for turbulence. The first stage of $10 < x/L_b < 65$ exhibits $U_0 \propto x^{-0.9}$ and $L \propto x^{0.45}$. It is only after $x/L_b \approx 65$ that U_0 exhibits a power law that is close to the high-Re scaling $U_0 \sim K^{1/2} \underset{\sim}{\propto} x^{-2/3}$ and $L \sim L_k \underset{\sim}{\propto} x^{1/3}$. As a result, none of the stratified cases considered here display the $U_0 \propto x^{-2/3}$ scaling in the 3D regime before buoyancy effects set in. It is worth noting that the $x^{-0.9}$ behavior of U_0 in the intermediate stage of the disk wake is similar to the approximately x^{-1} behavior found in the intermediate stage of sphere wakes at $Re = 3700$ by Pal *et al.* (2017), $Re = 10,000$ by Chongsiripinyo *et al.* (2019), fractal-plate wakes at $Re = 5000$ (DNS) and $Re = 50,000$ (laboratory experiment) by Dairay *et al.* (2015).

Stratified wakes evolve practically without being affected by buoyancy until approximately one buoyancy time scale ($Nt_b \approx 1$). At this point, the vertical mean Froude number decreases to and remains at $Fr_V \sim O(1)$ and the stratified wake then enters into a stratified turbulence regime (ST) which can be further subcategorized into 3 regimes: weakly stratified turbulence (WST), intermediately stratified turbulence (IST), and strongly stratified turbulence (SST) depending on the value of turbulent horizontal Froude number $Fr_h = u_h'/NL_{Hk}$. At the entry of the WST stage, $Fr_h = 1$, i.e. the large-eddy lengthscale (L_{Hk}) becomes equal to the Ozmidov lengthscale ($l_o = (\varepsilon_k/N^3)^{1/2}$). As the wake progresses in the WST stage, Fr_h reduces from $O(1)$ to $O(0.1)$ and, while the effect of buoyancy on the mean flow is significant, its effect on turbulence is insignificant. Thus, during WST that spans $1 \lesssim Nt_b \lesssim 5$, the mean flow progressively transitions into the non-equilibrium (NEQ) regime but turbulence remains approximately isotropic ($u_h' \approx u_z'$). A transition towards the next stage of IST takes place at $Fr_h \sim O(0.1)$ in the proximity of $Nt_b \approx 5$.

The IST stage is distinguished by progressively increasing turbulence anisotropy. In IST, while the mean flow has arrived at the NEQ-regime behavior of $U_0 \propto x^{-0.18}$, turbulence is still in transition towards a different regime, namely, SST.

The stratified wake enters into the third stage of SST, demarcated by the value of Fr_v asymptoting to a $O(1)$ value. We find that, at $Fr_h \approx 0.03$ which occurs at $Nt_b \approx 20$, the wake enters the SST regime with $Fr_v \to 0.65$. Indeed, a key feature of the SST regime of stratified flows in general is that buoyancy imposes a vertical length scale, $l_v \propto u'_h/N$, i.e. $Fr_v \to O(1)$ *const* (Billant & Chomaz, 2001), as has been seen in previous simulations of decaying homogeneous turbulence (de Bruyn Kops & Riley, 2019; Maffioli & Davidson, 2016). It is expected that SST lasts as long as the modified Reynolds number, $Re_h Fr_h^2 > 1$ (Riley & deBruynKops, 2003; Brethouwer *et al.*, 2007), which remains true in the F02 wake from $x/D \approx 40$ to the end of the domain at $x/D = 125$. In the SST regime of the wake, turbulence is strongly anisotropic ($u'_z \ll u'_h$) and arrives into the NEQ regime with $u'_h \sim U_0 \propto x^{-0.18}$ while $u'_z \propto x^{-1}$. Furthermore, the SST wake is patchy as inferred from visualizations of fluctuating dissipation rate, and temporal spectra are broadband.

Throughout the IST-SST period, the vertical mean lengthscale (wake height) is naturally selected by the flow so that mean inertial and buoyancy forces remain in balance, $L_V \sim U_0/N$ that yields $Fr_V \approx$ *const*. This leads to the continuous decrease in L_V to accommodate the ongoing U_0 decay. The need to obey conservation of momentum ($U_0 L_H L_V \approx$ *const.*) indicates that the wake width (L_H) is thus indirectly selected by buoyancy as $L_H \propto U_0^{-1} L_V^{-1} \propto U_0^{-2}$. It is worth noting that L_V exhibits a decreasing trend throughout the computational domain indicating that, unlike our prior low-Re simulations, the low-Re effect of viscous diffusion and its concomitant increase of L_V is absent in the present simulations.

It is worth noting that, in the present work, it is L_k and not L that possesses the power law close to the $x^{1/3}$ growth in the unstratified wake and the 3D region of stratified wakes. It is intriguing that the results for power laws satisfied by the mean velocity deficit and horizontal wake width from temporal-model simulations (e.g. Dommermuth *et al.* (2002); Brucker & Sarkar (2010); Diamessis *et al.* (2011)) are similar to power laws in the present work that are based on fluctuation ($\sqrt{K}$) and not mean profiles. A possible reason for the difference in the power laws for U_0 between temporal and body-inclusive simulations is the consequence of a large-scale structure introduced by the body into the wake that is not present in the initial conditions of the temporal simulations.

The present results suggest re-examination of the NEQ regime of stratified wakes. At $Nt_b \approx 1$ that has been taken to be the commencement of the NEQ wake, it is only the mean flow that is sufficiently influenced by buoyancy, i.e. the decay of U_0 is slowed down and the mean-based Froude number (Fr_V) becomes $O(1)$. In other words, L_V becomes $O(U_0/N)$. It is much further downstream, $Nt_b \approx 20$, when the turbulence-based Froude number (Fr_v) becomes $O(1)$, turbulence becomes strongly anisotropic with $u_z' \ll u_h'$, and the decay of turbulence is also reduced so that $u_h' \sim U_0$. The $U_0 \propto x^{-0.18}$ found for the NEQ disk wake is different from the previously found sphere-wake behavior of $U_0 \propto x^{-0.25}$ in the NEQ regime. Further study will be useful to ascertain how the geometry of the wake generator affects the exponent of the U_0 power law in the NEQ region of stratified wakes.

An overall picture of stratified wakes emerges when plotted in phase space. We choose centerline values of $(Re_h Fr_h^2, Fr_h)$ as the phase-space coordinates which is analogous to the study of stratified turbulence in a periodic box by de Bruyn Kops & Riley (2019) who use (Re_b, Fr_h) where Fr_h is defined using the horizontal r.m.s velocity and a horizontal integral length scale. The $Fr = 10$ and 2 wakes at $Re = 50,000$ come close in phase space once they enter ST at $Fr_h = 1$. Therefore, the $Fr = 10$ wake can be expected to access the SST regime at $Fr_h = O(0.01)$ similar to what is found for the $Fr = 2$ wake. The SST regime of the $Fr = 2$ wake commences at $x/L_b \approx 40$ and continues until the end of the domain which is about 85 body diameters away. For a given body Fr, the span of the SST regime is expected to increase with increasing body Re of the wake.

Stratification prolongs the life time of the wake. The mechanisms leading to the preservation of wake mean kinetic energy (MKE) originate in the WST/early-IST stages, where the NEQ regime of the mean flow is being established. In particular, the mean buoyancy flux is positive so that energy is transferred from APE to MKE and, additionally, production of TKE that acts as a sink of MKE is reduced. In the late-IST/SST stages, the decay rate of MKE remains relatively smaller as the production in the late wake remains small in normalized form. The decay rate of turbulent kinetic energy is initially increased in the WST/early-IST stages primarily because of negative buoyancy flux and increased dissipation. It is only later that the direct effect of reduced production sets in to further reduce the TKE. In the late-IST/early-SST stages, not only is production enhanced but also turbulence is energized by the injection from turbulent potential energy. Consequently, the TKE decay slows down similar to the buoyancy-induced slow down of U_0 that had occurred closer to the body. As mean and turbulent buoyancy fluxes are positive during the establishment of the mean and turbulence NEQ regimes, respectively, it is clear that stratification has a direct and positive effect on the prolongation of wake life. Only in the SST stage, does the turbulent buoyancy flux becomes negative, acting as a sink of TKE and to mix the buoyancy field.

The lee-wave induced ‘oscillatory modulation’ of U_0 reported in the DNS of the $Re = 3700$ sphere wake by Pal *et al.* (2017) is a manifestation of the transfer between APE and MKE in the NEQ regime. Oscillatory modulation is found in the present simulations as well showing its importance in the case of a disk as the wake generator as well as at an order of magnitude higher $Re = 50,000$.

In the unstratified wake, it is found that the decay of ε is not consistent with the classical $K^{3/2}/L_k$ scaling but is described better with the non-equilibrium scaling (Vassilicos, 2015) of the form $\varepsilon = C_\varepsilon(K^{3/2}/L_k)$ with $C_\varepsilon = Re^n_{Global}/Re^n_{Local} (\neq \text{const})$. In the $Fr = 2$

wake, the scaling $\varepsilon_k \sim u_h'^2 N$ appears valid as the wake approaches the SST regime in which there is turbulence ($Re_h Fr_h^2 \gtrsim O(1)$) but it is largely controlled by buoyancy.

Further research is required to explore the SST regime of the stratified turbulent wake. Although the SST regime is recognized in the $Fr = 2$ wake, it will be beneficial to further increase the buoyancy Reynolds number. A follow-up study of disk wakes is planned at a larger Re and a smaller Fr, a change that would increase Nt for the same x/L_b and $Re_h Fr_h^2$ for the same value of Nt.

The content of Chapter 6, Chongsiripinyo K. and Sarkar S., "Decay of turbulent wakes behind a disk in homogeneous and stratified fluids", has been submitted for publication in *J. Fluid Mech.* The dissertation author was the primary researcher and author of this paper.

Chapter 7

Conclusions

A series of numerical experiments has been conducted to improve our understanding of the dynamics of turbulent bluff-body wakes subject to density stratification. Body-inclusive simulations capable of naturally depositing deficit momentum into the fluid stream and forming realistic turbulent wakes were performed at intermediate-to-high Reynolds numbers and a wide range of Froude numbers.

Body-inclusive simulation of stratified flow past a bluff-body at $Re \geq O(10^3)$ is relatively new. During the first phase we have explored different tools in order to numerically represent a body, from the generalized-coordinate solver '*Fibre*', an in-house immersed boundary method (IBM) on a cartesian-coordinate system, to the IBM embedded in a cylindrical-coordinate grid using '*Eddy*'. The dissertation focuses on the second phase, presenting physics of stratified turbulent wakes in Chapter3-6. The important conclusions from the second phase of our studies are summarized here.

In Chapter 3, the sphere's wakes at an intermediate Reynolds number and a wide range of Froude number were investigated with the focus on dynamics of vorticity. Direct numerical simulations (DNS) were carried out at $Re = 3700$ and $Fr \in [\infty, 0.025]$. Visualization using the Q criterion reveals that the unstratified instantaneous vortical structures are tube-like and with no directional preference. Vortical structures are altered in their orientation but remain tube-like at moderate stratification, $Fr \sim O(1)$. Structures are flattened and horizontally oriented at stronger stratification, $Fr \leq 0.5$. At $Fr = 0.025$, pancake eddies and surfboard-like inclined structures emerge in the near wake. A new regime is found in strongly-stratified cases with $Fr \leq 0.25$ where enstrophy variance does not monotonically decrease as stratification is increased. Rather, increasing the stratification increases enstrophy variance near the body. This is quantified through the enstrophy transport equation. In the near wake, vortex stretching by fluctuating and mean strain are both responsible for enhancing vorticity. Increasing stratification to $Fr \sim O(1)$ tends to suppress vortex stretching. Upon further reduction of Fr below 0.25, the vortex stretching takes large values near the sphere and, consequently, enstrophy variance in the near wake increases. The increase in vortex stretching is associated with unsteady, intermittent shedding of the boundary layer from the sides of the sphere in highly-stratified wakes with $Fr < 0.25$.

In Chapter 4, $Re = 10^4$ sphere wakes at $Fr = \infty, 3, 1$ were simulated using large eddy simulation (LES) to assess the decay of the characteristic centerline velocity and the evolution of turbulent kinetic energy. ‘Oscillatory modulation’ that reflects the sinusoidal behavior of U_0 caused by the lee-wave pattern created by the sphere at $Re = 3700$ (Pal *et al.*, 2017) is found to occur at $Re = 10^4$ too. The so-called “wake collapse” is simply the first manifestation of the oscillatory modulation during $\pi Fr \leqslant x/D \leqslant 2\pi Fr$. In the non-equilibrium (NEQ) regime, the exponent m in the power law, $U_0 \propto x^m$, is found to be $m = -0.4$. The relative roles of all the terms in the turbulent kinetic energy budget are altered over the entire wake at $Fr = 1$. In particular, the net increase of TKE is concentrated close to the sphere due to the increase in the production and the decrease in the dissipation. The peak production term is significantly increased from the plunging of the shed shear layers towards the centerline. At the point of maximum production, $P/\epsilon \simeq 6$

compared to the unstratified-wake value of 2. However, the alteration of the production and dissipation observed only in the body-inclusive simulation has a short span, and the overall TKE of the $Fr = 1$ wake is smaller than that of the unstratified wake.

In Chapter 5, we revisit the classical self-similarity solutions of unstratified axisymmetric wakes (Tennekes & Lumley, 1972; George, 1989). The power-law exponents, m and n; as in $U_0/U_\infty \propto x^m$ and $\delta/D \propto x^n$; were theoretically found to be $(m_L, n_L) = (-1, 1/2)$ and $(m_H, n_H) = (-2/3, 1/3)$ for low-Re and high-Re wakes. These power laws were obtained from the low-Re ($\varepsilon \sim \nu U_0^2/\delta^2$) or the high-Re ($\varepsilon \sim U_0^3/\delta$) dissipation scaling. Our turbulent wake at $Re_G = UD/\nu = 10^4$ shows that while $(m, n) \approx (-1, 1/2)$, $\varepsilon \propto x^{-5/2}$ in disagreement with the theory. It is found that dissipation can, however, be scaled with the non-equilibrium dissipation scaling (Vassilicos, 2015) of the form $\epsilon = C_\epsilon K^{3/2}/\delta$ with $C_\epsilon = (Re_G/Re_l)^{1/2}$ where the local Reynolds number is taken to be $Re_l = U_0\delta/\nu$.

Lastly, Chapter 6 presents an investigation of the decay of high-Reynolds-number stratified wakes. This final part of the work is a major contribution of the thesis. LES of flow past a disk are performed at $Re = U_b L_b/\nu$=50,000 and at $Fr = U_b/NL_b = \infty$, 50, 10, 2 in a computational domain that extends to 125 disk diameters; here, U_b is the free-stream velocity, L_b is the disk diameter, ν is the fluid kinematic viscosity, and N is the buoyancy frequency. Unlike most other numerical studies of stratified wakes that use a temporal model, body-inclusive spatially-evolving simulations are performed. The evolution of mean flow and turbulence statistics is reported with particular attention to changes as the flow passes through different phases. Budgets of mean and turbulent kinetic energies are analyzed, reasons for the long-lived nature of stratified wakes are advanced, and the scaling of dissipation is discussed.

In the axisymmetric wake at $Fr = \infty$, it is found that the centerline deficit velocity (U_0) does not always scale with the turbulence velocity scale ($K^{1/2}$) contrary to classical theory. The mean flow decays in two stages with a break in slopes at $x/L_b \approx 65$ but no such transition is found for turbulence. The first stage of $10 < x/L_b < 65$ exhibits $U_0 \propto x^{-0.9}$ and $L \propto x^{0.45}$. It is only after $x/L_b \approx 65$ that U_0 exhibits a power law that is close to the high-Re scaling $U_0 \sim K^{1/2} \propto\!\!\!\sim x^{-2/3}$ and $L \sim L_k \propto\!\!\!\sim x^{1/3}$. As a result, none of the stratified cases considered here display the $U_0 \propto x^{-2/3}$ scaling in the 3D regime before buoyancy effects set in. It is worth noting that the $x^{-0.9}$ behavior of U_0 in the intermediate stage of the disk wake is similar to the approximately x^{-1} behavior found in the intermediate stage of sphere wakes at $Re = 3700$ by Pal *et al.* (2017), $Re = 10,000$ by Chongsiripinyo *et al.* (2019), fractal-plate wakes at $Re = 5000$ (DNS) and $Re = 50,000$ (laboratory experiment) by Dairay *et al.* (2015).

Stratified wakes evolve practically without being affected by buoyancy until approximately one buoyancy time scale ($Nt_b \approx 1$). At this point, the vertical mean Froude number decreases to and remains at $Fr_V \sim O(1)$ and the stratified wake then enters into a stratified turbulence regime (ST) which can be further subcategorized into 3 regimes: weakly stratified turbulence (WST), intermediately stratified turbulence (IST), and strongly stratified turbulence (SST) depending on the value of turbulent horizontal Froude number $Fr_h = u'_h/NL_{Hk}$. At the entry of the WST stage, $Fr_h = 1$, i.e. the large-eddy lengthscale (L_{Hk}) becomes equal to the Ozmidov lengthscale ($l_o = (\varepsilon_k/N^3)^{1/2}$). As the wake progresses in the WST stage, Fr_h reduces from $O(1)$ to $O(0.1)$ and, while the effect of buoyancy on the mean flow is significant, its effect on turbulence is insignificant. Thus, during WST that spans $1 \lesssim Nt_b \lesssim 5$, the mean flow progressively transitions into the non-equilibrium (NEQ) regime but turbulence remains approximately isotropic ($u'_h \approx u'_z$). A transition towards the next stage of IST takes place at $Fr_h \sim O(0.1)$ in the proximity of $Nt_b \approx 5$. The IST stage is distinguished by progressively increasing turbulence anisotropy. In IST, while the mean flow has arrived at the NEQ-regime behavior of $U_0 \propto x^{-0.18}$, turbulence is still in transition towards a different regime, namely, SST.

The stratified wake enters into the third stage of SST, demarcated by the value of

Fr_v asymptoting to a $O(1)$ value. We find that, at $Fr_h \approx 0.03$ which occurs at $Nt_b \approx 20$, the wake enters the SST regime with $Fr_v \to 0.65$. Indeed, a key feature of the SST regime of stratified flows in general is that buoyancy imposes a vertical length scale, $l_v \propto u'_h/N$, i.e. $Fr_v \to O(1)$ *const* (Billant & Chomaz, 2001), as has been seen in previous simulations of decaying homogeneous turbulence (de Bruyn Kops & Riley, 2019; Maffioli & Davidson, 2016). It is expected that SST lasts as long as the modified Reynolds number, $Re_h Fr_h^2 > 1$ (Riley & deBruynKops, 2003; Brethouwer *et al.*, 2007), which remains true in the F02 wake from $x/D \approx 40$ to the end of the domain at $x/D = 125$. In the SST regime of the wake, turbulence is strongly anisotropic ($u'_z \ll u'_h$) and arrives into the NEQ regime with $u'_h \sim U_0 \propto x^{-0.18}$ while $u'_z \propto x^{-1}$. Furthermore, the SST wake is patchy as inferred from visualizations of fluctuating dissipation rate, and temporal spectra are broadband.

Throughout the IST-SST period, the vertical mean lengthscale (wake height) is naturally selected by the flow so that mean inertial and buoyancy forces remain in balance, $L_V \sim U_0/N$ that yields $Fr_V \approx$ *const.* This leads to the continuous decrease in L_V to accommodate the ongoing U_0 decay. The need to obey conservation of momentum ($U_0 L_H L_V \approx$ *const.*) indicates that the wake width (L_H) is thus indirectly selected by buoyancy as $L_H \propto U_0^{-1} L_V^{-1} \propto U_0^{-2}$. It is worth noting that L_V exhibits a decreasing trend throughout the computational domain indicating that, unlike our prior low-Re simulations, the low-Re effect of viscous diffusion and its concomitant increase of L_V is absent in the present simulations.

It is worth noting that, in the present work, it is L_k and not L that possesses the power law close to the $x^{1/3}$ growth in the unstratified wake and the 3D region of stratified wakes. It is intriguing that the results for power laws satisfied by the mean velocity deficit and horizontal wake width from temporal-model simulations (e.g. Dommermuth *et al.* (2002); Brucker & Sarkar (2010); Diamessis *et al.* (2011)) are similar to power laws in the present work that are based on fluctuation ($\sqrt{K}$) and not mean profiles. A possible reason for the difference in the power laws for U_0 between temporal and body-inclusive simulations is the consequence of a large-scale structure introduced by the body into the wake that is not present in the initial conditions of the temporal simulations.

The present results suggest re-examination of the NEQ regime of stratified wakes. At $Nt_b \approx 1$ that has been taken to be the commencement of the NEQ wake, it is only the mean flow that is sufficiently influenced by buoyancy, i.e. the decay of U_0 is slowed down and the mean-based Froude number (Fr_V) becomes $O(1)$. In other words, L_V becomes $O(U_0/N)$. It is much further downstream, $Nt_b \approx 20$, when the turbulence-based Froude number (Fr_v) becomes $O(1)$, turbulence becomes strongly anisotropic with $u'_z \ll u'_h$, and the decay of turbulence is also reduced so that $u'_h \sim U_0$. The $U_0 \propto x^{-0.18}$ found for the NEQ disk wake is different from the previously found sphere-wake behavior of $U_0 \propto x^{-0.25}$ in the NEQ regime. Further study will be useful to ascertain how the geometry of the wake generator affects the exponent of the U_0 power law in the NEQ region of stratified wakes.

An overall picture of stratified wakes emerges when plotted in phase space. We choose centerline values of $(Re_h Fr_h^2, Fr_h)$ as the phase-space coordinates which is analogous to the study of stratified turbulence in a periodic box by de Bruyn Kops & Riley (2019) who use (Re_b, Fr_h) where Fr_h is defined using the horizontal r.m.s velocity and a horizontal integral length scale. The $Fr = 10$ and 2 wakes at $Re = 50,000$ come close in phase space once they enter ST at $Fr_h = 1$. Therefore, the $Fr = 10$ wake can be expected to access the SST regime at $Fr_h = O(0.01)$ similar to what is found for the $Fr = 2$ wake. The SST regime of the $Fr = 2$ wake commences at $x/L_b \approx 40$ and continues until the end of the domain which is about 85 body diameters away. For a given body Fr, the span of the SST regime is expected to increase with increasing body Re of the wake.

Stratification prolongs the life time of the wake. The mechanisms leading to the preservation of wake mean kinetic energy (MKE) originate in the WST/early-IST stages, where the NEQ regime of the mean flow is being established. In particular, the mean buoyancy flux is positive so that energy is transferred from APE to MKE and, additionally, production of TKE that acts as a sink of MKE is reduced. In the late-IST/SST stages, the decay rate of MKE remains relatively smaller as the production in the late wake remains small in normalized form. The decay rate of turbulent kinetic energy is initially increased in the WST/early-IST stages primarily because of negative buoyancy flux and increased dissipation. It is only later that the direct effect of reduced production sets in to further reduce the TKE. In the late-IST/early-SST stages, not only is production enhanced but also turbulence is energized by the injection from turbulent potential energy. Consequently, the TKE decay slows down similar to the buoyancy-induced slow down of U_0 that had occurred closer to the body. As mean and turbulent buoyancy fluxes are positive during the establishment of the mean and turbulence NEQ regimes, respectively, it is clear that stratification has a direct and positive effect on the prolongation of wake life. Only in the SST stage, does the turbulent buoyancy flux becomes negative, acting as a sink of TKE and to mix the buoyancy field.

The lee-wave induced 'oscillatory modulation' of U_0 reported in the DNS of the $Re = 3700$ sphere wake by Pal *et al.* (2017) is a manifestation of the transfer between APE and MKE in the NEQ regime. Oscillatory modulation is found in the present simulations as well showing its importance in the case of a disk as the wake generator as well as at an order of magnitude higher $Re = 50,000$.

In the unstratified wake, it is found that the decay of ε is not consistent with the classical $K^{3/2}/L_k$ scaling but is described better with the non-equilibrium scaling (Vassilicos, 2015) of the form $\varepsilon = C_\varepsilon(K^{3/2}/L_k)$ with $C_\varepsilon = Re^n_{Global}/Re^n_{Local}(\neq \text{const})$. In the $Fr = 2$ wake, the scaling $\varepsilon_k \sim u_h'^2 N$ appears valid as the wake approaches the SST regime in which there is turbulence ($Re_h Fr_h^2 \gtrsim O(1)$) but it is largely controlled by buoyancy.

Appendix A

A brief description of *Eddy*

All of the simulations presented in this dissertation were performed using '*Eddy*', a parallelized computational code written in FORTRAN 77/90. *Eddy* was first developed in 1993 by Elias Balaras. Over the past two decades, new features have been added, e.g., subgrid viscosity models for performing Large-*Eddy* Simulations (LES) and the Immersed Boundary Method (IBM). *Eddy* solves the governing equations in parallel using either a cartesian or a cylindrical coordinate system with one-dimensional domain decomposition. The ability to use IBM on a cylindrical coordinate grid together with the robust dynamic Smagorinsky model is attractive for simulating the high-Re turbulent wake behind an axisymmetric body such as a sphere or disk. The boundary layer on an axisymmetric body can then be well captured using a minimal number of grid points in contrast to IBM/Cartesian-system combinations such as de Stadler (2013) and Rapaka & Sarkar (2016). For density-stratified flow, the convection-diffusion equation for density transport was incorporated into *Eddy*. The following sections briefly summarize numerical algorithms used by *Eddy* in the preceding simulations.

A.1 Governing equations

The Eulerian representation of unsteady viscous flow for a Newtonian fluid can be described using the following governing equations in a cartesian coordinate system. For Boussinesq fluid, density variation enters the Navier-Stokes equations only through the buoyancy term. The incompressible Navier-Stokes momentum equation is given by

$$\frac{\partial u_i}{\partial t} + u_j \frac{\partial u_i}{\partial x_j} = -\frac{1}{\rho_0}\frac{\partial p}{\partial x_i} + \nu \frac{\partial^2 u_i}{\partial x_j \partial x_j} - \frac{\rho}{\rho_0} g \delta_{i3}. \tag{A.1}$$

Incompressibility is imposed by the volumn constraint

$$\frac{\partial u_i}{\partial x_i} = 0. \tag{A.2}$$

The convection-diffusion density transport equation is given by

$$\frac{\partial \rho}{\partial t} + u_j \frac{\partial \rho}{\partial x_j} = \kappa \frac{\partial^2 \rho}{\partial x_j \partial x_j}. \tag{A.3}$$

Turbulent flow contains a wide range of scales where the ratio of the smallest to largest length scales is of the order inversely proportional to $Re^{3/4}$. LES takes advantage of the idea, specifically Kolmogorov's second similarity hypothesis (Kolmogorov (1941)) that at sufficiently high Reynolds number, the statistics of the motions of scale l in the range $l_o \ll l \ll \eta$ have a universal form that is uniquely determined by ε independent of ν (Pope (2000)). In LES, sub-grid l-scale dynamics is modeled whereas larger-scale motions are directly solved. Depending on the choice of grid size, this can significantly reduce the computational power required to capture small-scale motions. Virtually all LES models utilize Kolmogorov's hypothesis of local isotropy in which the small-scale turbulent motions are statistically isotropic. By applying a spatial filter (~) to the governing equations (A.1)-(A.3), we obtain the following set of equations.

$$\frac{\partial \widetilde{u}_i}{\partial t} + \widetilde{u}_j \frac{\partial \widetilde{u}_i}{\partial x_j} = -\frac{1}{\rho_0}\frac{\partial \widetilde{p}}{\partial x_i} + \nu \frac{\partial^2 \widetilde{u}_i}{\partial x_j \partial x_j} - \frac{\widetilde{\rho}}{\rho_0} g \delta_{i3} - \frac{\partial \tau_{ij}}{\partial x_j} \tag{A.4}$$

$$\frac{\partial \widetilde{u}_i}{\partial x_i} = 0 \tag{A.5}$$

$$\frac{\partial \widetilde{\rho}}{\partial t} + \widetilde{u}_j \frac{\partial \widetilde{\rho}}{\partial x_j} = \kappa \frac{\partial^2 \widetilde{\rho}}{\partial x_j \partial x_j} - \frac{\partial \lambda_i}{\partial x_i} \tag{A.6}$$

The stress tensor, τ_{ij}=$\widetilde{u_i u_j}$-$\widetilde{u}_i \widetilde{u}_j$, represents the contribution of stresses from small-scale motion acting on the filtered velocity field. Analogously, λ_i=$\widetilde{u_i \rho}$-$\widetilde{u}_i \widetilde{\rho}$ represents small-scale density flux acting on the filtered density field.

A.2 Subgrid viscosity

To model the stress tensor τ_{ij}, the dynamic subgrid-scale eddy viscosity model of Germano *et al.* (1991), and later Lilly (1992), is employed. The advantage of modeling small scales with the approach of Germano *et al.* (1991) over Smagorinsky (1963) is its use of information available at the resolved scales. In essence, the method derives the subgrid tensor from its relation with the additional stress tensor obtained using a larger spatial filter (the so-called two test filter approach). Consider the following equation,

$$\frac{\partial u_i}{\partial t} + \frac{\partial u_i u_j}{\partial x_j} = \mathrm{R}_i. \tag{A.7}$$

Applying the first filter (level 1: $\widetilde{\square}$) gives,

$$\frac{\partial \widetilde{u}_i}{\partial t} + \frac{\partial \widetilde{u}_i \widetilde{u}_j}{\partial x_j} = \widetilde{R}_i - \frac{\partial \tau_{ij}}{\partial x_j}. \tag{A.8}$$

Applying the second filter (level 2: $\widehat{\square}$) to (A.8) and letting $L_{ij} = \widehat{\widetilde{u}_i \widetilde{u}_j} - \widehat{\widetilde{u}}_i \widehat{\widetilde{u}}_j$,

$$\frac{\partial \widehat{\widetilde{u}}_i}{\partial t} + \frac{\partial \widehat{\widetilde{u}}_i \widehat{\widetilde{u}}_j}{\partial x_j} = \widehat{\widetilde{\mathrm{R}}}_i - \frac{\partial \widehat{\tau}_{ij}}{\partial x_j} - \frac{\partial L_{ij}}{\partial x_j}. \tag{A.9}$$

The following Germano identity relates the subfilter stress tensor at the second filter level, T_{ij}, to quantities available at the first filter level, $\widetilde{u}_i$,

$$L_{ij} = T_{ij} - \widehat{\tau}_{ij} = \widehat{\widetilde{u}_i \widetilde{u}_j} - \widehat{\widetilde{u}}_i \widehat{\widetilde{u}}_j. \tag{A.10}$$

Apparently, L_{ij} represents the difference between the two stress tensors. Introducing the eddy viscosity model for the subfilter stresses at both filter levels yields

$$\tau_{ij} - \frac{1}{3}\delta_{ij}\tau_{kk} = -2\nu_t \widetilde{S}_{ij} = -2C_\tau \widetilde{\Delta}^2 |\widetilde{S}| \widetilde{S}_{ij}, \tag{A.11}$$

and

$$T_{ij} - \frac{1}{3}\delta_{ij}T_{kk} = -2\nu_T \widehat{\widetilde{S}}_{ij} = -2C_T \widehat{\widetilde{\Delta}}^2 |\widehat{\widetilde{S}}| \widehat{\widetilde{S}}_{ij}. \tag{A.12}$$

Substituting (A.11) and (A.12) into (A.10) gives

$$L_{ij} - \frac{1}{3}\delta_{ij}L_{kk} = -2\widetilde{\Delta}^2[(\widehat{\widetilde{\Delta}}/\widetilde{\Delta})^2 C_T |\widehat{\widetilde{S}}| \widehat{\widetilde{S}}_{ij} - \widehat{C_\tau |\widetilde{S}| \widetilde{S}_{ij}}]. \tag{A.13}$$

Let $C_T = C_\tau = C$. Generally, the variable C is assumed to be a weak function in space and can be taken out of the second filter operation, $\widehat{\Box}$. By introducing M_{ij},

$$M_{ij} = \widetilde{\Delta}^2[(\widehat{\widetilde{\Delta}}/\widetilde{\Delta})^2|\widehat{\widetilde{S}}|\widehat{\widetilde{S}}_{ij} - \widehat{|\widetilde{S}|\widetilde{S}_{ij}}]. \tag{A.14}$$

(A.13) can be abbreviated to

$$L_{ij} - \frac{1}{3}\delta_{ij}L_{kk} = -2CM_{ij}. \tag{A.15}$$

In determining the subgrid viscosity, $\nu_t = C\widetilde{\Delta}^2|\widetilde{S}|$, the only unknown variable C is solved using the least-square method proposed by Lilly (1992),

$$C = -\frac{1}{2}\frac{L_{ij}M_{ij}}{M_{ij}M_{ij}}. \tag{A.16}$$

The subgrid viscosity is thus obtained from

$$\nu_t = \frac{\langle L_{ij}M_{ij}\rangle}{\langle M_{ij}M_{ij}\rangle}\widetilde{\Delta}^2|\widetilde{S}|. \tag{A.17}$$

Here, $\langle\Box\rangle$ is an appropriate averaging. The variable C is calculated using Lagrangian averaging (as in Meneveau *et al.* (1996)) over fluid pathlines to avoid the possibility of C becoming locally negative. The present study sets the ratio between the second and first level filters, $\widehat{\widetilde{\Delta}}/\widetilde{\Delta}$, to be $\sqrt{6}$ as set forth by Lund (1997). Spatial filtering is simply done using a box-filter routine with the trapezodial rule for non-uniform grids.

The final form of the filtered non-dimensional governing equations can be written in a cartesian coordinate system as follows:

$$\frac{\partial \widetilde{u}_i}{\partial x_i} = 0 \tag{A.18}$$

$$\frac{\partial \widetilde{u}_i}{\partial t} + \widetilde{u}_j \frac{\partial \widetilde{u}_i}{\partial x_j} = -\frac{\partial \widetilde{p}}{\partial x_i} + \frac{1}{Re}\left(1 + \frac{\nu_s}{\nu}\right)\frac{\partial^2 \widetilde{u}_i}{\partial x_j \partial x_j} - \frac{1}{Fr^2}\widetilde{\rho}\delta_{i3} \tag{A.19}$$

$$\frac{\partial \widetilde{\rho}}{\partial t} + \widetilde{u}_j \frac{\partial \widetilde{\rho}}{\partial x_j} = \frac{1}{RePr}\left(1 + \frac{\kappa_s}{\kappa}\right)\frac{\partial^2 \widetilde{\rho}}{\partial x_j \partial x_j}, \tag{A.20}$$

where the relevant non-dimensional parameters are the Reynolds number, $Re = UD/\nu$, the Prandtl number, $Pr = \nu/k$, and the Froude number, $Fr = U/(ND)$. Here, U and D are characteristic velocity and lengthscale, N being the buoyancy frequency. There is an important assumption from which the subgrid diffusivity is determined. The large-eddy simulations performed in this work assume that the subgrid Prandtl number, ν_s/κ_s, is unity and therefore, κ_s is replaced by $\nu_s/1$. The non-dimensional filtered governing equations in a cylindrical coordinate system used in the simulations in chapter 4 and 6 are written as follows:

$$\frac{1}{r}\frac{\partial r\widetilde{u}_r}{\partial r} + \frac{1}{r}\frac{\partial \widetilde{u}_\theta}{\partial \theta} + \frac{\partial \widetilde{u}_x}{\partial x} = 0 \tag{A.21}$$

$$\begin{aligned}\frac{\partial \widetilde{u}_r}{\partial t} + (\vec{\widetilde{u}} \cdot \nabla)\widetilde{u}_r - \frac{u_\theta^2}{r} &= -\frac{\partial p}{\partial r} - \frac{1}{Fr^2}\widetilde{\rho}\hat{e}_r \cdot \hat{e}_z \\ &+ \frac{1}{Re}\left(1 + \frac{\nu_s}{\nu}\right)\left(\nabla^2 \widetilde{u}_r - \frac{\widetilde{u}_r}{r^2} - \frac{2}{r^2}\frac{\partial \widetilde{u}_\theta}{\partial \theta}\right)\end{aligned} \tag{A.22}$$

$$\begin{aligned}\frac{\partial \widetilde{u}_\theta}{\partial t} + (\vec{\widetilde{u}} \cdot \nabla)\widetilde{u}_\theta + \frac{\widetilde{u}_r \widetilde{u}_\theta}{r} &= -\frac{1}{r}\frac{\partial p}{\partial r} - \frac{1}{Fr^2}\widetilde{\rho}\hat{e}_\theta \cdot \hat{e}_z \\ &+ \frac{1}{Re}\left(1 + \frac{\nu_s}{\nu}\right)\left(\nabla^2 \widetilde{u}_\theta - \frac{\widetilde{u}_\theta}{r^2} + \frac{2}{r^2}\frac{\partial \widetilde{u}_r}{\partial \theta}\right)\end{aligned} \tag{A.23}$$

$$\frac{\partial \widetilde{u}_x}{\partial t} + (\vec{\widetilde{u}} \cdot \nabla)\widetilde{u}_x = -\frac{\partial p}{\partial x} + \frac{1}{Re}\left(1 + \frac{\nu_s}{\nu}\right)\nabla^2 \widetilde{u}_x - \frac{1}{Fr^2}\widetilde{\rho}\hat{e}_x \cdot \hat{e}_z \tag{A.24}$$

$$\frac{\partial \widetilde{\rho}}{\partial t} + (\vec{u} \cdot \nabla)\widetilde{\rho} = \frac{1}{RePr}\left(1 + \frac{\kappa_s}{\kappa}\right)\nabla^2 \widetilde{\rho} \tag{A.25}$$

where:

$$\vec{u} \cdot \nabla = u_r \frac{\partial}{\partial r} + \frac{u_\theta}{r}\frac{\partial}{\partial \theta} + u_x \frac{\partial}{\partial x} \quad \text{and} \quad \nabla^2 = \frac{1}{r}\frac{\partial}{\partial r}\left(r\frac{\partial}{\partial r}\right) + \frac{1}{r^2}\frac{\partial^2}{\partial \theta^2} + \frac{\partial^2}{\partial x^2} \tag{A.26}$$

A.3 Numerical methods

A.3.1 Spatial and temporal discretizations

For the turbulent wake behind an axisymmetric body, a cylindrical coordinate system is chosen over the cartesian coordinate system to reserve a sufficient number of grid points for resolving the boundary layer around the body. In using a cylindrical grid, the spatial discretization near the axis and the aspect ratios between azimuthal grid size and the other two directions can pose challenges. This section briefly describes numerical approaches for spatial and temporal discretizations including methods used to overcome such challenges. Derivative terms in the governing equations, (A.22) - (A.25) are spatially discretized using the standard second-order, central finite difference on a staggered grid, in which each component of velocity is located on the cell face respective to its direction while pressure and density are stored at the cell center. Along the axis ($r = 0$), a radial component of velocity, u_r, is obtained by interpolation from both sides ($u_r|_{\theta=0}$ and $u_r|_{\theta=\pi}$) where required. The spatially discretized equations are then discretized in time using a combination of explicit/implicit schemes.

A severe timestep constraint due to the small grid size in the azimuthal direction near the axis is overcome by temporally marching the azimuthal direction implicitly using the second-order Crank-Nicholson (CN2) scheme for both advection and diffusion terms. The other two directions are marched explicitly using the third-order Runge-Kutta (RK3) scheme. A detailed description of each scheme on a generalized curvilinear coordinate is given in Appendix B.

To concurrently solve the governing equations, *Eddy* employs one-dimensional domain decomposition. In the present study, parallelization in the streamwise direction has many advantages. First, the discretized system of governing equations is, in our case, not ‘stiff’ in the streamwise direction. If, however, there was to implicitly march the convection and diffusion terms in the streamwise direction, the performance of the code would be impractical. This is due to the fact that a pipeline algorithm is required to solve the tridiagonal matrix across multiple processor. Implicit marching is only required in the azimuthal direction where the tridiagonal matrix constructed during the predictor step is occupied by a single processor. Second, parallelization in one direction simplifies processor topology and thus reduces computational overhead. Third, the fact that the azimuthal direction is not decomposed allows for fast execution of Fourier transforms without non-local communications among processors. This allows us to efficiently solve for pressure correction without using a multigrid method.

A.3.2 Poisson equation

The present simulations use the fractional step method where one first solves for predicted (or intermediate) velocity using the mix explicit/implicit temporal marching scheme. This is followed by the correction step in which incompressibility is imposed by use of a pressure correction on the predicted velocity. The pressure equation is of type Poisson, constructed by taking the divergence of the governing Navier-Stokes equations. Since correction must be done after velocity prediction at the end of each RK3 substep, performance of the code is highly dependent on how fast one solves the Poisson equation. To address this challenge, *Eddy* takes advantage of the undecomposed azimuthal domain by transforming the Poisson equation into azimuthal Fourier modes. This results in a discretized Poisson equation with 5-point stencils. The resulting pentadiagonal system for each azimuthal wave number can then be solved directly without using an iterative method. The following elaboration is adapted from Chapter 2.3 of Yang (2005) which describes how *Eddy* handles the Poisson equation.

Consider the Poisson equation

$$\nabla^2\phi = f, \tag{A.27}$$

written in the discretized form on cylindrical coordinates as

$$\left[\frac{1}{r}\frac{\delta}{\delta r}\left(r\frac{\delta}{\delta r}\right) + \frac{1}{r^2}\frac{\delta^2}{\delta^2\theta} + \frac{\delta^2}{\delta^2 z}\right]\phi_{i,j,k} = f_{i,j,k}. \tag{A.28}$$

r, θ, and z denote respectively radial, azimuthal, and streamwise directions. Here, the solution procedure in cylindrical coordinates is discussed as the equation for cartesian coordinates is recovered when r in (A.28) is set to unity. Discretizing (A.28) yields

$$\begin{aligned}
&+\frac{1}{r^p_i(r^p_{i+1/2}-r^p_{i-1/2})}\left[r^p_{i+1/2}\left(\frac{\phi_{i+1,j,k}-\phi_{i,j,k}}{r^p_{i+1}-r^p_i}\right) - r^p_{i-1/2}\left(\frac{\phi_{i,j,k}-\phi_{i-1,j,k}}{r^p_i-r^p_{i-1}}\right)\right]\\
&+\frac{1}{r^{p2}_i(\theta^p_{j+1/2}-\theta^p_{j-1/2})}\left[\left(\frac{\phi_{i,j+1,k}-\phi_{i,j,k}}{\theta^p_{j+1}-\theta^p_j}\right) - \left(\frac{\phi_{i,j,k}-\phi_{i,j-1,k}}{\theta^p_j-\theta^p_{j-1}}\right)\right]\\
&+\frac{1}{z^p_{k+1/2}-z^p_{k-1/2}}\left[\left(\frac{\phi_{i,j,k+1}-\phi_{i,j,k}}{z^p_{k+1}-z^p_k}\right) - \left(\frac{\phi_{i,j,k}-\phi_{i,j,k-1}}{z^p_k-z^p_{k-1}}\right)\right]\\
&=f_{i,j,k}.
\end{aligned} \tag{A.29}$$

The superscript p as in $\Box^p$ denotes that $\Box$ is located at the same location as pressure (at cell center). Because variables are stored on the staggered grid system, $r^p_{i+1/2}$ can also be written as r^u_i or $r^p_{j-1/2}$ as r^v_{j-1}. Equation (A.29) can otherwise be rewritten using the following coordinate transformations

$$\xi = \frac{2\Delta\xi}{r_{i+1} - r_{i-1}}, \quad \eta = \frac{2\Delta\eta}{\theta_{j+1} - \theta_{j-1}}, \quad \zeta = \frac{2\Delta\zeta}{z_{k+1} - z_{k-1}}, \tag{A.30}$$

where $\Delta\xi$, $\Delta\eta$, and $\Delta\zeta$ are mapped computational grid sizes arbitrarily chosen to be of size 1. Equation (A.29) is abbreviated as

$$\begin{aligned}
&+\frac{1}{r_i^p}\xi_i^p\frac{1}{\Delta\xi^2}\left[r_i^u\xi_i^u(\phi_{i+1,j,k} - \phi_{i,j,k}) - r_{i-1}^u\xi_{i-1}^u(\phi_{i,j,k} - \phi_{i-1,j,k})\right]\\
&+\frac{1}{r_i^{p2}}\eta_j^p\frac{1}{\Delta\eta^2}\left[\eta_j^v(\phi_{i,j+1,k} - \phi_{i,j,k}) - \eta_{j-1}^v(\phi_{i,j,k} - \phi_{i,j-1,k})\right]\\
&+\zeta_k^p\frac{1}{\Delta\zeta^2}\left[\zeta_k^w(\phi_{i,j,k+1} - \phi_{i,j,k}) - \zeta_{k-1}^w(\phi_{i,j,k} - \phi_{i,j,k-1})\right]\\
&=f_{i,j,k}.
\end{aligned} \tag{A.31}$$

Rearranging (A.31) gives a 7-point stencils set of equation

$$\begin{aligned}
&am_i\phi_{i-1,j,k} + bm_i\phi_{i,j,k} + cm_i\phi_{i+1,j,k}\\
&+ al_j\phi_{i,j-1,k} + bl_j\phi_{i,j,k} + cl_j\phi_{i,j+1,k}\\
&+ an_k\phi_{i,j,k-1} + bn_k\phi_{i,j,k} + cn_k\phi_{i,j,k+1} = f_{i,j,k},
\end{aligned} \tag{A.32}$$

where $am_i = (\Delta\xi^2 r_i^p)^{-1}\xi_i^p r_{i-1}^u\xi_{i-1}^u$, $bm_i = -am_i - cm_i$, $cm_i = (\Delta\xi^2 r_i^p)^{-1}\xi_i^p r_i^u\xi_i^u$, $al_j = (\Delta\eta^2 r_i^{p2})^{-1}\eta_j^p\eta_{j-1}^v$, $bl_j = -al_j - cl_j$, $cl_j = (\Delta\eta^2 r_i^{p2})^{-1}\eta_j^p\eta_j^v$, $an_k = (\Delta\zeta^2)^{-1}\zeta_k^p\zeta_{k-1}^w$, $bn_k = -an_k - cn_k$, $cn_k = (\Delta\zeta^2)^{-1}\zeta_k^p\zeta_k^w$. An iterative method can be used to solve the set of equation (A.32) but, again, iteratively converging the solution of the Poisson equation is known to likely be a bottleneck when it comes to computational performance even with multigrid acceleration.

Fourier tranformation of (A.27) in the azimuthal direction yields a set of two-dimensional Helmholtz equations in the uncoupled wave number space,

$$\left[\frac{1}{r}\frac{\delta}{\delta r}\left(r\frac{\delta}{\delta r}\right)+\frac{\delta^2}{\delta^2 z}+\frac{1}{r^2}k_l'\right]\hat{\phi}_{i,j,l}=\hat{f}_{i,l,k}, \tag{A.33}$$

with the modified wave number k_l' defined as

$$k_l'=\frac{2}{\Delta\theta^2}\left[1-cos\left(\frac{2\pi l}{N_\theta}\right)\right]. \tag{A.34}$$

Here, l is the wave number, N_θ is the number of grid cells in the θ direction excluding ghost cells and $\Delta\theta$ is the cell size in the θ direction. (A.32) can be rewritten as

$$\begin{aligned} am_i\hat{\phi}_{i-1,l,k}+\left(bm_i-\frac{k_l'}{r_i^{p2}}\right)\hat{\phi}_{i,l,k}+cm_i\hat{\phi}_{i+1,l,k} \\ +an_k\hat{\phi}_{i,l,k-1}+bn_k\hat{\phi}_{i,l,k}+cn_k\hat{\phi}_{i,l,k+1}=\hat{f}_{i,l,k}. \end{aligned} \tag{A.35}$$

which can be solved separately for each wave number.

The real-number forward fast Fourier transform RFFTF routine from the FFTPACK library (Swarztrauber (1984)) is used for the forward transformation $f_{i,j,k}\rightarrow\hat{f}_{i,l,k}$. Then, the pentadiagonal system (A.35) for each wave number is directly solved for $\hat{\phi}$, using the BLKTRI routine with a generalized cyclic reduction algorithm (Swarztrauber (1974)). The major advantage of solving (A.35) directly is, again, that the solution is converged to machine accuracy with only one iteration, a great saving when compared with iterative solvers. Afterwards, the subroutine RFFTB from the FFTPACK library is used for the backward transformation $\hat{\phi}_{i,j,k}\rightarrow\phi_{i,l,k}$. Note that to be able to utilize the subroutines from FFTPACK, the computational grid must be uniform in the direction in which the fast Fourier transform (FFT) is performed.

In cases where periodic boundary conditions are used in both streamwise and spanwise directions, an FFT is also applied in the streamwise direction, and the resulting series of (cyclic) tridiagonal equations are solved using the (cyclic) tridiagonal system solver from *Numerical Recipes* (Press (1992)).

A.3.3 Immersed boundary method

In order to represent a solid body in a computational domain, the immersed boundary method (IBM) of Yang & Balaras (2006); Balaras (2004) is used. The advantage of using the immersed boundary method is its ability to embed a complex geometry into the computational domain. More importantly, one can avoid the use of a generalized curvilinear coordinate system that involves coordinate transformation leading to mixed derivatives that typically require a larger stencil. In practice, even though an increase in stencil size does not necessarily impact a computational speed, given that neighboring variables are usually stored together in memory space, it can cause a significant overhead if any reside non-locally. This section summarizes how the immersed boundary method works.

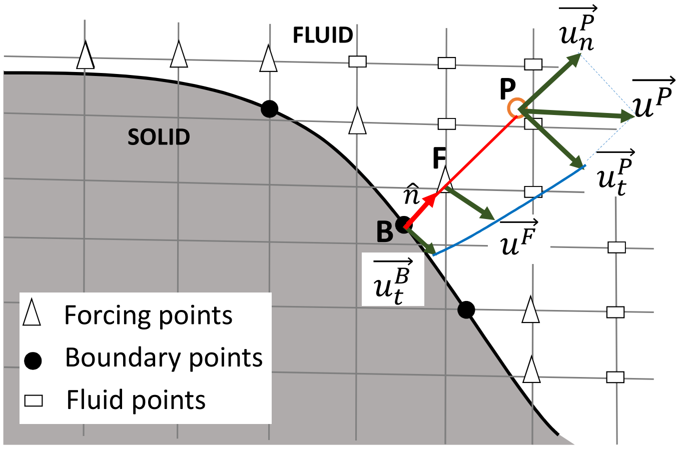

Figure A.1: Generalized interpolation stencil used in IBM for implementing appropriate boundary condition on the forcing points. Here, B is the boundary point, F represents the forcing point and P is the interpolation point. BF line segment is normal to the fluid-solid interface.

Consider a two-dimensional computational domain that contains an interface separating a solid body and fluid such as the one shown in Figure A.1. We first give definitions for grid points residing in different parts of the domain. The grid points inside the body are the 'solid points'. 'Fluid points' are located outside of the body. 'Forcing points' are fluid points in the vicinity of the interface boundary. Here, 'in the vicinity' means that a forcing point has at least one solid point as its neighbor. A 'boundary point' is identified on the interface where its distance to the nearest forcing point is minimal. A collection of 'marker points', read from the input file, defines the solid boundary. All simulations performed in the present work identify these points only at the beginning because the bodies, relative to the grids, are stationary. Readers are encouraged to consult Yang & Balaras (2006) regarding the process of identifying these points.

The idea behind an IBM method is to add a forcing term to the equations that govern fluid motion at a forcing point. The forcing term behaves similarly to how fluid at the forcing point perceives the influence from the interface. In the present study, fluid grids are designed such that points are concentrated near the bodies so that forcing points are inside the boundary layers. The forcing amplitude is estimated as follows. First, we draw a straight line connecting the forcing point (F) and its corresponding boundary point (B). Second, this straight line is then extended away from the boundary until it reaches the point (P) where all neighbors are fluid points. The distance between P and B is arbitrarily set. Third, we obtain velocity at point P by straight-forward weight-averaged interpolation from its neighbors. Finally, tangential velocity (to the interface) at the forcing point F is obtained from weight-averaged interpolation between the tangential velocity at point P and that of point B. The additional term thus forces fluid velocity at the forcing point towards the desired value.

Solving the governing equations with the IBM forcing term is done by estimating an artificial forcing for each forcing node using predicted velocity rather than velocity at a current step. Consider the following equation on the domain Ω for an immediate velocity

$\vec{u}^*$:

$$\frac{\vec{u}^* - \vec{u}^n}{\Delta t} = \frac{3}{2}H(\vec{u}^n) - \frac{1}{2}H(\vec{u}^n) + \frac{\delta p^n}{\delta \vec{x}} + \vec{f}^{n+1} \tag{A.36}$$

where the operator H contains the convective, viscous and subgrid stress terms. On forcing points Ψ, the forcing is calculated from

$$\vec{f}^{n+1} = \frac{\vec{u}^\psi - \vec{u}^n}{\Delta t} - \frac{3}{2}H(\vec{u}^n) + \frac{1}{2}H(\vec{u}^n) - \frac{\delta p^n}{\delta \vec{x}}. \tag{A.37}$$

In summary,

1. Calculate $\vec{u}^*$ from (A.36) without the forcing term.
2. Use the velocity field $\vec{u}^*$ to obtain velocity $\vec{u}^\psi$ at forcing points using the method explained previously.
3. Calculate $\vec{f}^{n+1}$ using (A.37).
4. Compute $\vec{u}^*$ from (A.36) but with the forcing term $\vec{f}^{n+1}$.
5. Solve the Poisson equation for pressure correction based on $\vec{u}^*$.
6. Obtain $\vec{u}^{n+1}$ and p^{n+1} by updating $\vec{u}^*$ and p^n.

A.4 Validation

An experiment was performed to validate the solver after the density transport equation was added. The experiment also allowed for evaluation of the subgrid viscosity and subgrid diffusivity. Validation is performed by comparing, with literatures, statistics of three-dimensional turbulent channel flow simulated both in unstratified and stratified environments.

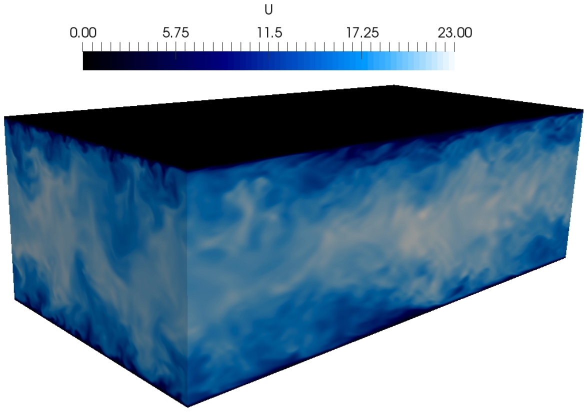

Figure A.2: Perspective view of the computational domain colored by instantaneous streamwise velocity of the unstratified turbulent channel flow at $Re_\tau = 395$ (DNS).

Table A.1: Simulation parameters. D denotes DNS and L denotes LES.

Case	Re_τ	Ri_τ	L_x/h	L_y/h	N_x	N_y	N_z	x^+	y^+	z^+_{wall}
D180.0	180	0	4π	$4\pi/3$	256	128	128	8.83	5.89	0.98
D180.18	180	18	4π	$4\pi/3$	256	128	128	8.83	5.89	0.98
D395.0	395	0	2π	π	256	192	192	9.69	6.46	0.30
L395.0	395	0	2π	π	64	160	192	38.77	7.75	0.30
L550.0	550	0	2π	π	128	128	256	27.00	13.50	1.30
L550.60	550	60	2π	π	128	128	256	27.00	13.50	1.30

The problem is setup inside a channel with periodicity in the streamwise and spanwise directions while the flow is confined by the no-slip top and bottom flat boundaries. We do not use the IBM to represent the walls as it has already been validated in Balaras (2004) and Yang & Balaras (2006). The flow is driven by an imposed favorable pressure gradient with nondimensional magnitude of -1. Friction velocity u_τ, channel half-height h, and density difference between the two walls, $\Delta\rho$ are used as the characteristic velocity, length scale, and density reference, respectively. The governing dimensionless set of equations are

$$\frac{\partial u_i}{\partial x_i} = 0, \tag{A.38}$$

$$\frac{\partial u_i}{\partial t} + u_j \frac{\partial u_i}{\partial x_j} = -\frac{\partial p}{\partial x_i} + \frac{1}{Re_\tau} \frac{\partial^2 u_i}{\partial x_j \partial x_j} - Ri_\tau \widetilde{\rho} \delta_{i3} - \frac{\partial \tau_{ij}}{\partial x_j}, \tag{A.39}$$

$$\frac{\partial \rho}{\partial t} + u_j \frac{\partial \rho}{\partial x_j} = \frac{1}{RePr} \frac{\partial^2 \rho}{\partial x_j \partial x_j} - \frac{\partial \lambda_j}{\partial x_j}, \tag{A.40}$$

With the dimensionless parameters,

$$Re_\tau = \frac{u_\tau h}{\nu}, \qquad Ri_\tau = \frac{\Delta \rho g h}{\rho_o u_\tau^2}, \qquad Pr = \frac{\nu}{k}. \tag{A.41}$$

where Re_τ, Ri_τ, and Pr are, respectively, Reynold number, Richardson number and Prandtl number. Pr is fixed at 0.7 while $Pr_{sgs} = \nu_{sgs}/k_{sgs}$ is fixed at 1.

Table 1 lists parameters for the 6 simulations including Re_τ and Ri_τ along with domain size and resolution. The domain sizes are chosen based on literature with which statistics are to be validated against, except at $Re_\tau = 550$ where we use a reduced domain size to save computational cost. The vertical grid spacing is compressed near the walls to resolve small-scale dynamics in the boundary layer and is stretched towards the centerline. For the DNS cases, the streamwise resolution is kept at $x^+ \equiv \Delta x/\delta_\nu = u_\tau \Delta x/\nu \leq 10$ and spanwise resolution is kept at $y^+ \approx 6$.

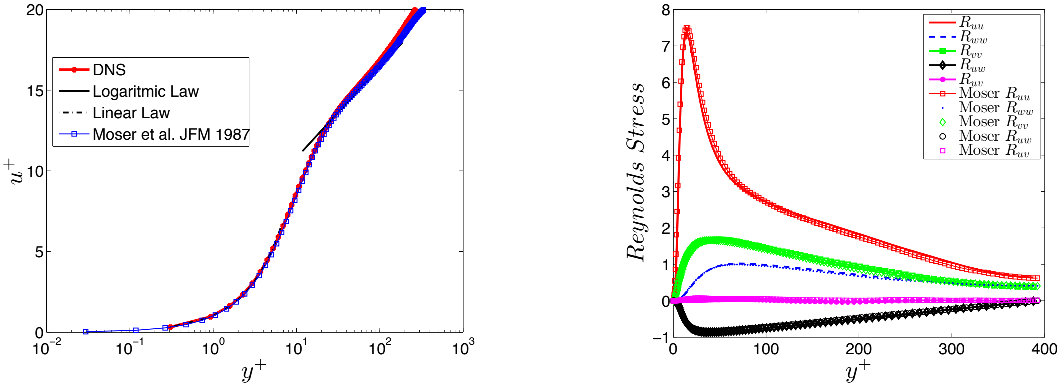

Figure A.4: DNS: $Re = 395$, $Ri = 0$ (Note: y is wall-normal direction in this plot)

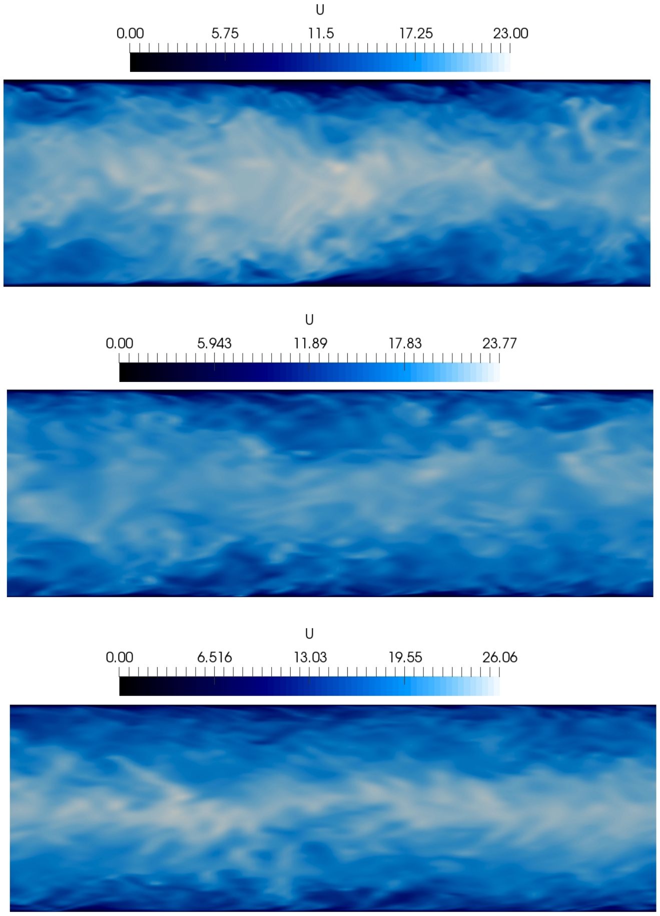

Figure A.3: Visualization of instantaneous streamwise velocity on the vertical cut. From top to bottom: D395.0, L550.0, and L550.60.

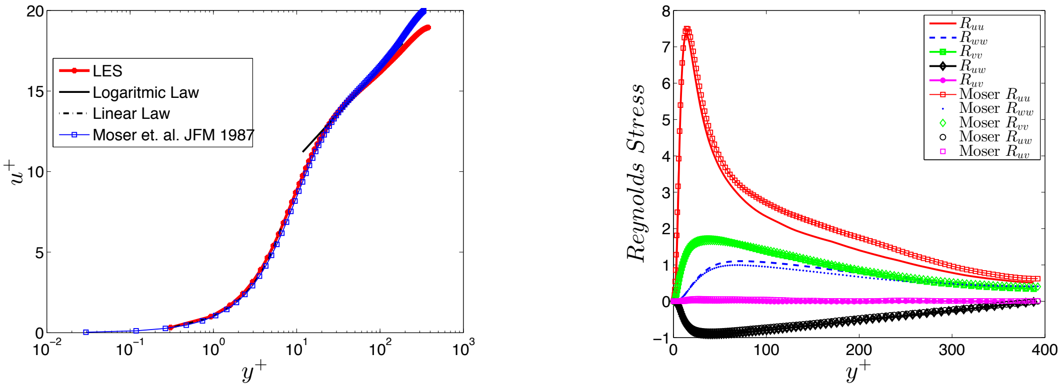

Figure A.5: LES: $Re = 395$, $Ri = 0$ (Note: y is wall-normal direction in this plot)

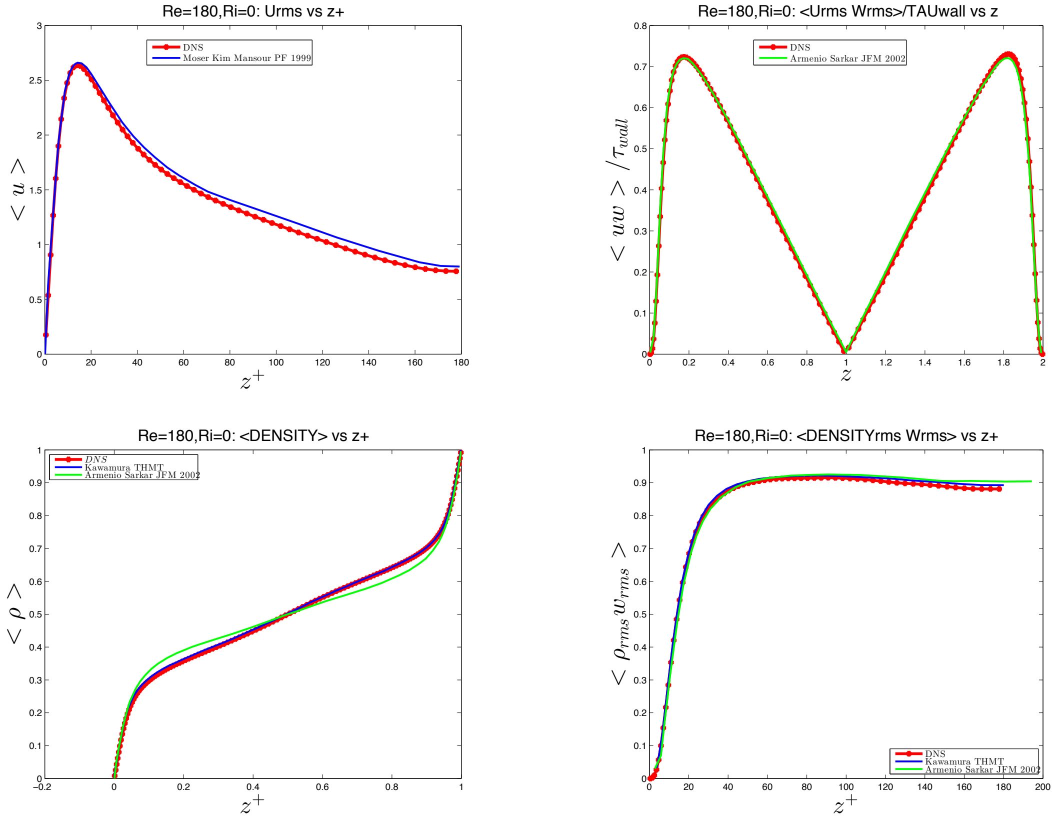

Figure A.6: DNS: $Re = 180,\ Ri = 0$

For the LES cases, a grid resolution is reduced by a factor of 3-4 relative to the DNS cases. The initial condition, for all the cases, is set by introducing uniform streamwise velocity at $u/u_\tau = 20$ while density is set as -0.5 and 0.5 at the top and bottom wall with linear variation inbetween. After $h/u_\tau \approx 2$, while the laminar boundary layer keeps developing, velocity fluctuations in the form of white noise are imposed throughout each vertical grid layer. The root-mean-square magnitude of the fluctuations is designed to distribute parabolically where the strongest noise is added near the wall. This mimics the nature of turbulent channel flow where turbulence is concentrated near the walls. The white-noise disturbance is sufficient to attain turbulence without having to introduce a complicated type of noise, i.e. different amplitudes at different wave numbers. The steady state is determined by a constant plane-averaged drag-coefficient on the wall.

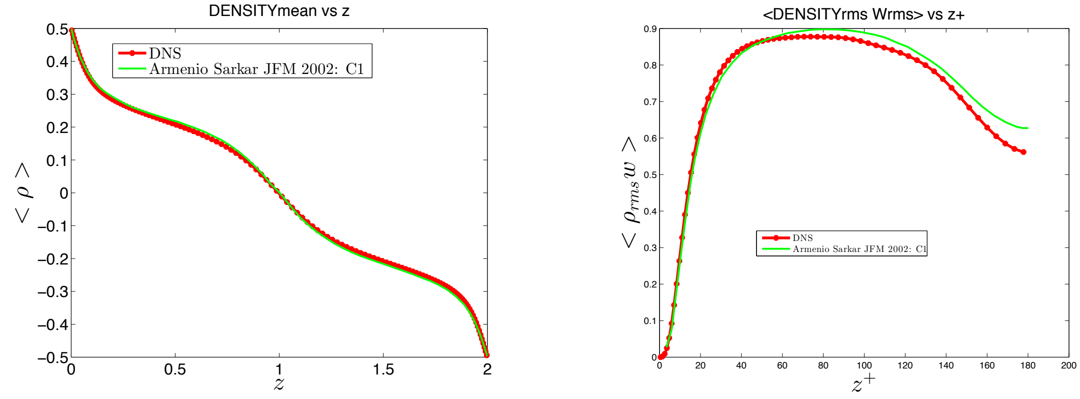

Figure A.7: DNS: $Re = 180,\ Ri = 18$

To validate stratified channel flow without a turbulence model, two-way communication between the Navier-Stokes equation (NSE) solver and the density equation (DE) solver is enabled. The strength of stratification is set as $Ri_\tau = 18$ (D180.18). Density profile and density flux are in good agreement with Armenio & Sarkar (2002), shown in figure A.7.

Some qualitative observations are made from the visualizations plotted in Figure A.3 for the D395.0, L550.0, and L550.60 cases. The low-speed (dark blue) fluid extends toward the centerline in large coherent patches at $Re_\tau = 395$ (Figure A.3 a). The low-speed fluid stays closer to the wall at higher $Re_\tau = 550$ (Figure A.3 b). The stratified case (Figure A.3 c) shows that there is a central layer of high-speed fluid with undulations and sheared structures at its peripheries. This “jet” feature is distinct because vertical mixing is suppressed in the central region where the gradient Richardson number is larger relative to that near the wall.

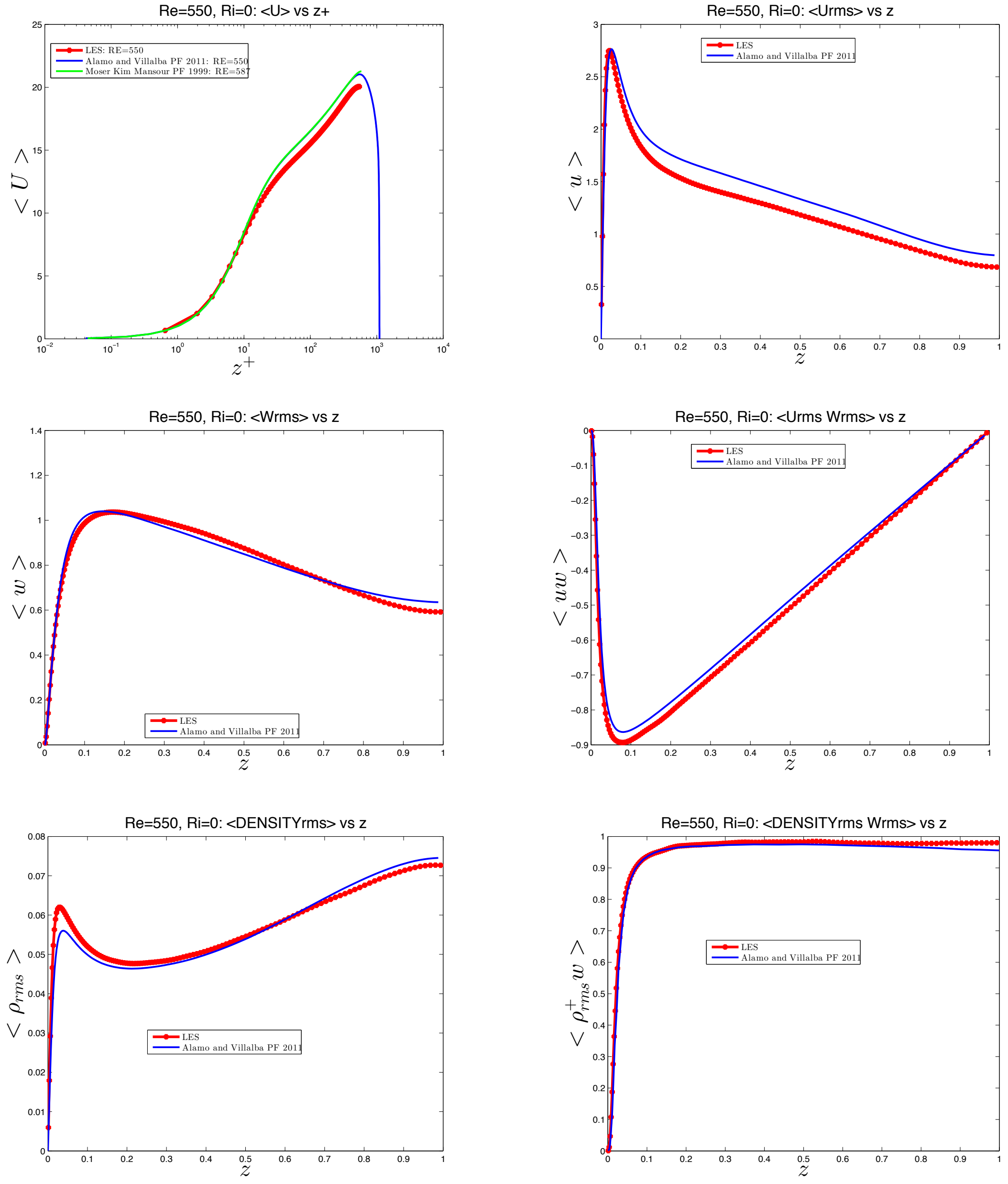

Figure A.8: LES: $Re = 550,\ Ri = 0$

We first validate the NSE solver while the DE solver is turned off. At $Re_\tau = 395$, unstratified channel flow simulations are performed using DNS and LES in cases D395.0 and L395.0. Velocity profiles and Reynolds stresses are compared against data of Moser *et al.* (1999), referred to as MKM from here on. All statistics are averaged spatially along the two periodic directions and also in time. The results are shown in Figures A.4 and A.5. For the DNS, the mean streamwise velocity profile and Reynolds stresses are in good agreement with the reference. For the LES, the mean streamwise velocity near the channel center is smaller than expected. The LES also slightly underpredicts longitudinal streamwise and vertical Reynolds stress components.

To validate the DE solver without a subgrid model, a DNS is performed at $Re_\tau = 180$ with density being a passive scalar ($Ri_\tau = 0$), referred to as case D180.0. Root-mean-square (rms) velocities are compared with that of MKM. Density profiles, density rms, and density flux are compared withArmenio & Sarkar (2002), referred the as AS, and Kawamura *et al.* (2000), referred to as KAK. The results are shown in Figure A.6. DNS slightly underpredicts turbulent intensities, compared to MKM, especially away from the wall. Fluctuating momentum flux $< uw >$ matches very well with the LES of AS. Density profiles, density rms, and density flux are in good agreement with KAK.

For the validation of a stratified channel flow with the subgrid model, LES is performed with $Re_\tau = 550$ and $Ri_\tau = 0$, 60. Velocity profiles, density profiles, velocity rms, density rms, fluctuating momentum flux, fluctuating density flux, and dissipation are compared with the DNS of Garcia-Villalba & Del Alamo (2011), referred to as GdA. The passive scalar is shown in Figure A.8 and the active scalar is shown in Figure A.9. For the passive scalar case, as compared to GdA, the LES underpredicts both mean and rms of streamwise velocity. This is due to the lack of near-wall resolution required to correctly capture small-scale fluctuations. Mean density (not shown) and turbulent density flux match well with GdA. Density rms is more energetic near the wall compared to that of AV. The active scalar case, at $Ri_\tau = 60$, is shown in Figure A.9. There is an underprediction of mean and rms of streamwise velocity and slight discrepancy in the density statistics. Note that in this case, the size of the computational domain is much smaller than that of GdA. Overall the LES is able to qualitatively capture the first and second order statistics.

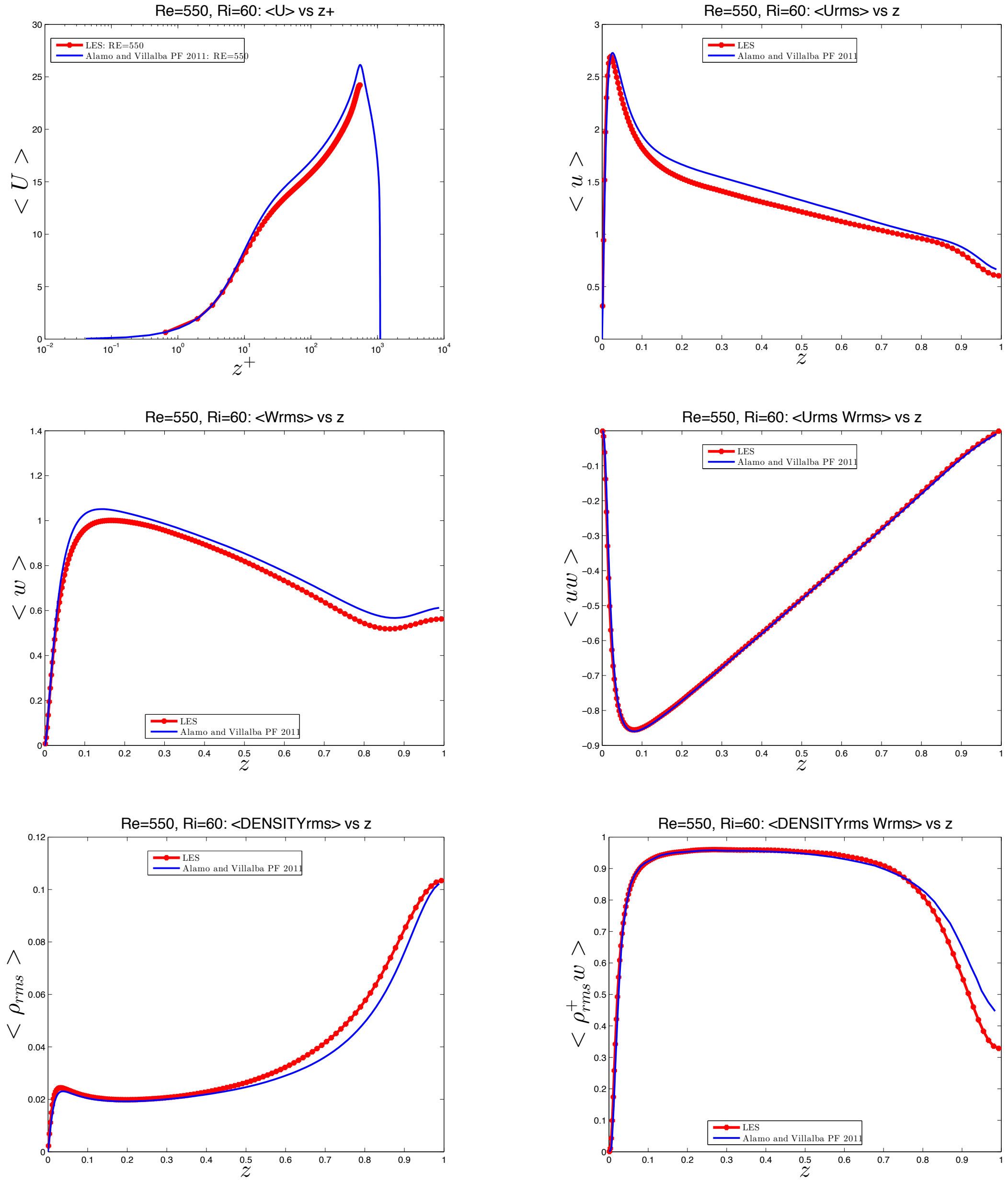

Figure A.9: LES: $Re = 550,\ Ri = 60$

Within the range of parameters simulated, the results are good. Some quantitative discrepancies come from the fact that computational domain size and resolution were chosen to be adequate rather than excellent.

The contents of this appendix are parts of unpublished technical reports written by the dissertation author.

Appendix B

A brief description of ***Fibre***

B.1 A generalized coordinate solver

The turbulent wake is a disturbance that naturally forms behind a body obstructing an incoming stream. Whether a turbulent wake is realistically realized in a computer simulation is to a large degree dependent on how it is generated. Generally, the body can either be placed inside a computational domain using an immersed-boundary method or on the boundary of a domain. However, both methods can be used in conjunction where a complex geometry is partially "wrapped" by a curvilinear grid and partially represented by immersed-boundary points. While the first method is employed by *Eddy* described in the previous section, the latter method used by another tool, *Fibre*, is the central focus in this section. While the advantages of using an IBM method have been laid out in the previous chapter, using a body-fitted grid allows for a more accurate representation of an solid-fluid interface. Although it comes with a higher computational cost, a body-fitted grid simulation avoids artificial forces perceived by fluid nodes. This is accomplished by wrapping a grid around a body's surface allowing straight-forward implementation of the no-slip boundary condition. Using a body-fitted grid is suitable whenever the dynamics on the surface of a body must be accurately captured as in the case of separation of a turbulent boundary layer. A simple example of using a body-fitted grid is a simulation of flow in a channel where the interfaces of the two bodies (the top and bottom walls) are “fitted” by a cartesian grid.

We started the project ‘*Fibre*’ and explored its usability particularly in the study of strongly stratified flow past a sphere in which statistics on a body are important. *Fibre* is a parallelized CFD solver capable of solving the incompressible Navier-Stokes equations and the density transport equation on a generalized curvilinear coordinate system. This chapter describes grid transformations, algorithms, external libraries, and parallelization used in *Fibre* as well as a validation of the solver.

B.2 Coordinate transformation

Solving the governing transport equations in a generalized curvilinear coordinate system requires an addition step called ‘coordinate transformation’ in which a physical law written on a cartesian system is transformed into the alternative form based on generalized curvilinear coordinates. Information related to the transformation is stored in the ‘Jacobi matrix’. In this context, ‘grid transformation’ is often used synonymously with coordinate transformation as the curvilinear grid has been transformed into the new computational cartesian grid.

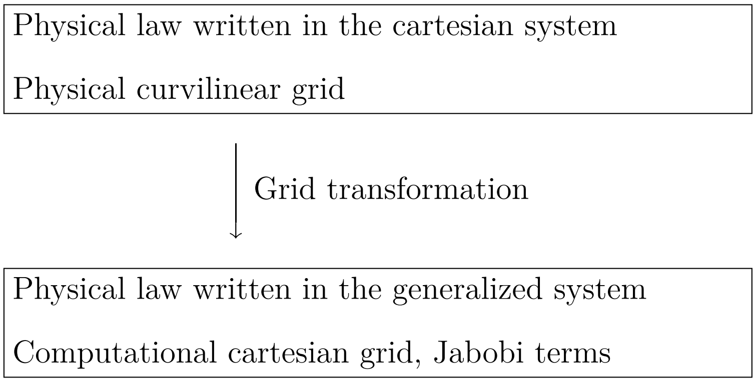

The transformation leads to additional coefficients for all spatial derivatives in the governing equations. Equations (B.1) and (B.2) give the Navier-Stokes equations before and after the transformation, respectively. x_i denotes the coordinate i of the cartesian system and ζ_i denotes the coordinate i of the generalized system.

$$\frac{\partial u_i}{\partial t} + \frac{\partial u_j u_i}{\partial x_j} = -\frac{\partial p}{\partial x_i} + \frac{1}{Re}\frac{\partial^2 u_i}{\partial x_j \partial x_j} - \frac{1}{Fr^2}\rho\delta_{i3} \tag{B.1}$$

$$\frac{\partial |J^{-1}| u_i}{\partial t} = -\frac{\partial C_{ni} P}{\partial \zeta_n} - \frac{\partial [C_{nj} u_j] u_i}{\partial \zeta_n} + \frac{1}{Re}\left(\frac{\partial}{\partial \zeta_n} G_{nj} \frac{\partial u_i}{\partial \zeta_j}\right) - \frac{1}{Fr^2}\rho\delta_{i3} \tag{B.2}$$

Here J^{-1}, C_{ij}, and G_{ij} are

$$J^{-1} = \begin{bmatrix} \partial x/\partial\zeta & \partial y/\partial\zeta & \partial z/\partial\zeta \\ \partial x/\partial\eta & \partial y/\partial\eta & \partial z/\partial\eta \\ \partial x/\partial\xi & \partial y/\partial\xi & \partial z/\partial\xi \end{bmatrix} =: [\partial x_i/\partial\zeta_j], \tag{B.3}$$

$$C_{ij} = |J^{-1}|\frac{\partial \zeta_i}{\partial x_j} \qquad G_{ij} = |J^{-1}|\frac{\partial \zeta_i}{\partial x_k}\frac{\partial \zeta_j}{\partial x_k}. \tag{B.4}$$

Physically, the determinant $|J^{-1}|$ is the volume ratio of the original cell to the transformed cell. C_{ij} and G_{ij} are grid elongation and skewness coefficients, respectively. The volume of a transformed cell is typically chosen to be unity.

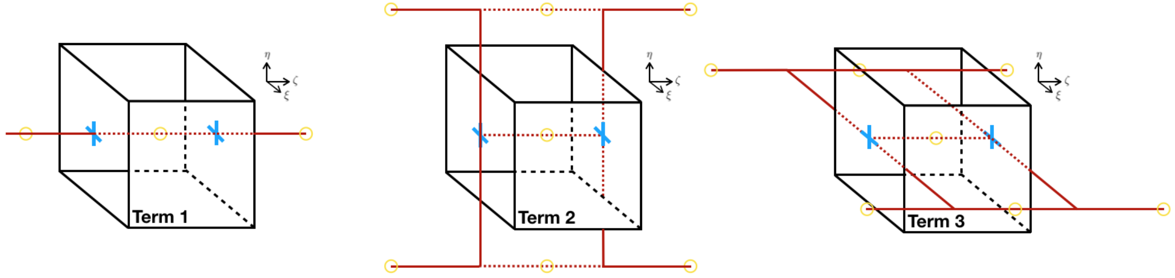

Figure B.1: Stencils used for computing B.6, B.7, and B.8.

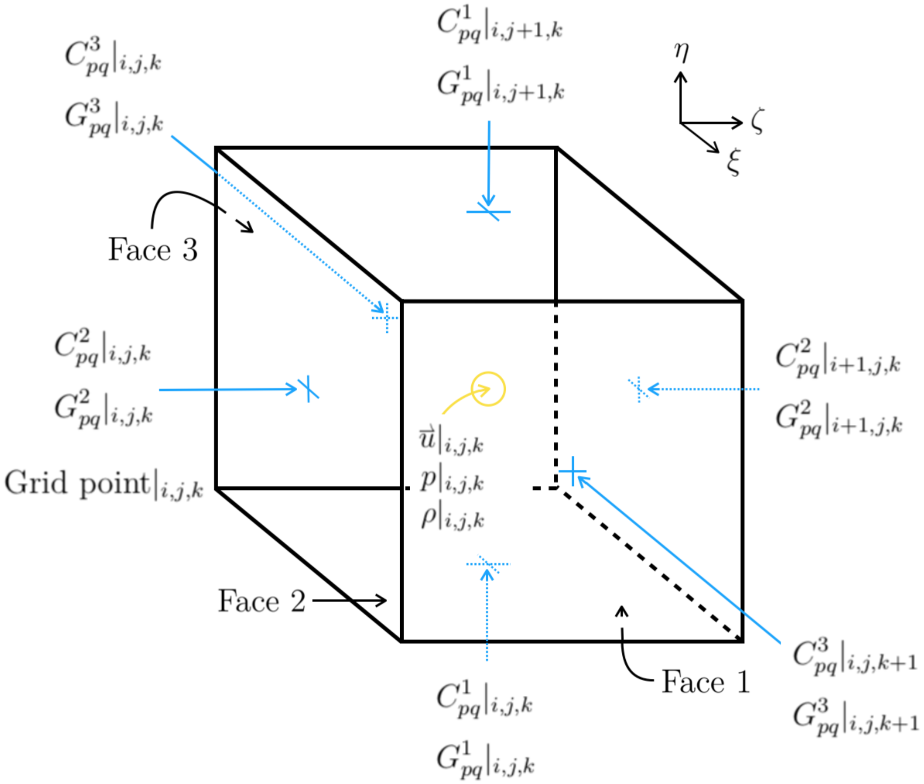

Figure B.2: A transformed computational cell associated with the grid point (i,j,k); where i, j, k are integer indices used to identify discrete space in the ζ, η, and ξ directions respectively.

B.3 Spatial discretization

B.3.1 Jacobi terms

Consider a cell (i,j,k) in a transformed computational domain; where (i,j,k) identifies the cell among other cells in the computational domain and has no relation with a component of the coordinates. The Jacobi terms, J^{-1}, C_{pq}, and G_{pq} as in (B.3) and (B.4) are defined on the cell's faces as shown in Figure B.2. To obtain C_{pq} and G_{pq}, we compute J^{-1} and perform inversion as follows.

1. Compute J^{-1} at every cell faces, denoted by $J^{-1,fc}$; where fc indicates cell face (1-3),

by calculating the 9 components in J^{-1}. For example, we can calculate the members of $J^{-1,2}$ of cell (i,j,k) as follows,

$$\begin{aligned}(\partial\vec{x}/\partial\zeta)|_{i,j,k} = 0.125 * (&+\vec{x}|_{i+1,j+1,k} + \vec{x}|_{i+1,j,k} + \vec{x}|_{i+1,j+1,k+1} + \vec{x}|_{i+1,j,k+1}\\ &- \vec{x}|_{i-1,j+1,k} - \vec{x}|_{i-1,j,k} - \vec{x}|_{i-1,j+1,k+1} - \vec{x}|_{i-1,j,k+1})\\ (\partial\vec{x}/\partial\eta)|_{i,j,k} = 0.5 * (&+\vec{x}|_{i,j+1,k} + \vec{x}|_{i,j+1,k+1} - \vec{x}|_{i,j,k} - \vec{x}|_{i,j,k+1})\\ (\partial\vec{x}/\partial\xi)|_{i,j,k} = 0.5 * (&+\vec{x}|_{i,j+1,k+1} + \vec{x}|_{i,j,k+1} - \vec{x}|_{i,j,k} - \vec{x}|_{i,j+1,k})\end{aligned}$$

2. Calculate $det(J^{-1,fc})$, denoted by $|J^{-1,fc}|$

3. The variable $|J^{-1}|$ in the governing equations (B.2) is an averaged value at the cell center calculated from the six surrounding faces:

$$|J^{-1}|_{i,j,k} = \frac{1}{6}\left(\sum_{fc=1}^{3} |J^{-1,fc}|_{i,j,k} + |J^{-1,1}|_{i,j+1,k} + |J^{-1,2}|_{i+1,j,k} + |J^{-1,3}|_{i,j,k+1}\right)$$

4. Compute $J^{fc} = [\partial\zeta_i/\partial x_j]$ simply by the straight-forward inversion, $J^{-1,fc}$:
$\{J^{-1,fc}\}^{-1} = det(J^{-1,fc})^{-1}\{cof(J^{-1})\}^T$

5. Calculate C_{pq} and G_{pq} at face fc, denoted by C_{pq}^{fc} and G_{pq}^{fc} from J^{fc}

B.3.2 Discretization

Discretizing (B.2) in space (ζ, η, ξ) is done simply with the second-order central finite difference scheme. As an example, consider the term (B.5) with Figure B.1 illustrating stencils used in the central finite difference.

$$\frac{\partial}{\partial\zeta_p}\left[G_{pq}\frac{\partial\phi}{\partial\zeta_q}\right] \tag{B.5}$$

(B.5) consists of 9 terms. Here we give examples of the discretized term 1 (p=1 and q=1), term 2 (p=1 and q=2), and term 3 (p=1 and $q = 3$).

$$\begin{aligned}\left(\frac{\delta}{\delta\zeta_1}\left[G_{11}\frac{\delta\phi}{\delta\zeta_1}\right]\right)_{i,j,k} &= \left[G_{11}\frac{\delta\phi}{\delta\zeta_1}\right]_{i+1/2,j,k} - \left[G_{11}\frac{\delta\phi}{\delta\zeta_1}\right]_{i-1/2,j,k} \\ &= + G_{11}^2|_{i+1,j,k}[\phi|_{i+1,j,k} - \phi|_{i,j,k}] \\ &\quad - G_{11}^2|_{i,j,k} \quad [\phi|_{i,j,k} - \phi|_{i-1,j,k}]\end{aligned} \tag{B.6}$$

$$\begin{aligned}\left(\frac{\delta}{\delta\zeta_1}\left[G_{12}\frac{\delta\phi}{\delta\zeta_2}\right]\right)_{i,j,k} &= \left[G_{12}\frac{\delta\phi}{\delta\zeta_2}\right]_{i+1/2,j,k} - \left[G_{12}\frac{\delta\phi}{\delta\zeta_2}\right]_{i-1/2,j,k} \\ &= + \frac{G_{12}^2|_{i+1,j,k}}{2}\left[+\frac{\phi|_{i,j+1,k} + \phi|_{i+1,j+1,k}}{2}\right. \\ &\qquad\qquad \left.-\frac{\phi|_{i,j-1,k} + \phi|_{i+1,j-1,k}}{2}\right] \\ &\quad - \frac{G_{12}^2|_{i,j,k}}{2} \quad \left[+\frac{\phi|_{i,j+1,k} + \phi|_{i-1,j+1,k}}{2}\right. \\ &\qquad\qquad \left.-\frac{\phi|_{i,j-1,k} + \phi|_{i-1,j-1,k}}{2}\right]\end{aligned} \tag{B.7}$$

$$\begin{aligned}\left(\frac{\delta}{\delta\zeta_1}\left[G_{13}\frac{\delta\phi}{\delta\zeta_3}\right]\right)_{i,j,k} &= \left[G_{13}\frac{\delta\phi}{\delta\zeta_3}\right]_{i+1/2,j,k} - \left[G_{13}\frac{\delta\phi}{\delta\zeta_3}\right]_{i-1/2,j,k} \\ &= + \frac{G_{13}^2|_{i+1,j,k}}{2}\left[+\frac{\phi|_{i,j,k+1} + \phi|_{i+1,j,k+1}}{2}\right. \\ &\qquad\qquad \left.-\frac{\phi|_{i,j,k-1} + \phi|_{i+1,j,k-1}}{2}\right] \\ &\quad - \frac{G_{13}^2|_{i,j,k}}{2} \quad \left[+\frac{\phi|_{i,j,k+1} + \phi|_{i-1,j,k+1}}{2}\right. \\ &\qquad\qquad \left.-\frac{\phi|_{i,j,k-1} + \phi|_{i-1,j,k-1}}{2}\right]\end{aligned} \tag{B.8}$$

B.4 Temporal discretization

The governing equations (B.2) are solved using the fractional-step method where a velocity field is sequentially advanced in multiple substeps (hence ‘fractional step’). Afterwards, the zero-divergence condition is imposed. Marching to an intermediate field requires a combination of the Alternating Direction Implicit method (ADI), the Crank-Nicolson method (CN), and the third-order low-storage Runge-Kutta method (RKW3).

B.4.1 Alternating Direction Implicit method

Fibre uses the Alternating Direction Implicit (ADI) method to march the viscous term in each spatial direction implicitly, one direction at a time. Suppose we want to solve (B.9). If we use the Euler method, the procedure is to perform implicit Euler in the x direction with explicit Euler in the y direction for first half ($\Delta t/2$), and vice versa for the second half $\Delta t/2$ as shown in (B.10) and (B.11).

$$\frac{\partial \phi}{\partial t} = \alpha \left[\frac{\partial^2 \phi}{\partial x^2} + \frac{\partial^2 \phi}{\partial y^2} \right] \tag{B.9}$$

$$\frac{\phi^{n+\frac{1}{2}} - \phi^n}{\Delta t/2} = \alpha \left[\frac{\partial^2 \phi^{n+\frac{1}{2}}}{\partial x^2} + \frac{\partial^2 \phi^n}{\partial y^2} \right] \tag{B.10}$$

$$\frac{\phi^{n+1} - \phi^{n+\frac{1}{2}}}{\Delta t/2} = \alpha \left[\frac{\partial^2 \phi^{n+\frac{1}{2}}}{\partial x^2} + \frac{\partial^2 \phi^{n+1}}{\partial y^2} \right] \tag{B.11}$$

B.4.2 Crank-Nicolson method

The Crank-Nicolson method equally splits the right hand side (rhs) input into two parts, the implicit and the explicit parts as shown in (B.12) and (B.13).

$$\frac{\partial \phi}{\partial t} = \alpha \frac{\partial^2 \phi}{\partial x^2} \tag{B.12}$$

$$\frac{\phi^{n+1} - \phi^n}{\Delta t} = \frac{\alpha}{2}\left[\frac{\partial^2 \phi^{n+1}}{\partial x^2} + \frac{\partial^2 \phi^n}{\partial x^2}\right] \tag{B.13}$$

B.4.3 Third order Runge-Kutta method

The third-order low-storage Runge-Kutta method (RKW3) uses only two storage variables. Marching is accomplished in three substeps briefly summarized here. Given an equation for ϕ,

$$\frac{\partial \phi}{\partial t} = \mathrm{R}(\phi). \tag{B.14}$$

RKW3 is done in the following manner,

$$\frac{\phi^{rk} - \phi^{rk-1}}{h^{rk}} = \beta^{rk}\mathrm{R}(\phi^{rk-1}) + \zeta^{rk}\mathrm{R}(\phi^{rk-2})\,. \tag{B.15}$$

Here, rk goes from substep 1 to substep 3. h, β, and ζ are given in Table B.1.

Table B.1: RKW3 parameters

Substep	$\bar{h}$	$\bar{\beta}$	$\bar{\zeta}$
1	$8\Delta t/15$	1	0
2	$2\Delta t/15$	25/8	-17/8
3	$1\Delta t/3$	9/4	-5/4

B.4.4 The ADI-CN-RK3 combined marching scheme

The algorithms briefly described above are used in combination to construct a set of temporally-discrete governing equations in the intermediate field. Essentially, the right hand side of equation (B.2) is split into terms that are to be marched explicitly and implicitly, shown as the subscripts *ex* and *im* in (B.16). Depending on the grid skewness G_{ij}, the diagonal parts of the viscous terms can be susceptible to the stiffness of the discretized systems and are marched implicitly. Since there are three viscous terms containing G_{11}, G_{22}, and G_{33}, the Alternating Direction Implicit method is used. At a given time, they are split into two parts using the Crank-Nicolson method. These steps are shown in (B.17), (B.18), and (B.19) as an example for the substep 1 of the RKW3 marching scheme. Note that $\square$ represents all the terms to be marched explicitly.

$$\begin{aligned}\frac{\partial J^{-1}u_i}{\partial t} = &\left[-\frac{\partial C_{ni}P}{\partial \zeta_n} - \frac{\partial [C_{nj}u_j]u_i}{\partial \zeta_n} + \frac{1}{Re}\left(\frac{\partial}{\partial \zeta_n} G_{nj}\frac{\partial u_i}{\partial \zeta_j}\right)_{n\neq j} - \frac{1}{Fr^2}\rho^{'}\delta_{i2}\right]_{ex} \\ &+ \left[\frac{1}{Re}\left(\frac{\partial}{\partial \zeta_n} G_{nj}\frac{\partial u_i}{\partial \zeta_j}\right)_{n=j}\right]_{im} \end{aligned} \tag{B.16}$$

$$\begin{aligned}J^{-1}u_i^{\star} = J^{-1}u_i^{n} + \beta^{(1)}h^{(1)}\square + \frac{1}{Re}\frac{h^{(1)}}{2}\left(\frac{\partial}{\partial \zeta}\left[G_{11}\frac{\partial u_i^n}{\partial \zeta}\right] + \frac{\partial}{\partial \zeta}\left[G_{11}\frac{\partial u_i^{\star}}{\partial \zeta}\right]\right) \\ + \frac{1}{Re}h^{(1)}\frac{\partial}{\partial \eta}\left[G_{22}\frac{\partial u_i^n}{\partial \eta}\right] + \frac{1}{Re}h^{(1)}\frac{\partial}{\partial \xi}\left[G_{33}\frac{\partial u_i^n}{\partial \xi}\right]\end{aligned} \tag{B.17}$$

$$J^{-1}u_i^{\star\star} = J^{-1}u_i^{\star} - \frac{1}{Re}\frac{h^{(1)}}{2}\frac{\partial}{\partial \eta}\left[G_{22}\frac{\partial u_i^n}{\partial \eta}\right] + \frac{1}{Re}\frac{h^{(1)}}{2}\frac{\partial}{\partial \eta}\left[G_{22}\frac{\partial u_i^{\star\star}}{\partial \eta}\right] \tag{B.18}$$

$$J^{-1}u_i^{\star\star\star} = J^{-1}u_i^{\star\star} - \frac{1}{Re}\frac{h^{(1)}}{2}\frac{\partial}{\partial\xi}\left[G_{33}\frac{\partial u_i^n}{\partial\xi}\right] + \frac{1}{Re}\frac{h^{(1)}}{2}\frac{\partial}{\partial\xi}\left[G_{33}\frac{\partial u_i^{\star\star\star}}{\partial\xi}\right] \tag{B.19}$$

Fibre computes $u_i^\star$, $u_i^{\star\star}$, $u_i^{\star\star\star}$ from the set of tridiagonal matrices constructed in the ζ, η, and ξ directions based respectively on (B.17), (B.18), and (B.19). The intermediate velocity $u_i^{\star\star\star}$ is the first step in the fractional-step scheme.

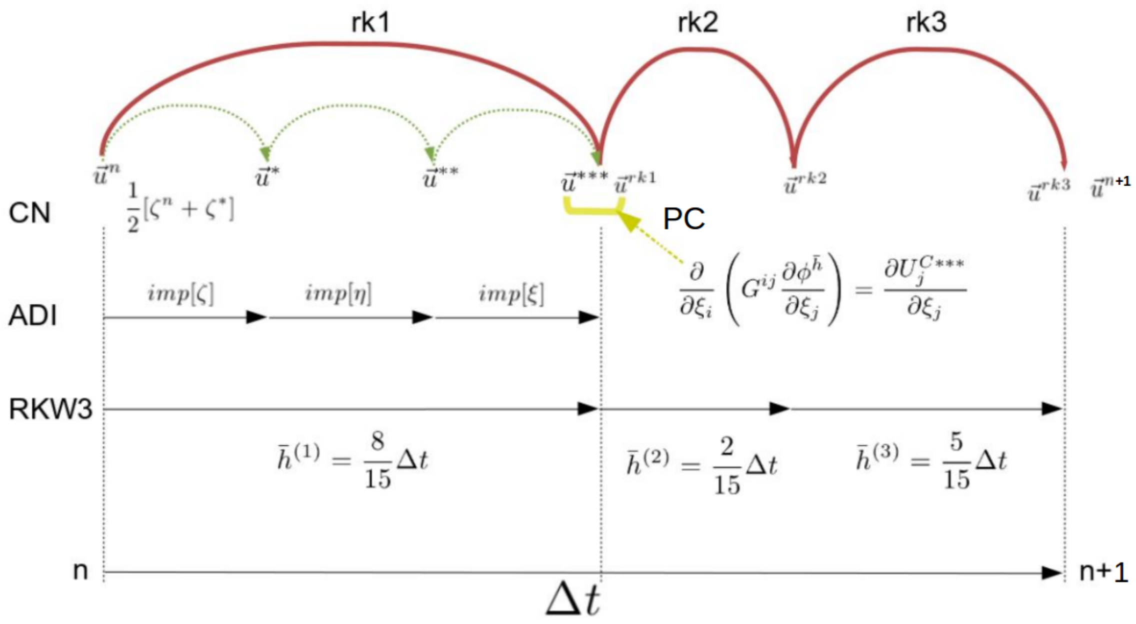

Figure B.3: The ADI-CN-RK3 combined marching scheme.

B.5 Thomas algorithm

Fibre employs the parallel Thomas algorithm with pipelining (either with or without periodic boundary conditions). It is a remarkably efficient algorithm used to solve a tridiagonal system such that those constructed from (B.17), (B.18), and (B.19) for $u^\star$, $u^{\star\star}$, and $u^{\star\star\star}$. Readers are encouraged to consult Bewley (2012) for a detailed description of the algorithm.

B.5.1 Sequential algorithm

Consider solving the problem $Ax = g$ for x resulting from spatial discretization of, for instance, (B.17) where A is a tridiagonal matrix:

$$\begin{bmatrix} b_0 & c_0 & & & & & & \\ a_1 & b_1 & c_1 & & & & & \\ & a_2 & b_2 & c_2 & & & & \\ & & . & . & . & & & \\ & & & . & . & . & & \\ & & & & a_{n-1} & b_{n-1} & c_{n-1} & \\ & & & & & a_n & b_n & c_n \end{bmatrix} \begin{bmatrix} x_0 \\ x_1 \\ x_2 \\ . \\ . \\ x_{n-1} \\ x_n \end{bmatrix} = \begin{bmatrix} g_0 \\ g_1 \\ g_2 \\ . \\ . \\ g_{n-1} \\ g_n \end{bmatrix} \tag{B.20}$$

The first 2 relations in (B.5.1) are,

$$b_0 x_0 + c_0 x_1 = g_0 \tag{B.21}$$

$$a_1 x_0 + b_1 x_1 + c_1 x_2 = g_1. \tag{B.22}$$

Substituting x_0 from (B.21) into x_0 in (B.22) gives

$$b_1^{'} x_1 + c_1 x_2 = g_1^{'} \tag{B.23}$$

where $b_1^{'} = \left[b_1 - a_1 b_0^{-1} c_0\right]$ and $g_1^{'} = \left[g_1 - a_1 b_0^{-1} g_0\right]$. The algorithm involves two steps, forward sweeping and backward substitution (or backward sweeping). During forward sweeping, the subdiagonal elements a_1-a_n are Gaussian eliminated. B.5.1 becomes

$$\begin{bmatrix} b_0 & c_0 & & & & & & \\ 0 & b_1^{'} & c_1 & & & & & \\ & 0 & b_2^{'} & c_2 & & & & \\ & & . & . & . & & & \\ & & & . & . & . & & \\ & & & & 0 & b_{n-1}^{'} & c_{n-1} & \\ & & & & & 0 & b_n^{'} & c_n \end{bmatrix} \begin{bmatrix} x_0 \\ x_1 \\ x_2 \\ . \\ . \\ x_{n-1} \\ x_n \end{bmatrix} = \begin{bmatrix} g_0 \\ g_1^{'} \\ g_2^{'} \\ . \\ . \\ g_{n-1}^{'} \\ g_n^{'} \end{bmatrix} \tag{B.24}$$

At the end of forward sweeping, we can solve for x_n as in $x_n = g_n^{'}/b_n^{'}$ in B.5.1. For the backward substitution, we sequentially solve for x_{n-1}-x_0 (equations $n-1$ until 0) as in $x_i = (g_i^{'} - c_i x_{i+1})/b_i^{'}$. Once completed, x_0-x_n are all solved.

If we encounter a system with periodic boundary condition, a modifed version of the Thomas algorithm is required. For example, for the grid in the Section B.8, periodic boundary conditions are enforced in the η direction. The algorithm is modified as follows. Consider the discretized system $Ax = g$ with periodicity as in (B.25) where $x_1 = x_{n-1}$ and $x_2 = x_n$.

$$\begin{bmatrix} b_1 & c_1 & & & & & a_1 \\ a_2 & b_2 & c_2 & & & & \\ & . & . & . & & & \\ & & . & . & . & & \\ & & & . & . & . & \\ & & & & a_{n-1} & b_{n-1} & c_{n-1} \\ c_n & & & & & a_n & b_n \end{bmatrix} \begin{bmatrix} x_1 \\ x_2 \\ . \\ . \\ . \\ x_{n-1} \\ x_n \end{bmatrix} = \begin{bmatrix} g_1 \\ g_2 \\ . \\ . \\ . \\ g_{n-1} \\ g_n \end{bmatrix} \tag{B.25}$$

The first step is to separate (B.25) into the tridiagonal system (B.26) and an addition equation (B.27)

$$\begin{bmatrix} b_1 & c_1 & & & & \\ a_2 & b_2 & c_2 & & & \\ & \cdot & \cdot & \cdot & & \\ & & \cdot & \cdot & \cdot & \\ & & & \cdot & \cdot & \cdot \\ & & & & a_{n-1} & b_{n-1} \end{bmatrix} \begin{bmatrix} x_1 \\ x_2 \\ \cdot \\ \cdot \\ \cdot \\ x_{n-1} \end{bmatrix} = \begin{bmatrix} g_1 \\ g_2 \\ \cdot \\ \cdot \\ \cdot \\ g_{n-1} \end{bmatrix} + \begin{bmatrix} -a_1 \\ 0 \\ 0 \\ \cdot \\ \cdot \\ -c_{n-1} \end{bmatrix} x_n \tag{B.26}$$

$$c_n x_1 + a_n x_{n-1} + b_n x_n = g_n. \tag{B.27}$$

Define $[A_c]$ as the tridiagonal matrix on the left hand side and $[g]$ as the g-column matrix on the right hand side. Let

$$[x] = [x1] + [x2]x_n \tag{B.28}$$

be the solution of the system (B.26) where

$$[x1] = [A_c]^{-1}[g] \tag{B.29}$$

$$[x2] = [A_c]^{-1}[-a_1 0 \cdots -c_{n-1}]^T. \tag{B.30}$$

Substituting x in (B.28) into x_1 and x_{n-1} in (B.27) gives

$$c_n(x1_1 + x2_1 x_n) + a_n(x1_{n-1} + x2_{n-1}x_n) + b_n x_n = g_n. \tag{B.31}$$

Rearrage B.31 for x_n

$$x_n = \frac{g_n - c_n x1_1 - a_n x1_{n-1}}{b_n + c_n x2_1 + a_n x2_{n-1}}. \tag{B.32}$$

The following steps are used to solve the system (B.25)

1. Construct (B.29) and (B.30)
2. Solve (B.29) and (B.30) for $[x1]$ and $[x2]$ from index 1 to index $n-1$
3. Substitute $[x1]$ and $[x2]$ into (B.32) and solve for x_n
4. Calculate $[x]$ from (B.28) using $[x1]$, $[x2]$, and x_n

B.5.2 Parallel algorithm

Fibre decomposes a computational domain into a number of smaller subdomains. Each contains an equal number of grid points and is chosen to be occupied by one process (we will use the word ‘CPU’ in place of the more proper term ‘process’). Figure B.4 provides an example of 4×4×4 CPU topology in the decomposed computational domain.

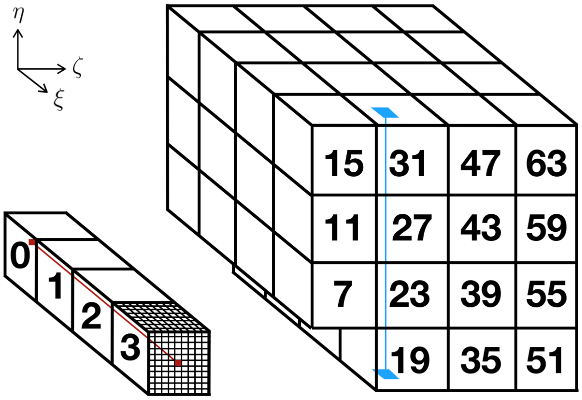

Figure B.4: Example of a 4×4×4 CPU topology in a single computational domain. Numbers in the figure represent an individual CPU’s rank (id).

$$
\begin{array}{c|ccccccccccc|c|}
 & b_s^{\prime\, i-1} & c_s^{i-1} & & & & & & & & & & . \\
\hdashline
 & 0 & b_s^{\prime\, i} & c_s^{i} & & & & & & & & & g_s^{\prime\, i} \\
 & & 0 & b_{s+1}^{\prime\, i} & c_{s+1}^{i} & & & & & & & & g_{s+1}^{\prime\, i} \\
\text{CPU}^{i} & & & . & . & . & & & & & & & . \\
 & & & & 0 & b_e^{\prime\, i} & c_e^{i} & & & & & & g_e^{\prime\, i} \\
\hdashline
 & & & & & a_s^{i+1} & b_s^{i+1} & c_s^{i+1} & & & & & g_s^{i+1} \\
\text{CPU}^{i+1} & & & & & & a_{s+1}^{i+1} & b_{s+1}^{i+1} & c_{s+1}^{i+1} & & & & g_{s+1}^{i+1} \\
 & & & & & & & . & . & . & & & . \\
 & & & & & & & & a_e^{i+1} & b_e^{i+1} & c_e^{i+1} & & g_e^{i+1} \\
\hdashline
 & & & & & & & & & a_s^{i+1} & . & . & .
\end{array}
\qquad (B.33)
$$

$$
\begin{array}{c|ccccccccccc|c|}
 & b_s^{\prime\, i-1} & c_s^{i-1} & & & & & & & & & & . \\
\hdashline
 & & b_s^{\prime\, i} & c_s^{i} & & & & & & & & & g_s^{\prime\, i} \\
 & & & b_{s+1}^{\prime\, i} & c_{s+1}^{i} & & & & & & & & g_{s+1}^{\prime\, i} \\
\text{CPU}^{i} & & & & . & . & & & & & & & . \\
 & & & & & b_e^{\prime\, i} & c_e^{i} & & & & & & g_e^{\prime\, i} \\
\hdashline
 & & & & & & b_s^{\prime\, i+1} & c_s^{i+1} & & & & & x_s^{i+1} \\
\text{CPU}^{i+1} & & & & & & & b_{s+1}^{\prime\, i+1} & c_{s+1}^{i+1} & & & & x_{s+1}^{i+1} \\
 & & & & & & & & . & . & & & . \\
 & & & & & & & & & b_e^{\prime\, i+1} & c_e^{i+1} & & x_e^{i+1} \\
\hdashline
 & & & & & & & & & & . & . &
\end{array}
\qquad (B.34)
$$

As a result of the decomposition, tridiagonal matrices and vectors emerge from spatially discretizing (B.17), (B.18), or (B.19) to span several CPUs. Consider figure B.4

as an example. The tridiagonal matrices constructed from the discretized version of (B.19) span over the entire ξ space index, e.g. over CPU$^{0-3}$ illustrated by the solid-red line in the figure . Similarly, the tridiagonal matrices constructed from the discretized version of (B.18) span over the entire η space index (e.g. over CPU$^{19-31}$).

Considering (B.33), forward sweeping is carried out starting at CPU^0. Once the sweeping reaches the interface between CPU^i and CPU^{i+1}, CPU^i sends $b_e^{\prime i}$, c_e^i, and $g_e^{\prime i}$ to CPU^{i+1}. Then, CPU^{i+1} continues to carry out the sweeping by sending data $b_e^{\prime i+1}$, c_e^{i+1}, and $g_e^{\prime i+1}$ to CPU^{i+2} and so on. After the forward sweeping is finalized, backward substitution starts and the sweep is done in reverse as shown in B.5.2. However, the only information being sent from CPU^{i+1} to CPU^i is x_s^{i+1}.

For a periodic system, we use the following steps:

1. Construct (B.29) and (B.30)
2. Use the parallel thomas subroutine to solve B.30 and B.30 for $[x1]$ and $[x2]$
3. CPU^0 owning the first block (contains node 1) sends $x1_1$ and $x2_1$ to CPU^N that owns the last block (contains node n)
4. CPU^N calculates x_n and broadcasts x_n to every CPU that owns a subsystem of (B.25)
5. Every CPU calculates $[x]$ from (B.28)

Notice that, by splitting (B.25) into (B.26) and (B.27), CPU^N solves the tridiagonal system (B.28) which has size one element less than the others.

B.5.3 Pipelining

In the previous subsection, we summarize how to solve a tridiagonal system in parallel. It is done simply by completing the forward/backward sweep and sending data to the proper neighbor in order to continue marching. CPU^i that finishes the forward sweep sends data to CPU^{i+1} until the last block is reached. Generally, each CPU can be responsible for thousands of tridiagonal subsystems contained in a single subdomain (or 'a block'). This subsection summarizes how to efficiently solve such a big system.

Consider a computational domain containing (nx, ny, nz) grid points. For the sake of simplicity, the domain is equally decomposed only in the y direction into NJ blocks so that CPU^0 occupies block 0, CPU^1 occupies block 1, and so on. Thus, each CPU owns a block of size $(nx, ny/NY, nz)$; given that ny/NY is, by design, an integer. Supposing that we choose to perform an implicit marching in the y direction, the resulting tridiagonal matrix is subdivided into NY sections. The easiest, however least efficient, way to solve these systems is to let CPU^0 solve all of its subsystems across the $(nx, ny/NY, nz)$ grid before sending data to CPU^1. That is, CPU^0 performs forward sweep at cell $(1, 1 \to ny/NY, 1)$, at cell $(1, 1 \to ny/NY, 2)$, and so on until cell $(nx, 1 \to ny/NY, nz)$. Next, CPU^0 packs the plane data with $nx * nz * 3$ elements (recall $b_e^{'i}$, c_e^i, and $g_e^{'i}$ in the previous subsection) at $(1 : nx, ny/NY, 1 : nz)$ and sends it to CPU^1. By following the same process for the subsequent CPUs until CPU^{NY-1} is reached, the backward substitution is then carried out in the same way from CPU^{NY-1} to CPU^0. The obvious drawback is that only one CPU is operating at a given time and the whole process will be even slower than using the serial version since there is additional communication overhead.

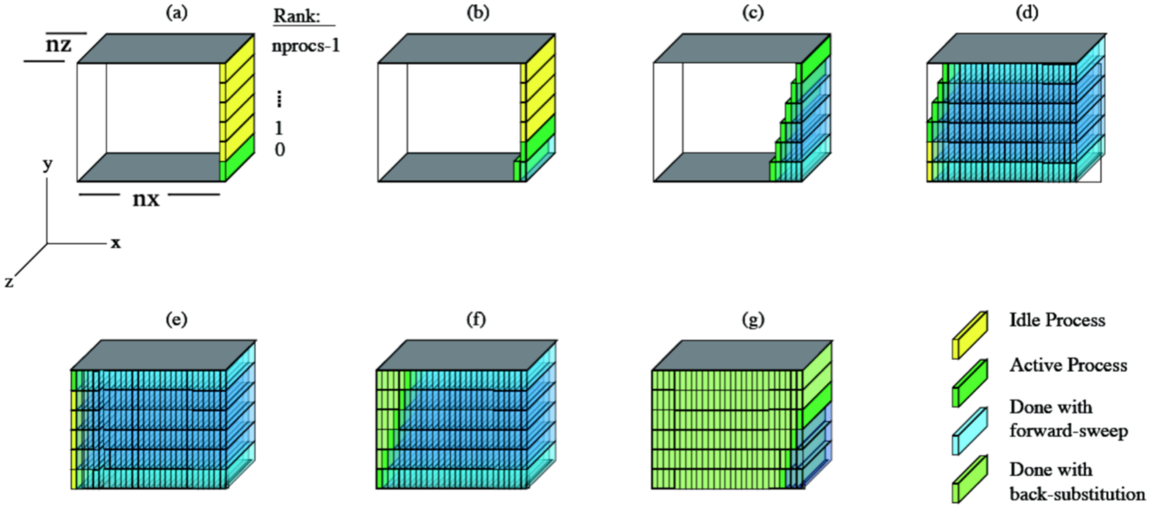

Figure B.5: Illustration of pipelining with the parallel Thomas algorithm. The figure is adapted from Figure VI.16 of Taylor (2008).

Pipelining is employed in an attempt to minimize the numbers of idle CPUs while optimizing communication overhead. In essence, rather than sweeping across the $(nx, ny/NY, nz)$ grid all at once, each CPU performs the sweeps only for a portion of the grid and shares data with its neighboring CPU in the sweep direction, downstream in a forward sweep and upstream for a backward sweep. A portion of the grid can be chosen for the first CPU with the others obeying the same portion. The example given here is called pencil-type pipelining. Consider figure B.5 and the following steps:

(a) CPU^0, process rank 0 in the figure, performs the forward sweep in the y direction at cell $(i, k) = (1, 1)$ from $(i, j, k) = (1, 1, 1)$ to $(i, j, k) = (1, ny/NY, 1)$; here i and k are dummy indices pointing to a grid location in x and z directions, respectively. CPU^0, then repeats the forward sweep until $(i, k) = (1, nz)$. Notice that the forward sweep is in the y direction but the 'pencil' aligns in the z direction. At this point, CPU^0 packs and passes data to CPU^1. The data is of size $nz * 3$ elements containing $b'^0_{ny/NY}$, $c^0_{ny/NY}$, and $g'^0_{ny/NY}$ for each $k \in [1, nz]$ (with 1-element width in the x direction, hence the word 'pencil')

(b) CPU^1 continues the forward sweep while CPU^0 starts solving the new tridiagonal system by shifting 1 step from the first block in the x, ‘slide’, direction. The ‘slide’ and ‘pencil’ directions can be swapped.

(c) CPU^1 passes data to CPU^2 for the sliding index $i = 1$, receives data from CPU^0 at the sliding index $i = 2$, and continues the forward sweep.

(d) The same process is carried out until CPU^{NY-1} reaches the slide index $i = nx$

(e) CPU^{NY-1} starts the backward sweep at the sliding index $i = nx$, shares data of size $nz * 1$-element containing x_1^{NY-1} for each $k \in [1, nz]$ with CPU^{NY-2}, and starts the backward sweep at the sliding index $i = nx - 1$.

(f) The backward sweeping process is carred out in the same way as in the forward sweep.

(g) Solving the system of tridiagonal matrices is finalized after CPU^0 finishes the backward sweep at the sliding index $i = 1$

B.5.4 Handling wake cut

So far, we are able to solve (B.17), (B.18), and (B.19) in parallel for $u^\star$, $u^{\star\star}$, and $u^{\star\star\star}$ using the parallel Thomas algorithm with pipelining. Now, consider an example of using *Fibre* to solve the problem of flow past a sphere. Figure B.7 shows an example of a C-type grid with indications of sphere body and boundary locations. The C-type grid is chosen due to its advantages in studying wake flow. In contrast to an O-type grid, a C-grid domain can be extended downstream without losing resolution or having to extend the grid upstream. A C-type grid is generated in two dimensions, such as in the Figure B.7. The two-dimensional C-type grid is then rotated around the centerline axis to form the complete three-dimensional fluid grid, shown in Figure B.6.

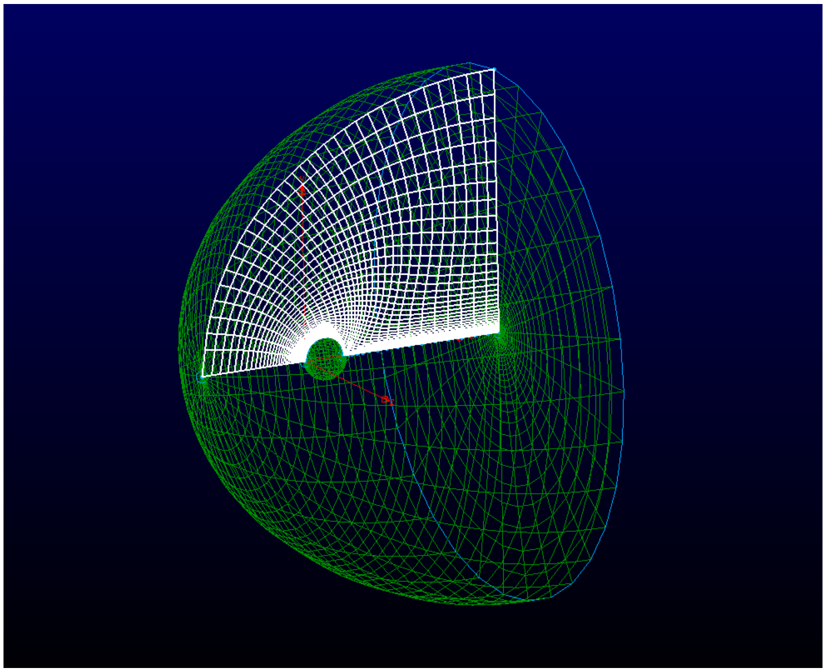

Figure B.6: Three-dimensional completed grid formed by revolving the C-type grid 360^o around the centerline.

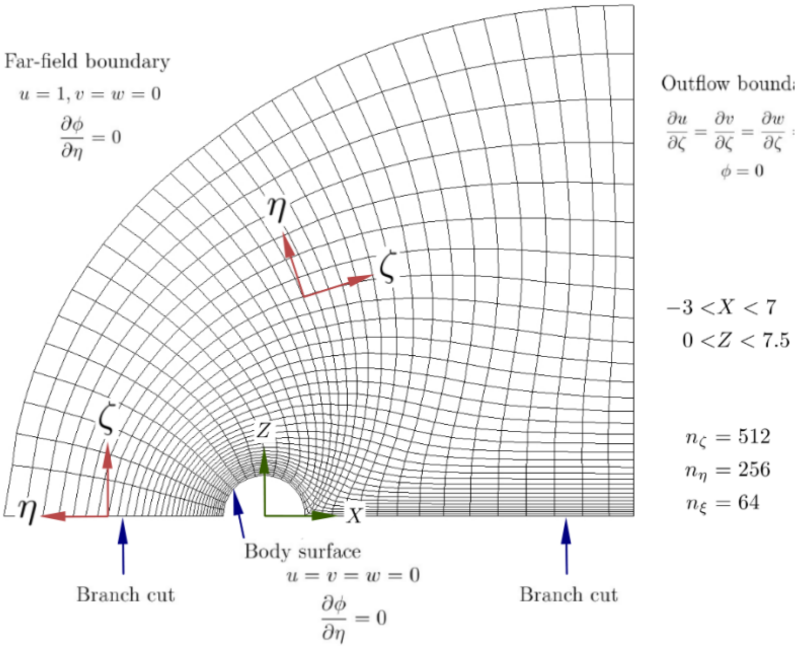

Figure B.7: C-type grid and boundary conditions used in the simulations of flow past a sphere.

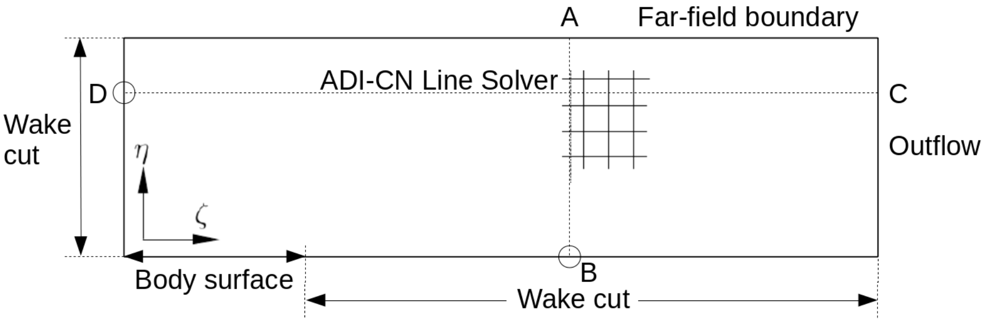

Figure B.8: The cartesian transformed grid from the curvilinear grid shown in Figure B.7.

Consider Figure B.8 showing the transformed grid. The left side of the domain parallel to the η direction, indicated by the word 'Wake cut', corresponds to the left 'Branch cut' part of the domain shown in Figure B.7. The left subsection of the bottom part of the transformed domain, the 'Body surface', corresponds to the bottom hemisphere part of the domain in Figure B.7. The right subsection of the bottom part of the transformed domain (wake cut) corresponds to the right branch cut part of the domain in Figure B.7. The words 'Wake cut' or 'Branch cut' represent a shared interface among CPUs that "cuts" through the centerline.

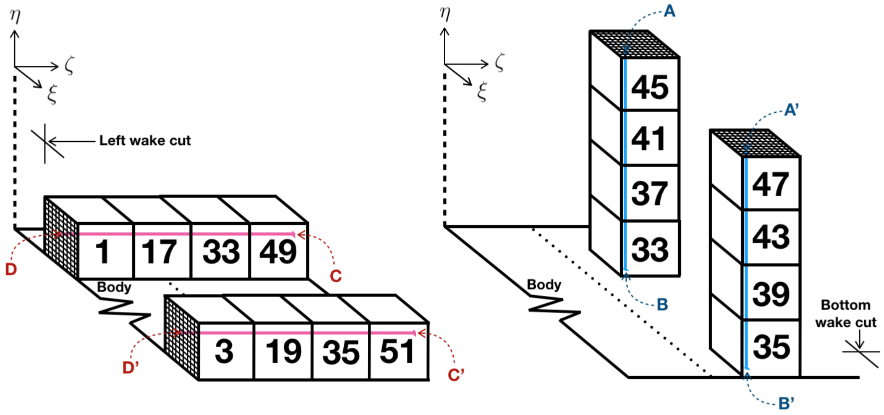

Figure B.9: Solving a tridiagonal system across a wake cut.

There are two directions that contain a wake cut, ζ and η. A tridiagonal system in the ζ direction, formed by discretizing (B.17), is interrupted with the wake cut on the left while that of the η direction, formed by discretizating (B.18), is interrupted with the wake cut at the bottom (except if it occupies the body surface). To handle the wake cut, the tridiagonal system from one side of the cut is merged with the system on the opposite side. Therefore, the resulting system is twice as large as the system without the cut.

To provide an example, consider solving a system in the η direction in the figure B.9 (right). In the forward sweeping, CPU^{45} owning point A starts solving from point A then passes information to CPU^{41} until the forward sweeping reaches CPU^{33}. Then, CPU^{33} owning point B passes the information to CPU^{35} owning point B$'$ on the other side of the cut. CPU^{35} keeps performing the forward sweep by sending data to CPU^{39} and so on until the sweep reaches A' owned by CPU^{47}. The backward substitution follows the same procedure by starting from point A$'$ and marching until the substitution reaches back to point A. The same process is employed for solving the tridiagonal matrix in the ζ direction starting from point C. Forward and backward sweeping are done using the pencil-type pipeline Thomas algorithm explained previously.

B.6 Pressure correction

Recall that *Fibre* uses a combination of the ADI-CN-RKW3 methods to obtain $u^{\star\star\star}$, the intermediate velocity. The remaining procedure in the fractional step method is to remove divergence residual from the projected velocity $u^{\star\star\star}$ at the end of each sub-RKW3 step. This step requires solving for pressure correction. As the name suggests, pressure is modified to account for the divergenceless field.

Rewriting equation (B.2) as (B.35); where $\square$ represents the advection, diffusion and baroclinic terms. (B.35) is temporally discretized into (B.36) and (B.37). Here, $u_i^{\star\star\star}$ denotes velocity at the third step of the ADI and h is a sub-time step of RKW3.

$$\frac{\partial J^{-1}u_i}{\partial t} = \square - \frac{\partial C_{ji}P}{\partial \zeta_j} \tag{B.35}$$

$$\frac{J^{-1}u_i^{\star\star\star} - J^{-1}u_i^n}{h} = \square^n - \frac{\partial C_{ji}P^n}{\partial \zeta_j} \tag{B.36}$$

$$\frac{J^{-1}u_i^{n+h} - J^{-1}u_i^n}{h} = \square^n - \frac{\partial C_{ji}P^{n+h}}{\partial \zeta_j} \tag{B.37}$$

(B.37)-(B.36) gives:

$$\frac{J^{-1}u_i^{n+h} - J^{-1}u_i^{\star\star\star}}{h} = -\frac{\partial C_{ji}\delta P^h}{\partial \zeta_j} \tag{B.38}$$

Taking divergence of (B.38) gives (B.39). Note that $\partial_i u_i^{n+h} = 0$.

$$\frac{1}{h}\frac{\partial}{\partial \zeta_j}\left[\frac{\partial \zeta_j}{\partial x_i}J^{-1}u_i^{\star\star\star}\right] = \frac{\partial}{\partial \zeta_k}\frac{\partial \zeta_k}{\partial x_i}\left[\frac{\partial}{\partial \zeta_j}J^{-1}\frac{\partial \zeta_j}{\partial x_i}\delta P^h\right] \tag{B.39}$$

This yields the Poisson equation (B.40) for pressure correction δP^h

$$\frac{\partial}{\partial \zeta_i}\frac{\partial}{\partial \zeta_j}\left[G_{ij}h\delta P^h\right] = \frac{\partial}{\partial \zeta_j}\left[C_{ji}u_i^{\star\star\star}\right] \tag{B.40}$$

Removing divergence from the $u^{\star\star\star}$ field is done by solving (B.40) for $\delta P^{\bar{h}}$ and computing $u_i^{n+\bar{h}}$ using (B.41).

$$u_i^{n+\bar{h}} = u_i^{\star\star\star} - \frac{1}{J^{-1}}\frac{\partial}{\partial \zeta_j}\left[C_{ji}\bar{h}P^{\bar{h}}\right] \tag{B.41}$$

The Poisson equation for pressure correction is solved using the Semi-Coarsening Multigrid routine in the HYPRE library. The divergence-free field $u^{n+\bar{h^{(1)}}}$ marks the end of RKW3 first sub step. We follow the same procedure until $u^{n+\bar{h^{(1)}}+\bar{h^{(2)}}+\bar{h^{(3)}}} = u^{n+1}$ is obtained. Figure B.3 illustrates the entire process.

HYPR is a library of scalable linear solvers and multigrid method (Falgout & Jones (2000); Falgout & Yang (2002)). Our choice of HYPRE stems from its ability to construct stencils at will. This allows a combination of multiple conditions on a single boundary. With the SStruct (Semi-Structured-Grid System) interface, HYPRE allows us to make connections between various ‘parts’ of a domain, a necessary requirement for handling wake cut. *Fibre* utilizes two solvers provided by HYPRE: 1) SMG, a parallel semicoarsening multigrid solver for linear systems (Brown *et al.* (2000)) and 2) BoomerAMG, a parallel implementation of the algebraic multigrid method (Ruge & Stüben (1987); Yang *et al.* (2002)).

Construction of stencils for each node (i,j,k) as a result of spatially discritizing (B.40) is summarized as follows. Consider (B.40) written in the form

$$\frac{\partial}{\partial \zeta_p}\left[G_{pq}\frac{\partial \phi}{\partial \zeta_q}\right] = \mathrm{R}. \tag{B.42}$$

The discritization of the left hand side of(B.42) for the first three terms is given in (B.6), (B.7), and (B.8). Discritization of the other terms and omitted here. The second-order central finite difference discretized version of (B.42) is

$$\begin{aligned}
&+ sc_0\phi|_{i,j,k}\\
&+ sc_1\phi|_{i-1,j,k} + sc_2\phi|_{i+1,j,k} + sc_3\phi|_{i,j-1,k}\\
&+ sc_4\phi|_{i,j+1,k} + sc_5\phi|_{i,j,k-1} + sc_6\phi|_{i,j,k+1}\\
&+ sc_7\phi|_{i,j-1,k-1} + sc_8\phi|_{i,j+1,k-1} + sc_9\phi|_{i,j+1,k+1}\\
&+ sc_{10}\phi|_{i,j-1,k+1} + sc_{11}\phi|_{i-1,j,k-1} + sc_{12}\phi|_{i-1,j,k+1}\\
&+ sc_{13}\phi|_{i+1,j,k+1} + sc_{14}\phi|_{i+1,j,k-1} + sc_{15}\phi|_{i-1,j-1,k}\\
&+ sc_{16}\phi|_{i+1,j-1,k} + sc_{17}\phi|_{i+1,j+1,k} + sc_{18}\phi|_{i-1,j+1,k} = \mathrm{R}|_{i,j,k},
\end{aligned} \tag{B.43}$$

where

$$sc_0 = -G^2_{11}|_{i+1,j,k} - G^2_{11}|_{i,j,k} - G^1_{22}|_{i,j+1,k} - G^1_{22}|_{i,j,k} - G^3_{33}|_{i,j,k+1} - G^3_{33}|_{i,j,k} \tag{B.44}$$

$$sc_1 = +G^2_{11}|_{i,j,k} \quad + 0.25(-G^1_{21}|_{i,j+1,k} + G^1_{21}|_{i,j,k} - G^3_{31}|_{i,j,k+1} + G^3_{31}|_{i,j,k}) \tag{B.45}$$

$$sc_2 = +G^2_{11}|_{i+1,j,k} + 0.25(+G^1_{21}|_{i,j+1,k} - G^1_{21}|_{i,j,k} + G^3_{31}|_{i,j,k+1} - G^3_{31}|_{i,j,k}) \tag{B.46}$$

$$sc_3 = +G^1_{22}|_{i,j,k} \quad + 0.25(-G^2_{12}|_{i+1,j,k} + G^2_{12}|_{i,j,k} - G^3_{32}|_{i,j,k+1} + G^3_{32}|_{i,j,k}) \tag{B.47}$$

$$sc_4 = +G^1_{22}|_{i,j+1,k} + 0.25(+G^2_{12}|_{i+1,j,k} - G^2_{12}|_{i,j,k} + G^3_{32}|_{i,j,k+1} - G^3_{32}|_{i,j,k}) \tag{B.48}$$

$$sc_5 = +G^3_{33}|_{i,j,k} \quad + 0.25(-G^2_{13}|_{i+1,j,k} + G^2_{13}|_{i,j,k} - G^1_{23}|_{i,j+1,k} + G^1_{23}|_{i,j,k}) \tag{B.49}$$

$$sc_6 = +G^3_{33}|_{i,j,k+1} + 0.25(+G^2_{13}|_{i+1,j,k} - G^2_{13}|_{i,j,k} + G^1_{23}|_{i,j+1,k} - G^1_{23}|_{i,j,k}) \tag{B.50}$$

$$sc_7 = 0.25(+G^1_{23}|_{i,j,k} \quad + G^3_{32}|_{i,j,k} \quad) \tag{B.51}$$

$$sc_8 = 0.25(-G^1_{23}|_{i,j+1,k} - G^3_{32}|_{i,j,k} \quad) \tag{B.52}$$

$$sc_9 = 0.25(+G^1_{23}|_{i,j+1,k} + G^3_{32}|_{i,j,k+1}) \tag{B.53}$$

$$sc_{10} = 0.25(-G^1_{23}|_{i,j,k} \quad - G^3_{32}|_{i,j,k+1}) \tag{B.54}$$

$$sc_{11} = 0.25(+G^2_{13}|_{i,j,k} \quad + G^3_{31}|_{i,j,k} \quad) \tag{B.55}$$

$$sc_{12} = 0.25(-G^2_{13}|_{i,j,k} \quad - G^3_{31}|_{i,j,k+1}) \tag{B.56}$$

$$sc_{13} = 0.25(+G^2_{13}|_{i+1,j,k} + G^3_{31}|_{i,j,k+1}) \tag{B.57}$$

$$sc_{14} = 0.25(-G^2_{13}|_{i+1,j,k} - G^3_{31}|_{i,j,k} \quad) \tag{B.58}$$

$$sc_{15} = 0.25(+G^2_{12}|_{i,j,k} \quad + G^1_{21}|_{i,j,k} \quad) \tag{B.59}$$

$$sc_{16} = 0.25(-G^2_{12}|_{i+1,j,k} - G^1_{21}|_{i,j,k} \quad) \tag{B.60}$$

$$sc_{17} = 0.25(+G^2_{12}|_{i+1,j,k} + G^1_{21}|_{i,j+1,k}) \tag{B.61}$$

$$sc_{18} = 0.25(-G^2_{12}|_{i,j,k} \quad - G^1_{21}|_{i,j+1,k}). \tag{B.62}$$

The locations of these stencils are chosen as shown in Figure B.10.

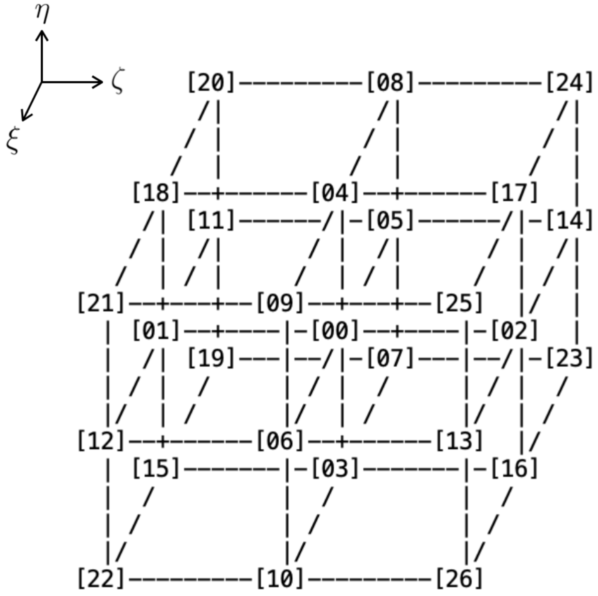

Figure B.10: Locations of stencils sc_0-sc_{18}.

Modification of these stencils is required for any cell containing a boundary/boundaries. For example, if the Dirichlet condition $\phi_{\text{outlet}} = 0$ is used at the outlet $\zeta_{\max}$, then $\phi_{i+1,:,:}{=}{-}\phi_{i,:,:}$. This indicates that when setting up all the stencils for the cell$_{i,j,k}$, $sc_0 = sc_0 - sc_2$ and so on for the stencils associated with $\phi_{i,:,:}$. Applying boundary conditions for any cell that contains more than one boundary is done in a similar manner.

B.6.1 Multigrid method

The brief description of *Fibre* would not be complete without the inclusion of the cornerstone method used to solve the Poisson-type pressure correction equation. As stated previously, *Fibre* is able to use the semi-coarsening multigrid (SMG) or the algebraic multigrid method (AMG) from the HYPRE library. The essential idea behind a multigrid method is that a solution to the Poisson-type problem can be decomposed into a linear combination of various modes, differentiated by spatial wave lengths. Different modes demand different numbers of iteration (or relaxation) to obtain an acceptably converged solution. Therefore, we ought to strategically optimize iterative steps for each mode in an attempt to minimize computational cost. As an example, a turnover time scale of an enormous eddy in a turbulent flow is much larger than that of a tiny eddy; and thus, in an attempt to numerically evolve the huge eddy with the tiny time step would be computationally costly and impractical. The idea of the multigrid method is, in a sense, similar to a multi-level large-eddy simulation in which multiple successive-coarsening grids with their own filtered governing equations are used.

While SMG relies on the geometry of a grid to perform coarsening, AMG makes a decision based solely on the matrix A, as in $A\vec{u} = \vec{\mathrm{f}}$. It builds an abstract geometry based on the so-called ‘graph’ consisting of ‘vertices’ (or nodes) and ‘links’, determined by the non-zero members of the matrix A. We will skip details regarding AMG in terms of node dependency, influence, and smoothness as there are already many excellent resources, i.e. Briggs & McCormick (2000). It is important, rather, to summarize the core concept and to include a simplified example of how a multigrid method works. The following explanation is summarized from Chapter 2 of Briggs & McCormick (2000).

B.6.1.1 Relaxation

Consider a sparse linear system, such as (B.43) for all of indices in a computational domain, to be solved using an iterative method on a single grid.

$$A\vec{u} = \vec{\mathrm{f}} \tag{B.63}$$

Here, A is a $n \times n$ matrix. We use $\vec{v}$ to denote an approximation to the exact solution $\vec{u}$, giving the error $\vec{e} = \vec{u} - \vec{v}$. Since the error $\vec{e}$ is as inaccessible as the exact solution itself, a computable measure of how well $\vec{v}$ approximates $\vec{u}$ is the residual, given by $\vec{r} = \vec{f} - A\vec{v}$. Using the definitions of $\vec{e}$ and $\vec{r}$, we obtain from (B.63) the residual equation

$$A\vec{e} = \vec{r}, \tag{B.64}$$

or,

$$\vec{u} = \vec{v} + A^{-1}\vec{r}. \tag{B.65}$$

Identifying $\vec{v}$ with the current approximation $\vec{v}^0$ and $\vec{u}$ with the new approximation $\vec{v}^1$, an iteration may be formed by taking

$$\vec{v}^{(1)} = \vec{v}^{(0)} + B\vec{r} \tag{B.66}$$

, where B is an approximation to A^{-1}. If B can be chosen to be close to A^{-1}, then the iteration should be effective. Letting R be a general iteration matrix stemming from an iterative technique that “relaxes” $\vec{v}$ towards $\vec{u}$, (B.66) can be written

$$\begin{aligned} \vec{v}^{(1)} = \vec{v}^{(0)} + B\vec{r}^{(0)} &= \vec{v}^{(0)} + B(\vec{\mathrm{f}} - A\vec{v}^{(0)}) \\ &= (I - BA)\vec{v}^{(0)} + B\vec{\mathrm{f}} \\ &= R\vec{v}^{(0)} + B\vec{\mathrm{f}}. \end{aligned} \tag{B.67}$$

Applying m iterations of R on $\vec{v}$ gives

$$\vec{v}^{(m)} = R^m\vec{v}^0 + [\sum_{n=1}^{m-1} R^n + I]B\vec{\mathrm{f}}. \tag{B.68}$$

Since the exact solution $\vec{u}$ satisfies (B.63) and can not be 'further relaxed', then

$$\vec{u} = R^m\vec{u} + [\sum_{n=1}^{m-1} R^n + I]B\vec{\mathrm{f}}. \tag{B.69}$$

Subtracting B.68 from B.69 gives the error in the mth approximation

$$\vec{e}^{(m)} = R^m\vec{e}^{(0)}. \tag{B.70}$$

It has been shown that

$$\lim_{m\to\infty} R^m = 0 \quad \text{if and only if} \quad \rho(R) < 1, \tag{B.71}$$

where $\rho(R) = max|\lambda(R)|$ is the spectral radius of the iteration matrix R. It follows that the iteration (B.68) converges for all initial guesses if and only if $\rho(R) < 1$. The eigenvalues of R can be related to the rate of decrease in e over iteration step. The fact that the eigenvectors of the matrix A correspond very closely to the eigenfunctions of the continuous model problem allows us to represent $e^{(0)}$ as a linear combination of A's eigenvectors $\vec{w}_k$,

$$\vec{e}^{(0)} = \sum_{k=1}^{n-1} c_k\vec{w}_k, \tag{B.72}$$

where the coefficient $c_k \in R$ gives the amount of each mode in the error. Substituting $\vec{e}^{(0)}$ from B.72 into B.70 gives

$$\vec{e}^{(m)} = R^m\vec{e}^{(0)} = \sum_{k=1}^{n-1} c_k R^m\vec{w}_k = \sum_{k=1}^{n-1} c_k\lambda_k^m(R)\vec{w}_k =: \sum_{k=1}^{n-1} \vec{e}_k^{(m)}. \tag{B.73}$$

Therefore, the kth mode of the mth iteration error is a result of a reduction of the kth mode of the initial error by a factor of $\lambda_k^m(R)$. To illustrate that the rate of damping of one mode differs from another, consider the following matrix A stemmed from discretization of a 1-dimensional system $A\vec{u} = \vec{f}$,

$$A = \begin{bmatrix} 2 & -1 & & & \\ -1 & 2 & -1 & & \\ & \cdot & \cdot & \cdot & \\ & & \cdot & \cdot & -1 \\ & & & -1 & 2 \end{bmatrix}. \tag{B.74}$$

A general framework to construct an iterative scheme is based on the concept of splitting $A = B - C$ where B is non singular. Setting $Bv^{(1)} - Cv^{(0)} = f$ yields

$$v^{(1)} = B^{-1}Cv^{(0)} + B^{-1}f. \tag{B.75}$$

Typically, the splitting $A = D - L - U$ is used; where D, L, and U are the diagonal, strictly lower and upper triangular parts of the matrix A. With this regular splitting, different iterative schemes can be obtained by choosing B and C. For example, choosing $B = \omega^{-1}D$ and $C = \omega^{-1}[(1-\omega)D + \omega(L+U)]$ leads to the weight Jacobi iteration, $v^{(1)} = [I - \omega D^{-1}A]v^{(0)} + \omega D^{-1}f$. The Gauss-Seidel iteration is a result of choosing $B = D - L$ and $C = U$, $v^{(1)} = (D-L)^{-1}Uv^{(0)} + (D-L)^{-1}f$. We can write

$$\vec{v}^{(1)} = R_J\vec{v}^{(0)} + D^{-1}\vec{f}, \tag{B.76}$$

where $R_J = D^{-1}(L+U)$ is the Jacobi iteration matrix obtained by setting $\omega = 1$. In the weight Jacobi method, $v^{(1)}$ is obtained from weight averaging $v^{(1)}$ from (B.76) and $v^{(0)}$ is written

$$\vec{v}^{(1)} = R_\omega\vec{v}^{(0)} + \omega D^{-1}\vec{f}, \tag{B.77}$$

where the weight Jacobi iteration matrix is given by $R_\omega = [(1-\omega)I + \omega R_J]$. It follows, from (B.6.1.1) and the definition of R_J and R_ω that

$$R_\omega = I - \frac{\omega}{2}\begin{bmatrix} 2 & -1 & & & \\ -1 & 2 & -1 & & \\ & \cdot & \cdot & \cdot & \\ & & \cdot & \cdot & -1 \\ & & & -1 & 2 \end{bmatrix}. \tag{B.78}$$

Since the eigenvalues of A are

$$\lambda_k(A) = 4sin^2\left(\frac{k\pi}{2n}\right), \qquad 1 \le k \le n-1, \tag{B.79}$$

it follows that the eigenvalues of R_ω are

$$\lambda_k(R_\omega) = 1 - \frac{\omega}{2}\lambda(A) = 1 - 2\omega sin^2\left(\frac{k\pi}{2n}\right), \qquad 1 \le k \le n-1. \tag{B.80}$$

Equation (B.80) indicates not only that $\rho(R_\omega) < 1$ for $0 < \omega < 1$ (guaranteeing convergence) but also that the damping factor varies as a function of wavenumber k for a given A with the chosen weight Jacobi method. Notice that with the Jacobi method ($\omega = 1$), both the high and low wave number components of the error are damped very slowly, $|\lambda| \to 1$. With $\omega = 1/2$, the high frequency components are damped much more quickly. As an aside, it is straight-forward to show that if we want to best damp the high frequency components with the chosen $n/2 \le k \le n-1$, the optimal value of ω is $2/3$. One important message is that the damping factor of each signal component is related to the eigenvalues of the iteration matrix and varies with the component wavenumber and the method of relaxation. There is an interesting aspect of (B.80) which arises when we want to find an optimal value of ω

that makes $\lambda_k(R_\omega)$ as small as possible for all k. Consider mode $k = 1$,

$$\begin{aligned}\lambda_{k=1}(R_\omega) &= 1 - 2\omega sin^2\left(\frac{\pi}{2n}\right)\\ &= 1 - 2\omega sin^2\left(\frac{\pi h}{2}\right) \approx 1 - \frac{\omega\pi^2 h^2}{2} \sim 1 - O(h^2), \qquad \text{(B.81)}\end{aligned}$$

where grid spacing $h = 1/n$ and n is number of grid points. The eigenvalues associated with the smoothest mode will always be close to 1 regardless of ω (for $0 < \omega \leq 1$). Decreasing the grid spacing h increases $\lambda_{k=1}$ resulting in the lesser reduction in the error, $\vec{e}^{(m)}_{k=1}$ associated with $k = 1$. This attempt to improve the accuracy of the solution worsens the convergence of not only $\lambda_{k=1}$ but all the smooth components of the error.

On one hand, this limitation guides us to use a coarser grid (increased grid spacing) to solve for smooth components since the smaller the grid spacing, the closer $\lambda_{k=1}$ is to 1. At the same time, we want to utilize a sufficiently high-resolution grid for oscillating components. A multigrid method exploits this idea by successively coarsening a grid and by recursively solving the residual equation on different levels. This is done in order to effectively relax components that are distinct in their wave numbers and to obtain an improved approximation to the exact solution. The idea of using successively coarser grids to correct an initial guess to the exact solution is called the correction scheme. It is also the basis of a strategy called nested iteration.

B.6.1.2 The correction scheme

In this part, the correction scheme is demonstrated using a two-grid scheme. Consider a one-dimensional problem $A\vec{u} = \vec{f}$ discretized on the grid Ω^x, where x denotes the grid resolution. An example using the correction scheme is as follows:

1. Starting at Ω^h, we relax m times on $A^h\vec{u}^h = \vec{\mathrm{f}}^h$ using B.77 with $\omega = 2/3$ and initial guess $\vec{v}^h$.

2. Compute the residual at Ω^h, $\vec{r}^h = \vec{\mathrm{f}}^h - A^h\vec{v}^h$.

3. Transfer the residual $\vec{r}^h$ to the next coarser level grid Ω^{2h} using straight injection, partial-weighting restriction, or full-weighting restriction defined with the operator I_h^{2h}; $\vec{r}^{2h} = I_h^{2h}\vec{r}^h$.

4. Solve $A^{2h}\vec{e}^{2h} = \vec{r}^{2h}$ for $\vec{e}^{2h}$.

5. Transfer the error $\vec{e}^{2h}$ to the fine level grid by interpolation, $\vec{e}^h = I_{2h}^h\vec{e}^{2h}$.

6. Correct the latest approximation $\vec{v}^h \leftarrow \vec{v}^h + \vec{e}^h$.

7. Repeat until residual at the fine level grid is sufficiently small.

Essentially, the correction scheme obtains an improved initial guess by solving the residual equation on the next level coarser grid. The two-grid scheme can be easily extended into the V-Cycle scheme, the μ-Cycle scheme, the full multigrid V-Cycle scheme, etc. This is because the fourth step itself (solving the residual equation) can be considered as to begin solve a new system $A^{h'}\vec{u}^{h'} = 0$ in which the same algorithm can be recursively called.

B.7 Density equation

Fibre solves the fluctuating density equation and imposes the effect of density variation on the Navier-Stokes equations under the Boussinesq approximation via the additional term $-Fr^{-2}\rho'\delta_{i3}$, on the right hand side of (B.1). The fluctuating density equation is formed by substituting the density decomposition $\rho^*(x_i^*, t) = \rho_0^* + \rho^*(z) + \rho'^*(x_i^*, t)$ into (B.82) and is then non-dimensionalized by (B.83) where the superscript $*$ denotes dimensional variable.

$$\frac{\partial \rho^*}{\partial t^*} + \frac{\partial u_j^* \rho^*}{\partial x_j^*} = \kappa \frac{\partial^2 \rho^*}{\partial x_j^* \partial x_j^*} \tag{B.82}$$

$$u_i = \frac{u_i^*}{U_c},\ x_i = \frac{x_i^*}{L_c},\ t = \frac{t^*}{L_c/U_c},\ p = \frac{p}{\rho_0 U_c^2},\ \rho = \frac{\rho^*}{-L_c \partial_z \rho(z)|_{bc}} \tag{B.83}$$

Note that the pressure term in (B.1) is now interpreted as there vertical gradient of the modified pressure accounting for hydrostatic pressure related to the linearly-stratified background density, $\rho^*(z)$. Also, notice that ρ'^* defined here accounts for both fluctuating density and density deviation.

$$\frac{\partial \rho'}{\partial t} + \frac{\partial u_j \rho'}{\partial x_j} = u_z + \frac{1}{RePr}\frac{\partial^2 \rho'}{\partial x_j \partial x_j} \tag{B.84}$$

To validate if the density equation is correctly implemented, we simulated a vertically oscillating sphere in stratified fluids and measure directions of propagating internal gravity waves. The directions are then compared with that of linear internal wave theory (Lighthill (1955)) in which propagating angle should satisfy the dispersion relation $\omega/N = cos(\theta)$ where ω, N, θ are vertical frequency of disturbance, buoyancy frequency of fluid, and propagating angle with respect to the vertical direction. Here, ω is assumed to be close to the frequency of the oscillating sphere. The simulations are setup using a C-type grid with vertical forcing. This resembles the entire computational domain being fixed in space and immersed in a vertically oscillating background stratified fluid. The boundary condition for ρ' at sphere's surface is $\partial_n \rho' = -\partial_n \rho(z)$ derived from the fact that the normal gradient of total density on the surface vanishes, $\partial_n \rho = 0 = \partial_n \rho(z) + \partial_n \rho'$. Note this is equivalent to $\rho' = 0$ and $\partial_n \rho_d = -\partial_n \rho(z)$ if we further decompose the fluctuating density into its deviation and a fluctuating component. Figure B.11 shows one validation case where θ is expected to be 45^o.

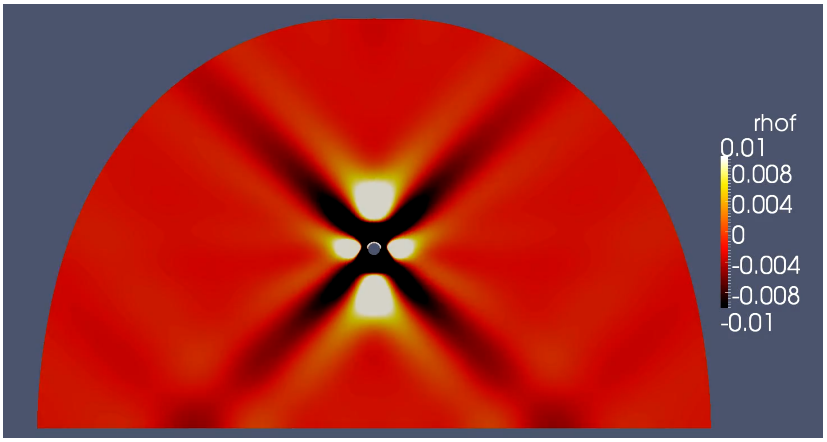

Figure B.11: Contour of fluctuating density on the vertical cut through the center of the vertically oscillating sphere. Oscillation frequency is set at 0.5N giving $\omega \simeq 0.50$N. The propagating angle is expected to be at $\theta = 45^o$.

B.8 Flow past a sphere

In this section, direct simulations of unstratified and stratified flow past a sphere at *Re*=3700 using *Fibre* are presented. The choice of *Re* allows validation against the unstratified flow past a sphere of Rodriguez *et al.* (2011). Two stratified cases are simulated at $Fr = U_\infty/ND = 1, 0.25$ using 256 CPUs. The simulations are done using the C-type grid similar to that of Figure B.7. The sphere's center is located at the origin, $(x, r) = (0, 0)$. The computational domain spans $-3 < x/D < 7$ and $-7.5 < z/D, y/d < 7.5$ where x is the streamwise direction, z and y are the vertical and the spanwise directions, respectively. The initial condition is set at $(u, v, w) = (1, 0, 0)$ throughout the entire computational domain. The boundary conditions and numbers of grid points are listed in Figure B.7. The outside of the 'C' is assigned a Dirichlet condition with the background constant free stream; $(u, v, w) = (1, 0, 0)$ and zero density fluctuation. The outflow is of type Neumann for all velocity and density fluctuations. No-slip boundary conditions are applied at the surface of sphere where, for the density, $\partial_n \rho' = -\partial_n \rho(z)$ is implemented. The variable ϕ in the figure represents pressure correction.

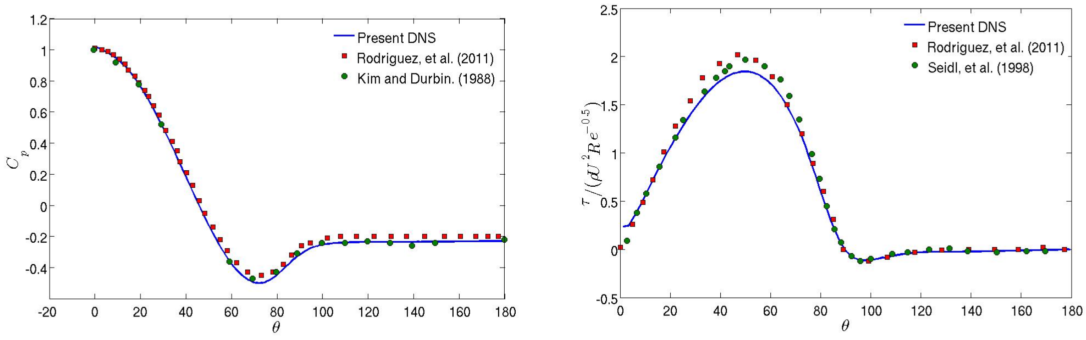

Figure B.12: Temporal and azimuthal averaged pressure and shear stress coefficients on the sphere surface, Cp and τ, for the unstratified flow past a sphere at $Re = 3700$.

Validation of the unstratified case is performed by examination of the distributions of mean pressure coefficient, mean skin friction coefficient on the body, and vortex shedding frequency. Due to the azimuthal invariance of statistics in the unstratified case, computation of the mean pressure and mean shear stress are done by averaging both in time and in the azimuthal direction.

Figure B.12 shows pressure and shear coefficients on the sphere surface in comparison to Rodriguez *et al.* (2011), Kim & Durbin (1988), and Seidl *et al.* (1997). The pressure coefficient agrees very well with the references. The shear coefficient also agrees well the with references except for the region where the shear coefficient changes abruptly between 40-60 degrees from the sphere's leading stagnation point where the underestimation could be improved with a higher grid resolution. Figure B.13 shows the power spectrum of radial velocity at the location $(x, r) = (2.4, 0.6)$ where r is in the radial direction. Two spectral peaks are observed. $St = 0.219$ is responsible for the large scale shedding frequency while $St = 0.8 - 0.9$ is responsible for the Kelvin-Helmholtz instability in the separated boundary layer. These frequencies agree well with the results of Rodriguez *et al.* (2011).

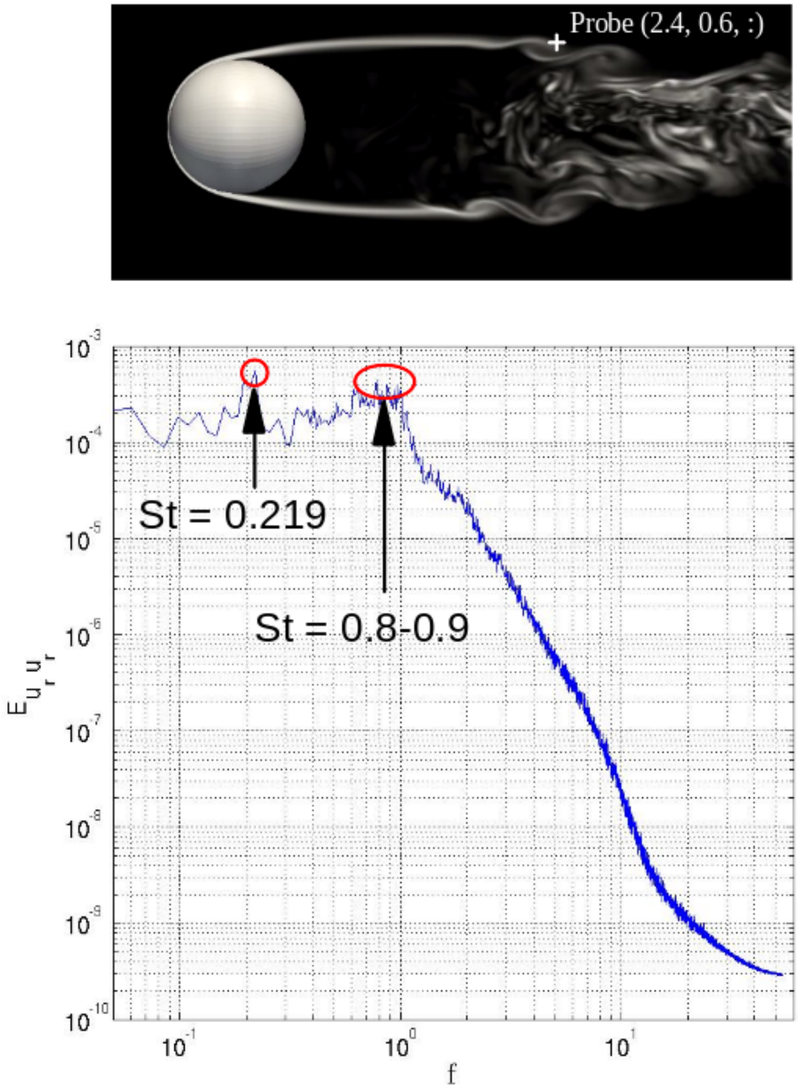

Figure B.13: Contour of the magnitude of azimuthal vorticity (top). Power spectra of the radial velocity fluctuation (bottom), probed at $(x, r) = (2.4, 0.6)$, showing two dominant Strouhal numbers associated with large-scale vortex shedding and small-scale instability at the shed shear layer.

Next, we introduce stratification to the flow. This is done by gradually decreasing Fr. Two cases are performed with $Fr = 1$ and $Fr = 0.25$. After decreasing Fr until reaching the desired values, the simulations are kept running for another cycle (one flow through). Figures B.14 and B.15 show vorticity magnitudes and total densities for the $Fr = 1$ and $Fr = 0.25$ cases.

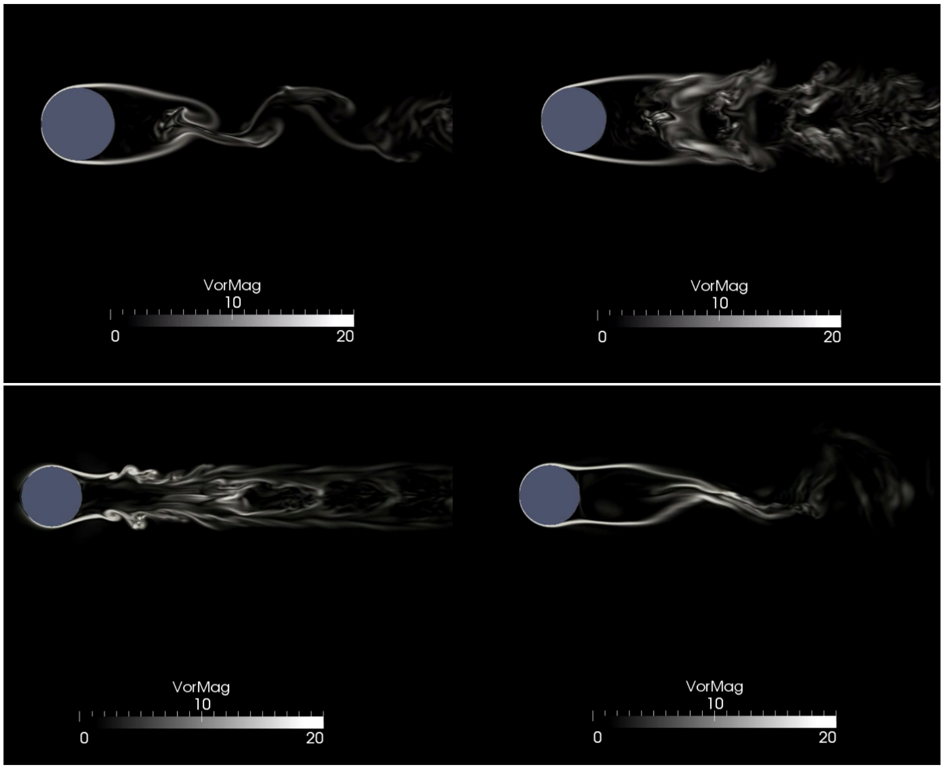

Figure B.14: Vorticity magnitude. Top: $Fr = 1$. Bottom: $Fr = 0.25$. Left: vertical cut. Right: horizontal cut.

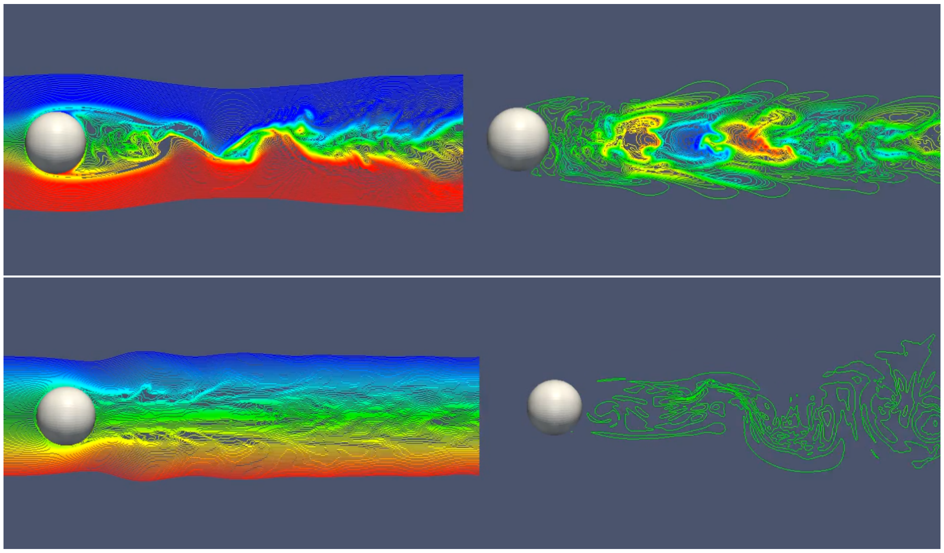

Figure B.15: Total density. Top: $Fr = 1$. Bottom: $Fr = 0.25$. The contour level spans from (blue) $-1 \le \rho \le 1$ (red).

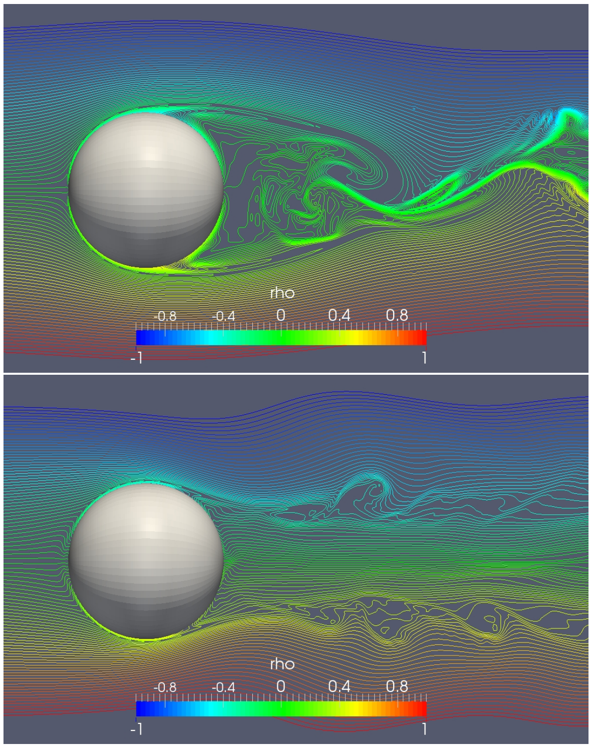

Figure B.16: Total density. Top: $Fr = 1$. Bottom: $Fr = 0.25$.

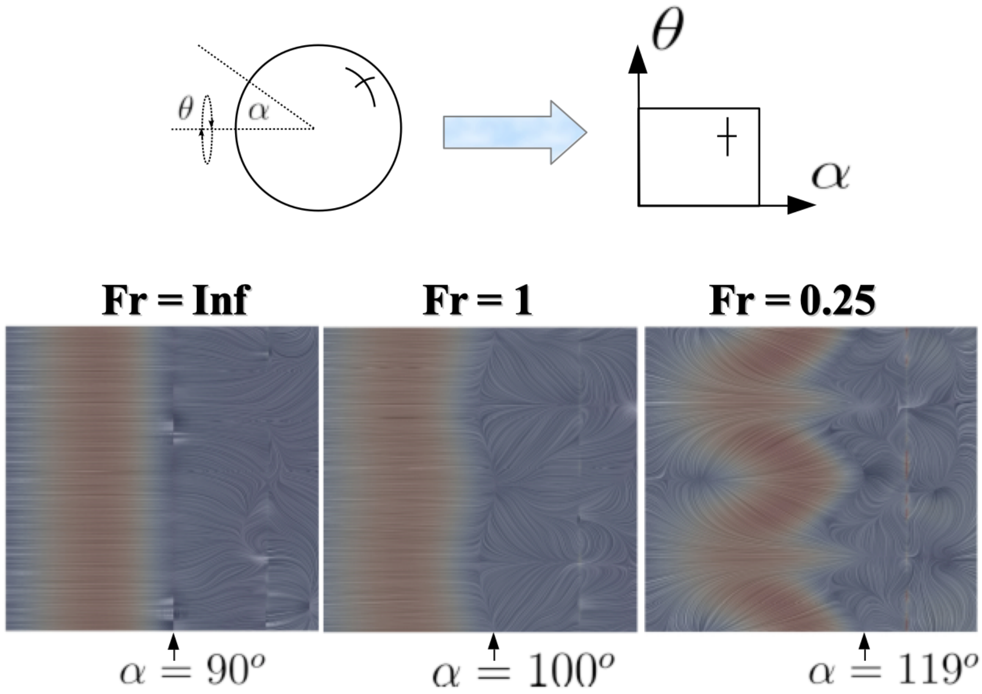

Figure B.17: Limiting streamlines.

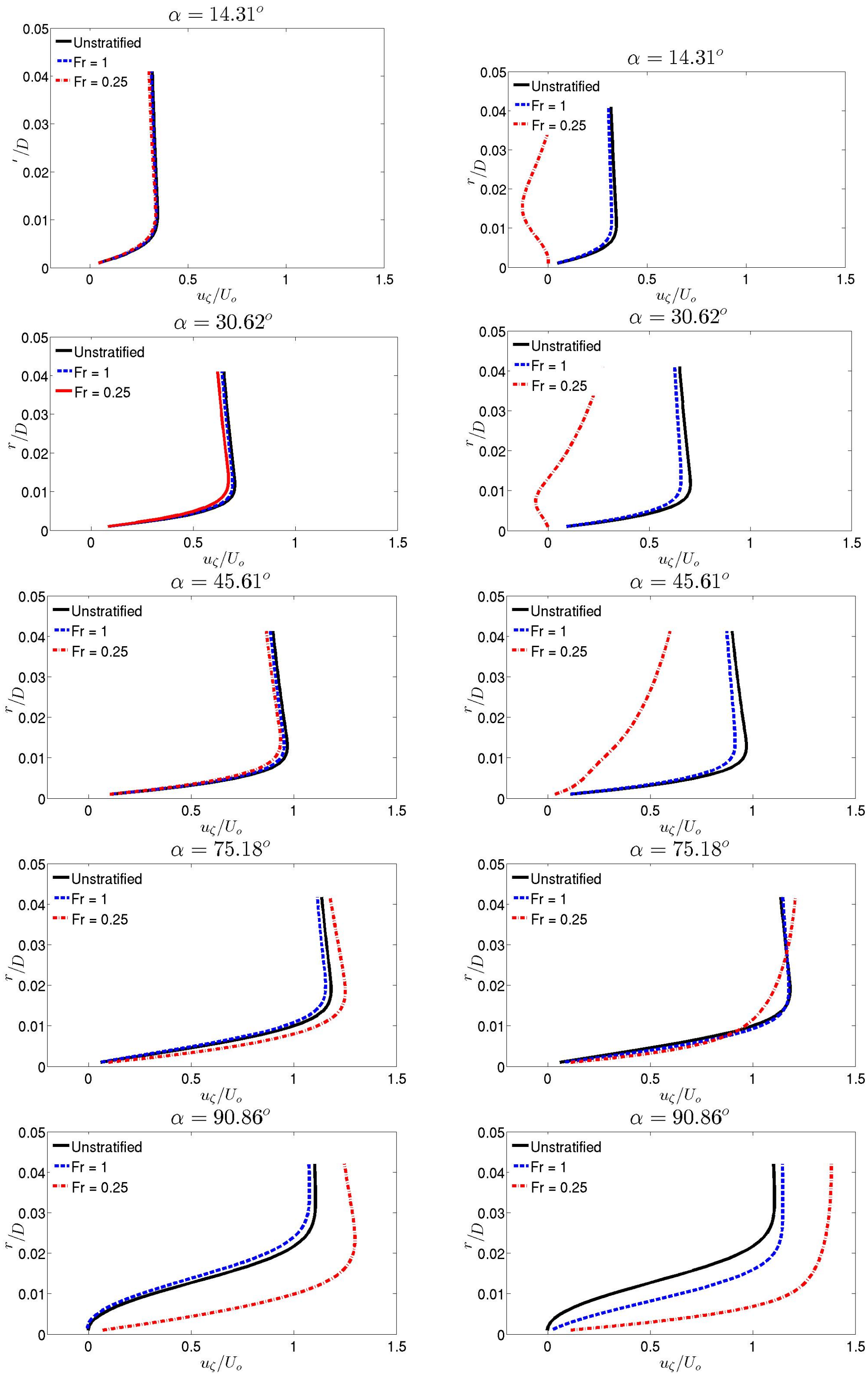

Figure B.18: Wall-normal horizontal profiles (left) and vertical profiles (right) of tangential velocity at the angle α measured from the forward stagnation point.

Some observations are detailed as follows. The vertical cuts of Figures B.14 and B.15 show the separated boundary layer on the vertical cut for both cases bending toward the centerline. This can also be seen in the magnified views in Figure B.16. At $Fr = 1$, a high density gradient package, periodically flapping vertically with $\mathrm{St} = 0.42$, is observed in the collapsed region. At $Fr = 0.25$, Kelvin-Helmholtz instabilities are observed closer to the sphere than those in the unstratified case. The boundary layer does not start developing from the sphere's leading edge as the incoming fluid situated below a certain height does not have enough kinetic energy to overcome the gravitational pull. This is why the separated shear layer does not bend completely toward the centerline. The effect of stratification at $Fr = 1$ on the boundary layer development in the horizontal plane is almost not noticable. On the other hand, $Fr = 0.25$ there is delayed separation in the horizontal. In the vertical cut, however, stratification delays separation for both cases. The limiting streamline, shown in Figure B.17, sees gradual deformations of the originally axisymmetric separation line in the unstratified case into a bow-tie shape at $Fr = 1$ and a star shape at $Fr = 0.25$.

B.9 Summary

We have successfully developed, from stratch, a generalized coordinate solver capable of solving the governing equations in parallel. Validations were performed with a vertically oscillating sphere in a stratified fluid and unstratified flow past a sphere. We obtained satisfactory results using *Fibre* to simulate stratified flows past a sphere at $Fr = 1$ and $Fr = 0.25$. Preliminary results from the simulations aided our understanding of the near-body dynamics of intermediately/strongly stratified flow past a bluff body and ignited our curiosity for the investigations presented in this thesis.

The contents of this appendix are parts of unpublished technical reports written by the dissertation author.

Appendix C

Kinetic energy equations

Derivations of the kinetic energy equations used in chapter 6 are recorded in this section. An alternative form of the turbulent kinetic energy (TKE) equation in which the subgrid stress is decomposed in a different manner is also included. A TKE budget without the subgrid contribution is described first followed by two forms including the subgrid contribution. A mean kinetic energy (MKE) budget is also presented. Derivations of turbulent and mean available potential energies (TAPE and MAPE) are synonymous to that of the TKE and MKE budget and are thus not included. Lastly, an explanation of calculating spatial derivatives is provided.

C.1 Turbulent kinetic energy

We start with the density-normalized physical law that governs an infinitestimal element acted upon by a stress tensor. Implementing the constitutive relation relating the stress tensor, f_{ij}, and the rate-of-deformation tensor, $\partial_j u_i$, we obtain $f_{ij} = (-p+\lambda\partial_m u_m)\delta_{ij} + 2\nu\partial_j u_i$. Here, the second kinemetic viscosity given by the Stoke's hypothesis, $\lambda = -2\nu/3$, indicates a friction coefficient associated with volumetric expansion (or dilatation). However, under the incompressible assumption, $\lambda\partial_m u_m$ vanishes. Note that since δ_{ij} and S_{ij} are symmetric, f_{ij} must also be symmetric. In summary,

$$D_t u_i = \partial_j f_{ij} = -\partial_i p + \partial_j \tau_{ij} = -\partial_i p + \nu \partial_{jj} u_i$$

where τ_{ij} is a shear stress tensor. Decomposing velocity and pressure into their means and fluctuations, $u_i = \overline{u_i} + u_i'$, yields

$$\begin{aligned} \partial_t \overline{u}_i + \partial_t u_i' = &- \overline{u}_j \partial_j \overline{u}_i - u_j' \partial_j \overline{u}_i - \overline{u}_j \partial_j u_i' - u_j' \partial_j u_i' \\ &- \partial_i \overline{p} - \partial_i p' + \nu \partial_{jj} \overline{u}_i + \nu \partial_{jj} u_i'. \end{aligned} \tag{C.1}$$

Multiplying C.1 with u_i' and taking an average gives

$$\begin{aligned} \partial_t (\overline{u_i' u_i'}/2) = &- \overline{u_i' u_j'} \partial_j \overline{u}_i - \overline{u}_j \partial_j (\overline{u_i' u_i'}/2) - \partial_j (\overline{u_i' u_i' u_j'}/2) \\ &- \partial_i \overline{p' u_i'} + \overline{\nu u_i' \partial_{jj} u_i'}|_A. \end{aligned} \tag{C.2}$$

Rewriting term A results in

$$\begin{aligned} \overline{\nu u_i' \partial_{jj} u_i'}|_A &= \nu \partial_{jj} (\overline{u_i' u_i'}/2)|_{A1} - \nu \overline{\partial_j u_i' \partial_j u_i'}|_{D1} \\ &= 2\nu \partial_i (\overline{u_j' S_{ij}'})|_{VT} - \nu \overline{\partial_j u_i' \partial_i u_j'}|_{D2} - \nu \overline{\partial_j u_i' \partial_j u_i'}|_{D1}. \end{aligned} \tag{C.3}$$

Therefore, the turbulent kinetic energy without a subgrid contribution becomes

$$\begin{aligned} \partial_t (\overline{u_i' u_i'}/2) = &- \overline{u}_j \partial_j (\overline{u_i' u_i'}/2) \quad (-\text{Advection}) \\ &- \overline{u_i' u_j'} \partial_j \overline{u}_i \quad (+\text{Production}) \\ &- \partial_i (\overline{p' u_i'}) - \partial_j (\overline{u_i' u_i' u_j'}/2) + 2\nu \partial_i (\overline{u_j' S_{ij}'}) \quad (-\text{Transport}) \\ &- \nu \overline{\partial_j u_i' \partial_j u_i'}|_{D1} - \nu \overline{\partial_j u_i' \partial_i u_j'}|_{D2} \quad (-\text{Dissipation}). \end{aligned} \tag{C.4}$$

Now, we consider the contribution from subgrid stress. The shear stress term can be written as a combination of ongrid and subgrid viscosities

$$Du_i = -\partial_i p + \partial_j(\tau_{ij} + \tau_{ij}^s). \tag{C.5}$$

The first form of the turbulent kinetic energy equation involves decomposition of the subgrid shear stress into its mean and fluctuating components

$$\tau_{ij}^s = \overline{\tau}_{ij}^s + \tau_{ij}'^s. \tag{C.6}$$

Therefore, the only term to be added to the evolution of turbulent kinetic energy, C.4, is $\overline{u_i'\partial_j\tau_{ij}'^s}$ which can be expanded into

$$\begin{aligned}\overline{u_i'\partial_j\tau_{ij}'^s} = &+\partial_j\overline{\tau_{ij}'^s u_i'} \quad (\text{Transport}^{\text{s}})\\ &-\overline{\tau_{ij}^s\partial_j u_i} \quad (\text{Dissipation}^{\text{s}})\\ &+\overline{\tau_{ij}'^s}\partial_j\overline{u'}_i \quad (\text{Production}^{\text{s}}).\end{aligned} \tag{C.7}$$

Here, the superscript $\Box^s$ does not necessarily indicate that mechanism $\Box$ happens at the subgrid level. It is rather a contribution of the subgrid stress.

The other form first expresses the subgrid shear stress as subgrid viscosity multiplied by strain rate, $\tau_{ij}^s = 2\nu_s S_{ij}$; $S_{ij} = (\partial_j u_i + \partial_i u_j)/2$. Then, only velocity is decomposed while the subgrid viscosity is chosen to remain composed as follows

$$\begin{aligned}\partial_j\tau_{ij}^s &= \partial_j\{2\nu_s S_{ij}\} = \partial_j\{\nu_s(\partial_j u_i + \partial_i u_j)\}\\ &= \nu_s\partial_{jj}u_i + \partial_j u_i\partial_j\nu_s + \partial_i u_j\partial_j\nu_s\\ &= \nu_s\partial_{jj}\overline{u}_i + \nu_s\partial_{jj}u_i' + \partial_j\overline{u}_i\partial_j\nu_s + \partial_j u_i'\partial_j\nu_s + \partial_i\overline{u}_j\partial_j\nu_s + \partial_i u_j'\partial_j\nu_s.\end{aligned} \tag{C.8}$$

As in the construction of the TKE equation, we first multiply C.8 with velocity fluctuations and take an average. Multiplying C.8 with u_i', and noting that $\overline{u_i'\partial_j\tau^s_{ij}} = \overline{u_i'\partial_j\tau'^s_{ij}}$, we obtain

$$\begin{aligned}\overline{u_i'\partial_j\tau'^s_{ij}} = &+ \overline{\nu_s u_i'\partial_{jj}u_i'}|_B + \overline{\nu_s u_i'}\partial_{jj}\overline{u}_i|_C + \overline{u_i'\partial_j\nu_s}\partial_j\overline{u}_i|_D \\ &+ \overline{u_i'\partial_j\nu_s}\partial_i\overline{u}_j|_E + \overline{u_i'\partial_j\nu_s\partial_j u_i'}|_F + \overline{u_i'\partial_j\nu_s\partial_i u_j'}|_X. \end{aligned} \tag{C.9}$$

Rewriting term B gives

$$\overline{\nu_s u_i'\partial_{jj}u_i'}|_B = \overline{\nu_s\partial_{jj}u_i'u_i'/2}|_{B1} - \overline{\nu_s\partial_j u_i'\partial_j u_i'}|_{B2}. \tag{C.10}$$

Consider $B1 + F$,

$$\overline{\nu_s\partial_{jj}u_i'u_i'/2}|_{B1} + \overline{u_i'\partial_j\nu_s\partial_j u_i'}|_F = \partial_j\overline{\{\nu_s\partial_j(u_i'u_i'/2)\}}|_{B1F}. \tag{C.11}$$

The physical meaning of the term $B1F$ is realized by the following expansion

$$\begin{aligned}\partial_j\overline{\{\nu_s\partial_j(u_i'u_i'/2\}}|_{B1F} &= + \partial_j\overline{\{\nu_s u_i'(\partial_j u_i' + \partial_i u_j' - \partial_i u_j')\}} \\ &= + \partial_j\{\overline{2\nu_s u_i'S'_{ij}}\}|_T \\ &\quad - \overline{\nu_s\partial_j u_i'\partial_i u_j'}|_{B3} \\ &\quad - \overline{u_i'\partial_j\nu_s\partial_i u_j'}|_{-X}. \end{aligned} \tag{C.12}$$

Here, the term T represents subgrid transport while the combination of $B2 + B3$ indicates subgrid dissipation. Note that the term $-X$ cancels out X. The combination of $C + D + E$,

$$\overline{\nu_s u_i'}\partial_{jj}\overline{u}_i|_C + \overline{u_i'\partial_j\nu_s}\partial_j\overline{u}_i|_D + \overline{u_i'\partial_j\nu_s}\partial_i\overline{u}_j|_E = \overline{u_i'\partial_j(2\nu_s\overline{S_{ij}})}|_P, \tag{C.13}$$

is the contribution to production of the subgrid viscosity. In conclusion,

$$\begin{aligned}\overline{u_i'\partial_j\tau_{ij}'^{s}} =& + \partial_j\{\overline{2\nu_s u_i' S_{ij}'}\} \quad (\text{Transport}^{\text{s}}) \\ & + \overline{u_i'\partial_j(2\nu_s\overline{S}_{ij})} \quad (\text{Production}^{\text{s}}) \\ & - \overline{\nu_s\partial_j u_i'\partial_j u_i'} - \overline{\nu_s\partial_j u_i'\partial_i u_j'} \quad (\text{Dissipation}^{\text{s}}) \qquad \text{(C.14)}\end{aligned}$$

can be considered an alternative form of the subgrid contribution to the turbulent kinetic energy equation. For a density-stratified flow under the Boussinesq approximation, the governing momentum equation C.1 includes $-g\rho^{-1}\rho\delta_{i3}$ on the right hand side. By multiplying the decomposed density $\rho = \overline{\rho} + \rho'$ by u_i' and taking an average, the turbulent kinetic energy equation in either form has an additional term

$$g\rho_0^{-1}\overline{\rho' u_i'}\delta_{i3} \quad (\text{Turbulent buoyancy flux}) \qquad \text{(C.15)}$$

otherwise known as turbulent buoyancy flux.

C.2 Mean kinetic energy

Deriving the mean kinetic energy budget is done by taking an average of C.1 and multiplying the result by the mean velocity. This gives

$$\begin{aligned}\partial_t(\overline{u}_i\overline{u}_i/2) =& - \overline{u}_j\partial_j(\overline{u}_i\overline{u}_i/2) - \overline{u}_i\partial_j\overline{u_i'u_j'} - \partial_i(\overline{u}_i\overline{p}) + \nu\overline{u}_i\partial_{jj}(\overline{u}_i) \\ =& - \overline{u}_j\partial_j(\overline{u}_i\overline{u}_i/2) \quad (-\text{Advection}) \\ & + \overline{u_i'u_j'}\partial_j\overline{u}_i \quad (-\text{Production}) \\ & + \partial_j\{-\overline{u}_j\overline{p} - \overline{u_i'u_j'}\overline{u}_i + \nu\partial_j(\overline{u}_i\overline{u}_i/2)\} \quad (-\text{Transport}) \\ & - \nu\partial_j\overline{u}_i\partial_j\overline{u}_i \quad (-\text{Dissipation}). \qquad \text{(C.16)}\end{aligned}$$

Adding the subgrid part by taking an average of C.6 and multiplying the result by the mean velocity yields

$$\begin{aligned}\overline{u}_i \partial_j \overline{\tau}^s_{ij} = &+ \partial_j(\overline{\tau}^s_{ij}\overline{u}_i) \quad (-\text{Transport}^{\text{s}}) \\ &- \overline{\tau}^s_{ij}\overline{S}_{ij} \quad (-\text{Production}^{\text{s}}).\end{aligned} \tag{C.17}$$

As in the TKE budget for a density-stratified flow under the Boussinesq approximation, the governing momentum equation C.1 includes $-g\rho^{-1}\rho\delta_{i3}$ on the right hand side. By multiplying the decomposed density $\rho = \overline{\rho} + \rho'$ by $\overline{u}_i$ and taking an average, the mean kinetic energy equation has an additional term

$$g\rho_0^{-1}\overline{u}_i\overline{\rho}\delta_{i3} \quad (\text{Mean buoyancy flux}). \tag{C.18}$$

otherwise known as mean buoyancy flux.

C.3 Computing the budgets

Lastly, budget calculations are finalized in the cartesian coordinate system. Spatial derivatives are computed in a simulated coordinate system, being either generalized curvilinear coordinates or cylindrical coordinates, after which a transformation into the cartesian coordinate system is performed. In the generalized coordinate system, the transformation

$$J^{-1}\partial_j u'_i = \partial_\zeta[(J^{-1}\partial_j\zeta)u'_i] + \partial_\eta[(J^{-1}\partial_j\eta)u'_i] + \partial_\xi[(J^{-1}\partial_j\xi)u'_i] \tag{C.19}$$

is used. Considered a subset of generalized curvilinear coordinates, the following transformation

$$\partial_y u_i' = cos\theta \partial_r u_i' - r^{-1} sin\theta \partial_\theta u_i' \tag{C.20}$$

$$\partial_z u_i' = sin\theta \partial_r u_i' - r^{-1} cos\theta \partial_\theta u_i' \tag{C.21}$$

is employed for the cylindrical coordinate system.

Appendix D

Enstrophy equation

The derivation of the fluctuating enstrophy equation appearing in chapter 3 is provided in this section. The derivation follows the exact procedure used in the previous section for the derivation of the turbulent kinetic energy budget. We start with the vorticity equation obtained from taking the curl of the governing linear momentum equation, shown in D.1.

$$\partial_t \omega_i + u_j \partial_j \omega_i = \omega_j \partial_j u_i + \nu \partial_{jj} \omega_i - g \rho^{-1} \varepsilon_{ijk} \partial_j \rho \delta_{k3} \tag{D.1}$$

Decomposing ω, u, and ρ into their mean and fluctuating components gives

$$\begin{aligned} \partial_t \overline{\omega}_i + \partial_t \omega'_i = & - \overline{u}_j \partial_j \overline{\omega}_i - \overline{u}_j \partial_j \omega'_i - u'_j \partial_j \overline{\omega}_i - u'_j \partial_j \omega'_i \\ & + \overline{\omega}_j \partial_j \overline{u}_i + \overline{\omega}_j \partial_j u'_i + \omega'_j \partial_j \overline{u}_i + \omega'_j \partial_j u'_i \\ & + \nu \partial_{jj} \overline{\omega}_i + \nu \partial_{jj} \omega'_i - g \rho^{-1} \varepsilon_{ijk} \partial_j \overline{\rho} \delta_{k3} - g \rho^{-1} \varepsilon_{ijk} \partial_j \rho' \delta_{k3}. \end{aligned} \tag{D.2}$$

Multiplying by ω_i' and taking an average yields

$$\begin{aligned}\overline{\omega_i' \partial_t \omega_i'} = &- \overline{u}_j \overline{\omega_i' \partial_j \omega_i'} - \overline{\omega_i' u_j'} \partial_j \overline{\omega}_i - \overline{\omega_i' u_j' \partial_j \omega_i'} \\ &+ \overline{\omega}_j \overline{\omega_i' \partial_j u_i'} + \overline{\omega_i' \omega_j' \partial_j \overline{u}_i} + \overline{\omega_i' \omega_j' \partial_j u_i'} \\ &+ \nu \overline{\omega_i' \partial_{jj} \omega_i'} - g \rho^{-1} \varepsilon_{ijk} \overline{\omega_i' \partial_j \rho'} \delta_{k3}. \end{aligned} \tag{D.3}$$

The viscous term can be rewritten as

$$\nu \overline{\omega_i' \partial_{jj} \omega_i'} = \nu \partial_{jj} \overline{\omega_i' \omega_i'}/2 - \nu \overline{\partial_j \omega_i' \partial_j \omega_i'}, \tag{D.4}$$

where the first term on the left hand side represents diffusion and the other represents dissipation of fluctuating enstrophy. Rearranging D.3 gives

$$\begin{aligned}\partial_t (\overline{\omega_i' \omega_i'}/2) = &- \overline{u}_j \partial_j \overline{\omega_i' \omega_i'}/2 - \overline{u_j' \omega_i'} \partial_j \overline{\omega}_i - \partial_j \overline{u_j' \omega_i' \omega_i'}/2 \\ &+ \overline{\omega_i' \omega_j' S_{ij}'} + \overline{\omega_i' \omega_j'} \overline{S}_{ij} + \overline{\omega}_j \overline{\omega_i' S_{ij}'} \\ &+ \nu \partial_{jj} \overline{\omega_i' \omega_i'}/2 - \nu \overline{\partial_j \omega_i' \partial_j \omega_i'} - g \rho^{-1} \varepsilon_{ijk} \overline{\omega_i' \partial_j \rho'} \delta_{k3}. \end{aligned} \tag{D.5}$$

Equation describing the evolution of mean-square turbulent vorticity is analogous to the turbulent kinetic energy budget which governs the evolution of mean-square velocity fluctuation. The gradient production, $-\overline{u_j' \omega_i'} \partial_j \overline{\omega}_i$, exchanges enstrophy between mean enstrophy, $\overline{\omega}_i \overline{\omega}_i$ and turbulent enstrophy, $\overline{\omega_i' \omega_i'}$. The transport term, $-\partial_j \overline{u_j' \omega_i' \omega_i'}/2$, describes advections of turbulent enstrophy by velocity fluctuations while the advection term, $-\overline{u}_j \partial_j \overline{\omega_i' \omega_i'}/2$, transports turbulent enstrophy by the mean velocity. Unlike in the TKE budget, turbulent enstrophy can be generated or removed by vortex stretching or squeezing. This process is described by the turbulent strain rate, S_{ij}', via $\overline{\omega_i' \omega_j' S_{ij}'}$ and by the mean strain rate, $\overline{S}_{ij}$, via $\overline{\omega_i' \omega_j'} \overline{S}_{ij}$. The term $\overline{\omega}_j \overline{\omega_i' S_{ij}'}$ represents stretching/tilting of mean vorticity by the turbulent strain rate. The "spatial curvature" of turbulent enstrophy is relaxed by the diffusion term, $\nu\partial_{jj}\overline{\omega_i'\omega_i'}/2$. The term $-\nu\overline{\partial_j\omega_i'\partial_j\omega_i'}$ represents the rate of diffusion of turbulent enstrophy. Lastly, density-stratified flow enables a mechanism called baroclinic torque given by $-g\rho^{-1}\varepsilon_{ijk}\overline{\omega_i'\partial_j\rho'}\delta_{k3}$.

Bibliography

Abdilghanie, A. M. & Diamessis, P. J. 2013 The internal gravity wave field emitted by a stably stratified turbulent wake. *J. Fluid Mech.* **720**, 104–139.

Armenio, V. & Sarkar, S. 2002 An investigation of stably stratified turbulent channel flow using large-eddy simulation. *J. Fluid Mech.* **459**, 1–42.

Balaras, E. 2004 Modeling complex boundaries using an external force field on fixed cartesian grids in large-eddy simulations. *Comput. Fluids* **33** (3), 375–404.

Beckers, M., Verzicco, R., Clercx, H. J. H. & Van Heijst, G. 2001 Dynamics of pancake-like vortices in a stratified fluid: experiments, model and numerical simulations. *J. Fluid Mech.* **433**, 1–27.

Bevilaqua, P. M. & Lykoudis, P. S. 1978 Turbulence memory in self-preserving wakes. *J. Fluid Mech.* **89** (3), 589–606.

Bewley, T. R. 2012 *Numerical Renaissance: simulation, optimization, & control*. Renaissance Press.

Billant, P. & Chomaz, J.-M. 2001 Self-similarity of strongly stratified inviscid flows. *Phys. Fluids* **13** (6), 1645–1651.

Bonnier, M., Bonneton, P. & Eiff, O. 1998 Far-wake of a sphere in a stably stratified fluid: characterization of the vortex structures. *Appl. Sci. Res.* **59** (2-3), 269–281.

Bonnier, M. & Eiff, O. 2002 Experimental investigation of the collapse of a turbulent wake in a stably stratified fluid. *Phys. Fluids* **14**, 791–801.

Brethouwer, G., Billant, P., Lindborg, E. & Chomaz, J. 2007 Scaling analysis and simulation of strongly stratified turbulent flows. *J. Fluid Mech.* **585**, 343–368.

Briggs, W. L. & McCormick, S. F. 2000 *A multigrid tutorial*, , vol. 72. SIAM.

Brown, P. N., Falgout, R. D. & Jones, J. E. 2000 Semicoarsening multigrid on distributed memory machines. *J. Sci. Comput.* **21** (5), 1823–1834.

Brucker, K. A. & Sarkar, S. 2010 A comparative study of self-propelled and towed wakes in a stratified fluid. *J. Fluid Mech.* **652**, 373–404.

de Bruyn Kops, S. M. & Riley, J. J. 2019 The effects of stable stratification on the decay of initially isotropic homogeneous turbulence. *J. Fluid Mech.* **860**, 787–821.

Chomaz, J. M., Bonneton, P., Butet, A., Perrier, M. & Hopfinger, E. J. 1992 Froude number dependence of the flow separation line on a sphere towed in a stratified fluid. *Phys. Fluids A* **4** (2), 254–258.

Chomaz, J.-M., Bonneton, P. & Hopfinger, E. J. 1993 The structure of the near wake of a sphere moving horizontally in a stratified fluid. *J. Fluid Mech.* **254**, 1–21.

Chongsiripinyo, K., Limdumrongtum, P., Pimpin, A. & Bunyajitradulya, A. 2008 Investigation of mixing structure in the near field of a jet in crossflow. In *Proceedings of The Twenty-Second Conference of Mechanical Engineering Network of Thailand*, pp. 15–17.

Chongsiripinyo, K., Pal, A. & Sarkar, S. 2017 On the vortex dynamics of flow past a sphere at Re= 3700 in a uniformly stratified fluid. *Phys. Fluids* **29** (2), 020704.

Chongsiripinyo, K., Pal, A. & Sarkar, S. 2019 Scaling laws in the axisymmetric wake of a sphere. In *Direct and Large-Eddy Simulation XI*, pp. 439–444. Springer.

Chongsiripinyo, K. & Sarkar, S. 2017 Effect of stratification on the turbulent wake behind a sphere at Re= 10,000. In *10th International Symposium on Turbulence and Shear Flow Phenomena (TSFP10), Chicago, USA*.

Constantinescu, G. & Squires, K. 2004 Numerical investigation of flow over a sphere in the subcritical and supercritical regimes. *Phys. Fluids* **16** (5), 1449–1466.

Dairay, T., Obligado, M. & Vassilicos, J. 2015 Non-equilibrium scaling laws in axisymmetric turbulent wakes. *J. Fluid Mech.* **781**, 166–195.

Diamessis, P. J., Domaradzki, J. A. & Hesthaven, J. S. 2005 A spectral multidomain penalty method model for the simulation of high Reynolds number localized incompressible stratified turbulence. *J. Comput. Phys.* **202** (1), 298–322.

Diamessis, P. J., Spedding, G. R. & Domaradzki, J. A. 2011 Similarity scaling and vorticity structure in high Reynolds number stably stratified turbulent wakes. *J. Fluid Mech.* **671**, 52–95.

Dommermuth, D. G., Rottman, J. W., Innis, G. E. & Novikov, E. A. 2002 Numerical simulation of the wake of a towed sphere in a weakly stratified fluid. *J. Fluid Mech.* **473**, 83–101.

Fail, R., Eyre, R. C. W. & Lawford, J. A. 1959 *Low-speed experiments on the wake characteristics of flat plates normal to an air stream.* HM Stationery Office.

Falgout, R. D. & Jones, J. E. 2000 Multigrid on massively parallel architectures. In *Multigrid Methods VI*, pp. 101–107. Springer.

Falgout, R. D. & Yang, U. M. 2002 hypre: A library of high performance preconditioners. In *International Conference on Computational Science*, pp. 632–641. Springer.

Flór, J.-B., Van Heijst, G. J. F. & Delfos, R. 1995 Decay of dipolar vortex structures in a stratified fluid. *Phys. Fluids* **7** (2), 374–383.

Garcia-Villalba, M. & Del Alamo, J. C. 2011 Turbulence modification by stable stratification in channel flow. *Phys. Fluids* **23** (4), 045104.

George, W. K. 1989 The self-preservation of turbulent flows and its relation to initial conditions and coherent structures. *Advances in Turbulence* pp. 39–73.

Germano, M., Piomelli, U., Moin, P. & Cabot, W. H. 1991 A dynamic subgrid-scale eddy viscosity model. *Phys. Fluids A* **3** (7), 1760–1765.

GI Taylor, M. 1915 I. eddy motion in the atmosphere. *Phil. Trans. R. Soc. Lond. A* **215** (523-537), 1–26.

Gibson, C., Chen, C. & Lin, S. 1968 Measurements of turbulent velocity and temperature fluctuations in the wake of a sphere. *AIAA Journal* **6** (4), 642–649.

Godoy-Diana, R. & Chomaz, J.-M. 2003 Effect of the schmidt number on the diffusion of axisymmetric pancake vortices in a stratified fluid. *Phys. Fluids* **15** (4), 1058–1064.

Godoy-Diana, R., Chomaz, J.-M. & Billant, P. 2004 Vertical length scale selection for pancake vortices in strongly stratified viscous fluids. *J. Fluid Mech.* **504**, 229–238.

Gourlay, M. J., Arendth, S. C., Fritts, D. C. & Werne, J. 2001 Numerical modeling of initially turbulent wakes with net momentum. *Phys. Fluids A* **13**, 3783–3802.

Hanazaki, H. 1988 A numerical study of three-dimensional stratified flow past a sphere. *J. Fluid Mech.* **192**, 393–419.

Hunt, J., Wray, A. & Moin, P. 1988 Eddies, streams, and convergence zones in turbulent flows. *Tech. Rep.*. CTR.

Jeong, J. & Hussain, F. 1995 On the identification of a vortex. *J. Fluid Mech.* **285**, 69–94.

Johansson, P. B., George, W. K. & Gourlay, M. J. 2003 Equilibrium similarity, effects of initial conditions and local Reynolds number on the axisymmetric wake. *Phys. Fluids* **15**, 603.

Kawamura, H., Abe, H. & Shingai, K. 2000 DNS of turbulence and heat transport in a channel flow with different Reynolds and prandtl numbers and boundary conditions. *Turbulence, Heat and Mass Transfer* **3**, 15–32.

Kim, H. J. & Durbin, P. A. 1988 Observations of the frequencies in a sphere wake and of drag increase by acoustic excitation. *Phys. Fluids* **31**, 3260–3265.

Kimura, Y. & Herring, J. R. 2012 Energy spectra of stably stratified turbulence. *J. Fluid Mech.* **698**, 19–50.

Kolmogorov, A. N. 1941 The local structure of turbulence in incompressible viscous fluid for very large Reynolds numbers. In *Dokl. Akad. Nauk SSSR*, , vol. 30, pp. 299–303.

Lighthill, M. J. 1955 *Waves in Fluids.* Cambridge University Press.

Lilly, D. K. 1983 Stratified turbulence and the mesoscale variability of the atmosphere. *J. Atmos. Sci.* **40** (3), 749–761.

Lilly, D. K. 1992 A proposed modification of the germano subgrid-scale closure method. *Phys. Fluids A* **4** (3), 633–635.

Lin, J. T. & Pao, Y. H. 1979 Wakes in stratified fluids. *Ann. Rev. Fluid Mech.* **11**, 317–338.

Lindborg, E. 2006 The energy cascade in a strongly stratified fluid. *J. Fluid Mech.* **550**, 207–242.

Lindborg, E. & Brethouwer, G. 2008 Vertical dispersion by stratified turbulence. *J. Fluid Mech.* **614**, 303–314.

Liu, H.-T. 1995 Energetics of grid turbulence in a stably stratified fluid. *J. Fluid Mech.* **296**, 127–157.

Lund, T. S. 1997 On the use of discrete filters for large eddy simulation. *Annual Research Briefs* pp. 83–95.

Maffioli, A. & Davidson, P. A. 2016 Dynamics of stratified turbulence decaying from a high buoyancy Reynolds number. *J. Fluid Mech.* **786**, 210–233.

Meneveau, C., Lund, T. S. & Cabot, W. H. 1996 A lagrangian dynamic subgrid-scale model of turbulence. *J. Fluid Mech.* **319**, 353–385.

Meunier, P., Diamessis, P. J. & Spedding, G. R. 2006 Self-preservation in stratified momentum wakes. *Phys. Fluids* **18** (10), 106601–106601.

Moser, R. D., Kim, J. & Mansour, N. N. 1999 Direct numerical simulation of turbulent channel flow up to Re= 590. *Phys. Fluids* **11** (4), 943–945.

Nedić, J., Vassilicos, J. C. & Ganapathisubramani, B. 2013 Axisymmetric turbulent wakes with new nonequilibrium similarity scalings. *Phys. Rev. Lett.* **111** (14), 144503.

Orr, T. S., Domaradzki, J. A., Spedding, G. R. & Constantinescu, G. S. 2015 Numerical simulations of the near wake of a sphere moving in a steady, horizontal motion through a linearly stratified fluid at Re= 1000. *Phys. Fluids* **27** (3), 035113.

Pacheco, P. 1997 *Parallel programming with MPI*. Morgan Kaufmann.

Pal, A., Sarkar, S., Posa, A. & Balaras, E. 2016 Regeneration of turbulent fluctuations in low-Froude number flow over a sphere at Reynolds number of 3700. *J. Fluid Mech.* **804 R2**, 1–11.

Pal, A., Sarkar, S., Posa, A. & Balaras, E. 2017 Direct numerical simulation of stratified flow past a sphere at a subcritical Reynolds number of 3700 and moderate Froude number. *J. Fluid Mech.* **826**, 5–31.

Pao, H. P. & Kao, T. W. 1977 Vortex structure in the wake of a sphere. *Phys. Fluids* **20** (2), 187–191.

Parnaudeau, P., Carlier, J., Heitz, D. & Lamballais, E. 2008 Experimental and numerical studies of the flow over a circular cylinder at Reynolds number 3900. *Phys. Fluids* **20** (8), 085101.

Pasquetti, R. 2011 Temporal/spatial simulation of the stratified far wake of a sphere. *Comput. Fluids* **40** (1), 179–187.

Pope, S. B. 2000 *Turbulent flows*. Cambridge university press.

Praud, O. 2005 The structure and dynamics of stratified dipolar vortices. *J. Fluid Mech.* **544**, 1–22.

Press, W. H. 1992 Numerical recipes in fortran: The art of computing.

Rapaka, N. R. & Sarkar, S. 2016 An immersed boundary method for direct and large eddy simulation of stratified flows in complex geometry. *J. Comput. Phys.* **322**, 511–534.

Redford, J. A., Castro, I. P. & Coleman, G. N. 2012 On the universality of turbulent axisymmetric wakes. *J. Fluid Mech.* **710**, 419.

Redford, J. A., Lund, T. S. & Coleman, G. N. 2015 A numerical study of a weakly stratified turbulent wake. *J. Fluid Mech.* **776**, 568–609.

Riley, J. J. & deBruynKops, S. M. 2003 Dynamics of turbulence strongly influenced by buoyancy. *Phys. Fluids* **15** (7), 2047–2059.

Riley, J. J. & Lelong, M.-P. 2000 Fluid motions in the presence of strong stable stratification. *Ann. Rev. Fluid Mech.* **32** (1), 613–657.

Riley, J. J. & Lindborg, E. 2008 Stratified turbulence: A possible interpretation of some geophysical turbulence measurements. *J. Atmos. Sci.* **65** (7), 2416–2424.

Riley, J. J., Metcalfe, R. W. & Weissman, M. A. 1981 Direct numerical simulations of homogeneous turbulence in density-stratified fluids. In *AIP Conference Proceedings*, , vol. 76, pp. 79–112. AIP.

Rodriguez, I., Borell, R., Lehmkuhl, O., Perez Segarra, C. & Oliva, A. 2011 Direct numerical simulation of the flow over a sphere at Re= 3700. *J. Fluid Mech.* **679**, 263–287.

Rodríguez, I., Lehmkuhl, O., Borrell, R. & Oliva, A. 2013 Flow dynamics in the turbulent wake of a sphere at sub-critical Reynolds numbers. *Computers & Fluids* **80**, 233–243.

Rossi, T. & Toivanen, J. 1999 A parallel fast direct solver for block tridiagonal systems with separable matrices of arbitrary dimension. *SIAM Journal on Scientific Computing* **20** (5), 1778–1793.

Ruge, J. W. & Stüben, K. 1987 Algebraic multigrid. In *Multigrid methods*, pp. 73–130. SIAM.

Saffman, P. G. 1967 Note on decay of homogeneous turbulence. *Phys. Fluids* **10** (6), 1349–1349.

Sakamoto, H. & Haniu, H. 1990 A study on vortex shedding from spheres in uniform flow. *J. Fluid Eng.* **112**, 386–392.

Schlichting, H. & Gersten, K. 1968 *Boundary layer theory*. Springer.

Seidl, V., Muzaferija, S. & Perić, M. 1997 Parallel dns with local grid refinement. *Appl. Sci. Res.* **59** (4), 379–394.

Seoud, R. E. & Vassilicos, J. C. 2007 Dissipation and decay of fractal-generated turbulence. *Phys. Fluids* **19** (10), 105108.

Smagorinsky, J. 1963 General circulation experiments with the primitive equations: I. the basic experiment. *Monthly weather review* **91** (3), 99–164.

Spedding, G. R. 1997 The evolution of initially turbulent bluff-body wakes at high internal Froude number. *J. Fluid Mech.* **337**, 283–301.

Spedding, G. R. 2001 Anisotropy in turbulence profiles of stratified wakes. *Phys. Fluids* **13** (8), 2361–2372.

Spedding, G. R. 2002 Vertical structure in stratified wakes with high initial Froude number. *J. Fluid Mech.* **454**, 71–112.

Spedding, G. R., Browand, F. K. & Fincham, A. M. 1996b Turbulence, similarity scaling and vortex geometry in the wake of a towed sphere in a stably stratified fluid. *J. Fluid Mech.* **314**, 53–103.

de Stadler, M. B. 2013 High resolution simulation of the turbulent wake behind a sphere in a stratified fluid. PhD thesis, UC San Diego.

de Stadler, M. B., Rapaka, N. R. & Sarkar, S. 2014 Large eddy simulation of the near to intermediate wake of a heated sphere at Re= 10,000. *Int. J. Heat. Fluid Flow* **49**, 2–10.

de Stadler, M. B. & Sarkar, S. 2012 Simulation of a propelled wake with moderate excess momentum in a stratified fluid. *J. Fluid Mech.* **692**, 28–52.

de Stadler, M. B., Sarkar, S. & Brucker, K. A. 2010 Effect of the prandtl number on a stratified turbulent wake. *Phys. Fluids* **22** (9), 095102.

Swarztrauber, P. N. 1974 A direct method for the discrete solution of separable elliptic equations. *SIAM Journal on Numerical Analysis* **11** (6), 1136–1150.

Swarztrauber, P. N. 1984 Fft algorithms for vector computers. *Parallel Computing* **1** (1), 45–63.

Taylor, G. I. 1922 Diffusion by continuous movements. *Proceedings of the london mathematical society* **2** (1), 196–212.

Taylor, J. R. 2008 Numerical simulations of the stratified oceanic bottom boundary layer. PhD thesis, UC San Diego.

Tennekes, H. & Lumley, J. L. 1972 *A first course in Turbulence*. Cambridge,Massachusetts: The MIT press.

Tomboulides, A. G. & Orszag, S. A. 2000 Numerical investigation of transitional and weak turbulent flow past a sphere. *J. Fluid Mech.* **416**, 45–73.

Townsend, A. A. 1976 *Structure of Turbulent Shear Flow*, 2nd edn. Cambridge University Press.

Uberoi, M. S. & Freymuth, P. 1970 Turbulent energy balance and spectra of axisymmetric wake. *Phys. Fluids* **13** (9), 2205–2210.

VanDine, A., Chongsiripinyo, K. & Sarkar, S. 2018 Hybrid spatially-evolving dns model of flow past a sphere. *Comput. Fluids* **171**, 41–52.

Vassilicos, J. C. 2015 Dissipation in turbulent flows. *Ann. Rev. Fluid Mech.* **47**, 95–114.

Yang, J. 2005 An embedded-boundary formulation for large-eddy simulation of turbulent flows interacting with moving boundaries. PhD thesis, U. Maryland, College Park.

Yang, J. & Balaras, E. 2006 An embedded-boundary formulation for large-eddy simulation of turbulent flows interacting with moving boundaries. *J. Comput. Phys.* **215** (1), 12–40.

Yang, U. M. *et al.* 2002 BoomerAMG: a parallel algebraic multigrid solver and preconditioner. *Applied Numerical Mathematics* **41** (1), 155–177.

Yun, G., Kim, D. & Choi, H. 2006 Vortical structures behind a sphere at subcritical Reynolds numbers. *Phys. Fluids* **18** (1), 5102.